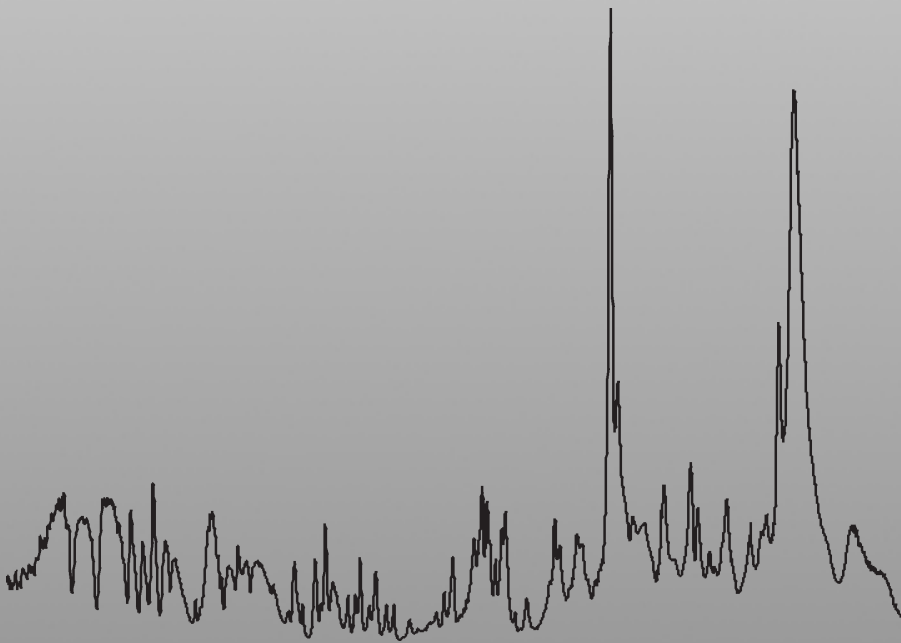


Energetics and ordering in strongly correlated oxides as seen in optics



Cristian Presura

Energetics and ordering in strongly correlated oxides as seen in optics

Front cover: Far-infrared spectrum of $\beta\text{-Na}_{0.33}\text{V}_2\text{O}_5$, for $\mathbf{E}\parallel\mathbf{b}$ (Chapter 4).

Back cover : Hamangia thinker: part of a statuary group, moulded in loam, discovered in a grave from the Neolithic necropole Cernavoda (Romania) belonging to the Hamangia civilization, approximately 5000-3000 BC.

MSC Ph.D.-thesis series 2003-04

ISSN 1570-1530



The work described in this thesis was performed in the Optical Solid State Physics group (part of the Materials Science Centre) at the Solid State Physics Laboratory of the University of Groningen, the Netherlands. The project was supported by the Dutch Foundation for Fundamental Research on Matter (FOM).

Rijksuniversiteit Groningen

Energetics and ordering in strongly correlated oxides as seen in optics

Proefschrift

ter verkrijging van het doctoraat in de
Wiskunde en Natuurwetenschappen
aan de Rijksuniversiteit Groningen
op gezag van de
Rector Magnificus, dr. F.Zwarts,
in het openbaar te verdedigen op
Vrijdag 23 mei 2003
om 14.15 uur

door

Cristian Nicolae Presura

geboren op 24 mei 1971
te Voineasa, Roemenië

Promotor : Prof. dr. D. van der Marel
Co-promotor : Dr. Ir. Paul van Loosdrecht

Beoordelingscommissie : Prof. dr. M. Golden
Prof. dr. D. I. Khomskii
Prof. dr. A. J. Leggett

ISBN : 90-367-1812-0.

Contents

1	Introduction	3
1.1	General Introduction	3
1.2	Vanadium Pentoxides	4
1.3	High temperature superconductors	6
2	Experimental Technique	11
2.1	General Introduction	11
2.2	Introduction to visible light ellipsometry	12
2.3	The influence of windows	15
2.4	Thin films	17
2.5	Magnetic Kerr effect	18
2.6	Normal incidence ellipsometry	20
2.7	Alignment of orthorhombic samples	22
3	Optical properties and electronic structure of α'-NaV_2O_5	25
3.1	Introduction	25
3.2	Optical measurements on α' - $\text{Na}_{1-x}\text{Ca}_x\text{V}_2\text{O}_5$	28
3.2.1	Details of sample preparation and experimental setup	28
3.2.2	Data collection and analyses	29
3.2.3	Main elements of the electronic structure	33
3.2.4	Discussion of the experimental spectra	34
3.3	Low temperature ellipsometry of α' - NaV_2O_5	39
3.3.1	Data collection and analyzes	39
3.3.2	Temperature dependence above the phase transition	42
3.3.3	Temperature dependence across the phase transition	45
3.3.4	Temperature dependence below the phase transition	45
3.4	Doping dependence of the far-infrared conductivity of α' - $\text{Na}_{1-x}\text{Ca}_x\text{V}_2\text{O}_5$	47
3.5	Optical measurements on α' - $\text{Na}_x\text{V}_2\text{O}_5$	51
3.6	Summary	53
4	Charge ordering signatures in the optical properties of β-$\text{Na}_{0.33}\text{V}_2\text{O}_5$	55
4.1	Introduction	55
4.2	The structure and thermodynamical properties	57
4.3	Description of the experiment	60
4.4	Room temperature data	60

4.4.1	High frequency excitations	60
4.4.2	Mid-Infrared feature	63
4.4.3	Far-infrared region	65
4.5	Low temperature data	66
4.5.1	The effect of the Na ordering on the optical spectra	66
4.5.2	Metal-insulator transition	67
4.6	Discussion	71
4.7	Summary	73
5	Coulomb energy in $Bi_2Sr_2CaCu_2O_{8+\delta}$	75
5.1	Introduction	75
5.2	BCS superconductors	77
5.3	The general form of the Coulomb interaction energy	79
5.4	Coulomb interaction energy of the layered gas	81
5.5	Coulomb energy in the low momentum sector: the " $\mathbf{k} = 0$ " approximation	83
5.6	Transfer of the spectral weight of the loss function	89
5.7	Coulomb interaction in the layered electron gas: the "DI" - approximation	93
5.8	Pair-correlation functions in the BCS theory	99
5.9	Summary	102
6	Summary	105
	Bibliography	109
	Samenvatting	117
	List of publications	121
	Acknowledgements	123

Chapter 1

Introduction

1.1 General Introduction

Transition metal oxides are compounds formed from oxygen and transition metals elements existing in the middle of the periodic table (Cu, V, Cr, etc.). Some of them have been used since ancient times as pigments, because they may present strong optical absorptions, which lead to color. Besides this, they exhibit a large variety of physical properties. They can be metals (CrO_2), semiconductors (Cu_2O) or large gap insulators (V_2O_5). Magnetically, they can behave as ferromagnets (CrO_2), ferrimagnets ($\gamma\text{-Fe}_2\text{O}_3$), or antiferromagnets ($\alpha\text{-Fe}_2\text{O}_3$). They could attain even superconductivity at relatively high temperatures ($\text{YBa}_2\text{Cu}_3\text{O}_{7-\delta}$).

A common characteristic of the most transition metal oxides is the small radial extent of the valence 3d orbitals, which is comparable with the interatomic distance, and thus the valence electrons may form narrow bands, or they could experience strong Coulomb interactions, leading to correlated motion. It is important to remember here that, in principal, Coulomb repulsion forces exist in any crystal, but do not lead immediately to a correlated electron motion. For example, the usual metals may be seen as a collection of non-interacting renormalized electrons. The reason is that the kinetic energy of the electrons, in a high density electron gas, is much larger than the interaction one.

In the transition metal oxides, the small radial extent of the valence 3d orbitals leads mainly to a strong on-site Coulomb repulsion. Here, the motion of electrons on some sites is strongly influenced by the partial presence of other electrons on those sites, and thus the motion may be correlated. This type of correlation is best exemplified by the antiferromagnetic materials, where the spin of two neighboring electrons orient in opposite direction, not because of the direct magnetic field produced by the spins, but because in this situation they can virtually hop between the two sites. We call a system *strongly correlated*, if taking into account this Coulomb interaction is essential in understanding the main physical properties.

Because the electrons in the transition metal oxides are highly correlated, a complicated relationship between the electronic, spin and lattice degrees of freedom may set in. Thus, the atomic character may be in competition with the itinerant character. In some cases, this may lead to exotic magnetic properties, since the localized character favor the local magnetic moment according to the Hund's rule, and the band character favors the

Pauli paramagnetism. Under specific conditions, the interplay of these degrees of freedom results in an equilibrium, where we can find regular patterns across the transition metal sites in the sample. Charge or spin ordering of the ground state may be easily found in many compounds. In addition, an ordering of the orbitals on which valence electrons reside may appear. This is proposed for example as the possible mechanism responsible for the temperature-induced magnetization reversal in YVO_3 [1].

If both localized and itinerant carriers exist in the material, coupling between them may arise. For example, strong coupling between correlated itinerant electrons and localized spins, both of 3d character, arises in $\text{R}_{1-x}\text{X}_x\text{MnO}_3$ (where $\text{R} = \text{La, Pr, Nd}$; $\text{X} = \text{Sr, Ca, Ba, Pb}$) compounds. This leads to giant magnetoresistance effects (a huge change of the resistance when the magnetic field is applied, such as four orders of magnitude change in thin films of $\text{Nd}_{0.7}\text{Sr}_{0.3}\text{MnO}_3$ [2]).

Many properties of the transition metal oxides can be fine-tuned with chemical substitution. The best examples of how sensitive the properties may be to chemical composition are the high temperature superconductors [3]. Here, a change of stoichiometry in $\text{YBa}_2\text{Cu}_3\text{O}_{7-\delta}$ from $\delta = 0$ to $\delta = 0.16$ turns an antiferromagnetic insulator into a superconductor.

Another property of many transition metal oxides is low dimensionality. Even though the interactions are clearly three-dimensional (the atoms stick together to form a three-dimensional crystal), the main physical properties may be considered as coming from electrons interacting only inside some planes (two dimension 2D) or lines (one dimension 1D). Examples of 2D materials are the high temperature superconductors [3], ladder compounds such as the α phase of the pentoxides [4], or triangular Kagomé lattices where geometric magnetic frustrations may occur [5]. As 1D system we may cite here the inorganic spin-Peierls material CuGeO_3 [6].

Low dimensionality creates also sensitivity when different parameters are changed. For example, in low-dimensional spin systems, quantum fluctuations could result in qualitatively different low-energy behavior. Haldane conjectured [7] that antiferromagnetic spin chains with integer spin would have a gap in the energy spectrum, whereas the spectrum of chains with half integer spins is gapless.

Many other examples of exotic properties of transition oxide materials may be enumerated here. However, we will concentrate next on the two classes of low dimensional oxides studied in this thesis: vanadium pentoxides doped with sodium (Chapters 3 and 4) and high temperature superconductors (Chapter 5). Both materials were studied experimentally using optical spectroscopy. An introduction to one of the spectroscopic techniques used, namely ellipsometry, is presented in Chapter 2.

1.2 Vanadium Pentoxides

Vanadium pentoxides represent an interesting class of transition metal oxides whose properties may be easily changed by chemical composition. This class is given by the parent insulating compound V_2O_5 [4]. The structure of V_2O_5 consists of layers of square pyramids of oxygen atoms surrounding a V^{+5} ion and thus, on pure chemical grounds, V has no valence 3d electrons. Here, many new vanadium pentoxides can be formed by

adding different electronic donors (A=Li, Na, Ca, Mg, etc.). The A atoms enter the space between the layers and act as electron donors for the V_2O_5 layers, creating three possible phases, α , β , γ [4].

Our results on the α phase of some vanadium pentoxides doped with sodium, namely α' - NaV_2O_5 , α' - $Na_{1-x}Ca_xV_2O_5$ ($0 \leq x \leq 0.2$) and α' - $Na_xV_2O_5$ ($0.85 \leq x \leq 1.00$) are presented in Chapter 3. Doping V_2O_5 with a lower concentration of Na atoms, such as in β - $Na_{0.33}V_2O_5$, creates the second β phase. Our results on the measurements on this β phase are presented in Chapter 4.

The α phase form a two-dimensional ladder pattern of V atoms. Its best known representant is α' - NaV_2O_5 , in particular because at $T_c=35K$ a phase transition occurs, below which two changes take place simultaneously [6]: a doubling of the unit cell along the ladder direction and an opening of a spin gap. At the time of its discovery it was wrongly suspected (because of a previous wrong determination of a crystal structure [8–10]) that the material presents a spin-Peierls transition (a transition where two by two electron spins of neighboring V atoms pair to form a singlet). This would have made α' - NaV_2O_5 the second inorganic material having a spin-Peierls transition after $CuGeO_3$ [6]. However, later measurements regard the material rather as a charge order system [11].

The mechanism of the phase transition, the main focus of research on α' - NaV_2O_5 , is at this point not explained, even though several proposals exist [11, 12]. The system is generally seen as a quarter-filled ladder compound with the spins carried by V-O-V molecular orbitals on the rungs of a ladder [10], and strong on-site Coulomb repulsion (thus, it is a strongly correlated electron system). The V-O-V unit behaves mainly as a H_2^+ molecule, with the ground state in a bonding state and the first excited state in an antibonding configuration. A peak would then evolve in the optical spectra corresponding to the bonding-antibonding transition of the on rung molecular orbitals. This peak was detected in measurements [13]. Later, however, other explanations were also proposed for the peak, including an on-site d-d transition between the crystal field split levels of the V-ions[14].

To discriminate between these possibilities, we conjectured that by doping α' - NaV_2O_5 with extra electrons, the intensity of the peak would show different behaviors. The electron doping is chemically realized in the single crystals samples of α' - $Na_{1-x}Ca_xV_2O_5$. These samples have been measured, and the results are presented and interpreted in the first part of Chapter 3. In addition, other temperature and doping dependencies of the vanadium pentoxides were measured, such as for α' - $Na_xV_2O_5$. We present the results of these as well, in the second part of Chapter 3.

In chapter 4, some measurements on the β phase of the vanadium pentoxides are presented, namely for β - $Na_{0.33}V_2O_5$ [15, 16]. This material is one-dimensional: the resistivity along the chain direction b is two order of magnitude smaller that the one perpendicular to the chains.

The interest in this material arose recently, because better grown stoichiometric samples show additional phase transitions missed by the older samples [17]. Below room temperature, the system undergoes three phase transitions: a structural phase transition which doubles the unit cell at $T_{Na} \simeq 240$ K, a metal-insulator transition at $T_{MI} = 136$ K (accompanied by a tripling of the unit cell along the b axis[18]) and a magnetic transition at $T_{CAF} = 22$ K [19, 20]. In addition, a transition into a superconducting state was

observed under high pressure[21].

These transitions, and the main electronic properties are not understood. Because the dilution of the donor electrons is high (one donated electron per 6 vanadium sites), the charge carriers are expected to acquire a polaronic character, in the sense that the movement of electrons disturbs the nuclei in their vicinity [22]. Strong electron-phonon coupling in $\beta\text{-Na}_{0.33}\text{V}_2\text{O}_5$ was earlier supposed to lead to formation of bipolarons [23].

The high dilution of the electrons donated to the V sites could also result in an almost equal redistribution of electrons on the three different V sites present at room temperature. This, in principle, would explain very naturally the tripling of the unit cell at the metal-insulator transition (remember that we have one donated electron per six sites). However, as pointed by Yamada in Ref. [17], the long range magnetic transition present in the system at $T_{CAF} = 22$ requires that the donated electrons are close to one another, and capable of interacting magnetically. This is surprising, since the dilution is high, and hence the distance between donated electrons is large (one should not compare this is with the situation in the high temperature oxides, since there the doped charge carriers go into an antiferromagnetic background, but in $\beta\text{-Na}_{0.33}\text{V}_2\text{O}_5$ they go on an "empty" lattice with no other d electrons present).

To give an answer to this type of considerations, more experimental data are needed. Optical measurements on $\beta\text{-Na}_{0.33}\text{V}_2\text{O}_5$ are scarce in literature, and they are almost completely absent for the new grown samples. That is why we considered that measurements in infrared and visible range could settle many important issues in this compound. In the Chapter 4 we present the results of our endeavor.

1.3 High temperature superconductors

The exotic properties of the oxides are probably best exemplified by the high temperature superconductors, which is the subject of chapter 5. These are layered structures of CuO_2 square patterns, interleaved by various cations layers which provide different doping to the CuO_2 planes. They are also generally named cuprates, even though high temperature superconductors without Cu have been found. If no doping is present, then the copper atom is in the Cu^{+2} configuration, having a hole (d^9 configuration) with a spin of $1/2$ on every Cu site. The system is then a Mott insulator, in the sense that a strong on-site Coulomb repulsion localizes the electron wave function, and the system does not conduct. Moreover, due to a super-exchange interaction between the Cu spins via the O atoms, the ground state of these undoped cuprates is antiferromagnetic.

There are two types of dopings which can be induced in the CuO_2 planes (by changing the concentration of cations, for example), electron and hole doping. The resulting phase diagram is presented in Fig. 1.1. As we can see, by doping, the Neél temperature (T_N) for the antiferromagnetic-paramagnetic transition decreases. The reason why this decrease is faster in the hole doped regime, has to do with how the doping affects the magnetic interaction. In the hole doped regime, holes enter into the oxygen p-orbital in the CuO_2 planes. This induces ferromagnetic coupling between the Cu^{+2} ions adjacent to the partially empty oxygen orbital. As a result, significant spin frustrations develop in the antiferromagnetic background, and a rapid decline of the Neél state is observed. On

the other hand, electron doping acts on the Cu^{+2} ions, giving rise to spinless Cu^+ ions, that dilute the antiferromagnetic background, but do not introduce strong spin frustrations, and hence the Neél state survives over a broader range of electron doping, as is schematically drawn in Fig. 1.1.

Upon further doping of carriers, long-range antiferromagnetism vanishes, and superconductivity sets in. This came in the beginning as a surprise, since the parent undoped compounds are insulators, in contrast to the "classical" superconductors, which are metals. More important however, is the high temperature of superconducting transition attained by the cuprates. This reaches as high as 134K at ambient pressure (and 164K with a pressure of 30GPa) in Hg- based system $\text{HgBa}_2\text{Ca}_2\text{Cu}_3\text{O}_{8+\delta}$. The transition temperature T_c for all hole-doped cuprates varies almost universally with the carrier concentration per Cu ion as $T_c = T_c^{max}[1 - 82.6(p - p_0)^2]$, where the maximum transition temperature T_c^{max} is obtained for $p = p_0 \sim 0.16$. The two doping regimes below and above p_0 are called underdoped and overdoped, respectively.

The high transition temperature of the hole doped superconducting cuprates has been the driving force behind a huge theoretical and experimental research on these compounds. An understanding of the basic mechanism leading to it is however still missing, unlike the case of classical superconductors, which are described remarkably well within the framework of BCS theory. This came both as a disappointment and as a challenge to the researchers in the field. The present situation looks like a game of puzzle, of which some of the lost puzzle pieces are recovered, but even assembled in some way, they still do not give the correct image. What is known, and what are generally accepted as the principal marks of the cuprates? We will try to summarize a small part of the immense knowledge accumulated over the past years.

A good understanding of the physics involved in the high temperature superconductors requires a correct identification of the basic building blocks, and a theory which binds these blocks together. BCS theory appeared in the beginning as a theory which, modified, may explain some of the physical properties of the superconducting cuprates. The usual ac Josephson effect frequency $2eV/h$ was still observed [24], and thus Cooper pairs may be still formed. The observed flux quantum was also found to be of the usual magnitude $hc/2e$ [25].

However, the basic building blocks of the BCS theory, the quasi-particles of the Fermi-liquid approach, were difficult to find in the normal state. This can be deduced from ARPES studies of the single particle spectral function [26], or indirectly from the analysis of different response functions of the system (such as spin or current) [27] and heat transfer [28]. Photoemission data at momentum $(0, \pi)$ in $\text{Bi}_2\text{Sr}_2\text{CaCu}_2\text{O}_{8+\delta}$ have revealed that quasi-particles may exist in the superconducting state, but they disappear slightly above T_c [29]. In addition, the optimally doped samples show the in-plane resistivity which decreases linearly as the temperature decreases, as opposite to the quadratic behavior predicted by the Fermi-liquid theory (though generally accepted, this observation is still doubted by some researchers, see [30]).

As a result, most researchers would disregard Fermi-liquid approach as applicable in the normal state, even though at asymptotically low temperature and energies the physics may be dominated by quasi-particles [31]. This is not completely surprising, since the cuprates are characterized by strong repulsion between electrons, and it does also not

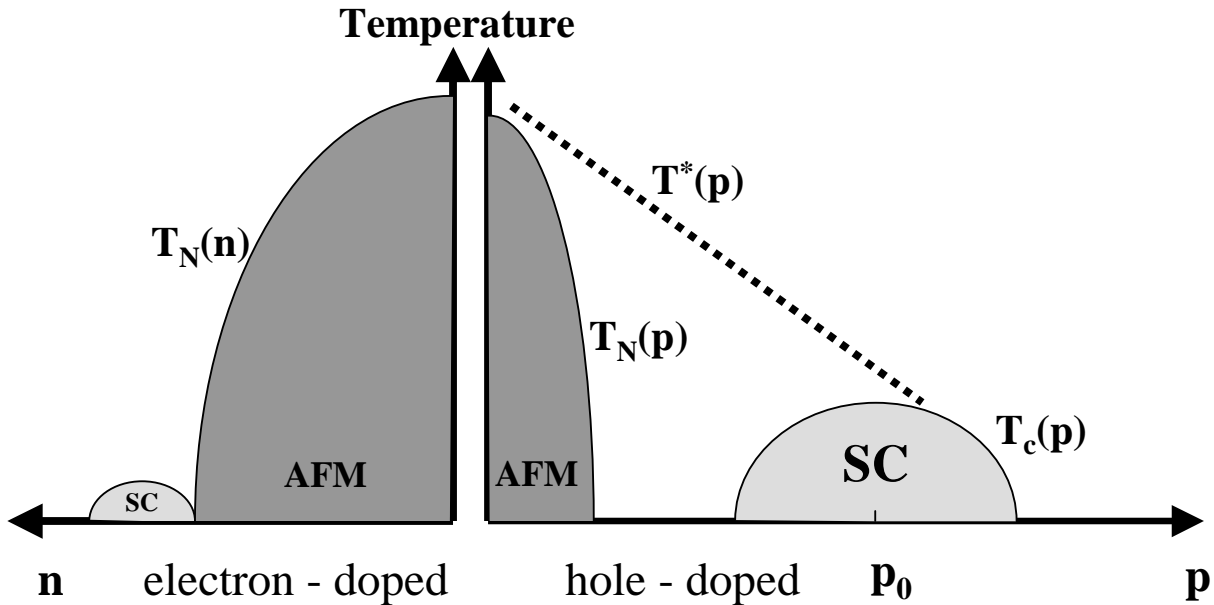


Figure 1.1: Generic phase diagram of the p-type and n-type cuprates. AFM designates the antiferromagnetic state, SC the superconducting state, and T_N , T_c , T^* are the Neel, superconducting and pseudogap transition temperatures, respectively.

completely disprove the BCS pair approach, but it led to the idea that maybe the pairing is different, for example a collective phenomenon [31].

The "glue" which binds the pair is another important ingredient to be found. In the classical superconductors, the "glue" is generated by the electron-phonon interaction. This explained why the transition temperature was so low, of the order of few or tens of K (the hierarchy gives $E_F \gg \hbar\omega_D \gg k_B T_c$). This is also the main reason why the phonon interaction is disregarded as the interaction responsible for the high transition temperature in the cuprates, even though electron-phonon influence was observed (see for example the ARPES data from Ref. [32]).

Some remaining candidates for the "glue" are the electrons themselves. For example, a 'triplet' state, which was found to give an excitation at around 41 meV in $\text{YBa}_2\text{Cu}_3\text{O}_{6.92}$ [33], was proposed to act as a binding agent [34]. Magnetically mediated superconductivity by quanta of the magnetic fluctuations was also observed in UPd_2Al_3 [35, 36]. This may come as a surprise, since magnetism and superconductivity look like oil and water, the Meissner effect assuring that the superconductor will expel the magnetic field passing through it. However, the pairing may be given by the spin fluctuations, as suggested by the recent discovery of a superconducting phase inside a ferromagnetic phase in UGe_2 [37].

More is known about the symmetry of the pair state. This has been long suspected to have a d-wave symmetry [38] (the order parameter changes sign under 90° rotation). By ingeniously designing tri-crystal substrates of SrTiO_3 , and rendering the surface with a scanning SQUID microscope, Kirtley and coworkers [39] have been able to confirm the d-wave symmetry of the order parameter, giving thus a big blow to the phonon coupling schemes, which would result in the s-symmetry of the order parameter. This type of

symmetry agrees also with the highly anisotropic form of the superconducting gap $\Delta(\mathbf{k})$ [40].

Because the parent undoped cuprates are Mott insulators, the Hubbard on-site Coulomb repulsion physics is expected to play an important role. As a result, many numerical computational procedures were dedicated to the problem. One of the first results to come out was the prediction of the so-called stripe order [41]. In the ground state, this consists of antiferromagnetic domains separated by domain walls on which the charge carriers reside. They could be in a static phase, or they could fluctuate. Their presence could explain very elegantly the position of the incommensurate magnetic peaks observed in neutron scattering measurements [42], as a function of the doping level. Later, more conclusive evidence for their presence was found [43, 44] in $\text{YBa}_2\text{Cu}_3\text{O}_{7-\delta}$. Whether superconductivity originates in charge stripes is still a matter of debate, with arguments pro [44] and against.

The high temperature superconductors are not only characterized by a low carrier concentration ($p_0 \sim 0.16$ yields about 10^{21}cm^{-3}), but also by a short coherence length, on the order of 2 or 3 lattice constants. This suggested that two "doped holes" in close proximity could form two-particle bound states, Cooper pairs, which would exist also in normal state [45], and then Bose-Einstein condense below T_c . This type of real space pairs was also dismissed (see for example the Ref. [31]), because then the chemical potential is expected to lie below the bottom of the band, whereas experimentally it is found to lie in the middle of the band.

Much attention was devoted over the time to the opening of the so-called "pseudogap", which appears in the underdoped and slightly doped samples below a temperature denoted by T^* in Fig. 1.1. The presence of the pseudogap manifests itself directly in infrared optical conductivity [46], or by plotting the frequency dependent scattering rate $1/\tau^*(\omega)$ [47], as a small spectral weight at low frequencies. Its evolution may be a sign of the collective physics associated with the growth of the electronic correlations. One option presented in Ref. [31], is that as the temperature is lowered, the antiferromagnetic fluctuations develop, and since the antiferromagnetic excitations have a gap, one might expect that these fluctuations would contribute to the pseudogap as well. It was also argued that the superconducting gap would emerge from the normal state pseudogap, which would have a d-wave symmetry as well [48]. A generally accepted picture of the origin of the pseudogap is however missing.

To account for the observed experimental facts, many proposals have been put forward. P.W. Anderson proposed in the beginning the interlayer tunnelling mechanism [3, 49], where superconductivity arises from tunnelling of electron pairs between the copper oxide planes. Later, however, Moler [50] and Tsvetkov [51] have disproved this theory by measuring the c-axis penetration depth and the interlayer plasma frequency of electron pair oscillations. They showed that interlayer tunnelling mechanism provides only 1% of the condensation energy in $\text{Tl}_2\text{Ba}_2\text{CuO}_6$.

A different approach was also invoked, a so-called Resonance Valence Bond (RVB) state [52], a quantum ground state of the electronic system, which may play a decisive role. This follows the belief that the Hubbard models, or simplified t - J models, lead to correlation effects which may play the leading role [53]. An important consequence of this theory is the spin-charge separation [54], in which low energy excitations consist of spinons

(no charge) and holons(no spin). However, no direct evidence for spin-charge separation has been obtained [55].

A phenomenological approach was used in creating the SO(5) theory [56]. It uses the fact that the HTSC emerges upon doping from the antiferromagnetic compounds. In the same way as a unification is usually done in the particle physics theories, SO(5) theory tries to unite the superconducting and antiferromagnetic phases in a larger symmetry group.

The superconducting state was also supposed to appear because frustrated kinetic energy of single charge carriers may be recovered when pairs are formed [57–59]. A model based on a kinetic energy driven mechanism of superconductivity may not require subtle induced attractions, since it may derive directly from a strong repulsion between electrons [31], but it would still require certain conditions, since a limited class of strongly correlated systems presents superconductivity. The same reduction of kinetic energy was invoked by Hirsch, who proposed a model in which the kinetic energy reduces when two holes come closer[60]. However, only recently, plausible experimental evidence was presented to support these scenarios, namely the optical measurements performed in the visible range for $Bi_2Sr_2CaCu_2O_{8+\delta}$ [61, 62], which showed that indeed the kinetic energy lowers in the superconducting state.

The behavior of the other part of the electron energy, namely the Coulomb correlation energy, is not known. Leggett [63] has proposed that this energy would decrease in the superconducting state, as a result of the improved screening due to Cooper pair formation. He also proposed that the saving of the Coulomb energy would take place primarily at midinfrared frequencies (0.1-2 eV) and small momentum vectors $q \leq 0.3\text{\AA}^{-1}$. Some attempts have been done to measure these changes using Electron Energy Loss Spectroscopy, but they proved unsuccessful, due to resolution problems of the technique.

Optical spectroscopy does have the necessary resolution, but it probes the response of the system at much smaller momenta (given by the frequency of the light used). However, it may provide useful indications. With these thought in mind, we endeavored ourselves to measure carefully the temperature dependence of the optical properties for the underdoped and optimally doped $Bi_2Sr_2CaCu_2O_{8+\delta}$, and interpret the data in terms of the Coulomb energy stored in the center of the Brillouin Zone, following an approach developed earlier by Nozieres and Pines [64]. We hoped that our quest will cover one more piece of the puzzle of the high temperature superconductors. The results are presented in the last chapter of the thesis (chapter 5).

Chapter 2

Experimental Technique

2.1 General Introduction

The presence of the visible light coming from the sun was essential to the evolution of the present forms of life, not only because it was a source of energy. The sunlight, scattered from different objects, carries also an information about the objects themselves, for example their color, form or dimensions. This type of information was crucial in the species's fight for survival. To receive this information, the species developed molecular receptors in the visible part of spectrum (which has energies of about 1eV). The intensity of this reaching the earth is high, and the energies of the first absorbtions in molecules may be around 1eV, making them suitable as detectors. In that perspective, the present optical spectroscopy is just an improvement of the technique of receiving even more information about the objects themselves, with the use of better sources, detectors, etc.

The incoming sunlight has three main characteristics: wavelength, polarization and intensity. As known, there are three molecule receptors to "measure" the spectral distribution of the incoming light. The relative intensities given by the three sensors is measured, thus providing us with the colorful image of the world. This is basically the only thing which the human eye, and thus humans, can observe easily on some incoming light. The small wavelenghts of the light (about $1\mu m$, thousand time smaller than the usual observable value of $1mm$) can be observed only via some type of experiments, like diffraction. The same happens with the quanta of light. It is interesting to note that the human eye responds to absorbtion of a single quanta [65, 66], that is a single molecular receptor is able to have a single absorbtion transition, and transmit further the information to the brain. The signal is however not allowed to reach the brain, by some neural filters, unless at least about 9 different photons are detected within less than 100 ms [65]. That is to avoid the "quantum noise" in the low intensity light!

The polarization of light was not very important to the evolution of humans, because the light coming from the sun is unpolarized, even though by reflection and refraction with air molecules or different objects it acquires a certain degree of polarization. The portion of the sky which is 90° away from the sun tends in this way to be partially polarized. This is important for some insects, like bees for example. They use the sun as a compass, being able to see the polarization pattern of the sky [67]. A Danish archaeologist, Thorkild Ramskou, suggested [68] that the Vikings might have used also the polarization of the

skylight, for navigation purposes. Their sagas describe some "sunstones", which the Vikings would have used on a cloudy weather when reaching the coast of North-America. A small, clear patch of sky close to the zenith would have been enough for determining the position of the sun. Later, it was shown directly by Wilhelm K. von Haidinger (1795-1871), that even the human eye can distinguish different states of polarization, thanks to a small aberration or "defect".

As mentioned, after reflection on different surfaces, the light tends to be partially polarized. The effect is well known to the fishermen whom, using polarized sun glasses, can filter part of the sunlight reflected by the surface of the sea, having thus a better image of the movement of the fishes below the surface. Reflections from different surfaces polarize partially the light in different ways. In that sense, a measure of the way the light is polarized after reflection is a measure of the surface properties.

2.2 Introduction to visible light ellipsometry

There are many ways in which a measurement of the reflected polarized light can take place. All use however some components called polarizers, which linearly polarize the light when travelling through them, and possible quarter-wave plates. For example, the nulling ellipsometer technique uses one polarizer before the light touches the surface, and a quarter-wave plate together with another polarizer (the analyzer) after the light is reflected. The orientations of the quarter-wave plate and the analyzer are varied until no light passes through the analyzer. From these orientations one extracts the surface properties. Modern nulling ellipsometers use computers to rotate the elements and to automatically calculate the ellipsometry signal very quickly. However, the nulling technique is not ideal for automated instruments because it is based on measuring a zero signal. This was an advantage in the early ellipsometers because the human eye is very sensitive to small changes in the signal around the 'null'. However, modern light detectors exhibit significantly higher noise at low intensities.

Another technique is Phase Modulated Ellipsometry, where the polarization of the light is modulated by a Photo-modulator. We encounter also Rotating Polarizer Ellipsometer and Rotating Analyzer Ellipsometer. We will deal in the course of this theses with an Rotating Polarizer Ellipsometer, and in Fig. 2.1 we detail its method.

As we can see from Fig. 2.1, the monochromatic light given by the monochromator passes through a fixed polarizer before touching the surface. This produces linearly polarized light that can be decomposed theoretically into two linearly polarized components, one in the plane of incidence (E_p^i) and one perpendicular to it (E_s^i), having the same phase. Because of the geometry, if the sample measured is a bulk isotropic sample, the two components are still linearly polarized after reflection on the sample, but the two phases and amplitudes are now different. We can quantify this by defining different reflectivity coefficients for the p and s components:

$$\tilde{R}_p = \frac{\tilde{E}_p^r}{\tilde{E}_p^i}; \tilde{R}_s = \frac{\tilde{E}_s^r}{\tilde{E}_s^i}; \quad (2.1)$$

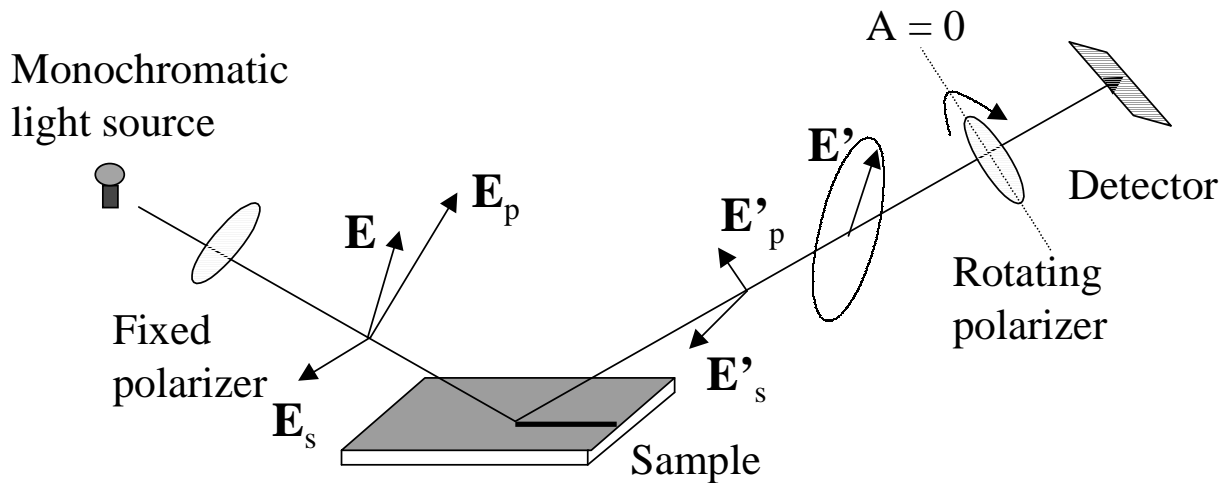


Figure 2.1: The principle of a Rotating Analyzer Ellipsometer, described in text

where \sim denotes complex numbers, and i and r stand for incidence and reflected beams. In more general cases, when the sample is anisotropic, one should use the general Jones matrices formalism [69] to define a reflection matrix:

$$\begin{pmatrix} \tilde{E}_p^r \\ \tilde{E}_s^r \end{pmatrix} = \begin{pmatrix} \tilde{R}_{pp} & \tilde{R}_{ps} \\ \tilde{R}_{sp} & \tilde{R}_{ss} \end{pmatrix} \begin{pmatrix} \tilde{E}_p^i \\ \tilde{E}_s^i \end{pmatrix} \quad (2.2)$$

In any of the two cases, anisotropic or isotropic, the recomposed light after reflection is elliptically polarized, because the relative amplitudes and phases of the two p and s components have changed. The light ellipse is described basically by two numbers, its orientation with the respect of the plane of incidence, and the ratio of the two principal axes. These two real numbers are measured by the two remaining parts of the equipment (see Fig. 2.1), the rotating polarizer (the analyzer) and the detector.

By rotating the analyzer, we can measure the intensity on the detector as a function of the analyzer angle A . Because of the ellipse of the light, it has a simple sinusoidal form:

$$I_D = I_0[1 + \alpha \cos(2A) + \beta \sin(2A)] \quad (2.3)$$

By fitting the measured curve, we can obtain the values of α and β , and the only thing left is to correlate them to the properties of the sample, namely the dielectric function. A general anisotropic sample is described however by a three-dimensional complex tensor, and one measurement is not sufficient. If the sample is orthorhombic, this tensor can be reduced to 6 real numbers, provided the orientation of the sample is known, and thus, in principle, three measurements are sufficient to find the tensor.

The case of isotropic samples is the simplest, since the dielectric tensor reduces to a single complex number for each frequency. One measurement is thus sufficient. Here we can define the complex ratio:

$$\tilde{\rho} = \tan \Psi e^{i\Delta} = \frac{\tilde{R}_{pp}}{\tilde{R}_{ss}} \quad (2.4)$$

and then the coefficients α and β from 2.3 can be then expressed as :

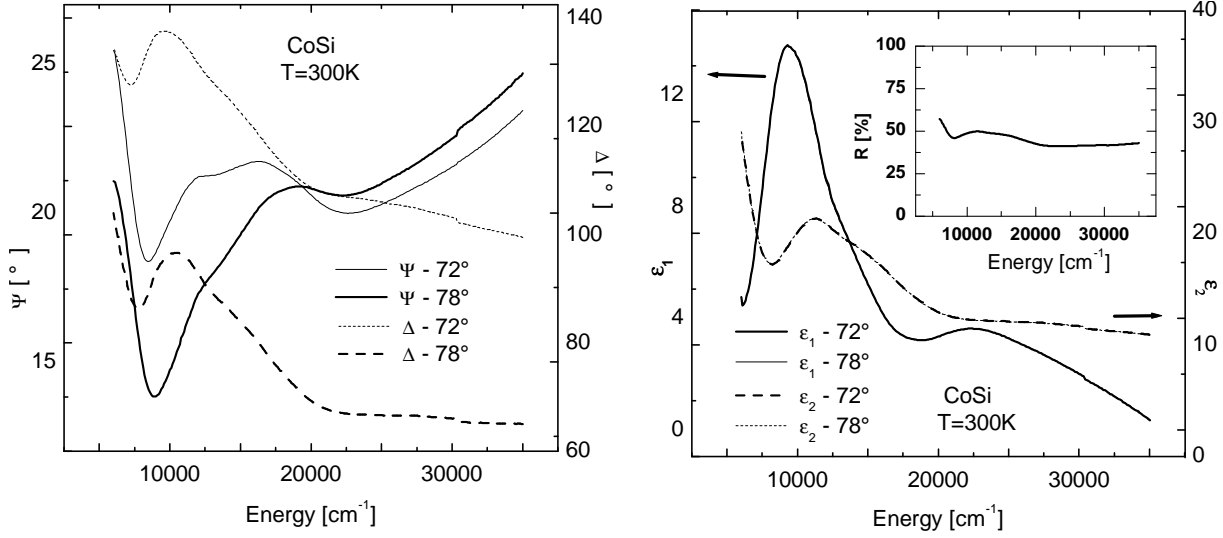


Figure 2.2: Left panel: Ψ and Δ for two angles of incidence, measured for CoSi. Right panel: The corresponding dielectric functions ϵ_1 and ϵ_2 calculated using Formula 2.9. Inset of right panel: the reflectivity at normal incidence.

$$\alpha = \frac{\tan^2 \Psi - \tan^2 P}{\tan^2 \Psi + \tan^2 P} \quad (2.5)$$

$$\beta = \frac{2 \tan \Psi \cos \Delta \tan P}{\tan^2 \Psi + \tan^2 P} \quad (2.6)$$

where P is the angle of the first polarizer, which is kept fixed during the measurements. Inverting these two equations, we obtain [69]:

$$\tan(\Psi) = \sqrt{\frac{1 + \alpha}{1 - \alpha}} |\tan(P)| \quad (2.7)$$

$$\cos(\Delta) = \frac{\beta}{\sqrt{1 - \alpha^2}} |\tan P| \quad (2.8)$$

From the equations above we can have access to the values Δ and Ψ , which are not only connected to the dielectric properties of the surface measured, but also geometry dependent. The relation between $\tilde{\rho}$ and the dielectric function $\tilde{\epsilon}$ is obtained with the use of Fresnel reflection laws [69], leading for an isotropic sample the following result:

$$\tilde{\epsilon} = \sin^2 \theta \left[1 + \tan^2 \theta \left(\frac{1 - \tilde{\rho}}{1 + \tilde{\rho}} \right)^2 \right] \quad (2.9)$$

where θ is the angle of incidence. Later in the thesis, we will use this relation for anisotropic samples as well. However, in that case, we will call the function $\tilde{\epsilon}$ the *pseudo-dielectric* function, to stress the fact that it does not describe the real dielectric tensor.

In Fig. 2.2 we present the measurements on an isotropic material, namely CoSi. The left panel shows the measured Ψ and Δ , for two angles of incidence. As we can see, there is a strong angular dependence of these two experimental quantities. The corresponding dielectric functions, calculated with formula 2.9 are presented in the right panel of Fig 2.2. The two angle of incidence measurements give the same dielectric functions, as expected, showing thus the precision of the experimental instrument.

A well known advantage of ellipsometry is that one can measure directly the two components of the complex dielectric function of an isotropic sample. This is opposed to reflectivity measurements, where one measures a single experimental function, namely the reflectivity, and one uses Kramer-Kronig relations to calculate the complex dielectric function[70]. A less obvious advantage is provided by the resolution of the instrument to measure frequency dependent changes. As we can see from the inset of Fig. 2.2, the reflectivity of CoSi is not strongly frequency dependent in the measured range (about 20%), but Ψ and Δ are (about 50%). Other advantages of ellipsometry, as opposed to reflectivity, include the fact that it does not need a reference to measure the absolute values.

It is interesting to note that, since the instrument measures changes in polarization of light, it probably should have been named polarimeter. However, when the technique was well established to receive a name, the name polarimeter was already in use for a different instrument, which measures the specific rotation of optically active materials. Since the state of the light is elliptical after reflecting off the surface, as we have seen above, the term ellipsometer was chosen.

2.3 The influence of windows

Measuring at low temperatures implies the presence of a cryostat. Ellipsometry is a technique sensitive to thin layers, and one should use lower pressures than in the usual reflectivity measurements. That is because the layer which is formed by air condensing on the surface of the sample is easily detected in ellipsometry. We have used an Ultra High Vacuum cryostat, with a base pressure of $2 * 10^{-8} mbar$ at room temperature, before starting the cooling. After a rapid cooling process of about half hour to 4K, the pressure in the chamber reaches $2 * 10^{-9} mbar$ very quickly, due to the fact that the cold finger of the cryostat acts as a cryogenic pump. We have checked that a measurement time of few hours assures that no "ice" grows on the sample to values detectable by the ellipsometer.

A second problem introduced by the presence of windows is the change in the polarization state of the incoming and outgoing light. We used quartz windows, which preserve the polarization state if the incoming beam enters perpendicular on the windows. However, due to the particular construction geometry of the cryostat, the light enters at a slightly tilted angle. This misalignment leads to different values of the measured Ψ and Δ . However, the changes introduced by the windows are not temperature dependent, and thus one could correct for them, knowing the room temperature values of Ψ and Δ in the presence and in the absence of the windows. This can be done, most easily if the windows have been aligned at least perpendicular to the plane of incidence.

If the windows are placed perpendicular to the plane of incidence, and for an isotropic

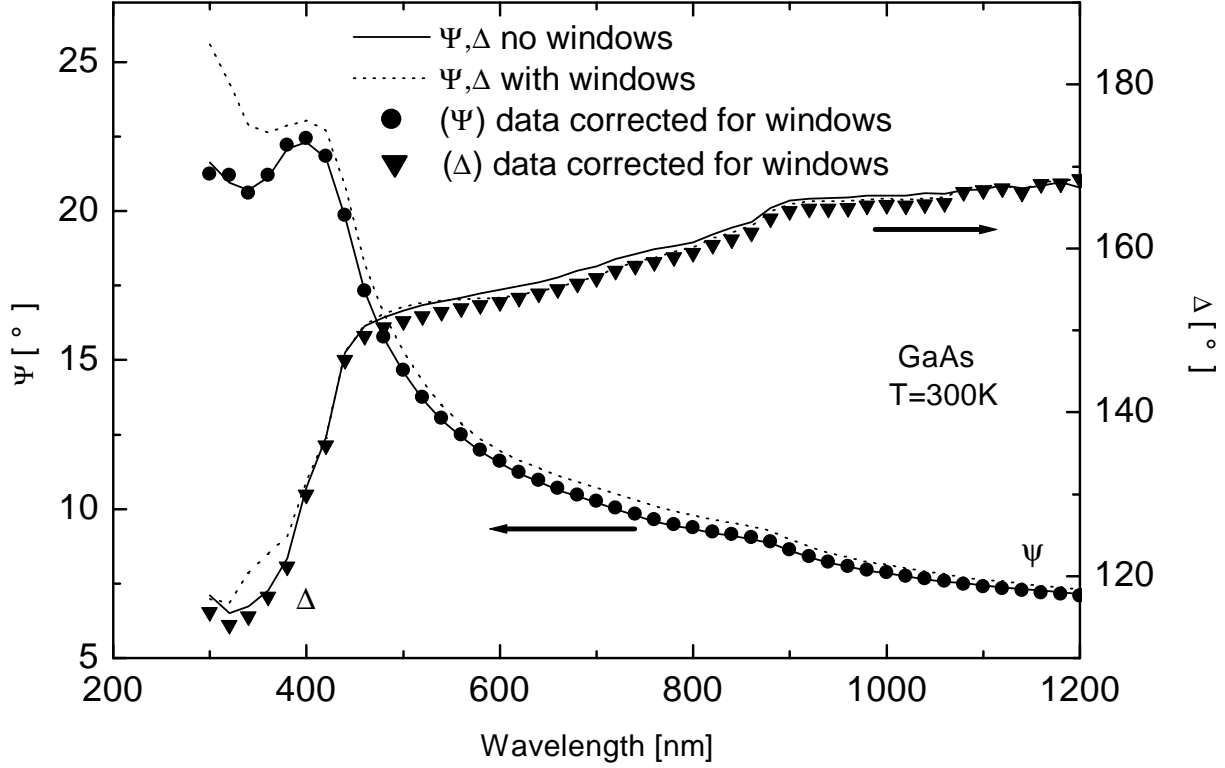


Figure 2.3: Two measurements of Ψ and Δ performed in the absence of windows (solid line) and in their presence (dotted line). The points present the correction which was performed on the data measured with windows, described in the text.

sample, each component of the light beam (p and s , see Fig. 2.1) preserves independently its orientation. In other words, the p -polarized light remains p -polarized after entering the first window of the cryostat, reflecting the surface, and passing through the exit window. However, every time the light beam hits the surface of a window, some part of the p and s components is reflected. Since the windows are tilted, one component is reflected more than the other. This modifies also the ratio of the transmitted components, so after the whole chain window-sample-window, the ratio of the p and s components are modified. We can write the following relation:

$$\tilde{E}_p^e = \tilde{E}_p^i * \tilde{R}_p^{wind1} * \tilde{R}_p^{sample} * \tilde{R}_p^{wind2} \quad (2.10)$$

$$\tilde{E}_s^e = \tilde{E}_s^i * \tilde{R}_s^{wind1} * \tilde{R}_s^{sample} * \tilde{R}_s^{wind2} \quad (2.11)$$

where \tilde{R} represents the complex reflectivity of different components, and \tilde{E} is the electric field (in the complex form) of the incoming (i) or exiting (e) light beam. The effect of the two windows can now be rewritten in a simpler relation, if we divide the upper relations, and use the definition 2.4 :

$$\tilde{\rho}_{wp} = \tilde{\rho}_{wind} * \tilde{\rho}_{wa} \quad (2.12)$$

where wp stands for the measurements with windows being present, and wa for the

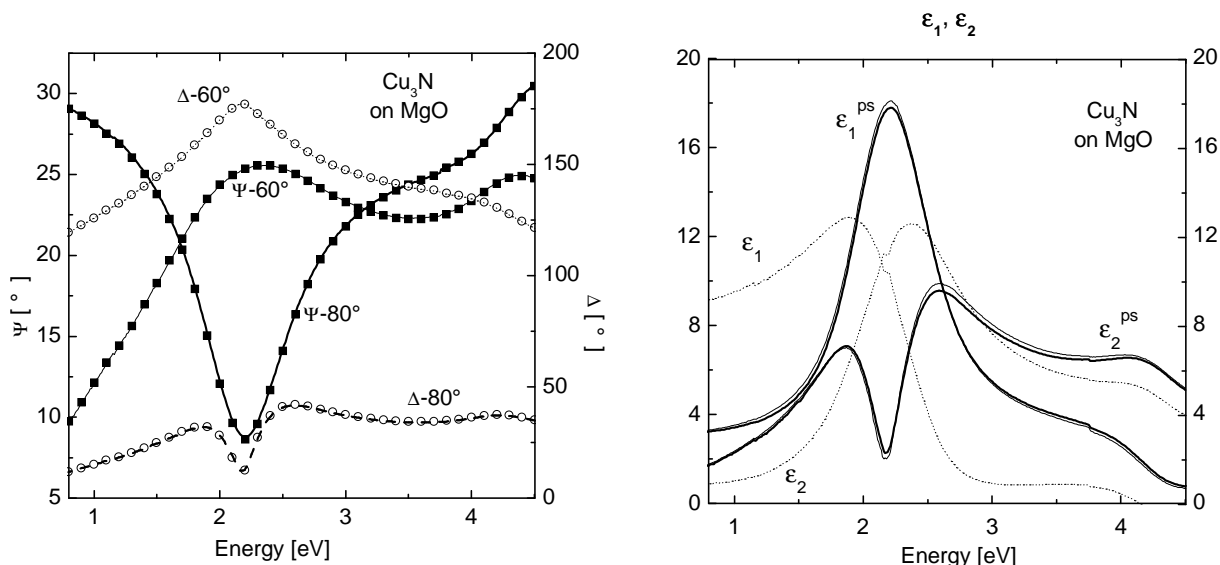


Figure 2.4: Left panel: Measured Ψ and Δ together with the fit, for a Cu_3N thin film (18.6 nm) grown at 150° on a MgO substrate. Right panel: The corresponding *pseudo-dielectric* functions (for the whole system) at the angles of incidence 60° (thin solid line) and 80° (thick solid line). The dotted lines represent the calculated ϵ_1 and ϵ_2 of Cu_3N from the fit.

measurements with windows absent. We see thus the way in which the corrections can be done for the measurements at low temperatures. One measures the room temperature sample with and without the windows, obtaining $\tilde{\rho}_{wp}$ and $\tilde{\rho}_{wa}$. Replacing this into 2.4 one gets $\tilde{\rho}_{wind}$, the window correction values. At low temperatures, one measures $\tilde{\rho}_{wp}^T$, and uses the previously found value $\tilde{\rho}_{wind}$ (which is temperature independent) and 2.4 to obtain the correct complex ratio of the sample $\tilde{\rho}_{wa}^T$.

In Fig. 2.3 we have checked this procedure, by two measurements on GaAs performed in the presence and absence of the windows. Prior to this, two other measurements were performed in the same configuration for FeSi, from which the influence of the windows was calculated using 2.12, namely $\tilde{\rho}_{wind}$. This was used to correct the values measured on GaAs in the presence of windows $\tilde{\rho}_{wp}$, to see if we obtain the same values as for the measurements done in absence of the windows. As we can see from figure 2.12, the corrected values (represented as symbols) are located closely to the values obtained from the measurements done in the absence of the windows, showing that the correction procedure is working.

2.4 Thin films

Probably the widest industrial application of ellipsometry today is the monitoring of the thickness and properties of thin films. The sensitivity of an ellipsometer is such that a change in film thickness of a few Angstroms is usually easy to detect. If a film is thin enough to show an interference color pattern then it will probably be a good ellipsometric sample. This effect is a result of the interference which takes place between the first part

of the light beam reflected from the surface of the thin film, with the one reflected from the surface of the film/substrate interface.

A proper description of the system gives a relation between the measured parameters α , β and the intrinsic dielectric functions of both the substrate and thin film, and the thickness of the latter [69]. Depending on the known dielectric properties and the thickness of the thin film, a number of measurements may be necessary to extract the information. For example, if the dielectric function of the substrate is known, two measurements would be, in principle, sufficient to extract the dielectric function of an isotropic thin layer and its thickness. It turns out however that, in practice, the *pseudo-dielectric* function of the system is hardly angle dependent. Thus, most of the time, it is very difficult to determine the exact thickness of the thin layer, if its dielectric function is not known, or at least some information it is supplied about its general behavior. To exemplify this effect, we present here measurements on a Cu_3N layer (see Fig. 2.4).

Copper nitrides have attracted considerable attention as a new material for optical storage devices. In Fig. 2.4 we present optical measurements performed at room temperature on a thin layer of Cu_3N (about 18nm) grown at 150° on MgO [71], with the incidence polarizer kept fixed at 45° . The measurements have taken place for two angles of incidence, 60° and 80° . From the lefthand side panel of Fig. 2.4 we see a strong angle dependence of the measured experimental values Ψ and Δ . As discussed previously, in principle, this means that we have 4 measured real numbers for each frequency, and thus we would be able to find out both the thickness and the complex dielectric function of the film, that is three real numbers at one frequency.

However, correlations in the measured data prevent this from happening. A better way to see this is to plot the *pseudo-dielectric* function defined in Formula 2.9. From the righthand side panel of Fig. 2.4 we see that the two *pseudo-dielectric* functions $\epsilon_{1,2}^{ps}$ for the two angles of incidence come almost one on the top of the other, as mentioned previously. That means that the the big changes in Ψ and Δ were given only by the angle of incidence. A trial to fit both $\tilde{\epsilon}$ and the thickness of the thin film, has given values from 2nm to 50nm for the thickness. We therefore had to use a different technique to measure the thickness, namely X-Ray diffraction, and than use the resulting thickness to calculate the intrinsic dielectric function of Cu_3N . The result is presented in the righthand panel of Fig. 2.4.

2.5 Magnetic Kerr effect

As discussed previously, in general non-isotropic materials, the dielectric function describing the optical properties is a complex tensor $\tilde{\epsilon}^T$. This tensor has three equal diagonal terms $\tilde{\epsilon}$, and no off-diagonal terms for an isotropic sample. The presence of a static magnetic field \mathbf{B} influences this tensor. For an isotropic sample it acquires off-diagonal terms in the plane perpendicular to the magnetic field. If the magnetic field \mathbf{B} is oriented along the x -axis, there is a non-zero off-diagonal element which couples the y - and z -components of the optical \mathbf{E} -field. The dielectric tensor $\tilde{\epsilon}^T$ becomes:

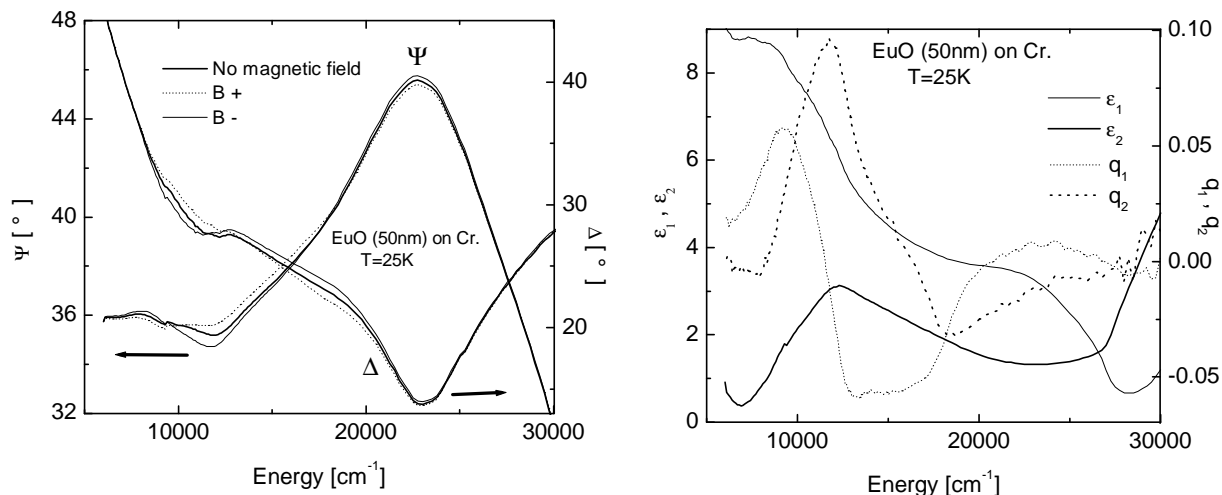


Figure 2.5: Left panel: The influence of the magnetic field, oriented in the plane of the sample and in the plane of incidence, on a film of EuO. The opposite directions of the fields are designated by + and -. Right panel: The calculated diagonal (ϵ_1, ϵ_2) and non-diagonal (q_1, q_2) dielectric functions.

$$\tilde{\epsilon}^T = \begin{pmatrix} \tilde{\epsilon} & 0 & 0 \\ 0 & \tilde{\epsilon} & i\tilde{\mathbf{q}}\tilde{\epsilon} \\ 0 & -i\tilde{\mathbf{q}}\tilde{\epsilon} & \tilde{\epsilon} \end{pmatrix} \quad (2.13)$$

where $\tilde{\epsilon} = \epsilon_1 + i\epsilon_2$ and $\tilde{\mathbf{q}} = q_1 + iq_2$.

The effect of a static magnetic field on the dielectric tensor leads thus to measurable magneto-optical effects. If these effects are observed in transmission, they are referred to as Faraday effects (discovered by Michael Faraday). If they are measured in the reflection configuration, they are referred to as the Kerr effects (by the name of its discoverer, the Reverend J. C. Kerr).

EuO is a material known to present Kerr rotations and colossal magneto-resistance [72]. We have measured the Kerr effect for a thin film of EuO (50 nm) grown on a Cr layer. The film was grown as described in Ref. [72], and later kept in air for more than two weeks, prior to the optical experiments described here. In Fig. 2.5 we present magneto-optical measurements done on EuO. The sample was measured at $T = 25K$. First, measurements in the absence of magnetic field were performed. Knowing the thickness of the sample, and the optical properties of the Cr layer on which the EuO thin film is grown, we determined the dielectric function $\tilde{\epsilon}$ of the isotropic EuO. The results are presented in the righthand panel of Fig. 2.5. The sample presents a broad absorption spectrum around 12000cm^{-1} and an onset of a stronger absorption at 25000cm^{-1} .

We then applied a magnetic field of the order of $0.01T$, which was aligned at the intersection of the surface plane with the plane of incidence (along x), in two opposite directions. From the lefthand panel of Fig. 2.5 we see that changes are observed in Ψ and Δ . They are less than one degree, and cannot be explained only by the small value of the magnetic field. We believe that also the degradation of the layer kept in ambient pressure for a long time played a role.

A new model for the experiment was created, using the tensor 2.13, the known thickness of the layer, its previously calculated diagonal term $\tilde{\epsilon}$, geometry factors, and the known optical properties of Cr. The data measured in the presence of the field was then fitted with the new model, leading to the off-diagonal $\tilde{\mathbf{q}}$ presented in the right panel of Fig. 2.5. The absolute value of $\tilde{\mathbf{q}}$ is a result of the magnitude of the applied magnetic field \mathbf{B} . The plots show that the imaginary part the off-diagonal term $\tilde{\mathbf{q}}$ is larger also around 12000cm^{-1} suggesting thus that the splitting induced by the magnetic field acts on the same energy levels responsible for the transition.

It also shows that one can use bare ellipsometry measurements to calculate the off-diagonal terms of magneto-optical media.

2.6 Normal incidence ellipsometry

Usual ellipsometry is done at the Brewster angle. This is defined as the angle where the reflection of the p -polarized component is minimal. It was shown that this minimum is zero in the case of isotropic transparent samples [69]. Measuring at this angle assures a large ratio between the s -polarized and p -polarized components, and thus an easier way to measure the parameters of the ellipse.

Normal incidence ellipsometry is useless thus for isotropic samples, since the incoming polarized light remains linearly polarized after the reflection. There are, however, cases in which ellipsometry at normal incidence may yield some information, and below we will present such an example.

CuO is a monoclinic crystal, which presents interest mainly in connection with the problem of high temperature superconductors [73]. It is an optical biaxial crystal, in the sense that its axis b is perpendicular to the ac plane, but the axes a and c are not perpendicular to each other, forming an angle of 99.5° . In a system of orthogonal coordinates xyz with $x\parallel a$, $y\parallel b$, and z lying in the ac plane, the axis z is slightly tilted towards the axis c . The dielectric tensor can be written as:

$$\tilde{\epsilon}^T = \begin{pmatrix} \tilde{\epsilon}_{xx} & 0 & \tilde{\epsilon}_{xz} \\ 0 & \tilde{\epsilon}_{yy} & 0 \\ \tilde{\epsilon}_{zx} & 0 & \tilde{\epsilon}_{zz} \end{pmatrix} \quad (2.14)$$

where $\tilde{\epsilon}_{xz} = \tilde{\epsilon}_{zx}$ in the absence of magnetic field.

In principle, if all terms from the above matrix would be real, the matrix can be diagonalized, meaning that one can choose a different orthogonal system of coordinates $x'y'z'$ for which the tensor $\tilde{\epsilon}^T$ would have only diagonal terms. The y' axes of the new system may be chosen as the old one, but the new $x'z'$ system would be rotated in the ac plane with respect to the old xy system. The angle between the two systems would be given by [74]:

$$\tan 2\varphi = \frac{2\epsilon_{xz}}{\epsilon_{xx} - \epsilon_{zz}} \quad (2.15)$$

This angle would describe the rotation of the principal axes within the ac plane. Because the dielectric function ϵ is frequency dependent, the angle φ is also frequency dependent.

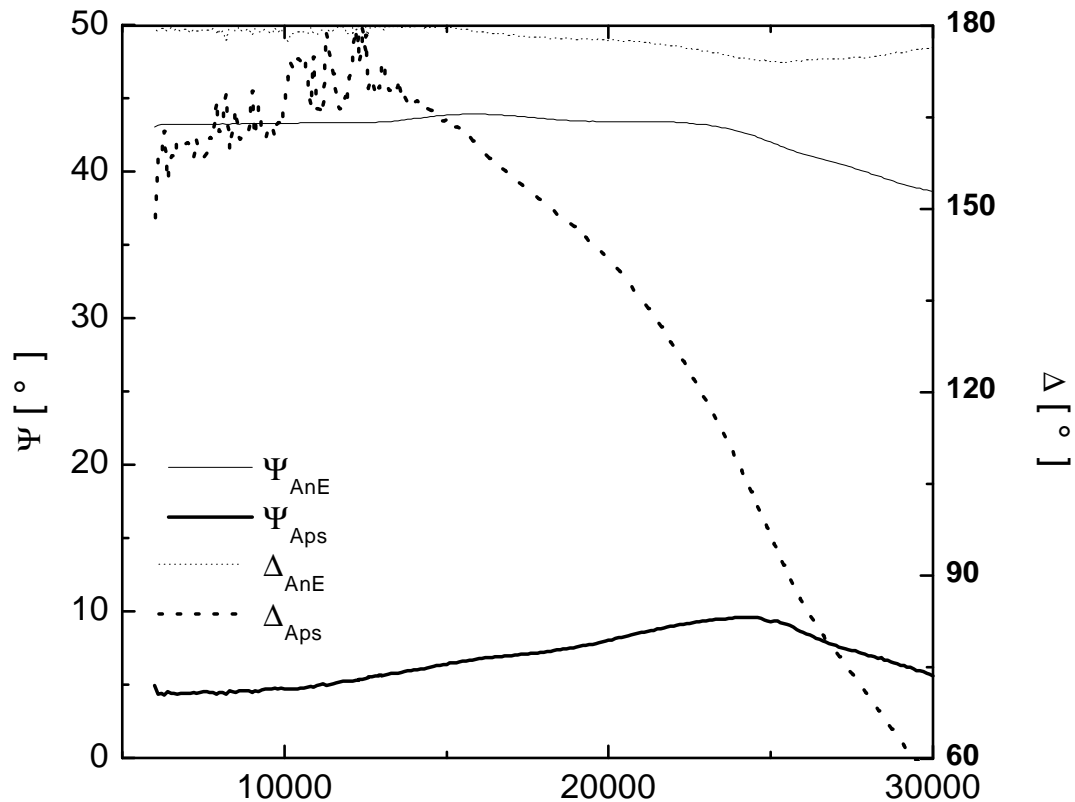


Figure 2.6: "Normal" AnE and Anisotropic Aps ellipsometry functions Ψ and Δ measured on CuO close to normal incidence (the angle of incidence is $\theta=11^\circ$)

In the general case however, the dielectric function is complex, and one usually diagonalizes the real part and imaginary part of the dielectric tensor $\tilde{\epsilon}^T$ separately. The formula 2.14 may still be used, but it will lead to a complex angle of rotation φ . We want to exemplify in this subchapter that, by doing normal incidence ellipsometry, one can have direct access to it.

Consider the dielectric tensor only in the ac plane, given by

$$\tilde{\epsilon}_{ac} = \begin{pmatrix} \tilde{\epsilon}_{xx} & \tilde{\epsilon}_{xz} \\ \tilde{\epsilon}_{zx} & \tilde{\epsilon}_{zz} \end{pmatrix} \quad (2.16)$$

For normal incidence, this is related directly to the Jones matrix of the complex reflectivity tensor \tilde{R} (defined in 2.1) by the following relation [74]:

$$\tilde{\epsilon}_{ac} = \left[(1 - \tilde{R})(1 + \tilde{R})^{-1} \right]^2 \quad (2.17)$$

A direct use of this formula in 2.15, yields the following relation:

$$\tan 2\varphi = \frac{2\tilde{R}_{xz}}{\tilde{R}_{xx} - \tilde{R}_{zz}} \quad (2.18)$$

We have aligned the sample close to normal incidence, with $x||p$ and $z||s$. Even if we discuss here normal incidence, we will refer to p and s , where p indicates now the direction x on the sample surface and s perpendicular to that. We may thus write:

$$\tan 2\varphi = \frac{2\tilde{R}_{ps}/\tilde{R}_{pp}}{1 - \tilde{R}_{ss}/\tilde{R}_{pp}} \quad (2.19)$$

The values of the two complex ratios in 2.19 are directly available in a special type of ellipsometric measurement, called generalized ellipsometry. This differs from the usual type of ellipsometry measurements where the first polarizer is kept at 45° by choosing different angles. The idea of this type of measurements is that, for a general anisotropic sample, the coefficients α and β are not given by the simple relations 2.6, but by a more complicated relation [75]:

$$\alpha = \frac{(|\tilde{R}_{pp}|^2 - |\tilde{R}_{sp}|^2) + (|\tilde{R}_{ps}|^2 - |\tilde{R}_{ss}|^2) \tan^2 P + 2[\operatorname{Re}(\tilde{R}_{pp} \tilde{R}_{ps}^*) - \operatorname{Re}(\tilde{R}_{ss} \tilde{R}_{sp}^*)] \tan P}{(|\tilde{R}_{pp}|^2 + |\tilde{R}_{sp}|^2) + (|\tilde{R}_{ss}|^2 + |\tilde{R}_{ps}|^2) \tan^2 P + 2[\operatorname{Re}(\tilde{R}_{pp} \tilde{R}_{ps}^*) + \operatorname{Re}(\tilde{R}_{ss} \tilde{R}_{sp}^*)] \tan P}$$

$$\beta = \frac{2[\operatorname{Re}(\tilde{R}_{pp} \tilde{R}_{sp}^*) + \operatorname{Re}(\tilde{R}_{ss} \tilde{R}_{ps}^*)] \tan^2 P + [\operatorname{Re}(\tilde{R}_{pp} \tilde{R}_{ss}^*) + \operatorname{Re}(\tilde{R}_{sp} \tilde{R}_{ps}^*)] \tan P}{(|\tilde{R}_{pp}|^2 + |\tilde{R}_{sp}|^2) + (|\tilde{R}_{ss}|^2 + |\tilde{R}_{ps}|^2) \tan^2 P + 2[\operatorname{Re}(\tilde{R}_{pp} \tilde{R}_{ps}^*) + \operatorname{Re}(\tilde{R}_{ss} \tilde{R}_{sp}^*)] \tan P}$$

If the sample is anisotropic, one can do measurements at the same angle of incidence for more angles of the fixed polarizer P, and fit all the data together. One can thus obtain the "normal" ratio: $\tilde{\rho}_{AnE} = \tilde{R}_{pp} / \tilde{R}_{ss}$, the anisotropic "p into s" ratio $\tilde{\rho}_{Aps} = \tilde{R}_{ps} / \tilde{R}_{pp}$ and "s into p" $\tilde{\rho}_{Aps} = \tilde{R}_{sp} / \tilde{R}_{ss}$. Equation 2.19 can be rewritten as:

$$\tan 2\varphi = \frac{2\tilde{\rho}_{Aps}}{1 - 1/\tilde{\rho}_{AnE}} \quad (2.20)$$

We have done a generalized anisotropy measurement on the *ac* face of the CuO sample, aligned with the *a* axis in the plane of incidence($a||x||p$). The configuration was close to normal incidence, with an angle of incidence of $\theta=11^\circ$. The results of $\tilde{\rho}_{AnE}$ and $\tilde{\rho}_{Aps}$ are presented in the Fig. 2.6, using their corresponding values of Ψ and Δ , according to 2.4. Then, the real and imaginary parts of the complex angle φ were calculated using 2.20 and presented in the righthand panel of Fig. 2.7. In the lefthand panel of the same figure, the *pseudo-dielectric* function of CuO is presented for $\mathbf{E}||\mathbf{a}$ and $\mathbf{E} \perp \mathbf{a}$.

As we can see from Fig. 2.7, the values of $\operatorname{Im}[\varphi]$ and $\operatorname{Re}[\varphi]$ are quite small, on the order of few degrees. This is expected, since the angle between the *a* and *c* axes is close to 90° . The imaginary part of φ is positive and shows an absorption behavior, and $\operatorname{Re}[\varphi]$ a dispersive behavior. For the moment, it is not clear to us how the values of the complex φ can be related to the orientation of the eigenmodes of different transitions. It is interesting to note however, that $\operatorname{Im}[\varphi]$ has a similar behavior as the imaginary part of the pseudo-dielectric function for $\mathbf{E} \perp \mathbf{a}$ (see Fig. 2.7), with a peak around 25000cm^{-1} . The latter comes from a transition which takes place mainly along the *c* axis. It is thus expected that the eigenmodes of this transition are tilted with respect to the ones of the *a* axis, giving the behavior of $\operatorname{Im}[\varphi]$.

2.7 Alignment of orthorhombic samples

An unusual use of the visible ellipsometer may be the alignment of orthorhombic samples. This may sound not very important, but it is practical when measuring the

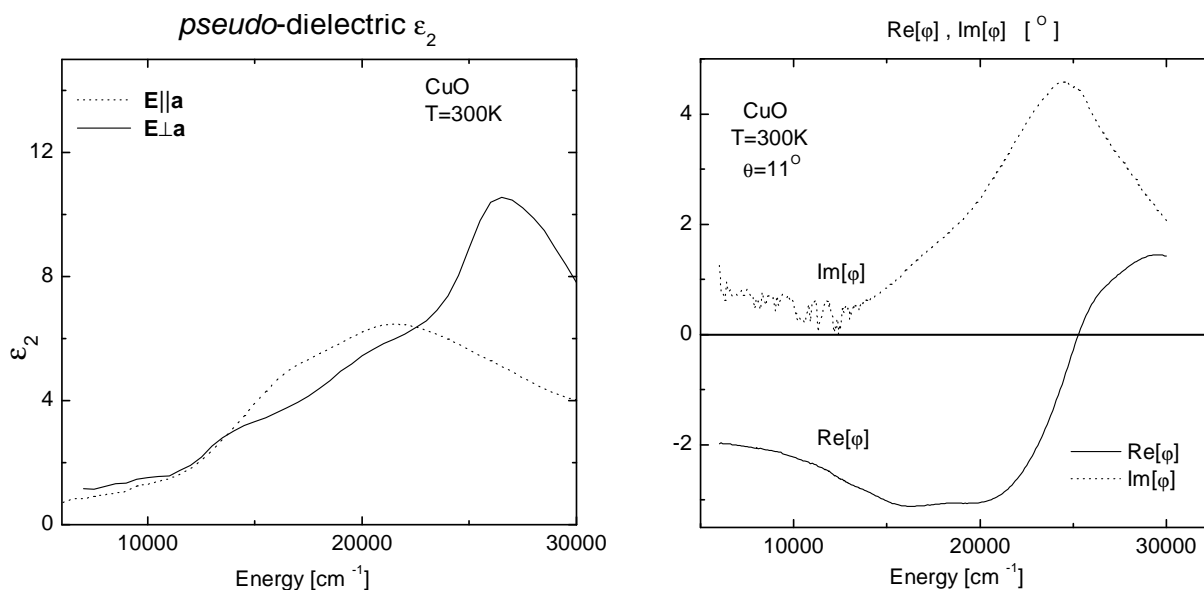


Figure 2.7: Left panel: Imaginary part of the pseudo-dielectric function measured on the (101) plane for $\mathbf{E} \parallel \mathbf{a}$ (the angle of incidence is $\theta = 65^\circ$) and $\mathbf{E} \perp \mathbf{a}$ ($\theta = 65^\circ$). Right panel: The real and imaginary part of the complex angle describing the rotation of the principal dielectric axes (see text).

samples themselves, since it reduces the time needed to align the samples in the X-Ray diffractometer.

The principle of this alignment is simple. Usually we want to align the axes of the orthorhombic sample with the axes of the equipment. If the sample is already cut along one plane (and this was ab plane in the case of α' - NaV_2O_5) we want then to align one axis, a or b , in the plane of incidence. This can be done by testing the polarization of the outcoming light. The s polarized component must in this case remain s polarized after reflection, due to symmetry, and the same must hold for the p polarized component.

Thus an easy check can be done directly by irradiating the sample with only s polarized light ($P=90^\circ$), and rotate the surface of the sample, until the outcoming light presents no p component. In this case the outcoming beam is again linearly polarized at 90° with respect to the plane of incidence if the orthorhombic sample is correctly aligned. The electric field on the detector must have then the following angular dependence

$$E \sim \sin(A) \quad (2.21)$$

and thus the intensity on the detector can be written as:

$$I_D \sim \sin^2(A) \sim 1 - \cos(2A) \quad (2.22)$$

Comparing this with the intensity on the detector given by 2.3 we obtain $\alpha = -1$ and $\beta = 0$. Thus, a linearly polarized light beam at 90° with respect to the plane of incidence gives $\alpha = -1$ and $\beta = 0$. The only thing left to do in order to align the sample, is to rotate the surface of the sample until $\alpha = -1$ and $\beta = 0$.

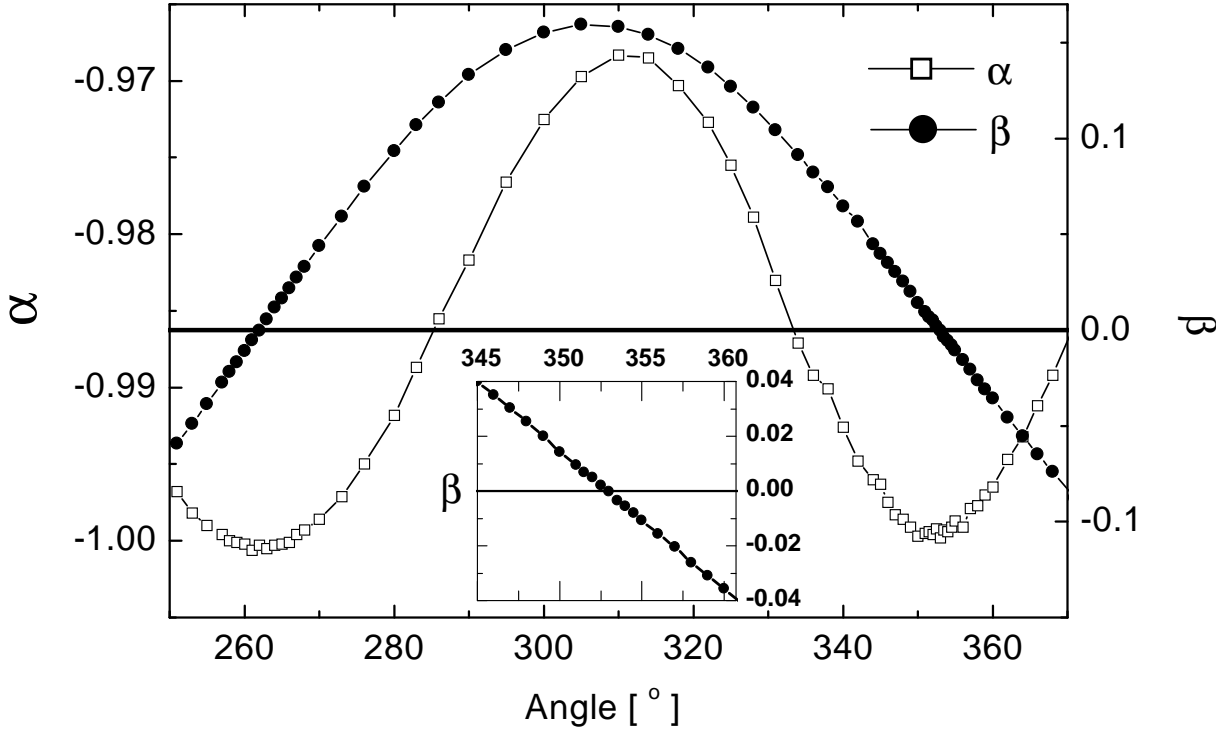


Figure 2.8: The response of the ellipsometer as a function of the rotation of the sample around the normal of its measured plane, for an anisotropic material. The polarizer angle is $P=90^\circ$ the angle of incidence $\theta = 60^\circ$ frequency of the light $\omega=9800\text{cm}^{-1}$ and the surface measured is ab of α' - NaV_2O_5 . Inset: a zoom in for β crossing zero.

In Fig 2.8 we present such a measurement done on the ab surface of α' - NaV_2O_5 . The polarizer angle is $P=90^\circ$ the angle of incidence $\theta=60^\circ$ and the frequency used is $\omega=9800\text{cm}^{-1}$. As we can see, the sensitivity of β crossing zero is much larger than that of α reaching -1. From the inset of Fig 2.8 we estimate that the sensitivity of the equipment is in this case smaller than 0.4° .

This does not represent however the error in the alignment of the sample, since systematic errors may appear. Thus, in our case, the crossing of β to zero happens at 353° and 262° . The difference between these two angles is 91° showing thus that a systematic error of 1° exists. However, we have checked using X-ray diffraction technique, that the β crossing of the zero corresponds indeed to the sample having one axis in the plane of incidence, the error between these two techniques being less than 2° . We want to stress however that this procedure may not work always, for example for the ab plane of the high temperature superconductors, since they present usually a small in-plane anisotropy.

Chapter 3

Optical properties and electronic structure of α' - NaV_2O_5

The dielectric function of α' - $\text{Na}_{1-x}\text{Ca}_x\text{V}_2\text{O}_5$ ($0 \leq x \leq 0.2$) was measured for the \mathbf{a} and \mathbf{b} axes in the photon energy range 0.8-4.5 eV at room temperature. By varying the Ca-concentration we control the relative abundancy of V^{4+} and V^{5+} . We observe that the intensity of the main optical absorption peak at 1 eV for $\mathbf{E} \parallel \mathbf{a}$ is proportional to the number of V^{5+} -ions. This rules out its interpretation as a V^{4+} $d-d$ excitation, and it establishes that this is the on-rung bonding-antibonding transition.

The temperature dependence of the 1 eV peak was measured for temperatures down to 4K in α' - NaV_2O_5 . The peak shows a pronounced decrease of its intensity upon increasing temperature, with an activation energy of about 25meV. No appreciable shift of its frequency was found, showing that the change in the valence state of individual V atoms at the phase transition is smaller than 0.06e. A remarkable inflection of this temperature dependence at the phase transition at 34 K indicates that the low temperature phase is associated with charge ordering.

The far infrared measurements on electron doped α' - $\text{Na}_{1-x}\text{Ca}_x\text{V}_2\text{O}_5$ ($0 \leq x \leq 0.2$) samples do not reveal metallic behavior, in contrast to the usual doped anti-ferromagnetic insulators, such as the high temperature superconductors. The Na deficient single crystals α' - $\text{Na}_x\text{V}_2\text{O}_5$ ($0.85 \leq x \leq 1.00$) present new optical transitions at about 2.8eV for $\mathbf{E} \parallel \mathbf{a}$ and 3.2eV for $\mathbf{E} \parallel \mathbf{b}$, with a spectrum which "converges" to the one of V_2O_5 .

3.1 Introduction

α' - NaV_2O_5 is subject of intensive research as a result of its remarkable physical properties. It belongs to the larger group of α' vanadium pentoxides, with the chemical formula AV_2O_5 [4] (A= Li, Na, Ca, Mg, etc.) Their structure is remarkably similar to that of the parent compound V_2O_5 , which consists of layers of square pyramids of O surrounding a V^{5+} ion (see Fig. 4.1). The layers are kept together via weak forces, which account for the easy cleavage of this oxide along (001).

The A atoms enter the space between the layers and act as electron donors for the V_2O_5 layers. In α' - NaV_2O_5 each Na atom donates one electron per every two V atoms. These

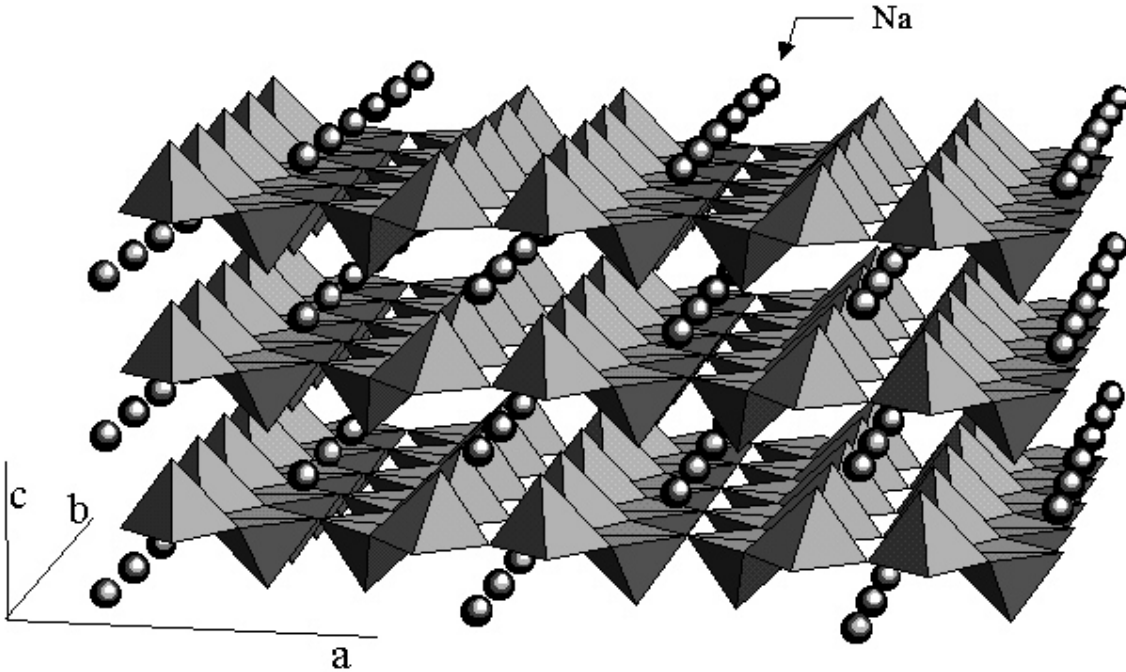


Figure 3.1: The layered structure of α' - NaV_2O_5 .

can be considered, in a simple picture, having no $3d$ electrons in V_2O_5 , thus, in α' - NaV_2O_5 every second V atom would acquire one $3d$ electron, and the system is quarter-filled.

The basic building blocks forming the two-dimensional V_2O_5 layers are parallel two-leg ladders of V atoms bridged by O atoms (see Fig.3.2). It is believed that the main physics is described by the $3d_{xy}$ orbitals of the V atoms. On the rung of the ladder they are coupled through virtual hopping via π -bonded $2p_y$ states [10, 76] of the rung oxygen atoms, indicated schematically in Fig.3.2. Along the legs of the ladder they are also coupled via π -bonded $2p_x$ states of the other oxygen atoms. The effective hopping parameter between V-sites are $t_{\perp} \approx -0.3\text{eV}$ on the same rung, and $t_{\parallel} \approx -0.2\text{eV}$ along the legs of the ladder[10].

At $T_c=35\text{K}$ a phase transition occurs, below which mainly two changes take place [6]: (i) A doubling of the unit cell along the ladder direction, (ii) opening of a spin gap. A big interest arose in this material when the opening of the spin gap was discovered at the same temperature where the lattice doubles along the ladder direction. At that time it was wrongly believed that the ladder consists of V^{4+} and V^{5+} linear chains [77]. In other words, the electrons donated by the Na atoms would stay only on one side of ladder, forming a linear chain. Then a natural explanation of the opening of the spin gap at the same temperature where the unit cell doubles is the spin-Peierls transition. This is a transition where two by two electron spins of neighboring V atoms pair to form a singlet, giving rise thus to the spin gap. The atoms move also closer together to increase the value of the binding magnetic energy, at the expense of the lattice energy, giving also the doubling of the unit cell in the chain direction. This would have made α' - NaV_2O_5 the second inorganic material having a spin-Peierls transition after CuGeO_3 [6].

Later however, it turned out from X-ray diffraction measurements, that, at room tem-

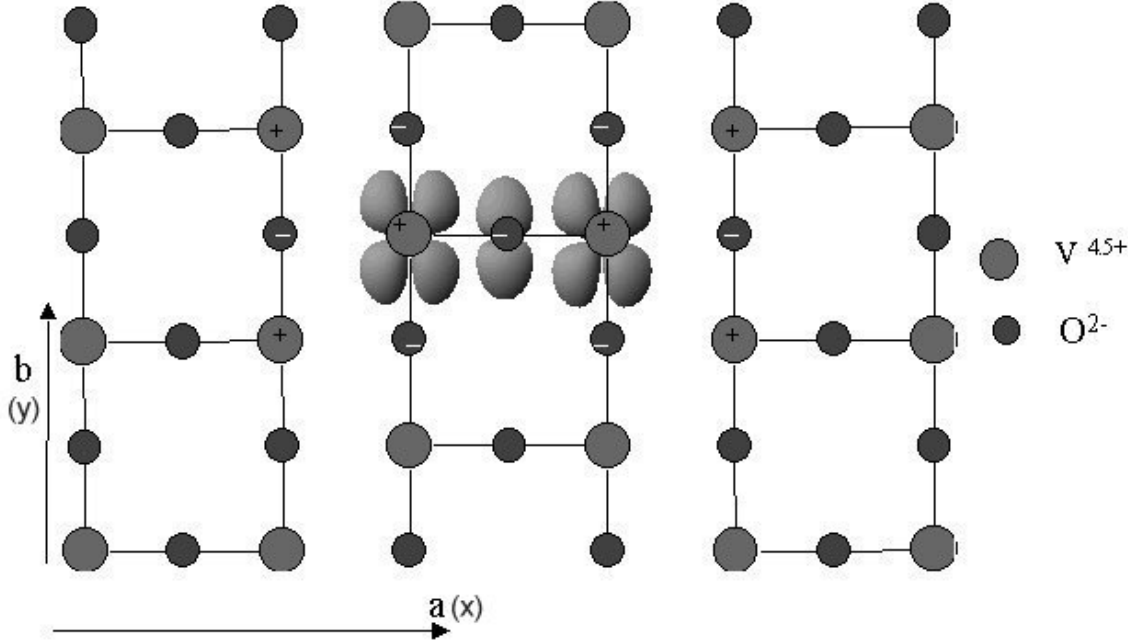


Figure 3.2: The ladders formed by V atoms bridged by O atoms. The $3d_{xy}$ orbitals of V coupled through virtual hopping via π -bonded O $2p_y$ states is presented.

perature, all V-ions are crystallographically equivalent[8–10], and thus they do not form one-dimensional chains of V^{5+} . The type of transition was now questioned. Experimentally, the transition temperature was found not to change much when applying a magnetic field, in contradiction also with the behavior expected from spin-Peierls theory [78, 79]. Analysis of the specific heat anomaly at T_c also suggest [80] that only a small fraction of the released entropy is connected with the magnetic subsystem.

Alternatively, a *zig-zag* charge ordering was proposed to take place at T_c [11], the appearance of a spin-gap being only a side effect. Later, extensive work was done to determine the α' - NaV_2O_5 structure below T_c . The main results from all measurements confirmed the proposed zig-zag pattern of V sites [81, 82]. In addition, there are several experimental hints for a charge redistribution below the phase transition, *e.g.* unaccounted for changes in entropy[83], splitting of the V-NMR lines[84], inequivalent V-sites observed with XPS[81]. At this moment, zig-zag charge ordering is the leading candidate [85–88] for describing the properties of the ground state.

The mechanism of the phase transition, the main focus of research on α' - NaV_2O_5 is at this point not explained, even though several proposals exist. One mechanism proposed [12] includes a symmetry broken configuration of the V-O-V rung, in which the movement of the O atom towards one of the V atoms creates a stronger V-O bonding and an additional spin singlet formation. Other proposal is the "spin-isospin" model [85], in which a proximity to a quantum critical point exists.

The solution of the α' - NaV_2O_5 problem lies in the understanding of the electronic properties above and below T_c . Optical spectroscopy is a useful tool in revealing these properties. This chapter presents the work which was done in Ref.[89] and Ref.[90] on optical conductivity in the visible range. The temperature dependent optical conductivity

of α' - NaV_2O_5 was measured in Ref. [90], the α' - $\text{Na}_{1-x}\text{Ca}_x\text{V}_2\text{O}_5$ doping dependence in Ref. [89] and that of α' - $\text{Na}_x\text{V}_2\text{O}_5$ in Ref. [91]. In addition, this chapter presents the doping dependence of the infrared optical conductivity of α' - $\text{Na}_{0.8}\text{Ca}_{0.2}\text{V}_2\text{O}_5$ which shows no metallic behavior.

3.2 Optical measurements on α' - $\text{Na}_{1-x}\text{Ca}_x\text{V}_2\text{O}_5$

At room temperature, the vanadium atoms have a uniform valence of +4.5, which indicates a quarter-filled band, and suggests a metallic state. However, optical measurements [13, 14, 89, 90] show insulating behavior. The charge gap seems to be around 1eV in both directions. For $\mathbf{E}\parallel\mathbf{a}$ the optical spectra exhibit a strong absorption peak at 0.9 eV, and for $\mathbf{E}\parallel\mathbf{b}$ a broader peak appears at 1.2 eV.

Early density-functional calculations [10] indicated that α' - NaV_2O_5 can be seen as a quarter-filled ladder compound with the spins carried by V-O-V molecular orbitals on the rungs of the ladder. In other words, because the hopping in the rung $t_\perp \approx -0.3\text{eV}$ is bigger than the one along the legs of the ladders $t_\parallel \approx -0.2\text{eV}$, the system forms first bonding-type molecular orbital states, made up of the $3d_{xy}$ orbitals of a V-O-V rung. The antibonding orbitals would be at $2|t_\perp| \approx 0.6\text{eV}$ higher in energy. The bonding orbitals are coupled then with each other via the hopping term $t_\parallel \approx -0.2\text{eV}$, giving thus rise to a dispersion along the b direction. As presented in Ref. [10] the system would then have a charge gap of roughly $2|t_\perp| \approx 0.6\text{eV}$. At this frequency a peak would evolve in the $\mathbf{E}\parallel\mathbf{a}$ optical spectra corresponding to the bonding-antibonding transition of the on rung molecular orbitals V-O-V. The value is close to 0.9 eV, and suggests thus the origin of the 0.9 eV peak for the $\mathbf{E}\parallel\mathbf{a}$ optical spectra [13].

Later however, other explanations were proposed for the 0.9 eV peak in $\sigma_a(\omega)$ of α' - NaV_2O_5 including an on-site d-d transition between the crystal field split levels of the V-ions[14]. To discriminate between these possibilities, we conjectured that by doping α' - NaV_2O_5 with extra electrons, the intensity of the 0.9 eV peak would present opposite behaviors: the intensity would decrease for a bonding-antibonding excitation, or the intensity would increase for an on-site $d-d$ transition. The electron doping is chemically realized in the single crystals samples of α' - $\text{Na}_{1-x}\text{Ca}_x\text{V}_2\text{O}_5$ which thus have to be measured.

3.2.1 Details of sample preparation and experimental setup

Partial substitution of the Na^+ with Ca^{2+} leaves the α' crystal structure of α' - $\text{Na}_{1-x}\text{Ca}_x\text{V}_2\text{O}_5$ intact, but alters the relative abundance of V^{4+} and V^{5+} , $\text{V}^{4+} : \text{V}^{5+} = (1+x) : (1-x)$. Here we report spectroscopic ellipsometry measurements on α' - $\text{Na}_{1-x}\text{Ca}_x\text{V}_2\text{O}_5$ ($x=0, 0.075$ and 0.15), in the energy range 0.8-4.5 eV. We employ the dependence of the optical spectra on the $\text{V}^{4+} : \text{V}^{5+}$ ratio to identify the main components in the optical spectra, which in turn we use to reveal the electronic structure of this material.

The crystals (CR8, 45008, and 45010) had dimensions of approximately 2, 1 and 0.3 mm along the a , b , and c axes respectively. The samples 45008 and 45010 were prepared from NaVO_3 flux [6]. In a first step a mixture of Na_2CO_3 and V_2O_5 is heated up to 550

C in air to form NaVO_3 . In a second step the NaVO_3 is mixed with VO_2 in the ratio of 8:1 and then heated up to 800 C in an evacuated quartz tube and cooled down at a rate of 1 K per hour. The excess NaVO_3 was dissolved in water. The doped samples were produced by substituting in the first step Na_2CO_3 by CaCO_3 .

The chemical composition of the samples has been determined using Energy Dispersive X-ray Fluorescence microprobe measurements. The results showed that the real Ca content of some samples was smaller than the nominal one (with a factor of 0.75), and that position dependent variations of the Na stoichiometry are below 2%. A standard spectroscopic ellipsometer, described in the first chapter, was used to collect ellipsometric data in the range of 6000 to 35000 cm^{-1} , from the ab planes of the crystals, using two different crystal orientations. It was used also to measure normal incidence reflectivity spectra of the bc plane with the electric field vector along the c -direction.

3.2.2 Data collection and analyses

We performed ellipsometric measurements on the (001) surfaces of the crystals both with the plane of incidence of the light along the a and the b axis. An angle of incidence θ , of 66° , was used in all experiments. As discussed in the first chapter, ellipsometry provides directly the amplitude and phase of the ratio of the reflectivity coefficients of p - and s -polarized light [69] $r_p(\omega)/r_s(\omega)$. For an anisotropic crystal with the three optical axes oriented along the surface normal ($p \perp$), perpendicular to the plane of incidence (s), and along the intersection of the plane of incidence and the surface ($p \parallel$), this ratio is related to the dielectric tensor elements along these three directions ($\epsilon_{p\perp}$, ϵ_s , and $\epsilon_{p\parallel}$) according to the expression [89]:

$$\frac{r_p}{r_s} = \frac{\left[\sqrt{\epsilon_{p\parallel}\epsilon_{p\perp}} \cos \theta - \sqrt{\epsilon_{p\perp} - \sin^2 \theta} \right] \left[\cos \theta + \sqrt{\epsilon_s - \sin^2 \theta} \right]}{\left[\sqrt{\epsilon_{p\parallel}\epsilon_{p\perp}} \cos \theta + \sqrt{\epsilon_{p\perp} - \sin^2 \theta} \right] \left[\cos \theta - \sqrt{\epsilon_s - \sin^2 \theta} \right]} \quad (3.1)$$

To extract the dielectric constant from the ellipsometric parameters we proceed in two steps: First the *pseudo-dielectric* functions along the optical axes are extracted from the ellipsometric data using the inversion formula given in the first chapter:

$$\epsilon_{p\parallel}^{ps} = \sin^2 \theta \left(1 + \tan^2 \theta \left(\frac{1 - r_p/r_s}{1 + r_p/r_s} \right)^2 \right) \quad (3.2)$$

For isotropic crystals this expression provides the dielectric function directly. The *pseudo-dielectric* function is close to the dielectric tensor elements along the intersection of the plane of incidence and the crystal surface[92]. A biaxial crystal like α' - NaV_2O_5 has three complex dielectric functions, ϵ_a , ϵ_b and ϵ_c along each optical axis, and an ellipsometric measurement involves all three tensor components of the dielectric matrix. In addition to the pseudo-dielectric functions displayed Fig.3.3a, $\epsilon_c(\omega)$ is required. No ac or bc crystal-planes were available large enough to do ellipsometry with our setup.

We therefore measured the c -axis reflectivity (Fig. 3.3b) of the bc -plane of the pristine material (sample CR3). The spectrum contains no absorption peaks in the frequency range below 2.5eV, as was reported earlier [93, 94], and a very weak absorption at high

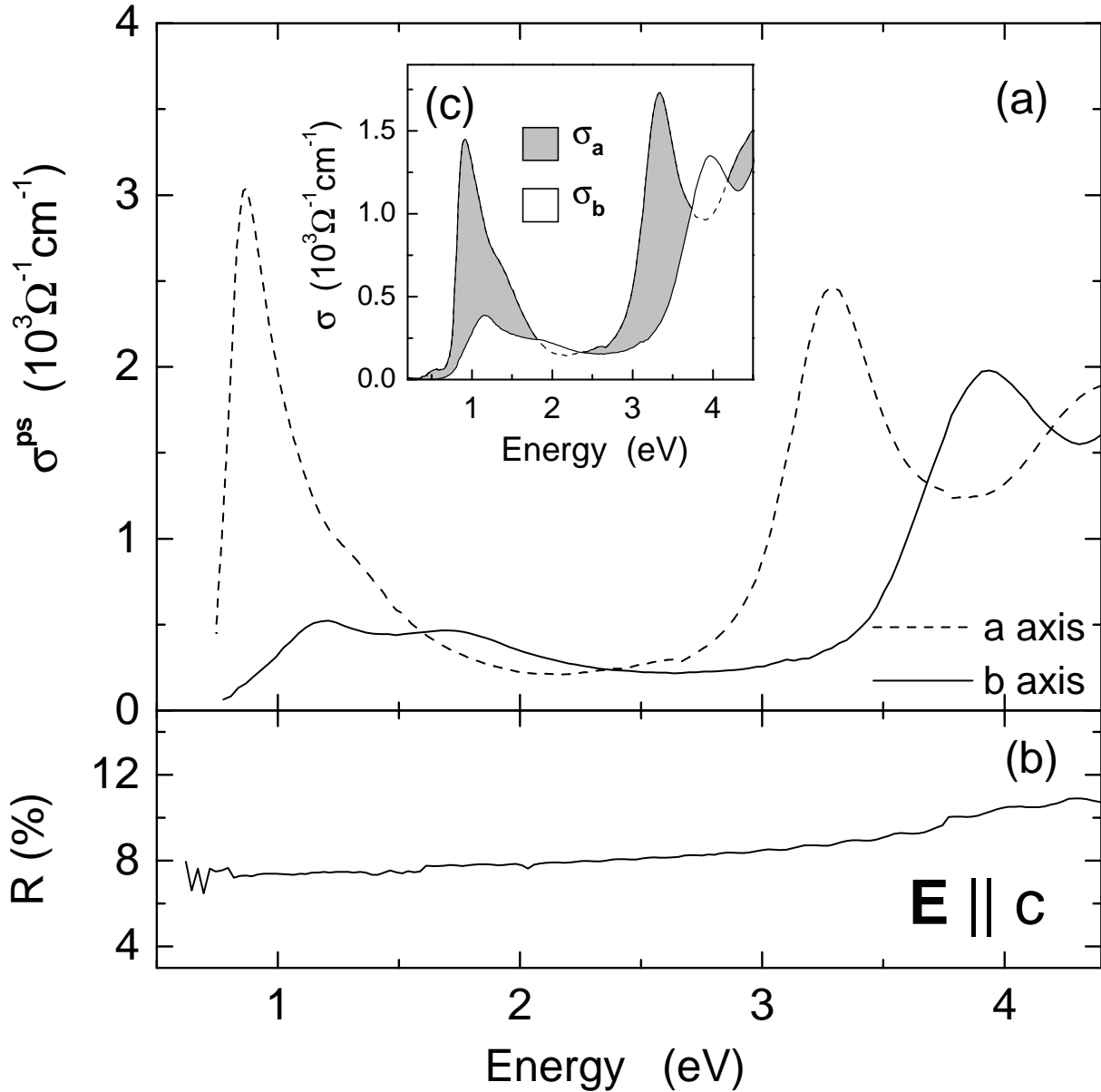


Figure 3.3: (a) Pseudo-optical conductivity $\sigma_1^{ps}(\omega)$ of α' - NaV_2O_5 at $T = 300\text{K}$. The spectra were taken on the (001) surface with a and b axes successively lying in the plane of incidence. (b) $E \parallel c$ reflectivity at $T = 300\text{K}$. (c) Optical conductivity $\sigma_a(\omega)$ and $\sigma_b(\omega)$ corrected for contributions of the c -axis dielectric function to $\sigma_1^{ps}(\omega)$.

frequencies around 4eV, providing a reliable determination of the dielectric function ϵ_c using Kramers-Kronig analysis. Due to the absence of strong resonances, ϵ_c has a minor influence on the recorded ellipsometric spectra. In Fig. 3.3c the optical conductivity is displayed taking into account all corrections due to the anisotropy. We see that the conversion from $\epsilon^{ps}(\omega)$ to $\epsilon(\omega)$ leads, in essence, to a factor 0.5 re-scaling of $\sigma(\omega)$. The shape of the optical conductivity remains however almost unchanged.

The data presented in Fig. 3.3 are in general agreement with previous results [13, 14]

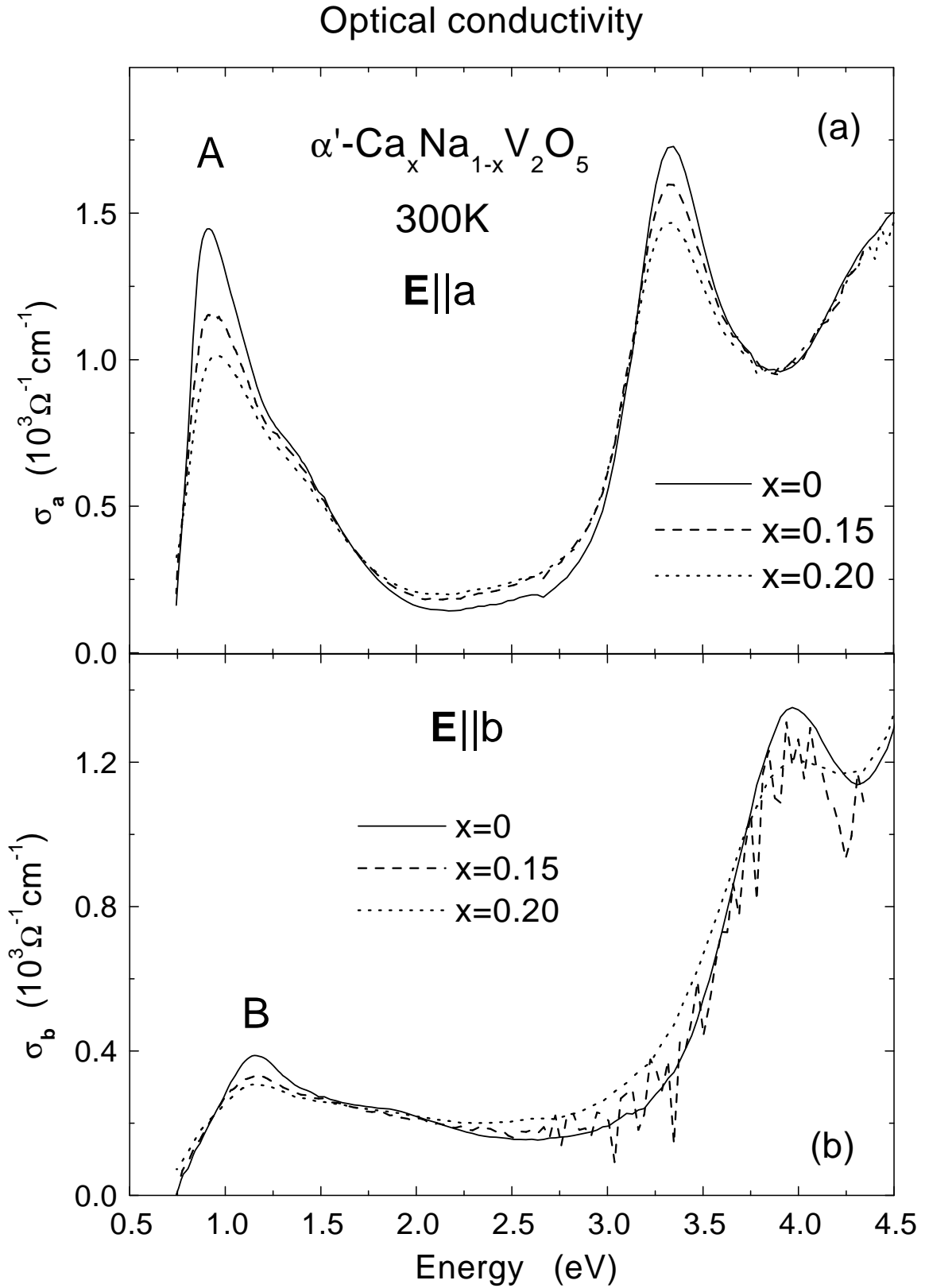


Figure 3.4: Optical conductivity at $T = 300\text{K}$ of $\text{Re } \sigma(\omega)$ of $\text{Ca}_x\text{Na}_{1-x}\text{V}_2\text{O}_5$ for $x=0$ (solid), $x=0.15$ (dash) and $x=0.20$ (dot): $E \parallel a$ (panel a) and $E \parallel b$ (panel b)

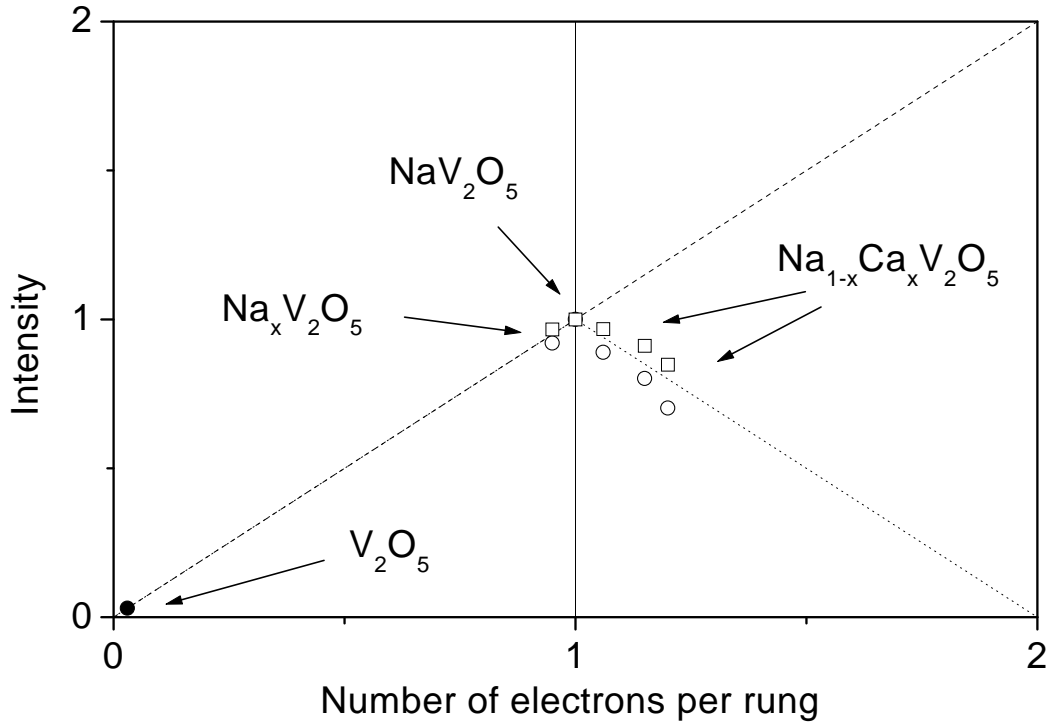


Figure 3.5: Intensity of peak A calculated by integrating optical conductivity up to 1.9eV (squares), or by using the height of the peak (circles) in $\text{Ca}_x\text{Na}_{1-x}\text{V}_2\text{O}_5$ for $x=0.06$, $x=0.15$ and $x=0.20$ and in $\text{Na}_x\text{V}_2\text{O}_5$ for $x=0.95$. The values are normalized to NaV_2O_5 intensity. The dashed line indicates the theoretical intensity of on-site V d-d transitions versus doping. The dotted line indicates the theoretical intensity according to the model Hamiltonian Eq.3.3.

using Kramers-Kronig analysis of reflectivity data. Along the a -direction we observe a peak at 0.9 eV with a shoulder at 1.4 eV, a peak at 3.3 eV and the slope of a peak above 4.2 eV, outside our spectral window. A similar blue-shifted sequence is observed along the b -direction. The 0.9eV peak drops rather sharply and extrapolates to zero at 0.7 eV. However, weak absorption has been observed within the entire far and mid-infrared range[13, 94]. The strong optical absorption within the entire visible spectrum causes the characteristic black appearance of this material.

In Fig. 3.4 we present the results on the α' - $\text{Na}_{1-x}\text{Ca}_x\text{V}_2\text{O}_5$ single crystals. The peak position at 0.9 eV appear to be doping independent, but the striking observation is that the *intensity* of the peaks depends strongly on doping. In particular, the measured intensity of the 1 eV peak for the a axis is directly proportional to $1 - x$ (Fig. 3.5). The 1 eV peak for the b axis shows also a decrease upon doping.

3.2.3 Main elements of the electronic structure

Before entering the interpretation of the data, we need to discuss in some more detail the main elements of the electronic structure of these compounds. The basic building block of the crystal structure of α' - NaV_2O_5 is formed by V-O-V dimers (see Fig. 3.2). These dimers form the rungs of quasi one-dimensional ladders. The V-ions forming the rungs are bonded along the ladder direction via oxygen ions.

The backbone of the electronic structure is formed by the oxygen $2p$ and V $3d$ states. Photoelectron spectroscopy[95] has provided crucial information on the occupied electronic levels: the oxygen $2p$ states have the lowest energy (the highest binding energy). They form a band about 4 eV wide, which is fully occupied. The occupied part of the V $3d$ states is located about 3 eV above the top of the oxygen bands. Due to ligand field splittings the V $3d$ manifold is spread over a range of at least 3 eV. The $3d_{xy}$ of the V^{4+} is occupied with one electron. The unoccupied d_{xz} and d_{yz} levels have an energy at least 1 eV higher. These in turn are located about 2 eV below the $d_{x^2-y^2}$ and the d_{z^2} levels[10]. The relevance of the O $2p$ bands is that they provide a path for virtual hopping processes between the V-sites. The coupling between V-sites is through virtual hopping via π -bonded O $2p_y$ states, indicated schematically in Fig. 3.2 and Fig.3.7b. The effective hopping parameter between V-sites is $t_{\perp} \approx -0.3\text{eV}$ on the same rung, and $t_{\parallel} \approx -0.2\text{eV}$ along the legs of the ladder[96, 97]. The number of electrons is one per pair of V-atoms. Approaching the ladders as a linear array of rungs, weakly coupled along the direction of the ladder, results in a model of electrons occupying a narrow band of states formed by the symmetric combination of the two V $3d$ -states forming the rungs, hereafter referred to as V-V bonding levels.

Hence, we see that the basic building block are the pairs of V $3d$ states, together forming the rungs of the ladders. The essential charge and spin degrees of freedom of a single rung are identical to the Heitler-London model of the H_2^+ ion, with the V $3d_{xy}$ states playing the role of the H $1s$ states[96]. The relevant Hamiltonian is

$$H = t_{\perp} \sum_{\sigma} \left\{ d_{L\sigma}^{\dagger} d_{R\sigma} + d_{R\sigma}^{\dagger} d_{L\sigma} \right\} + \frac{\Delta}{2} \sum_{\sigma} \left\{ n_{L\sigma} - n_{R\sigma} \right\} + U \left\{ n_{L\uparrow} n_{L\downarrow} + n_{R\uparrow} n_{R\downarrow} \right\} \quad (3.3)$$

where $d_{L(R),\sigma}^{\dagger}$ creates an electron in the lefthand (righthand) d_{xy} orbital on the rung, and σ is the spin-index. The bias potential Δ between the two V-sites accounts for a possible left/right charge imbalance[13]. The most relevant states for the ground state are $d_{L,xy}$ and $d_{R,xy}$. Pure NaV_2O_5 contains one electron per rung in the ground state. Important in the present discussion are the eigenstates and energies of a rung with 0, 1 or 2 electrons. The eigenstates and energies are listed in Table 3.1.

In Fig. 3.6 the level diagram is displayed. In this representation $N_e = 0(2)$ corresponds to the one electron removal(addition) states, for noninteracting electron picture indicated as the "occupied" ("empty") states. In Fig.3.7 we display the same information represented as the one electron removal and addition spectral function. For non-interacting electrons this represents the occupied (left) and unoccupied (right) states.

In the absence of electron-electron interactions, here represented by the on-site Hubbard repulsion parameter U , the Fermi energy would be located in the middle of the bonding band, resulting in a metallic conductor. In Figs.3.6 and 3.7 we have adopted

N_e	State vector	Energy
0	$ 0\rangle$	0
1	$ ^2B_\sigma\rangle = (ud_{L\sigma}^\dagger + vd_{R\sigma}^\dagger) 0\rangle$ $ ^2A_\sigma\rangle = (vd_{L\sigma}^\dagger - ud_{R\sigma}^\dagger) 0\rangle$	$-\frac{1}{2}E_{CT} - E_F$ $+\frac{1}{2}E_{CT} - E_F$
2	$ ^1\tilde{L}R\rangle = \alpha_K ^1LR\rangle + \beta_K ^1E\rangle$ $ ^3LR_1\rangle = d_{L\uparrow}^\dagger d_{R\uparrow}^\dagger 0\rangle$ $ ^3LR_0\rangle = \sqrt{\frac{1}{2}}(d_{L\uparrow}^\dagger d_{R\downarrow}^\dagger + d_{L\downarrow}^\dagger d_{R\uparrow}^\dagger) 0\rangle$ $ ^3LR_{-1}\rangle = d_{L\downarrow}^\dagger d_{R\downarrow}^\dagger 0\rangle$ $ ^1\tilde{O}\rangle = \alpha_\Delta ^1O\rangle + \beta_\Delta\alpha_K ^1E\rangle - \beta_\Delta\beta_K ^1LR\rangle$ $ ^1\tilde{E}\rangle = \alpha_\Delta\alpha_K ^1E\rangle - \alpha_\Delta\beta_K ^1LR\rangle - \beta_\Delta ^1O\rangle$	$-K - 2E_F$ $-2E_F$ $-2E_F$ $-2E_F$ $U + K/2 - \sqrt{(K/2)^2 + \Delta^2} - 2E_F$ $U + K/2 + \sqrt{(K/2)^2 + \Delta^2} - 2E_F$
Definitions		
	$\frac{u}{v} \equiv \sqrt{1 + [\Delta/2t_\perp]^2 + [\Delta/2t_\parallel]}$ $ ^1LR\rangle \equiv \sqrt{\frac{1}{2}}(d_{L\uparrow}^\dagger d_{R\downarrow}^\dagger - d_{L\downarrow}^\dagger d_{R\uparrow}^\dagger) 0\rangle$ $ ^1E\rangle \equiv \sqrt{\frac{1}{2}}(d_{L\uparrow}^\dagger d_{L\downarrow}^\dagger + d_{R\uparrow}^\dagger d_{R\downarrow}^\dagger) 0\rangle$ $ ^1O\rangle = \sqrt{\frac{1}{2}}(d_{L\uparrow}^\dagger d_{L\downarrow}^\dagger - d_{R\uparrow}^\dagger d_{R\downarrow}^\dagger) 0\rangle$	$E_{CT} \equiv \sqrt{4t_\perp^2 + \Delta^2}$ $K \equiv \sqrt{U^2/4 + 4t_\perp^2} - U/2$ $\frac{\alpha_K}{\beta_K} \equiv \sqrt{1 + [U/4t_\perp]^2 + [U/4t_\parallel]}$ $\frac{\alpha_\Delta}{\beta_\Delta} \equiv \sqrt{1 + [K/2\Delta]^2 + [K/2\Delta]}$

Table 3.1: Eigenstates and energies of a rung with $N_e=0, 1$ and 2 electrons. The $N_e=2$ state vectors and energies were derived for the limit $\Delta \ll U$.

$U = 4$ eV. The model now predicts a gap of order $E_{CT} \simeq 1$ eV. The Fermi energy is located within this gap. The fact that these materials are insulating therefore is associated with the large on-site Hubbard interaction.

The excitation of an electron across the gap involves a change of occupancy of *two* of the rungs: The final state has one empty and one doubly occupied rung. It is important in this context, that the two electrons $|^3,1LR\rangle$ are in a *correlated* state: in the limit $U \rightarrow \infty$ one electron is located on the lefthand V-atom and the other on the righthand V-atom, because their repulsion would be infinite if sitting on the same atom.

3.2.4 Discussion of the experimental spectra

The 0.9 eV peak marks the fundamental gap of the optical spectrum. The interpretation of this peak was subject of a scientific controversy. Several interpretations have been put forward:

1. Transitions between linear combinations of V $3d_{xy}$ -states of the two V-ions forming the rungs[10, 13, 96]. In Refs.[10] and [96] even and odd combinations were considered. The 0.9 eV peak in $\sigma_a(\omega)$ (peak A) would then correspond to the transition from V-V bonding to antibonding combinations on the same rung[13] (Fig.3.7b). In Ref.[13] this model was extended to allow lop-sided linear combinations of the same orbitals, so that the 0.9 eV peak is a transition between left- and right-oriented linear combinations.
2. On-site d-d transitions between the crystal field split levels of the V-ions[14]. Because V^{5+} has no occupied 3d-levels, such processes involve the V^{4+} ions.

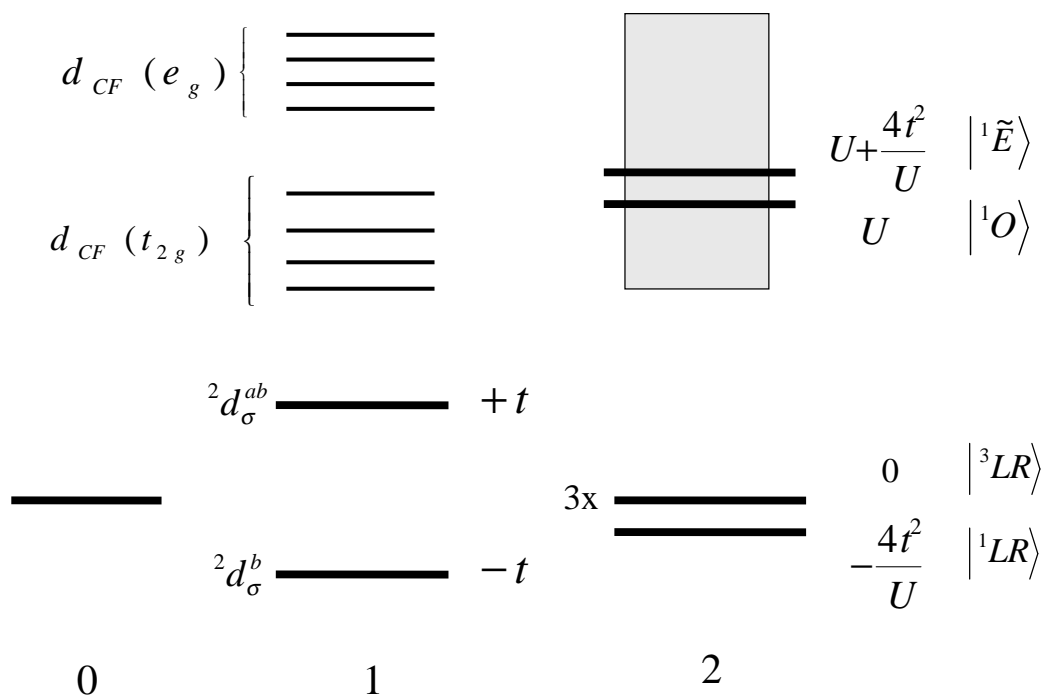


Figure 3.6: Diagram of the many-body eigenstates of a VOV rung, occupied with 0, 1 and 2 electrons, obtained within the Heitler-London model for $U = 4eV$, $\Delta = 0.8eV$, and $t = t_{\perp} = 0.3eV$.

3. Transitions between the on-rung V $3d_{xy}$ bonding combination and final states of d_{xz} and d_{yz} character[98].

The last two assignments are motivated by the fact that in α' - $\text{Na}_{1-x}\text{Ca}_x\text{V}_2\text{O}_5$ the optical selection rules allow on-site d-d transitions by virtue of the low point-symmetry at the V-sites. Optical transitions having values below 2 eV were also seen in V_6O_{13} and VO_2 . In V_2O_5 they have very small intensities, and were attributed to defects [99].

To determine which one of these assignments is true, we have measured the doping dependence of the 0.9 eV peak in $\sigma_a(\omega)$ in Ca-substituted α' - NaV_2O_5 (Fig.3.4a). Because Ca is divalent, substituting Na with Ca has the effect of increasing the average density of V^{4+} ions. In the local d-d scenario the intensity of the on-site V $3d$ - $3d$ transitions would be proportional to the density of V^{4+} ions. As a result the intensity of on-site d-d transitions would increase upon substituting Na with Ca. In Fig. 3.5 we display the experimentally observed doping dependence of the intensity together with the theoretical expectation within this scenario. Clearly the experimental intensity of the 0.9 eV peak in Fig. 3.4 behaves opposite to the expected behaviour of dd transitions. This definitely rules out item number 2 of the above list.

This also rules out item number 3 presented in Ref.[98]: if the transition from the V $3d_{xy}^+$ bonding combination to the d_{xz} and d_{yz} orbitals involves mainly transitions among orbitals at the same site, the same argument as for item 2 applies. If it involves mainly

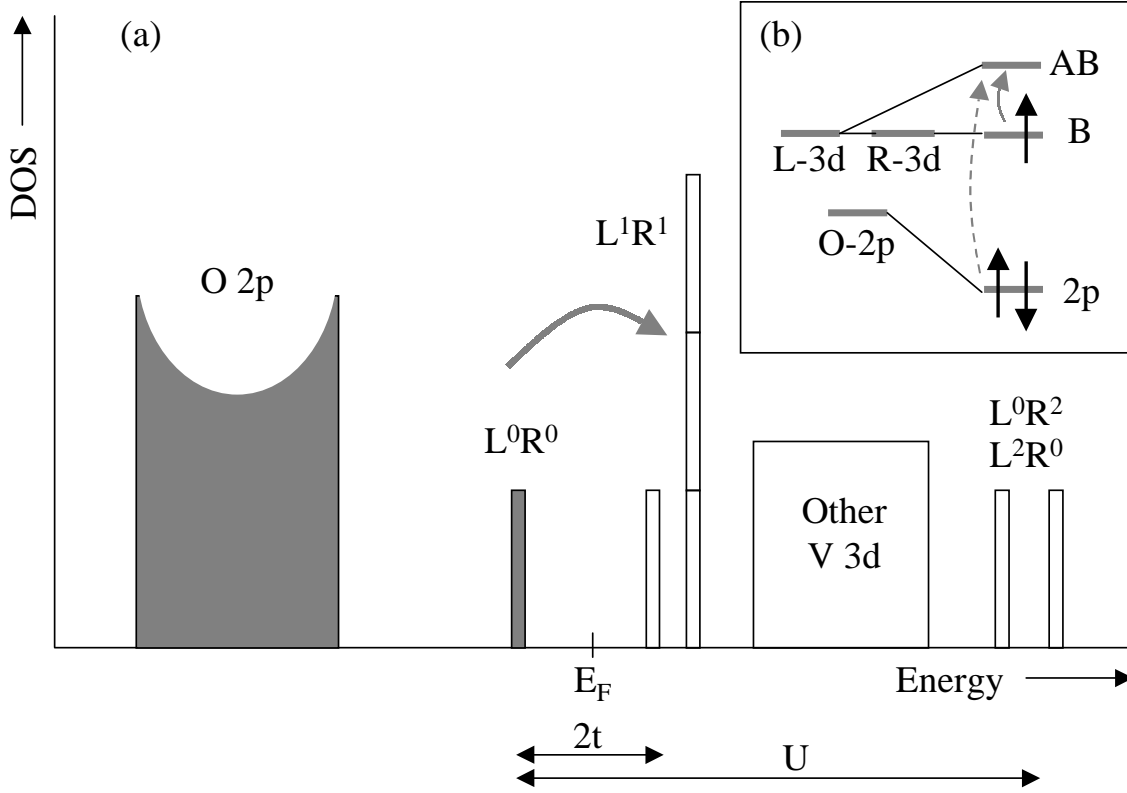


Figure 3.7: Occupied and unoccupied density of states obtained within the Heitler-London model for $U = 4eV$ (a), and the schematic diagram of the relevant energy levels of the V_2O clusters forming a rung (b). L and R refer to orbitals associated to the left and right V sites, respectively.

transitions between molecular orbitals formed by different sites on the same rung, the transition from the $\text{V } 3d_{xy}^+$ bonding combination to the antibonding $\text{V } 3d_{xy}^-$ would still be the dominant transition.

To explain the intensity decrease of about $x\%$ upon substituting $x\%$ of the Na ions with Ca (see Fig.3.5), let us have a look at the many-body nature of the ground state and the excited state properties of NaV_2O_5 . The rungs which are occupied with two electrons due to the Ca-doping will be in the many-body ground state (see Table 3.1) $|^1\tilde{L}\tilde{R}\rangle$. Due to the validity of dipole selection rules, the optical excitation with the electric field along the rung-direction is $|^1\tilde{L}\tilde{R}\rangle \rightarrow |^1\tilde{O}\rangle$. The energy to make this excitation is $\frac{1}{2}U + \sqrt{U^2/4 + 4t_\perp^2}$. Hence the effects of Ca doping are (i) to remove the peak at $E_{CT} \approx 1eV$ for the rungs receiving the extra electron, and (ii) to place a new peak at an energy $U \approx 4eV$. Hence, the observed $x\%$ decrease of intensity of the $|B\rangle \rightarrow |A\rangle$ transition peak for the $x\%$ Ca doped sample is in excellent quantitative agreement with the expected value.

Using the tight binding sum rule

$$\int \sigma(\omega)d\omega = (ed/\hbar)^2\pi t_\perp/(2V)\langle d_{L\sigma}^\dagger d_{R\sigma} + \text{h.c.} \rangle \quad (3.4)$$

the *intensity* of the $|^1\tilde{LR}\rangle \rightarrow |^1\tilde{O}\rangle$ peak relative to the 0.9 eV peak of the singly occupied rungs is (assuming $\Delta = 0$ for a doubly occupied rung):

$$\frac{I(0) + I(2)}{2I(1)} = \frac{\alpha_K\beta_K}{uv} = \sqrt{\frac{1}{1 + (U/4t)^2}} \approx \frac{4t_\perp}{U} \quad (3.5)$$

With the parameters relevant to NaV_2O_5 this implies that the $|^1\tilde{LR}\rangle \rightarrow |^1\tilde{O}\rangle, |^1\tilde{E}\rangle$ transitions have factor 2-4 smaller spectral weight than the $|B\rangle \rightarrow |A\rangle$ transition. The fact that we do not see an additional spectral weight at around 4 eV in the Ca doped samples does not disprove the above arguments. Besides the fact that this spectral weight is small, it can occur above 4.5 eV, or in the proximity of the 3.5eV peak, in which case its doping dependence is hindered.

Hence we conclude that only the assignment of item number 1 is consistent with our data: The 1eV peak in $\sigma_a(\omega)$ is the on-rung $|^2B_\sigma\rangle \rightarrow |^2A_\sigma\rangle$ transition with an excitation energy $E_{CT} \equiv \sqrt{4t_\perp^2 + \Delta^2}$.

The 1.1 eV peak in $\sigma_b(\omega)$ (peak B) involves transitions between neighboring rungs along the ladder. In the non-interacting model ($U = 0$) this would correspond to a Drude-Lorentz optical conductivity centered at $\omega = 0$, with a spectral weight

$$\int_0^\infty \sigma_b(\omega) d\omega = (e/\hbar)^2 t_\parallel \pi b (2ac)^{-1} \quad (3.6)$$

As a result of the correlation gap in the density of states, indicated in Fig. 3.7a, the optically induced transfer of electrons between neighboring rungs results in a final state with one rung empty, and a neighboring rung doubly occupied, in other words, an electron hole pair consisting of a hole in the band below E_F , and an electron in the empty state above E_F indicated in Fig. 3.7a. This corresponds to the process

$$2|^2B_\sigma\rangle \rightarrow |^3,1LR\rangle + |0\rangle \quad (3.7)$$

Note that the final state wavefunction is qualitatively different from the on-rung bonding-antibonding excitations considered above, even though the excitations are close in energy: it involves one rung with no electron, and a neighboring rung with one electron occupying each V-atom. The energy of this process is approximately $2t_\perp + \delta V$, where δV represents the increase in Coulomb interaction energy by bringing two electrons together on the same rung. Since the distance between the electrons changes from about 5.0\AA to 3.4\AA , and taking into account a screening factor $\epsilon \approx 6$, we estimate that $\delta V \simeq 0.2eV$.

This value of δV corresponds closely to the difference in peak positions along the a and b directions. According to this interpretation the absorption at 1.1 eV along b corresponds to the creation of a free electron and hole, capable of carrying electrical currents. The on-rung excitation at 0.9 eV along the a -direction is a localized (charge neutral) excitation, in other words an exciton. In this case the energy of the exciton involves the states of a single electron only, whereas the free carrier states involve many-body interactions.

Doping with Ca creates doubly occupied rungs, whose ground state energy is not $2|^2B_\sigma\rangle$ but $|^1\tilde{LR}\rangle$. Consequently, the electrons on these rungs will not be involved in the processes of Eq. 3.7, thus decreasing the intensity of the B peak upon doping, as seen from Fig. 3.4b.

The room temperature crystal structure has four V-atoms per unit cell, organized in ladders with up and down oriented apical oxygens alternating along the a -direction, resulting in a double degeneracy of the electronic states discussed above. The coupling between adjacent ladders lifts the degeneracy of these states, resulting in a "Davidov" splitting of the peaks A and B. This can create the two additional "shoulders" in $\sigma(\omega)$ at 1.4 and 1.7 eV for peak A and B respectively.

With ARPES[95] it has been observed that an energy of 3 eV separates the $V3d$ band from the $O2p$. We therefore attribute the peaks at 3.3 eV in $\sigma_a(\omega)$ and the peak at 4 eV in $\sigma_b(\omega)$ to transitions of the type

$$|^2B_\sigma \rangle \rightarrow |2p^1LR \rangle \quad (3.8)$$

where the $2p$ hole is located on the oxygen on the same rung for peak A (see Fig. 3.7b), and in between the rungs for peak B. This is further supported by previous optical measurements on V_2O_5 [99], which showed a peak at about 3 eV. In V_2O_5 all V-ions have a formal $V3d^0$ configuration, hence the 3 eV peak cannot be attributed to d-d transitions. However, the $O2p \rightarrow V3d$ transitions should appear at approximately the same photon energy as in NaV_2O_5 , which further supports our assignment of the 3 eV peak in NaV_2O_5 to $O2p \rightarrow V3d$ transitions.

In summary, we have measured the dielectric function along the a and b axes of $\text{Ca}_x\text{Na}_{1-x}\text{V}_2\text{O}_5$ for $x=0, 0.06, 0.15$ and $x=0.20$. The 0.9 eV peak in $\sigma_a(\omega)$ was shown experimentally to be a bonding-antibonding transition inside the V_2O rung and not a vanadium d-d transition due to crystal field splitting. We identified the 3.3eV peak in $\sigma_a(\omega)$ as the transition from the oxygen orbitals to the antibonding one of the V_2O rung. This strongly supports the notion, previously expressed in Refs [10, 13, 96] that NaV_2O_5 is an insulator due to a combination of three factors: a crystal field splitting, an on-site Hubbard interaction, and an on-rung bonding-antibonding splitting of the two $V3d_{xy}$ orbitals, each of which is large compared to the inter-rung hopping parameter.

The above proposed assignment of the 0.9eV peak for $\mathbf{E} \parallel \mathbf{a}$, as a bonding-antibonding transition within the Heitler-London model [89], was confirmed by later calculations. We can cite here band structure calculations done within the local spin density approximation (LSDA) + U , taking into account a large Coulomb on site interaction ($U = 2 - 3\text{eV}$) [100]. Also the $t - J - V$ numerical calculations on clusters of vanadium atoms leads to the same results [97, 101].

However, we want to mention that very recent *ab initio* cluster calculations [76, 102] propose a different picture than the one accepted up to now in literature, and presented above. Usually, it is believed that the p_y orbital of the on rung oxygen atom has two electrons, but the calculations cited above suggest that it has mainly one electron. In other words, the p_y orbital of O would have only one electron, and the two V atoms would have each a full electron on its d_{xy} orbital. The V-O-V rung would have thus predominant $V 3d_{xy}^1 - O2p_y^1 - V3d_{xy}^1$ character, rather than $V 3d_{xy}^{0.5} - O2p_y^2 - V3d_{xy}^{0.5}$. The implications of this picture, if true, are still not considered in the literature, even though some attempts are emerging [12]. However, as the interpretation of the 0.9eV peak for $\mathbf{E} \parallel \mathbf{a}$ is concerned, it does not change substantially. According to Ref.[76], it does not correspond to a transfer of charge from the O atom to the V ones, but rather to a

redistribution of electrons on the V atoms, as in the bonding-antibonding picture. This results however in a different spin coupling scheme [12].

3.3 Low temperature ellipsometry of α' - NaV_2O_5

Here we present the measurements of the optical conductivity of α' - NaV_2O_5 in the visible range, as a function of temperature [90]. In our spectra we observe a strong temperature dependence of the 0.9eV peak for $\mathbf{E} \parallel \mathbf{a}$. This was considered [90] to be an indication of a strong charge redistribution between the rungs of the ladders at elevated temperature, which at the same time provides a channel for electrical conductivity with an activation energy of about 25 meV. In a later work [103], this behavior is explained by the destruction of short-range antiferromagnetic correlations. We also report a remarkable inflection of the temperature dependence at the phase transition, which was interpreted [90] as an inflection of the charge redistribution process due to a particular correlated electronic state in which the charge and spin degrees of freedom are frozen out simultaneously.

3.3.1 Data collection and analyzes

The crystal (sample CR8) with dimensions of approximately 2, 3 and 0.3 mm along the a , b , and c axes respectively, was mounted in a ultra high vacuum (UHV) optical cryostat in order to prevent the formation of "ice" on the surface. The pressure was about 10^{-8} mbar at 300K and reached 10^{-9} mbar at 4K.

We performed ellipsometric measurements on the (001) surfaces of the crystals both with the plane of incidence of the light along the a and the b axis. An angle of incidence Θ of 80° was used in all experiments. In the previous section we described the details of the procedure followed to obtain $\epsilon(\omega)$. The results are presented in Fig. 3.8 and Fig .3.9.

Based on the doping dependence of the optical spectra of $\text{Na}_{1-x}\text{Ca}_x\text{VO}_5$ we established in the previous section [89] the assignments made in Refs.[10, 13, 96], namely that the peaks at around 1 eV along the a and b directions are due to transitions between linear combinations of V $3d_{xy}$ -states of the two V-ions forming the rungs[10, 13, 96]. In Refs.[10] and [96] even and odd combinations were considered. The 0.9 eV peak in $\sigma_a(\omega)$ (peak A in Fig. 3.8) would then correspond to the transition from V-V bonding to antibonding combinations on the same rung[13]. In Ref.[13] this model was extended to allow lop-sided linear combinations of the same orbitals, so that the 0.9 eV peak then is a transition between left- and right-oriented linear combinations. Our work presented in Ref. [89], and in the previous section, definitely rules out the assignment of these peaks to crystal field-type $Vd - d$ transitions proposed in Refs. [14, 98].

The 1.1 eV peak in $\sigma_b(\omega)$ (peak B in Fig .3.9) involves transitions between neighboring rungs along the ladder. As a result of the correlation gap in the density of states, the optically induced transfer of electrons between neighboring rungs results in a final state with one rung empty, and a neighboring rung doubly occupied, in other words, an electron hole pair consisting of a hole in the band below E_F , and an electron in the empty state above E_F . Note that the final state wavefunction is qualitatively different from the on-rung

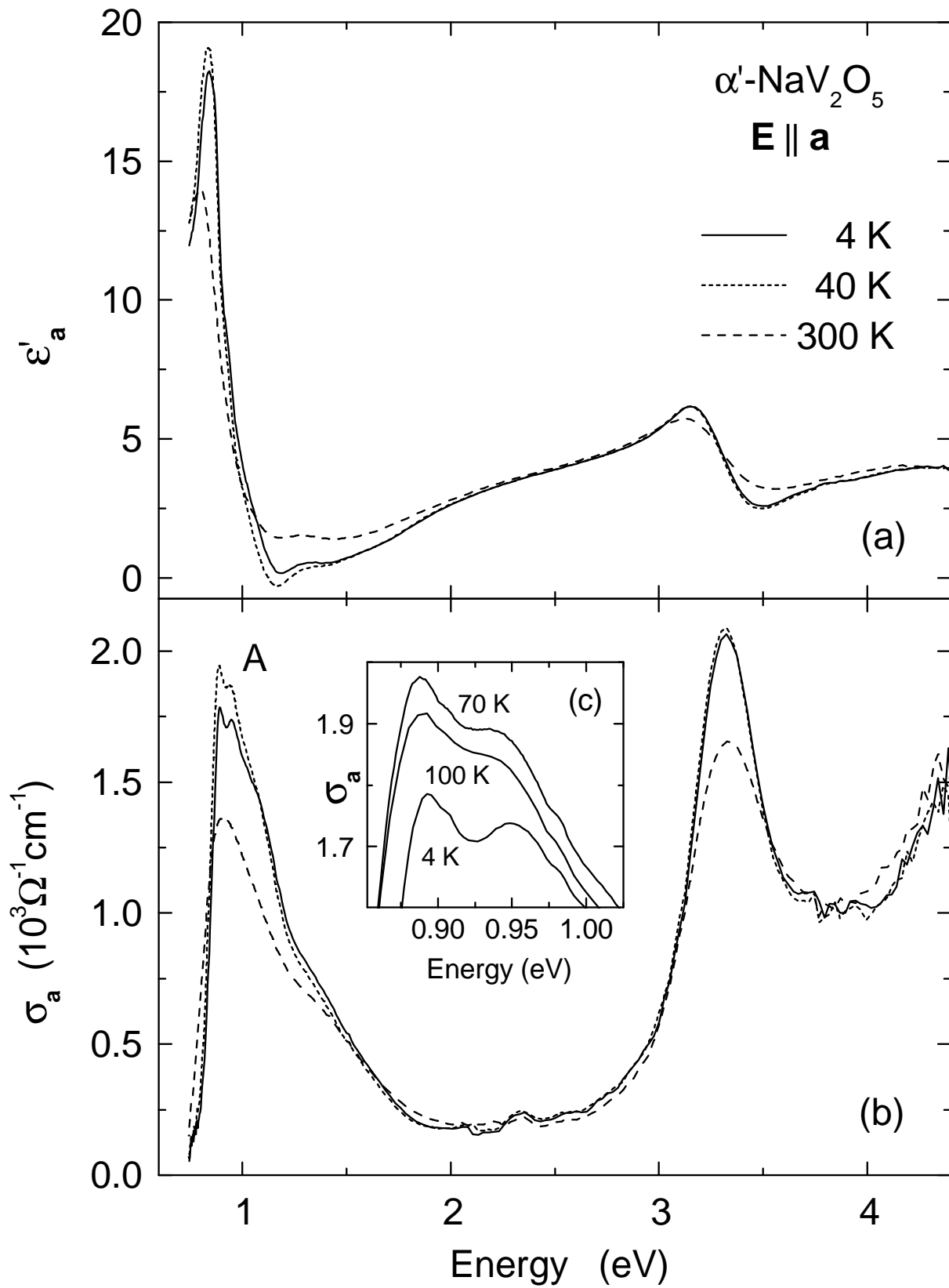


Figure 3.8: Real part $\epsilon'(\omega)$ of the complex dielectric function (panel a), and optical conductivity $\sigma_1(\omega)$ (panel b), for $E \parallel a$. Inset c): zoom in for the optical conductivity.

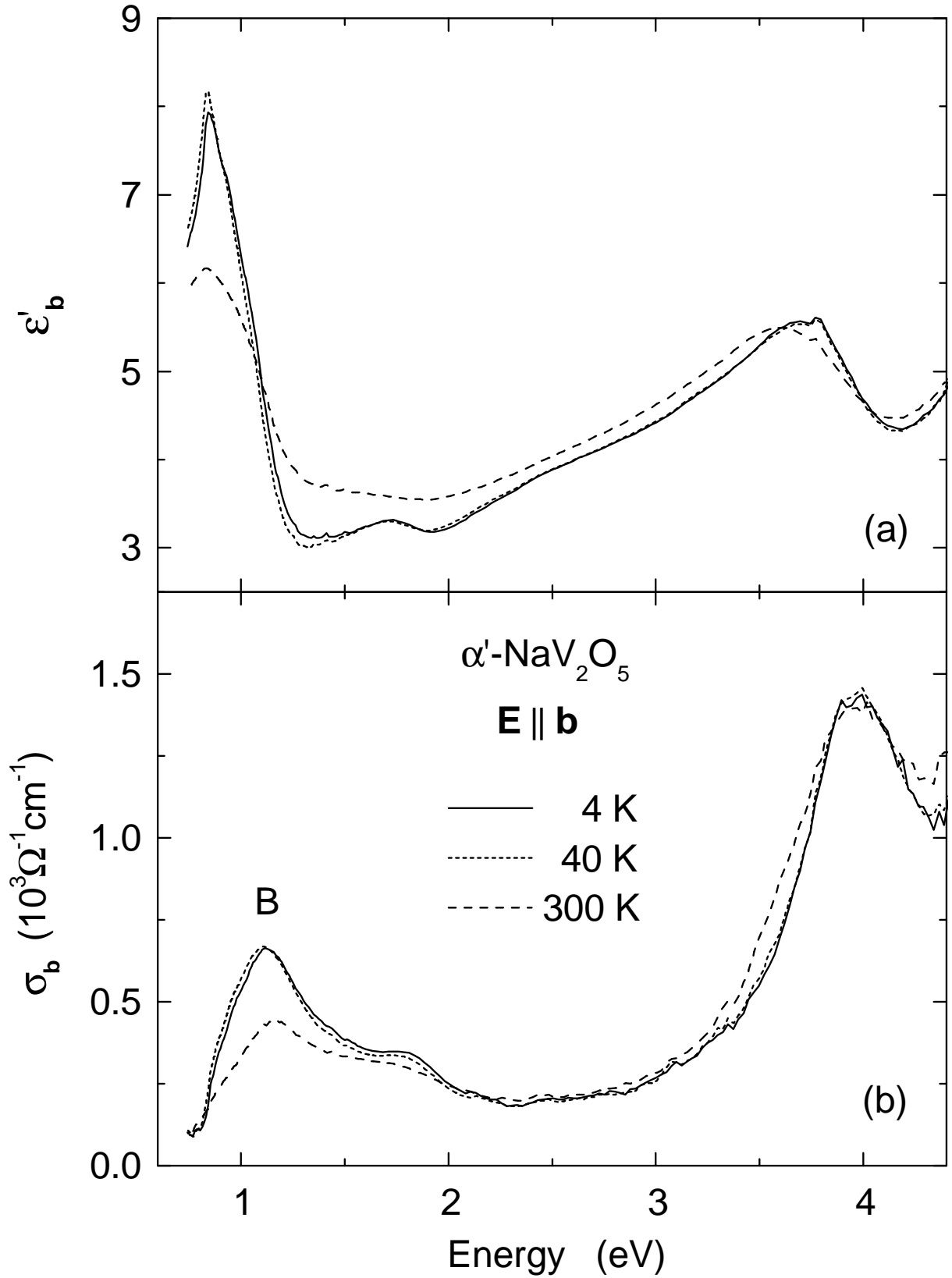


Figure 3.9: Real part $\epsilon'(\omega)$ of the complex dielectric function (panel a), and optical conductivity $\sigma_1(\omega)$ (panel b), for $E \parallel b$.

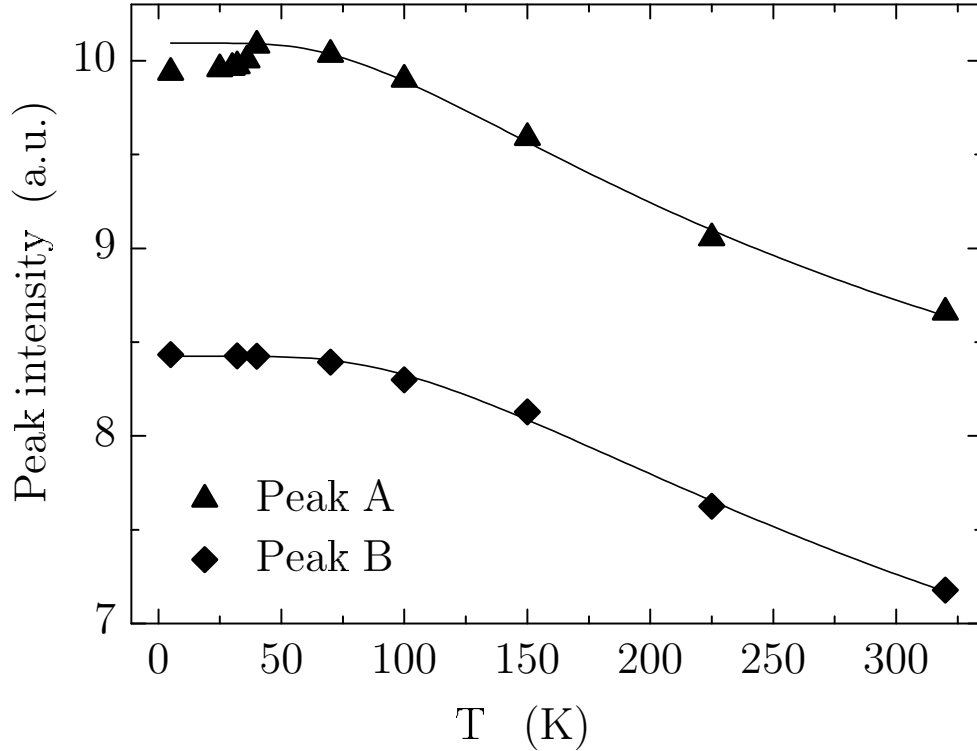


Figure 3.10: Intensity of the 1 eV peaks detected along the a and b axes (peak A and B, respectively), plotted vs. temperature. Solid lines are fits to the formula $I(T) = I_0(1 - f e^{-E_0/T})$.

bonding-antibonding excitations considered above (peak A), even though the excitation energies are the same[89] : it involves one rung with no electron, and a neighboring rung with one electron occupying each V-atom. We associate the lower energy of peak A compared to peak B with the attractive electron-hole Coulomb interaction, favoring on-rung electron-hole pairs.

Optical transitions having values below 2eV were also seen in V_6O_{13} and VO_2 . In V_2O_5 they have very small intensities, and were attributed to defects [99]. The peak at 3.3 eV in $\sigma_a(\omega)$ was attributed to a transition from the $2p$ orbital of oxygen to the antibonding level within the same V_2O cluster[89].

3.3.2 Temperature dependence above the phase transition

Let us now address the temperature dependence of the spectra. As we can see in Fig. 3.8b and 3.9b, there is a strong decrease of the *intensity* of the peaks A and B with the increase of the temperature. The spectral weight for both cases is not transferred to low frequencies[13]. The spectral weight of the B peak seems to be recovered up to and above 4eV. The spectral weight of the 3.3eV peak in the a direction is recovered also in the nearby high frequencies [93, 98], whereas the intensity of the A peak is not recovered up to 3 eV [93].

The evolution of the 1 eV peaks can be seen from Fig. 3.10, where the integrated intensities in $\sigma_1(\omega)$ from 0.75 eV to 2.25 eV were plotted as a function of temperature. The data was fitted with an activation energy formula $I(T) = I_0(1 - f e^{-E_0/T})$. It gave $f=0.35$ and $E_0=286\text{K}$ for the a direction, and $f=0.47$ and $E_0=370\text{K}$ for the b direction. From the fits we see that the activation energy E_0 is about 25meV, which is very small for the frequency range of the peaks, but is comparable to the activation energy in resistivity measurements at low temperatures [104]. A decrease of the intensity of the A peak takes place below the phase transition, but otherwise there are no features related to it. The splitting of the A peak of about 55meV (Fig.3.8c) exists even at 100K. Judging from its sharp shape and the value of splitting, it can be attributed to a phonon side-band.

Band structure calculations have indicated that the d_{xy} orbitals are well separated from the other d orbitals [10] and ESR experiments have led to g-values which indicate the complete quenching of the orbital momentum [105]. There are then no other low-lying crystal levels, about 25 meV above the ground state, to play a role in the temperature dependence behavior of the A peak. Comparing the doping dependence of the A peak in $\text{Ca}_x\text{Na}_{1-x}\text{V}_2\text{O}_5$ [89] and the high temperature dependence from Fig.3.8b we see that the two behaviors resembles each other, presenting no shifting or splitting with respect to one another. But, as discussed in Ref [89], the intensity of the A peak decreases upon doping because doping induces doubly occupied rungs. The same mechanism can then be responsible for the decrease of the intensity of the A peak with increasing temperature. The bonding-antibonding transition (A peak) on the rung will have a reduced intensity, as there are fewer singly occupied rungs, as in the case of $\text{Ca}_x\text{Na}_{1-x}\text{V}_2\text{O}_5$ [89]. The transitions on the doubly occupied rungs are at an energy U , around 4 eV, with a factor $(t_\perp/U)^2$ reduction of the original spectral weight[89]. The activation energy of 25meV would then be the energy required to redistribute the electrons between the rungs, either on the same ladder, or between different ladders. Eventually, at very high temperatures, only half of the rungs would be occupied with one electron, so the intensity of the A peak would be at half the low temperature value ($f = 0.5$ in the fitting formula of Fig.3.10).

At first glance, the processes leading to partial emptying of rungs, while doubly occupying others, would seem to be of the order of the energy of peak B (1eV), which corresponds exactly to such a process and one may wonder how such a low energy scale could exist. However, processes involving the *collective* motion of charge can be at a much lower energy than the single particle charge transfer, as a result of short range (nearest neighbor) Coulomb interactions. An example of such a collective mode is the zig-zag ordering [11, 97] involving an (almost) soft charge mode for k at the Brillouin zone boundary. These *charge* modes, because k is at the BZ boundary, can appear only indirectly (*e.g.* phonon assisted) in $\sigma(\omega)$, and therefore are at best weakly infrared active. Under favorable conditions the *spin* degrees of freedom[13] in addition results in a weak but finite $\sigma(\omega)$. Another way in which the electrons can move from one rung to another is by forming topological defects, such as domain walls separating charge ordering domains. Macroscopically this could lead to double occupancy of some rungs and emptying others.

Recent calculations on a t-J-V model [103], motivated by our work [90], proposed however a different picture for explaining this temperature dependence. In Ref.[103] it is argued that a simple charge ordering model based on a simple isospin picture [11, 85] does not lead to the strong temperature effects observed, and one has to include either a

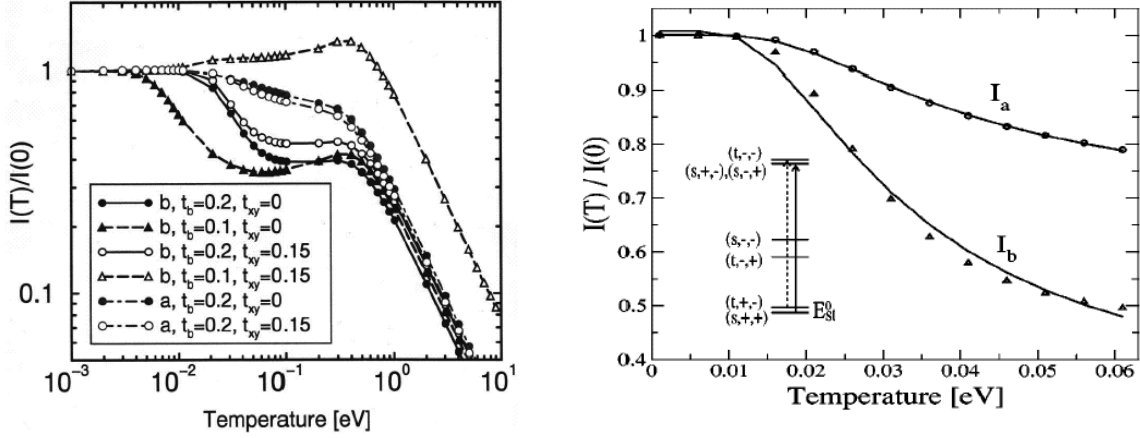


Figure 3.11: Left panel: Integrated optical conductivity for a (dot-dashed) and b (solid and dashed lines) calculated for the 1eV peaks in the t - J - V model for different parameters. Right panel: Integrated optical conductivity for two standard parameters in a selected temperature interval. Both graphs are reproduced from Ref. [103]

more complete spin-pseudo spin model [85], or a t - J - V picture. In Fig. 3.11 we reproduce the results from Ref.[103]. In both panels, the calculated integrated optical intensity (IOC), roughly corresponding to the integrating intensity in the 1eV peaks, is presented as a function of temperature. In the left panel two energy scales are recognized. First, there is a decrease of the IOC at a temperature around $J \propto t_b^2/V_a$, which was reported to be $J = 48.2$ meV in Ref.[6] and $J = 37.9$ meV in Ref.[106, 107]. This is thus of the order of room temperature, where we indeed see the changes. A stronger decrease in IOC takes place at higher temperatures of the order $T \geq V_b$ which is around $V_b \approx 1\text{eV}$, thus at much higher temperatures. That is why the isospin model without spins would fail to predict the temperature changes at the observed temperatures. A zoom in on the measured temperature range for the selected parameters $t_b = 0.2\text{eV}$ and $t_{xy} = 0.15\text{eV}$ is presented in the right panel of Fig. 3.11. The temperature dependence resembles indeed the measured data presented in Fig. 3.10.

The fact that the 25meV energy scale of the temperature changes is much smaller than the optical gap of 1eV is not entirely surprising. In fact, there are experiments which indicate charge degrees of freedom at a much lower energy. Resistivity measurements yielded an energy gap ranging from 30meV at lower temperatures to 75 meV at high temperatures [104]. The dielectric loss ϵ'' for frequency of 16.5 GHz along b direction is rather constant up to 150 K and then increases very rapidly above 200K [87] (so that the microwave signal is lost at room temperature), meaning that an absorption peak could start to evolve at 200K for very low frequencies. A low frequency continuum was observed near 25 meV with infrared spectroscopy [13] and at 75 meV with Raman spectroscopy [14]. Also infrared measurements [13] found that $\sigma_{1,a}$ increases with increasing temperature.

3.3.3 Temperature dependence across the phase transition

Perhaps most striking of all is the fact that the *peak positions* turn out to be temperature independent throughout the entire temperature range and also across the phase transition. This behavior should be contrasted with the remarkable splitting of the V-NMR lines in two components below the phase transition[84]. It has been suggested [10] that the T_c marks the transition from a high temperature phase where every rung is occupied with an electron residing in a H_2^+ type bonding orbital (formed by the two V $3d_{xy}$ orbitals), to a low temperature phase, where the system is in a charge ordered state (*e.g.* the zigzag ordered state[11, 108] with an alternation of V^{4+} and V^{5+} states, or, as suggested in Refs. [81, 109] with $\text{V}^{4+}/\text{V}^{5+}$ ladders and $\text{V}^{4.5+}/\text{V}^{4.5+}$ ladders alternating). In Refs.[13, 97] estimates have been made of the potential energy difference between the left and righthand V-sites on the same rung, in order to reproduce the correct intensity and photon-energy of the 1 eV peak along a , as well as producing a $\text{V}^{4.9+}/\text{V}^{4.1+}$ distribution between left and right. This turned out to be $\Delta = V_L - V_R \approx 0.8\text{eV}$, with an effective hopping parameter $t_{\perp} \approx 0.4\text{eV}$.

To have $\text{V}^{4.5+}/\text{V}^{4.5+}$ above and $\text{V}^{4+}/\text{V}^{5+}$ below the phase transition, requires that the potential energy difference changes from $\Delta = 0.8\text{eV}$ below T_c to 0 at and above T_c . As a result the "1 eV peak" would shift from 0.89 eV to 0.8 eV in the temperature interval between 0 and 34 K, and would remain constant above T_c . The observed shift is less than 0.03 eV within the entire temperature interval, and less than 0.01 eV between 0 and 34 K. This suggests that the change in Δ (and consequently the charge of the V atoms) at the phase transition is very small. In fact, a change of Δ from 0.1eV to 0 across T_c , compatible with the experimental results, would yield a change in the valence state from $\text{V}^{4.44+}/\text{V}^{4.56+}$ to $\text{V}^{4.5+}/\text{V}^{4.5+}$ between 0 and 34 K, which is an almost negligible effect. Thus we conclude that, irrespective of the possible charge configurations $\text{V}^{4.5+}/\text{V}^{4.5+}$ or $\text{V}^{5+}/\text{V}^{4+}$, the changes in the charges of the V atoms at the phase transitions are very small (smaller than $0.06e$).

Recent *ab initio* cluster calculations [12, 102] confirmed that the charge redistribution at the phase transition is indeed very small. There is an apparent contradiction with the inelastic neutron scattering experiments [110], which predicted large effects at the phase transition. This was explained in Ref. [102] by the fact that the inelastic neutron measurements are more sensitive to the spin ordering, which is believed to be different than the charge ordering [102].

3.3.4 Temperature dependence below the phase transition

The suppression of intensity below the phase transition (Fig.3.10) seems to mark a redistribution of charge which is associated with the spin gap. X-ray diffraction indicates that the superstructure below T_c consists of a group of 4 rungs [109]: 2 neighboring rungs of the central ladder, 1 on the left-hand and 1 on the right-hand ladder. The presence of a spin-gap indicates that the 4 spins of this structural unit form an $S = 0$ state below T_c .

To account for the absence of a change of the valence of the V atoms at the phase transition, as well as for the slight doubly occupancy below the phase transition, the following scenario has been put forward. Below T_c the structure would be formed by

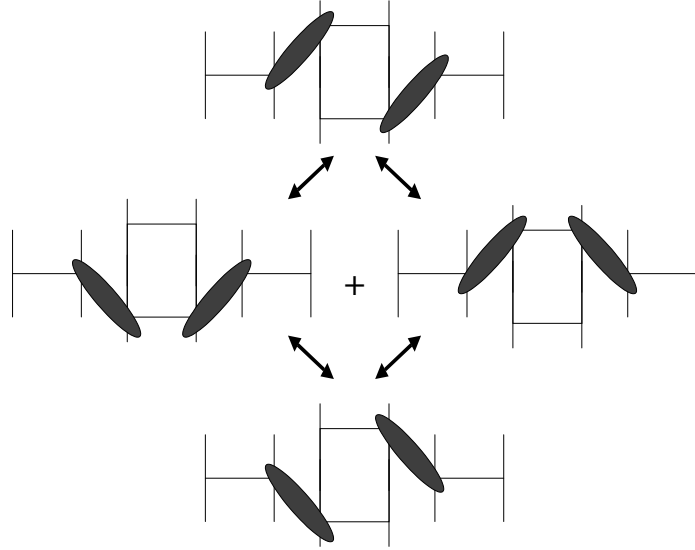


Figure 3.12: The correlated electron state in the low temperature phase is a superposition of the four configurations displayed in the figure.

singlets (see Fig. 3.12). If they are arranged in a quantum mechanical configuration, as in Fig 3.12, this gives a slight double occupancy of the rungs. The reduced intensity in our spectra below T_c then reflects the amount of singlet character involving doubly occupied rungs. Passing the phase transition they would evolve independently. This would result in a random configuration with an average valence of +4.5 for the V atoms, and also a spin susceptibility for high temperature phase due to appearance of some free spins. The nature of the weak charge-redistribution which we observe at low temperature would then be manifestly *quantum mechanical*.

A different explanation of the fact that, across the phase transition, the intensity has a small (about 1% from Fig. 3.10) but a sharp change, may include the shifting of the atoms. Indeed, they would change the interatomic distances, affecting directly the integrated optical conductivity, according to Formula (2) of Ref. [13]. A contra-argument to this is however that the change is observed only along the a axis.

In summary, we have measured the temperature dependence of the dielectric function along the a and b axes of α' - NaV_2O_5 in the photon energy range 0.8-4.5 eV for temperatures down to 4K. No appreciable shifts of the 1 eV peaks were found, thus showing that the change in the valence state of the V atoms at the phase transition is very small (smaller than $0.06e$). A strong decrease of the 1 eV peaks with increasing temperature was observed. We assigned [90] this temperature dependence behavior to collective charge redistribution, namely the redistribution of the electrons among the rungs resulting in double occupation of some rungs as temperature increases, with an activation energy of about 25meV. A more complex approach, involving the destruction of the short-range antiferromagnetic correlation has been also put forward [103]. Below the phase transition, a small (about 1%) but sharp decrease of intensity of the 0.9 eV peak in $\sigma_a(\omega)$ was found. It was attributed to a finite probability of having, in the singlet state below T_c , configurations with electron pairs occupying the same rung. A simple picture in which

the intensity decreases just as result of changing the atomic distances across the phase transition is however much more probable.

3.4 Doping dependence of the far-infrared conductivity of α' - $\text{Na}_{1-x}\text{Ca}_x\text{V}_2\text{O}_5$

As discussed already, a very useful tool in the study of strongly correlated systems is doping. This leads to spectacular effects in the doped anti-ferromagnetic insulators, such as the high temperature superconductors. Going away from the "right" stoichiometry, or by replacing the atoms forming the charge reservoirs, would in principle change the density of mobile charge carriers. In most cases, where a model of "rigid" bands may be assumed, they give metallic behavior, due to the fact that the bands are now only partially filled.

However, a non-stoichiometric compound presents one additional complication: probable disorder of the substituting atoms or vacancies created. This may, or may not, play an important role in the dynamics of the charge carriers. In the high-temperature superconductors for example, it is generally accepted that this role is small. In the case of β - $\text{Na}_x\text{V}_2\text{O}_5$ this influence is big, and leads probably to the suppression of metallicity. The magnitude of this influence is given by many factors, including the magnitude of the potential of the random donors (acceptors), screening, and type of the charge carries.

If the random potential is stronger than approximately twice the width of the band, Anderson localization of the charge carriers is expected indeed to take place[111]. If the charge carriers are small polarons, they are also usually bound to the donor (or acceptor) sites [22]. Particulary the one-dimensional metals are susceptible to the influence of the random fields, since the carriers are confined to a chain which may be "broken" by a single impurity potential, and they cannot go around the impurity as it would be possible in higher dimensions. The system looses then easily its metallic behavior.

A single crystal sample of α' - $\text{Na}_{0.8}\text{Ca}_{0.2}\text{V}_2\text{O}_5$ was measured in the far-infrared range. As discussed above, the Ca doping introduces 20% more electrons in the vanadium ladder. In a "rigid" band picture this is thus expected to be a metal.

In Fig. 3.13 we present the normal incidence reflectivity measurements for the two possible polarizations of the light $\mathbf{E}\parallel\mathbf{a}$ and $\mathbf{E}\parallel\mathbf{b}$. The surface measured was (001). From Fig. 3.13 we remark immediately the absence of a Drude peak for both polarizations, showing thus the lack of metallicity. However, even though the α' - $\text{Na}_{0.8}\text{Ca}_{0.2}\text{V}_2\text{O}_5$ sample measured was plane parallel, the fringes present in the α' - NaV_2O_5 for $\mathbf{E}\parallel\mathbf{b}$ at low frequencies are not present in α' - $\text{Na}_{0.8}\text{Ca}_{0.2}\text{V}_2\text{O}_5$. This suggest that the low frequency conductivity of α' - $\text{Na}_{0.8}\text{Ca}_{0.2}\text{V}_2\text{O}_5$ is higher than that of α' - NaV_2O_5 as expected, but not sufficiently high to give metallic behavior. In Fig. 3.14 we present the optical conductivity $\sigma_1(\omega)$ obtained from the Kramer-Kronig transformations. The lack of metallicity is clear in this plot as well.

We think that the insulating behavior still present in the α' - $\text{Na}_{0.8}\text{Ca}_{0.2}\text{V}_2\text{O}_5$ single crystals is caused by the Ca atoms which localize the charge carriers. This can take place easily in a one-dimensional system such as α' - NaV_2O_5 as discussed above.

From Fig. 3.14 we see that the far-infrared spectra of α' - NaV_2O_5 and α' - $\text{Na}_{0.8}\text{Ca}_{0.2}\text{V}_2\text{O}_5$

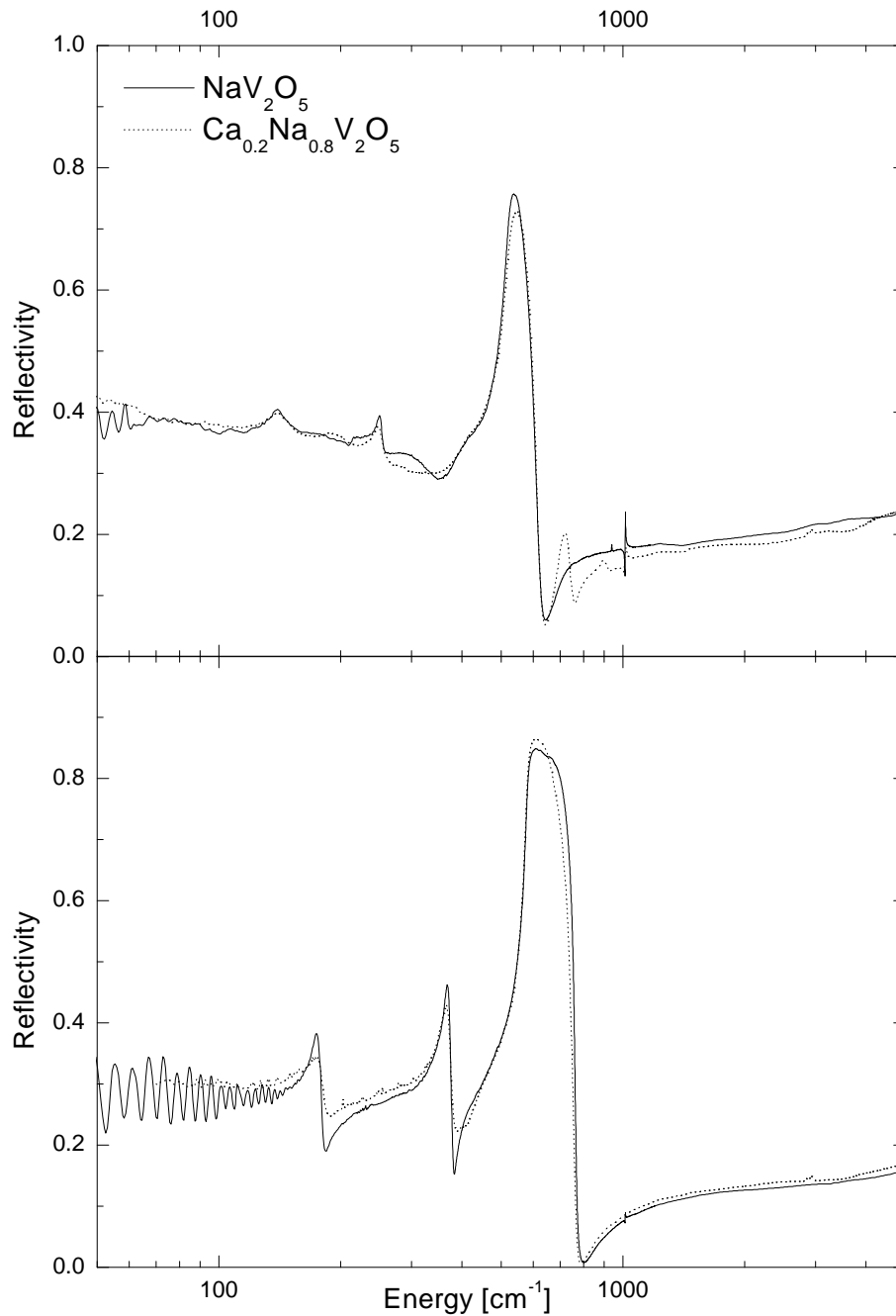


Figure 3.13: Room temperature frequency dependence of the reflectivity for $\mathbf{E}\parallel\mathbf{a}$ (upper panel) and $\mathbf{E}\parallel\mathbf{b}$ (lower panel)

look quite similar, as expected due to the small Ca concentration. There seems to be no noticeable difference for the $\mathbf{E}\parallel\mathbf{b}$ polarization. For the $\mathbf{E}\parallel\mathbf{a}$ few differences can be noticed. First, a new peak with a shape of a broader phonon, evolves around 720cm^{-1} upon doping. This should be in principle compared with the far infrared spectrum of α' - CaV_2O_5 where a phonon could be naturally found for this polarization. Unfortunately, there are no measurements done up to now for crystals. Far infrared measurements on powder

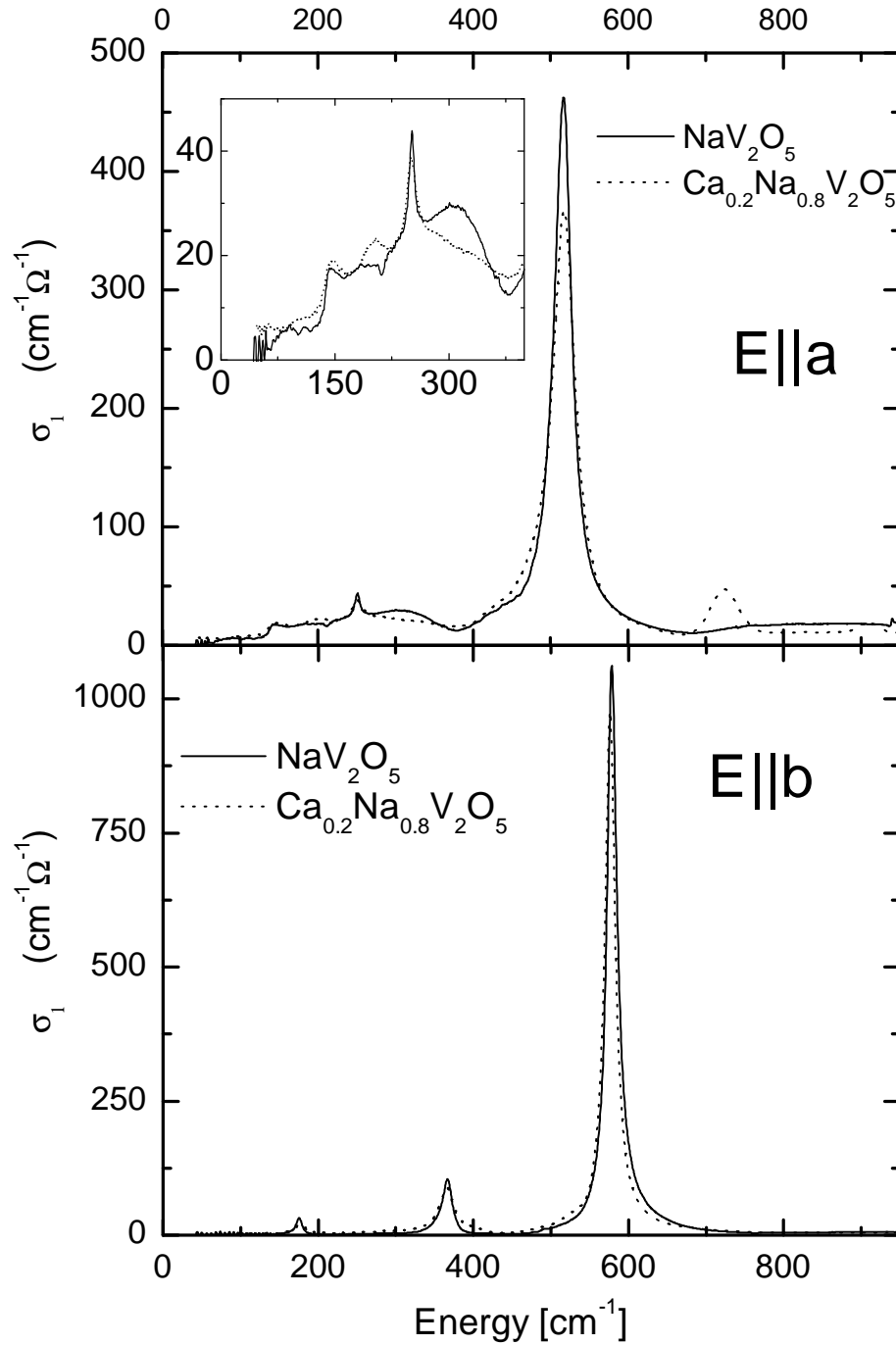


Figure 3.14: Optical conductivity $\sigma_1(\omega)$ of α' - $\text{Na}_{0.8}\text{Ca}_{0.2}\text{V}_2\text{O}_5$ at room temperature for $E||a$ (upper panel) and $E||b$ (lower panel).

α' - CaV_2O_5 [112] show however no peak around 720cm^{-1} . From Figure 3.14 we see that the spectral weight in the 505cm^{-1} phonon of α' - NaV_2O_5 seems to be recovered in the 720cm^{-1} peak of α' - $\text{Na}_{0.8}\text{Ca}_{0.2}\text{V}_2\text{O}_5$. In other words, the V-O₃ stretching phonon which appears at 505cm^{-1} in α' - NaV_2O_5 [112] must evolve now in a mode with a much higher frequency in α' - $\text{Na}_{0.8}\text{Ca}_{0.2}\text{V}_2\text{O}_5$ at 720cm^{-1} . This is however much higher

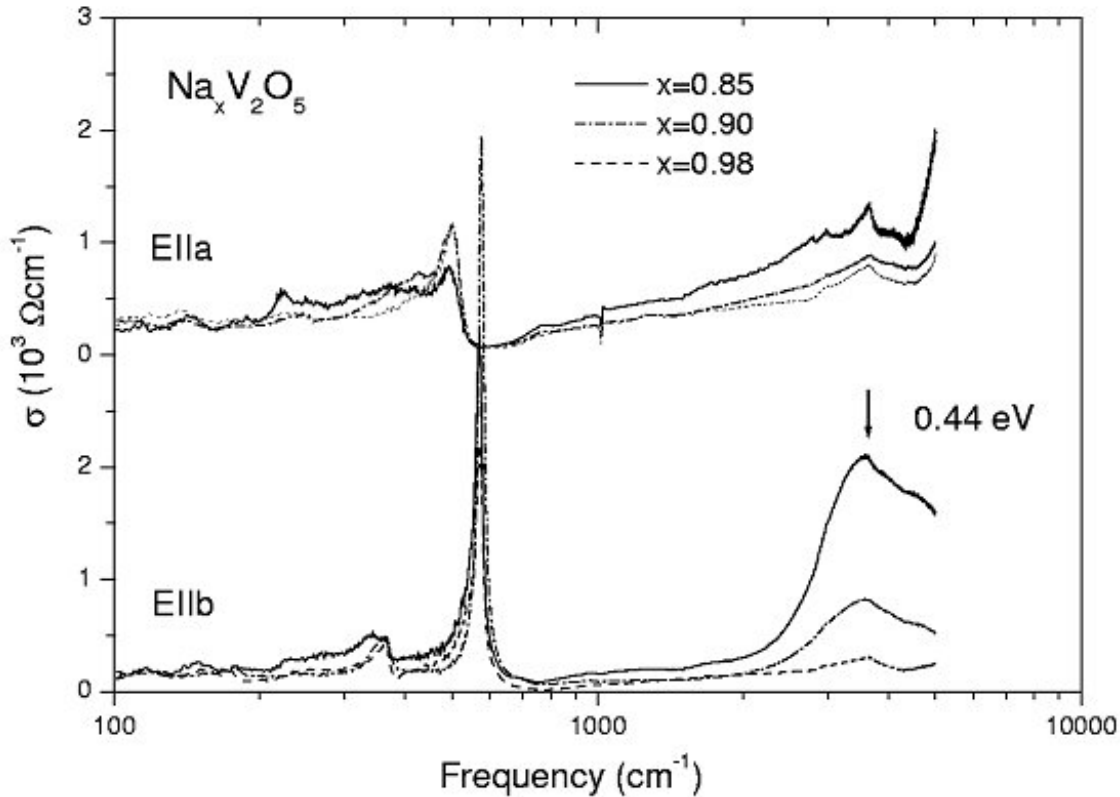


Figure 3.15: Far infrared optical conductivity of α' - $\text{Na}_x\text{V}_2\text{O}_5$ reproduced from Ref. [91]. Inset: Schematic representation of the $V3d_{x,y}$ -IB transitions proposed in Ref. [91] for the 0.44eV peak.

than the stretching V-O_3 frequency of 515cm^{-1} attributed in Ref. [112] from the powder measurements of α' - CaV_2O_5 .

Moreover, Ca is a heavier atom than Na atom, thus, in principle, no phonon peaks would be expected at higher frequencies than the one observed (at 505cm^{-1}) in α' - NaV_2O_5 . One explanation of this apparent contradiction may be that the 720cm^{-1} absorption peak is due to a localized vibration due to the Ca atoms within a Ca-free environment, and thus may not be necessarily present at the same frequency in α' - CaV_2O_5 .

Besides the appearance of a new phonon peak, we remark the diminution of the far infrared continuum which appears around 300cm^{-1} . The presence of the continuum is still unexplained in literature, even though a few explanations have been proposed. They include the "charge magnon" picture [13], and the photoexcitation of a three particle continuum: two spinons plus a low energy charge excitation [85]. The FIR continuum is related to the special physics of α' - NaV_2O_5 and probably disappears in α' - CaV_2O_5 , as seems to be suggested from the measurements of the powder samples in Ref. [112]. It is thus not unexpected that its intensity decreases. The same seems to happen with the continuum around 900cm^{-1} which decreases as well in α' - $\text{Na}_{0.8}\text{Ca}_{0.2}\text{V}_2\text{O}_5$ as compared with α' - NaV_2O_5 .

Optical measurements have previously been done on sodium deficient α' - $\text{Na}_x\text{V}_2\text{O}_5$ samples, which can be seen as hole doped α' - NaV_2O_5 , as opposed to the electron doped

α' - $\text{Na}_{1-x}\text{Ca}_x\text{V}_2\text{O}_5$. They are reproduced in Fig.3.15 from Ref. [91]. As we can see, they also didn't show metallic behavior. In addition, transport measurements on the sodium deficient samples α' - $\text{Na}_x\text{V}_2\text{O}_5$ [113] revealed that the doping into the 1-D chain by means of Na-deficiency does not induce clean metallic behavior. The conductivity, even though increased with Na deficiency, has a temperature dependence consistent with variable range hopping model.

3.5 Optical measurements on α' - $\text{Na}_x\text{V}_2\text{O}_5$

In the α' - $\text{Na}_x\text{V}_2\text{O}_5$ case, the sodium deficiency does not alter the α' crystal structure [6] down to $x=0.7$, but changes the relative abundance of V^{4+} and V^{5+} as in the case of α' - $\text{Na}_{1-x}\text{Ca}_x\text{V}_2\text{O}_5$, but in the case of Na deficiency more "extra" holes (V^{5+}) are introduced.

The optical properties of sodium-deficient α' - $\text{Na}_x\text{V}_2\text{O}_5$ ($0.85 \leq x \leq 1.00$) single crystals have been analyzed from 0.75 to 4.5 eV, using spectroscopic ellipsometry, at room temperature. The samples had dimensions typically of about $2 \times 4 \times 0.4$ mm³ in the a , b , and c axes, respectively. The ellipsometric measurements were done on the (001) surfaces of the crystals, with the plane of incidence along the a and b axes successively. The results of the *pseudo-dielectric* functions, given by the formula 3.2, are presented in Fig.3.16.

The bands at the energies 0.9, 1.2 and 3.2 eV for $\mathbf{E} \parallel \mathbf{a}$ and 1.2, 1.6 and 3.7 eV for $\mathbf{E} \parallel \mathbf{b}$ are found in accordance with previously presented measurements on α' - NaV_2O_5 and α' - $\text{Na}_{1-x}\text{Ca}_x\text{V}_2\text{O}_5$. The sodium deficiency causes the activation of new optical transitions at about 2.8 eV for $\mathbf{E} \parallel \mathbf{a}$ and 3.2 eV for $\mathbf{E} \parallel \mathbf{b}$. The 1.2 eV peak for $\mathbf{E} \parallel \mathbf{b}$ does not extrapolate to zero at low frequencies, suggesting the existence of a peak at lower frequencies. Indeed, the far-infrared measurements performed in [91] confirmed the existence of a peak at 0.44 eV for $\mathbf{E} \parallel \mathbf{b}$, as we can see from Fig. 3.15, which was reproduced from Ref.[91]. The 2.8 eV peak which evolves in the sodium-deficient samples for $\mathbf{E} \parallel \mathbf{a}$ was found [91] to be responsible for the resonant behavior of the (aa) polarized Raman spectra. The intensity of the 495-cm⁻¹ mode, presented in the inset of Fig.3 of Ref.[91], mimic the change of optical conductivity presented here.

At a first glance, the $\mathbf{E} \parallel \mathbf{a}$ spectrum of the sodium-deficient samples should be a superposition of the V_2O_5 spectra given by the empty rungs of the ladder, and that of α' - NaV_2O_5 given by the rungs having a single electron, and this seems to be the case for the visible part of the spectra. Measurements on V_2O_5 for $\mathbf{E} \parallel \mathbf{a}$ (which is the same direction in α' - NaV_2O_5) show the appearance of a single high-intensity peak at 2.8 eV [114–116] with only a shoulder around 3.2eV. In Fig. 3.17 we have reproduced the dielectric function of the V_2O_5 from Ref. [114] for comparison. Also in the c direction of V_2O_5 (which is the b direction in the notations of the α' - NaV_2O_5 unit cell) a broad feature around 3 eV exists, and only a shoulder around 3.8eV (see also Fig. 3.17). In other words, through the appearance of the 2.8eV peak for $\mathbf{E} \parallel \mathbf{a}$ and 3.2 eV peak for $\mathbf{E} \parallel \mathbf{b}$, the spectrum "converges" to the one of V_2O_5 [114].

This is however not true in the far-infrared range, where a new peak evolves around 0.44 eV for $\mathbf{E} \parallel \mathbf{b}$, which does not exist in V_2O_5 (see Fig.3.15). Its high frequency side is observed also in Fig.3.16. This peak is probably connected with the lack of metallicity in the sodium-deficient samples, and resembles the polaronic peak present in β - $\text{Na}_{0.33}\text{V}_2\text{O}_5$,

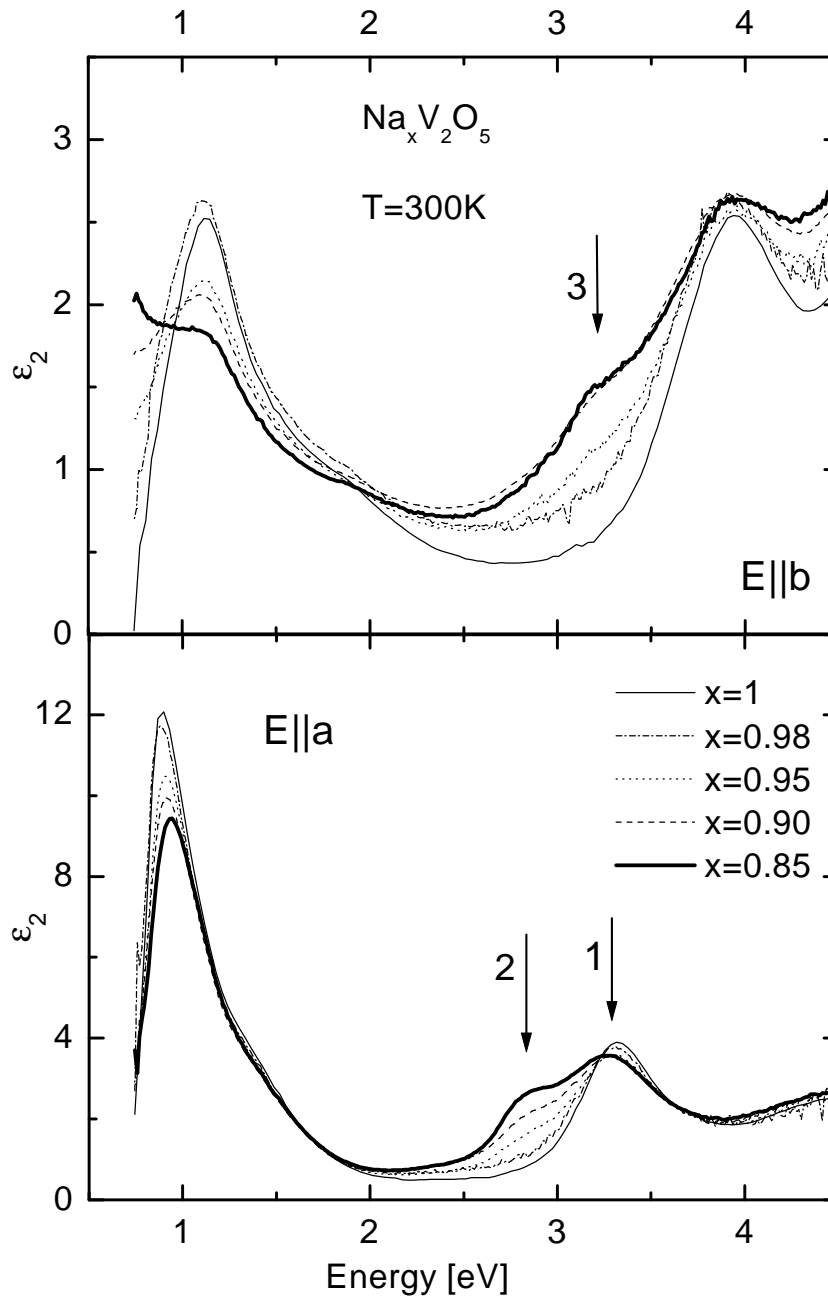


Figure 3.16: The imaginary part of the dielectric function for α' - $\text{Na}_x\text{V}_2\text{O}_5$ at room temperature, for $\mathbf{E}\parallel\mathbf{b}$ (upper panel) and $\mathbf{E}\parallel\mathbf{a}$ (lower panel)

which we will discuss in the next chapter.

When comparing the spectra from the α' - $\text{Na}_x\text{V}_2\text{O}_5$ samples presented in Fig. 3.16 with the ones from V_2O_5 presented in Fig. 3.17, a striking difference regarding the amplitude of the 3eV features is observed. Indeed, the intensity of these absorptions in α' - NaV_2O_5 seems to be about 4 times smaller than in V_2O_5 for $\mathbf{E}\parallel\mathbf{a}$, and 3 times for $\mathbf{E}\parallel\mathbf{b}$. As previously discussed, they are usually interpreted as transition from the $2p$ orbitals of oxygen to the $3d$ orbitals of vanadium. In V_2O_5 there are no d electrons, and the $2p$

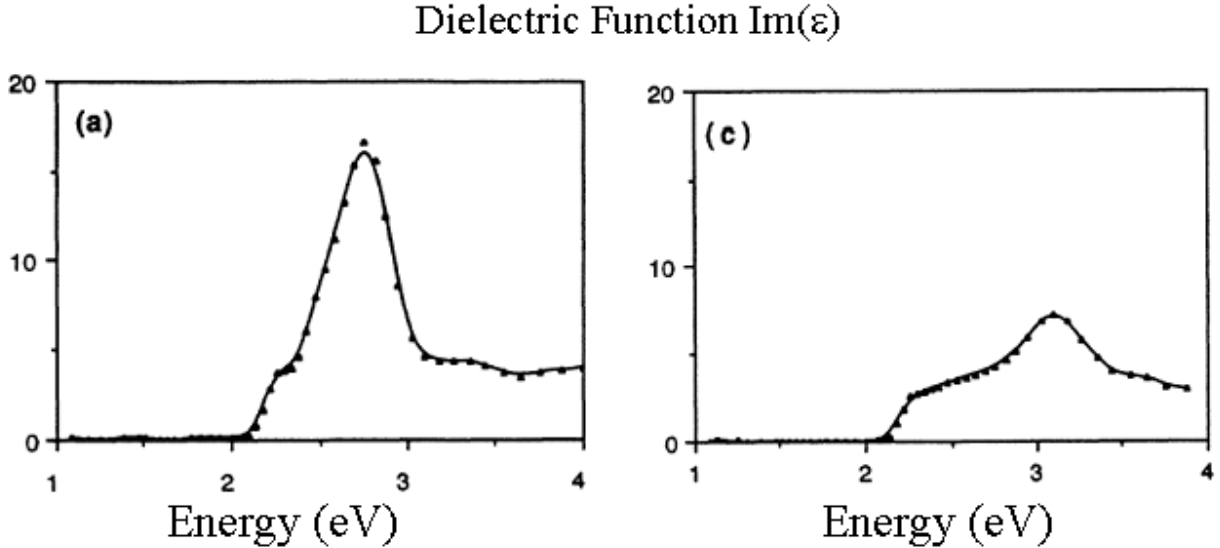


Figure 3.17: The imaginary part of the optical dielectric function of V_2O_5 reproduced from Ref. [114]. The crystallographic axes (a) and (c) are presented. They correspond to the a axis and b axis respectively in α' - NaV_2O_5 .

orbitals of oxygen are believed to be fully occupied, giving thus a maximum in the intensity of this transitions. In α' - NaV_2O_5 new electrons coming from the Na atoms are spread over the $3d_{xy}$ orbitals of vanadium. Some of the previous transitions from the $2p$ orbitals of oxygen to the $3d$ orbitals of vanadium will have now a final state containing two $3d$ electrons on the same V atom, and thus a higher energy (increased about 3eV, which is the value of the on-site Coulomb repulsion energy). The intensity in the 3eV structures will then decrease. This explanation may not be sufficient, since in a simple picture, on the basis of the number of $3d$ electrons of α' - NaV_2O_5 we would expect that the intensity would decrease with only a factor of two. It could be possible that the occupancy of the $2p$ orbitals of the O atoms of the ladder is also smaller (the $2p$ orbitals are not fully occupied) as was already suggested by very recent *ab initio* cluster calculations [76, 102].

3.6 Summary

An important role in understanding the physics of α' - NaV_2O_5 is played by the absorption peak present at 1 eV for $\mathbf{E}||\mathbf{a}$ in the dielectric function. We have been able to rule out its interpretation as a V^{4+} $d-d$ excitation, and establish that this is an on-rung bonding-antibonding transition. For that, we have measured the dielectric function of the a and b axes of α' - $\text{Na}_{1-x}\text{Ca}_x\text{V}_2\text{O}_5$ ($0 \leq x \leq 0.2$) in the photon energy range 0.8-4.5 eV at room temperature. By varying the Ca-concentration in this compounds, the relative abundancy of V^{4+} and V^{5+} was chemically controlled. The doping dependence of the intensity of the 1 eV peak for $\mathbf{E}||\mathbf{a}$ is in agreement with this transition being an on-rung bonding-antibonding transition.

The temperature dependence of the dielectric function of α' - NaV_2O_5 was also monitored. In special, the temperature dependence of the 1 eV peak (measured down to 4K)

showed an interesting behavior, namely a decrease of its intensity upon increasing temperature, with an activation energy of about 25meV (thus much smaller than the position of the peak). At the phase transition, no appreciable shift of its frequency was found. Because the 1eV was previously established as being a bonding-antibonding transition, a correlation could be established between its peak position and the valence of the individual vanadium ions. In this way, we have been able to show that, at the phase transition, the change in the valence of the vanadium ions is smaller than $0.06e$.

In addition to optical dielectric measurements in the visible range, far infrared measurements were also performed on the electron doped α' -Na_{1-x}Ca_xV₂O₅ ($0 \leq x \leq 0.2$). Contrary to what is expected from the usual doped anti-ferromagnetic insulators, the samples did not reveal metallic behavior.

The hole doping of α' -NaV₂O₅ is realized in the Na deficient single crystals of α' -Na_xV₂O₅ ($0.85 \leq x \leq 1.00$). We have measured their optical conductivity in the visible range, and show that they present new optical transitions at about 2.8eV for $\mathbf{E} \parallel \mathbf{a}$ and 3.2eV for $\mathbf{E} \parallel \mathbf{b}$.

Chapter 4

Charge ordering signatures in the optical properties of $\beta\text{-Na}_{0.33}\text{V}_2\text{O}_5$

Temperature dependent optical spectra are reported for $\beta\text{-Na}_{0.33}\text{V}_2\text{O}_5$. The sodium ordering transition at $T_{\text{Na}} = 240$ K, and in particular the charge ordering transition at $T_{\text{MI}} = 136$ K strongly influence the optical spectra. The metal-insulator transition at T_{MI} leads to the opening of a pseudogap ($\hbar\omega = 1700$ cm^{-1}), and to the appearance of a large number of optical phonons. These observations, and the presence of a mid-infrared band, typical for low-dimensional metals, strongly suggests that the charge carriers in $\beta\text{-Na}_{0.33}\text{V}_2\text{O}_5$ are small polarons.

4.1 Introduction

In some solid state materials, the movement of the electrons may be considered as taking place in a rigid environment of nuclei, and in others the vibrational degrees of freedom of the nuclei must be taken into account. A general criteria of distinguishing the two cases is given by the Born-Oppenheimer principle. Consider the case when the electron density is high. Then the Fermi velocity v_F of electrons is also high. As a result, because the mass of nuclei is much higher than that of the electrons, the nuclei can't "follow" the electronic excitations any more. Consequently, the electrons can be seen as moving in an rigid environment given by the average potential of the nuclei. However, if the system of electrons is very dilute, v_F is no longer large, and the above Born-Oppenheimer limit breaks down. The nuclei can now "follow" partly the electrons. The electron moves in the crystal disturbing the nuclei in its vicinity, forming a so-called *polaron*.

The literature makes a distinction [117] between materials where the electron affect the atoms at large distances (large polarons) and the electrons which affect the atoms only at small distances (*small polarons*). There does not seem to be a general experimental criteria for clearly identifying when this polaronic behavior is big enough to be taken into account. However, there are specific characteristics, and those include optical spectra, as it is the case for the material studied in this chapter, $\beta\text{-Na}_{0.33}\text{V}_2\text{O}_5$.

In some polaronic materials, such as Fe_3O_4 and Ti_4O_7 [118], a metal-insulator transition (MIT) is induced by small polaron ordering (Verwey state) at a certain temperature. In general, low dimensional metals feature a variety of MIT resulting from electron-phonon or electron-electron interactions. In charge density wave systems, like NbSe_3 [119] and $\text{K}_{0.3}\text{MoO}_3$ [120, 121], a MI transition is induced by a strong electron-phonon coupling (Peierls state). Also in systems lacking sufficiently strong electron-phonon interaction, such as for instance $(\text{Me}_2 - \text{DCNQI})_2\text{Li}_{1-x}\text{Cu}_x$ [122, 123], a MIT may occur due to charge ordering resulting from electronic Coulomb interactions (Wigner crystal).

Materials presenting a MIT in the cases where the properties are dominated by electron-phonon interaction often show the appearance of a large number of phonons in the infrared spectrum in the insulating state (along the chain direction if they are one-dimensional). This phenomena has been found in several materials [118–121], including those showing a Verwey transition. One of the intriguing features is that they may show a so called mid-infrared band in the optical spectra. It has been argued that for Fe_2O_3 [124] and many other materials [117] that the mid-infrared band can be understood as a polaronic response. However, also materials where Hubbard physics dominates may show a relatively strong mid-infrared band resulting from intra-band transitions [122, 123, 125, 126].

We present here another 1D material showing a MIT, namely $\beta\text{-Na}_{0.33}\text{V}_2\text{O}_5$ which has the above discussed features: 1) in the insulating state many new infrared active phonons develop in the chain direction and 2) a strong mid-infrared band is present. The recent discovery [17] of a clear metal-insulator transition (MIT) in the vanadium bronze $\beta\text{-Na}_{0.33}\text{V}_2\text{O}_5$ has sparked a revival of interest in this quasi-1D metallic system. In addition to the MIT, where a redistribution of the charge carriers on the V atoms was proposed to take place [127], $\beta\text{-Na}_{0.33}\text{V}_2\text{O}_5$ undergoes a structural sodium ordering transition at higher temperatures, a magnetic transition at low temperatures, and a transition into a superconducting state under high pressure [21].

In our data we observe the appearance of a large number of optical phonons in the chain direction, just below the MIT, which can be put in connection with similar effects on the usual CDW systems. This effect was clearly established in the 1D charge density wave systems NbSe_3 [119] and $\text{K}_{0.3}\text{MoO}_3$ [120, 121], where the new phonon lines evolve below the Peierls transition temperature. The effect was explained by M.J.Rice [128] for the 1D organic semiconductor $\text{TEA}(\text{TCNQ})_2$ in terms of the so-called phase-phonons. They result from the coupling of the molecular vibrations to the conduction electrons, enhancing thus their optical intensity in the chain direction, which otherwise may be small or not present due to symmetry reasons. The model worked in the case of NbSe_3 [119] as well.

The same appearance of many new phonon lines below a certain temperature was observed in the polaronic materials Fe_3O_4 and Ti_4O_7 [118]. Their case can be very relevant to our material, since both materials present the Verwey transition (that is the ordering, below a certain temperature, of otherwise random small polarons, due to a good balance between their kinetic and correlation energy) as it was also proposed for $\beta\text{-Na}_x\text{V}_2\text{O}_5$ [22]. The appearance of the sharp phonon lines below the Verwey temperature transition is however not yet explained. In Ref. [118], three models are put forward for Fe_3O_4 and Ti_4O_7 , including a fingerprint of bipolaronic order, tunnelling through a double well potential barrier, or the phase-phonon approach of M.J.Rice [128]. There are other similarities with these materials, which include the proposed presence of *bi*-polarons

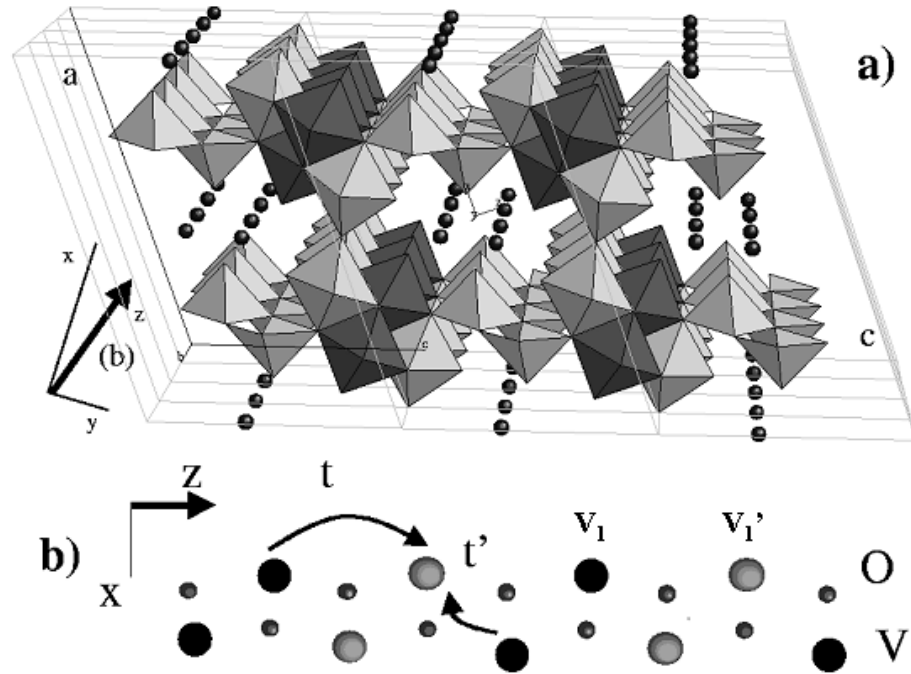


Figure 4.1: a) Room temperature structure of $\beta\text{-Na}_{0.33}\text{V}_2\text{O}_5$. The available V sites are: V_1 (dark octahedra), V_2 (light octahedra) and V_3 (light pyramids). b) An enlarged view of the zig-zag chain consisting of two types of V_1 atoms below T_{Na} . At room temperature the positions of V_1 are equivalent.

in $\beta\text{-Na}_{0.33}\text{V}_2\text{O}_5$ [23] and Ti_4O_7 [129].

A second similarity, as mentioned above, is the presence in $\beta\text{-Na}_{0.33}\text{V}_2\text{O}_5$ of a mid-infrared feature around 3000cm^{-1} for light polarized along the chain direction. A similar feature is present also in Fe_3O_4 , and it was assigned to the small-polaron transitions [124]. However, we found no temperature dependence in the low frequency region above the MIT transition, in contrast to the expected [117] and measured [130] behavior of the small polarons. The presence of *bi*-polarons in $\beta\text{-Na}_{0.33}\text{V}_2\text{O}_5$ (proposed by Chakraverty [23] in conjunction with low temperature specific heat measurements) has been put under question by later measurements of the temperature dependence of the magnetic susceptibility [17], which indicated that the spins remain unpaired for any temperature, implying that spin-zero bi-polarons, if present at all, represent an insignificant fraction of the polaronic charge carriers.

4.2 The structure and thermodynamical properties

The room temperature crystal structure [15, 16] of $\beta\text{-Na}_x\text{V}_2\text{O}_5$ is shown in Fig. 4.1. For $x = 1/3$, the unit cell is described by the formula $\text{NaV}_6\text{O}_{15}$. The six vanadium atoms occupy three pairs of crystallographically distinct sites, labelled V_1 (dark octahedra), V_2 (light octahedra) and V_3 (light pyramids). The Na atoms occupy lattice positions which can be represented as a ladder along the b axis (small black circles in Fig. 4.1).

In Nuclear Magnetic Resonance measurements it has been observed [131] that the ^{23}Na

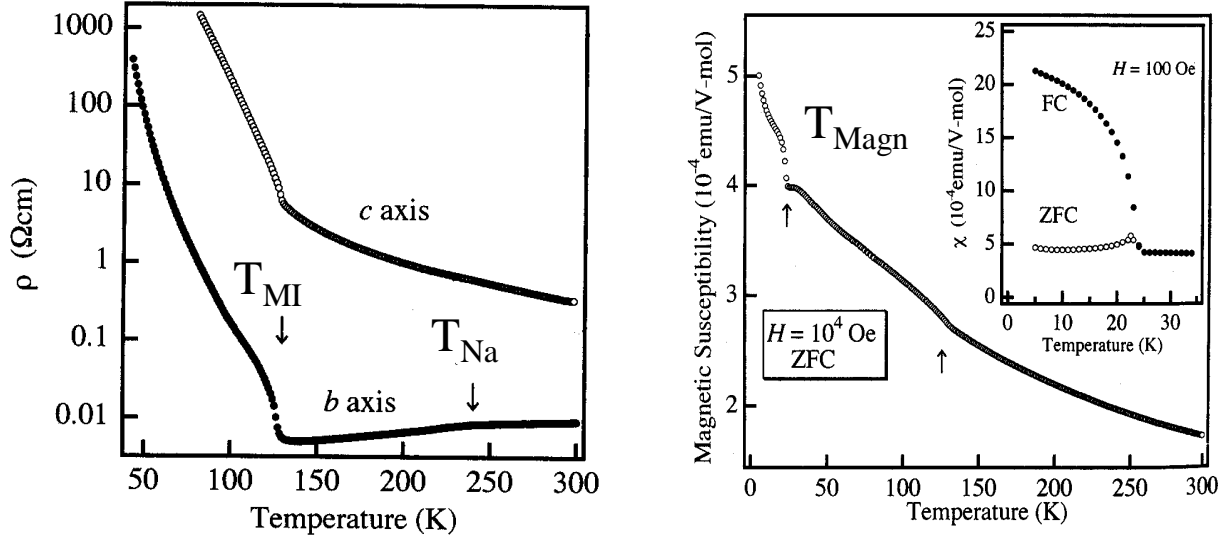


Figure 4.2: Lefthand panel: Temperature dependence of the resistivity for $\beta\text{-Na}_{0.33}\text{V}_2\text{O}_5$. Righthand panel: Temperature dependence of the magnetic susceptibility. Both figures are reproduced from Ref. [17].

nuclei have no Knight shift, and consequently are monovalent, donating thus their outer s -shell electrons to the V atoms. There is a controversy, between old and new measurements, as regards on which V atoms these Na electrons go. In 1970 Goodenough [132] argued, on the basis of the V - O bond lengths, that the electrons should enter either the d_{yz} orbital of the V_1 atoms or the d_{zx} orbital of the V_2 atom, preferably the first one. The x, y, z axes are presented in Fig.4.1, according to the choice of Goodenough [132]. He pointed out that the electron, if present on the V_1 site, would hop on site V_3 via the intermediary O atom, so a small occupancy of V_3 would be expected as well in that case. Later, from the measurements of the nuclear quadrupole effect [131] and anisotropic Knight shift of the ^{51}V site [133], it was reported that most of the Na donated electrons are stabilized on the d_{yz} -orbitals of V_1 . A small fraction would be presented on the V_3 as well [131, 134, 135], but the V_2 chain would be empty. However, recent measurements [127] report that these electrons are shared among all three V chains above $T_{MI} \simeq 130\text{K}$, and that they condense either on the V_1 or the V_2 chain below $T_{MI} \simeq 130\text{K}$.

For $x = 1/3$ in $\beta\text{-Na}_x\text{V}_2\text{O}_5$ only 50 % of the lattice sites forming the Na ladder is occupied. One possibility is that each rung of the Na ladder hosts one Na atom randomly distributed between the lefthand and righthand side of the ladder. A recent paper [136] suggests that the Na atoms may also form regular zigzag chains along the b axis, with a $2b$ periodicity. Perpendicular to the b axis these zigzag chains would be randomly distributed, and thus the probability of occupation for one site would be half on average.

Below room temperature, the system undergoes three phase transitions, shown in Figures 4.2 and 4.3. Around $T_{Na} \simeq 240\text{K}$ a 2^{nd} order structural phase transition takes place to a low temperature structure where the unit cell is doubled along the b direction, as revealed by X-ray diffraction[17]. Recently it was reported [136] that this transition takes place in two steps: a resistivity anomaly at $T_{Na-2D} = 240\text{K}$ was observed and a hysteretic phase transition at $T_{Na-3D} = 222\text{K}$. Generally, it is believed that the reported

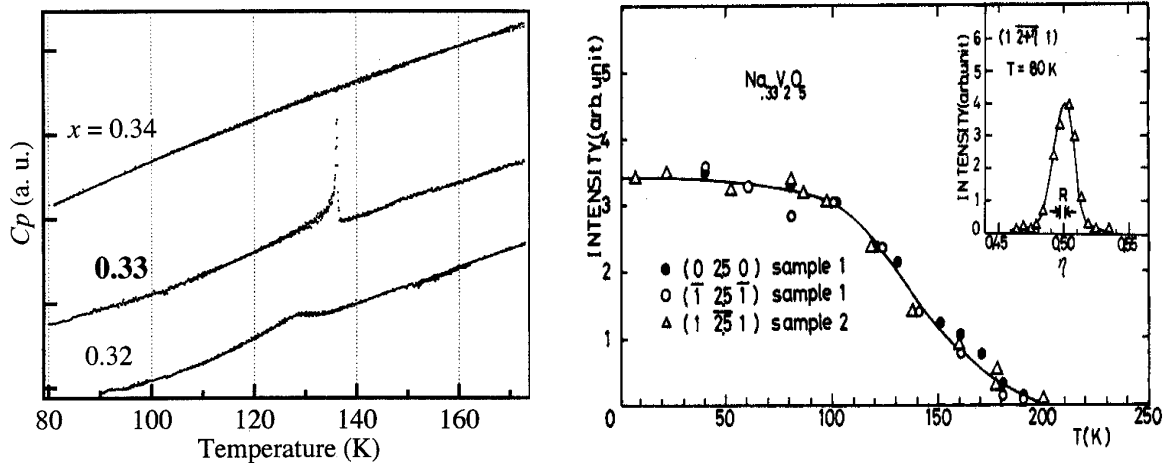


Figure 4.3: Left panel: Temperature dependence of the heat capacity for the stoichiometric and off-stoichiometric β - $\text{Na}_x\text{V}_2\text{O}_5$ samples from Ref. [17]. Right panel: Temperature dependence of the X-Ray diffraction peak revealing the doubling of the unit cell below T_{Na} from Ref. [137]

doubling of the unit cell is a result of the zig-zag pattern of Na atoms being present below T_{Na} . Lowering the temperature, a transition from metal above $T_{\text{MI}} = 136$ K to insulator below T_{MI} takes place. This is accompanied by a tripling of the unit cell along the b axis[18]. A magnetic transition from paramagnet above $T_{\text{CAF}} = 22$ K to a canted anti-ferromagnet below T_{CAF} [19, 20] is also present.

These transitions are evident from the measurements presented in Fig. 4.2 and Fig. 4.3. In the left panel of Fig. 4.2 the resistivity data is reproduced from [17]. It shows the one-dimensional behavior of β - $\text{Na}_{0.33}\text{V}_2\text{O}_5$: the resistivity along the chain direction b is two order of magnitude smaller than the one perpendicular to the chains. The metal insulator transition is presented around $T_{\text{MI}} = 136$ K, above which a metallic behavior is observed. Above $T_{\text{Na}} \simeq 240$ K the resistivity for the b axis presents a plateau.

However, the metallic characteristics are rapidly lost for dopings away from $x = 0.33$ [17], and the MIT disappears as well (see Fig.4.3). The presence of metallic behavior for only a sharply defined charge carrier concentration is different from conventional MIT in 2 or 3 dimensions, where the metallic phase occurs in a broad range of carrier densities above the critical value. The strange doping dependence of β - $\text{Na}_{0.33}\text{V}_2\text{O}_5$ is probably due to the combination of (i) quasi one-dimensionality and (ii) broken translational invariance due to excess Na^+ -ions or Na-vacancies when $x \neq 1/3$. In other words, the potential created by the neighboring Na atoms influences the movement of the electrons. Doping away from $1/3$ would create an empty or fully occupied rung of the Na ladder. This creates a greater disturbing potential for the electrons than the rung occupied with exactly one Na atom, as in the case for $x = 1/3$.

The righthand panel of Fig. 4.2 presents the magnetic susceptibility of β - $\text{Na}_{0.33}\text{V}_2\text{O}_5$. If the magnetic transition at T_{Magn} is easily visible, the other two transitions are hardly visible. Fig.4.3 presents two other important aspects of the β - $\text{Na}_{0.33}\text{V}_2\text{O}_5$ samples. First, the MI transition at T_{MI} is very sensitive to doping, as mentioned earlier. For a doping

of $x = 0.34$ the transition already disappears, and the sample is insulating at all temperatures [17]. The righthand side panel shows the intensity of the X-ray diffraction peak related to the doubling of the unit cell. It is a result of the presence of the zig-zag Na chains below T_{Na} . The figure shows that this peak develops gradually, suggesting that in fact the metal-insulator transition takes place at $T_{MI} = 136\text{K}$, when the Na atoms are fully ordered in zig-zag chains. This would strengthen our previous argument that the Na potential influences strongly the movement of the electrons of the V chains. The way it is doing it is unexpected, since at high temperature, where there is more disorder, the system is metallic. However, the ordering which takes place below T_{Na} allows the formation of the insulating state, as will be argued in the remainder of this chapter.

4.3 Description of the experiment

Single crystals have been prepared as described in [17]. Two crystals with dimensions of $6 \times 1 \times 0.5$ mm have been used for collecting optical spectra, giving identical results. One of them was checked on the X-ray diffractometer that it presents the tripling of the unit cell at T_{MI} having thus the right stoichiometry. Because of the needle shape of the crystals, only one crystal face available was measured, namely (101).

We measured the reflectivity in the range 20-6000 cm^{-1} as a function of temperature with polarization parallel to the b -direction (*i.e.* parallel to the conducting chains) and with the polarization perpendicular to b . In Fig. 4.4 the reflectivity spectra are displayed for some selected temperatures. In the inset Fig. 4.4e the reflectivity for the two samples is compared. At low frequencies, the one which was plane parallel presented interference fringes for $\mathbf{E} \parallel \mathbf{b}$, showing thus the insulating behavior of this direction.

In addition, we did temperature dependent spectroscopic ellipsometry measurements and room temperature reflectivity measurements from 6000 to 36000 cm^{-1} . With the help of Kramers-Kronig relations, the optical conductivity was calculated between 20 and 36000 cm^{-1} (Fig. 4.5).

4.4 Room temperature data

Optical spectrum of a sample is a powerful tool in determining its electronic properties. Its main features reflect the dipole allowed electronic excitations of the sample. For example, the presence of a Drude peak implies a metallic behavior, and a constant reflectivity for $\omega \rightarrow 0$ implies insulating behavior. The richness of the spectrum (as presented in 4.4) may add additional information to the already established main features. We will try to approach the presentation of the measured data by beginning with the high frequency part, in Fig. 4.5.

4.4.1 High frequency excitations

Prominent bands around 3 eV similar to those in Fig. 4.5 have been observed in α' - NaV_2O_5 [90], and also in its "matrix material" V_2O_5 [114–116]. They correspond to charge transfer excitations between the occupied oxygen $2p$ levels and the empty vanadium

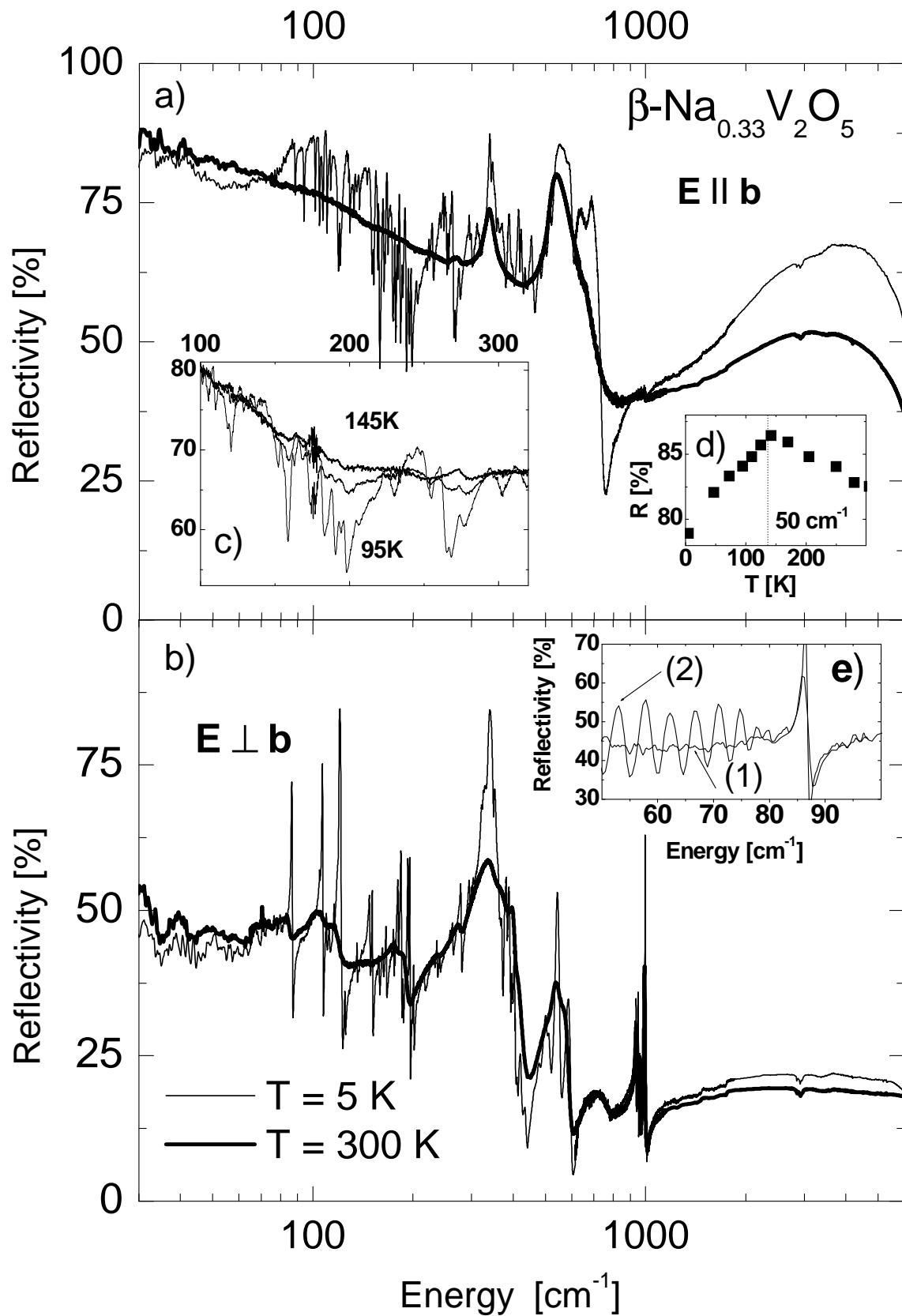


Figure 4.4: a) and b) Reflectivity spectra of $\beta\text{-Na}_{0.33}\text{V}_2\text{O}_5$. Inset c): Zoom in for the $\mathbf{E} \parallel \mathbf{b}$ polarization. Inset d) Temperature dependence of the reflectivity for a selected frequency. Inset e) Reflectivity of the insulating direction $\mathbf{E} \perp \mathbf{b}$ for two samples measured. The presence of fringes on the plane-parallel sample (2) shows that the samples are transparent for this polarization.

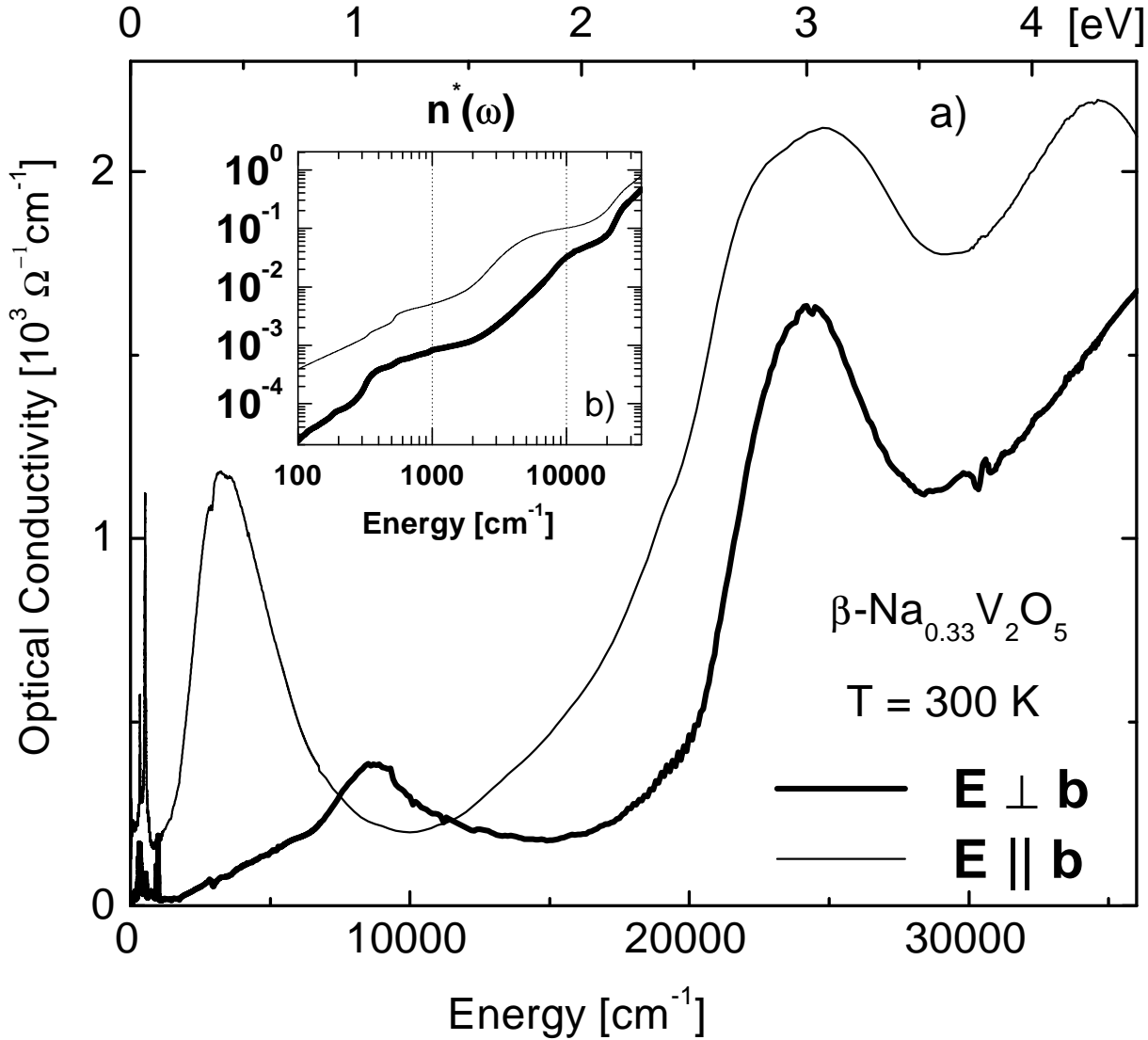


Figure 4.5: Optical conductivity at room temperature. Inset: The effective number of electrons per V atom, calculated with formula 4.1 for two polarizations: $\mathbf{E} \parallel \mathbf{b}$ (thin line) and $\mathbf{E} \perp \mathbf{b}$ (thick line)

$3d$ states. This is important, because the insulating V_2O_5 has no electron donors for the V chains. In a simple picture, there would be no electrons on the V- $3d$ orbitals in V_2O_5 . Most probably however, their occupancy is not zero, since some covalent V-O bonds exist, being especially strong for the shortest bonds. However, the electrons present in this covalent bonds play no role in the low excitations, which mainly determine the physical properties. The fact that there are no excitations lower than 3eV in V_2O_5 strongly suggest that those excitations lower than 3eV, which are presented in the doped V_2O_5 related compounds, come only from the Na donated electrons.

For $E \perp b$, $\sigma(\omega)$ of $\beta\text{-Na}_{0.33}\text{V}_2\text{O}_5$ has an intense peak at 1eV (see Fig.4.5). By integrating the intensity below the peak, and adopting the bare mass m_e and charge e for the electrons, as well as the density of the V atoms n_V , we can calculate an effective

V-O	α' -NaV ₂ O ₅ T=300K	α' -NaV ₂ O ₅ T=15K	β -Na _x V ₂ O ₅ T=300K
V _a -O [\AA]	1.83	1.89	1.95
V _b -O [\AA]	1.83	1.76	1.78
Angle [$^\circ$]	140.8	141.5	134.24
V _a -V _b [\AA]	3.44	3.44	3.44

Table 4.1: The dimensions of the V₁-O₅-V₃ bond unit in β -Na_{0.33}V₂O₅ and of the rung V-O-V bond in α' -NaV₂O₅ (The V_a and V_b refer to the vanadium atoms of the V-O-V bond considered). The values are taken from Ref. [15] and Ref. [81].

number of electrons per V atom taking part in transition:

$$8 \int_0^{\omega_m} \sigma(\omega) d\omega = n^*(\omega_m) \frac{4\pi n_V e^2}{m_e}. \quad (4.1)$$

If integrating only the valence electron transitions up to ∞ , this should yield $n^*(\infty) = 1/6$, the average occupation number of 3d electrons on V atoms. The result is presented in the inset in Fig.4.5. We obtain a n^* of about 0.052 if the integration is carried out up to 15000 cm⁻¹ that is $n^*(15000) = 0.052$. This number is only three times smaller than the average occupation number of 3d electrons on V atoms, which is $n = 1/6$. In analogy with the case of α' -NaV₂O₅ [89], this transition cannot be an on-site $d-d$ transition, because its intensity is high. On-site $d-d$ transitions are optically forbidden by symmetry in the free atom, but in the crystal they can be visible, due to breaking of this symmetry. However, their intensity would be small, and this is not case here. Thus it may be a charge transfer transition.

In α' -NaV₂O₅ a transition around the same energy has been attributed to a bonding-antibonding transition inside the V-O-V rung [89, 90]. As discussed in the introduction, in β -Na_{0.33}V₂O₅ it was suggested that most of the electrons occupy the V₁ chains [131, 133, 135], even though new measurements suggest that the electrons are spread on all three V sites [127]. If the donated 3d electrons occupy mainly the V₁, a very good candidate exists for this transition. To create the transition at 1 eV in the direction $E \perp b$ and in the plane (101), the electron may hop to the V₃ due to a large V₁-O-V₃ angle. The V₁-V₃ direction is also close to the direction of the polarization of the light.

In fact, the molecular unit V₁(d_{yz}) - O₅(p) - V₃(t_{2g}), was also identified by Goodenough [132] as giving strong electron-phonon interaction. In Table 4.1 we present a comparison between the V-O-V rung molecular unit of α' -NaV₂O₅ and the unit V₁-O₅-V₃ of β -Na_xV₂O₅. As we can see, the values are quite close. However, one should also note that in β -Na_{0.33}V₂O₅ the V atoms have different on-site potential, since they are inequivalent. The shape is also broader in the case of β -Na_{0.33}V₂O₅. Its intensity is smaller as compared to the case of α' -NaV₂O₅ because the number of electrons is also smaller.

4.4.2 Mid-Infrared feature

In a previous study [138], a minimum in the $\mathbf{E} \parallel \mathbf{b}$ reflectivity at 7200 cm⁻¹ has been attributed to a plasma edge. We can see from the Fig. 4.5 that the main contribution

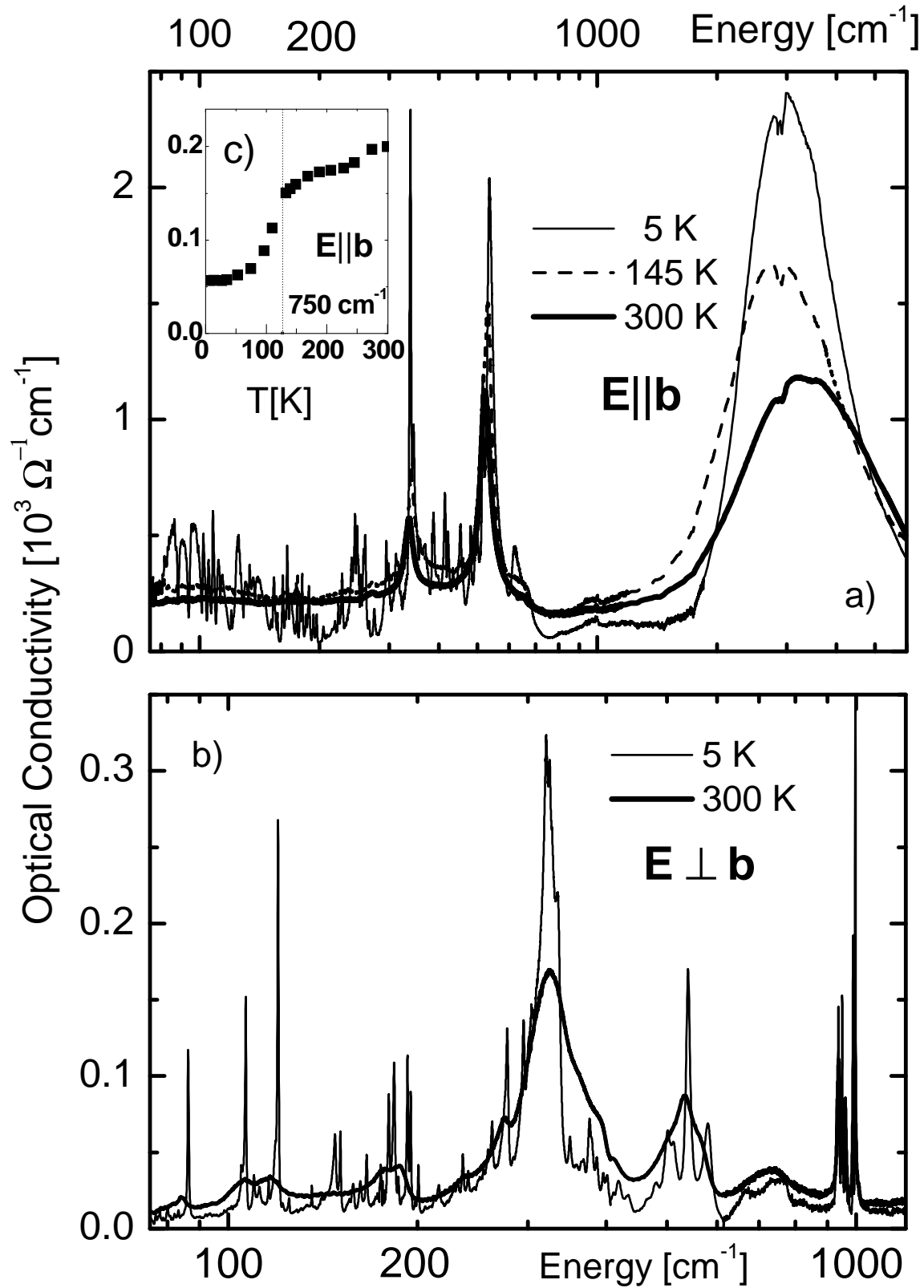


Figure 4.6: Optical conductivity for $\mathbf{E} \parallel \mathbf{b}$ (a) and $\mathbf{E} \perp \mathbf{b}$ (b), plotted for few frequencies. The two small deaps on the top of the mid-infrared feature (around 3000cm^{-1}) for $\mathbf{E} \parallel \mathbf{b}$ (a) come from water absorption. Inset c): Temperature dependence of the optical conductivity for a selected frequency.

to the oscillator strength associated with this plasma minimum arises from a prominent mid-infrared band centered at 3000 cm^{-1} , and not from the free carriers. From the inset of Fig. 4.5 the spectral weight of the mid-infrared feature estimated from n^* at 10000 cm^{-1} is about 0.1, that is $n^*(10000) \simeq 0.1$. This is close to the average occupation number $n = 1/6$ of $3d$ electrons on V atoms. The high oscillator strength of the mid-infrared peak as shown by the value of n^* shows that it is given by the doped carriers.

As mentioned earlier, mid infrared peaks are predicted by various models, including the small polaron model [117, 124] and Hubbard chains [123, 139]. As known, away from half filling, the Hubbard chain gives metallic behavior. At filling close to $1/4$, it also give a peak at frequencies slightly higher than the hopping parameter t [123]. However, there is no exact knowledge of the room temperature filling in $\beta\text{-Na}_{0.33}\text{V}_2\text{O}_5$. Previous anisotropic Knight shift data [133] suggested that most of the Na donated electrons are stabilized on V_1 . Later, the presence on all three V sites was reported[127]. It could be possible that most of the electrons are actually located on a single type of V site, since a large redistribution of electrons at the MIT[127] would give new mid-infrared peaks in the optical spectrum of both axes, which is not observed in the present work. The system can be thus close to $1/4$ filling, and if the electrons would stay mainly on V_1 they would form two weakly coupled linear chains [140] (see Fig.4.1b). The hopping parameter inside the chain would be $t = 0.2\text{eV}$ [140], thus close to the energy of the mid-infrared peak. However, the spectral weight of the low frequency part of the mid-infrared peak up to 1500cm^{-1} is about 10% of the total mid-infrared feature (see the inset of Fig.4.5), much smaller however than the Drude weight expected from calculations [125, 141], which exceeds 50%. Thus, the Hubbard model alone cannot account for the large amount of oscillator strength present in the mid infrared peak.

On the other hand, the small polaron presents in optical conductivity not only a peak at few times the frequency of phonons [117], but also a finite conductivity at low frequencies. Our mid-infrared feature has a finite conductivity at low frequencies (see Fig. 4.6), which extrapolates to $200\text{ }\Omega^{-1}\text{cm}^{-1}$ a value somewhat higher than the DC conductivity $100\text{ }\Omega^{-1}\text{cm}^{-1}$ [17].

4.4.3 Far-infrared region

One can see from Fig.4.4 that $\beta\text{-Na}_{0.33}\text{V}_2\text{O}_5$ is indeed a quasi 1D conductor: at low frequencies, the b -axis reflectivity extrapolates to 100 % for $\omega \rightarrow 0$, which is a characteristic feature of a conducting material. The corresponding extrapolated conductivity is about $200\text{ }\Omega^{-1}\text{cm}^{-1}$ (see Fig.4.6a). This value is somewhat higher than the DC conductivity $100\text{ }\Omega^{-1}\text{cm}^{-1}$ obtained previously [17]. For $\mathbf{E} \perp \mathbf{b}$ the reflectivity is characteristic of an insulating material, and optical conductivity extrapolates to very low values.

At room temperature two prominent optical phonons are visible at 340cm^{-1} and 530 cm^{-1} $\mathbf{E} \parallel \mathbf{b}$, and several other for the perpendicular polarization $\mathbf{E} \perp \mathbf{b}$, as we can see from Fig.4.6b. The complex of phonons around 970cm^{-1} in the $\mathbf{E} \perp \mathbf{b}$ spectrum (see Fig. 4.6b and Fig. 4.7) may be attributed to the vibrations of the short bonds $V_1\text{-O}_4$, $V_2\text{-O}_6$, $V_3\text{-O}_8$. As can be seen from the structure [15], these bonds are perpendicular to the b axis, explaining the absence of this vibrations in the $\mathbf{E} \parallel \mathbf{b}$ spectrum. Their high frequency is a result of the the fact that the bonds are short.

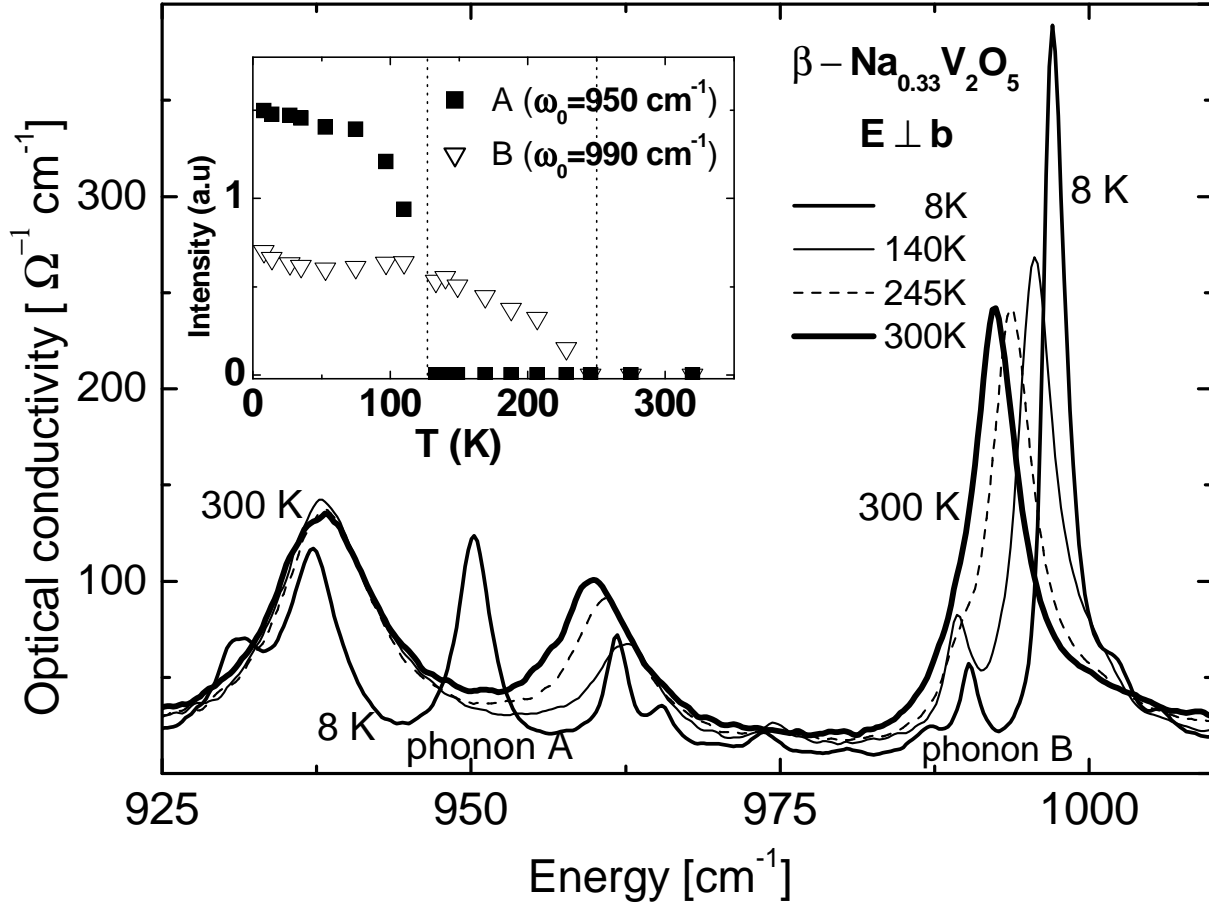


Figure 4.7: The phonons given by the shortest V-O bonds presented only in the optical spectrum for $E \perp b$. Inset: Temperature dependence of the intensity of two phonons: 990 cm^{-1} (empty triangles) and 950 cm^{-1} (full squares) present in this spectrum.

The presence of strong electron-phonon coupling is deduced by integrating the intensity in the phonon peaks for $E \parallel b$, and using the ionic charges of the atoms. The resulting effective charge would be $e^* = 1$ in the case of no electron-phonon coupling, but instead we obtain $e^* = 1.9$ at 300 K.

4.5 Low temperature data

In this section we present the evolution of the measured optical conductivity through the three phase transitions present in $\beta\text{-Na}_{0.33}\text{V}_2\text{O}_5$: Na atom ordering ($T_{\text{Na}} \simeq 240\text{K}$), metal-insulator transition ($T_{\text{MI}} \simeq 136\text{K}$), and the magnetic transition ($T_{\text{Magn}} = 22\text{K}$).

4.5.1 The effect of the Na ordering on the optical spectra

The phase transition at $T_{\text{Na}} \simeq 240\text{K}$ has little effect on the infrared spectra of the metallic axis, but it presents new phonons in the insulating direction. A clear case where the intensity develops for $T < T_{\text{Na}}$ is formed by the phonon at 990 cm^{-1} which gradually

develops in the insulating direction (see inset of Fig. 4.7). The same 2^{nd} order type evolution with temperature has been observed for the intensity of X-ray satellites [137] corresponding to the doubling of the unit cell which take place below T_{MI} thus to the Na ordering (see Fig. 4.3). They both suggest that the MIT takes place at a temperature where the Na atoms are fully ordered. This would strengthen our previous argument that the Na potential influences strongly the movement of the electrons of the V chains.

4.5.2 Metal-insulator transition

The MIT has a clear effect on the optical spectra of the metallic axis (see Fig. 4.6a). At 4K the low frequency part of the mid infrared feature, below 1700cm^{-1} , it looks more like a pseudo-gap. Inside this pseudo-gap, a large number of sharp optical absorption lines evolve. This is exemplified also by the temperature dependence of $\sigma(\omega)$ for 750cm^{-1} shown in the inset Fig. 4.6c. The way this pseudo-gap develops below the MIT is similar to the temperature dependence of the low frequency part of the polaronic peak at 0.6eV in magnetite [130]. There, below the Verwey transition T_V , the low frequency part of the mid-infrared feature (the polaronic peak in that case) goes to zero, and thus the opening of a gap was deduced [130]. In a similar fashion our low frequency part of the mid-infrared peak at 3000cm^{-1} would go to zero, if the phonons and some electronic continuum would not be present below 1700cm^{-1} .

There is however a major difference between magnetite and our sample. The gap which opens in magnetite below the Verwey transition T_V has the same energy as the activation energy of D.C. electrical conductivity at low temperatures [130]. In $\beta\text{-Na}_{0.33}\text{V}_2\text{O}_5$ the activation energy of the D.C. conductivity estimated between 85K and 42K is 46meV [17] (about 371cm^{-1}). Thus, this is much smaller than our observed energy of the pseudo-gap, which is about 1700cm^{-1} . It looks like this pseudo-gap is not directly related to the physical mechanism which determines the MIT, because the gap is expected to have an energy close to the activation energy of the D.C. conductivity. In fact, we can calculate a gap using the B.C.S. formula for the gap [142], $2\Delta = 3.5 * k_B * T_{MI} = 317\text{cm}^{-1}$ or $\Delta = 158\text{cm}^{-1}$ and this is indeed of the order of the activation energy of the D.C. conductivity, even though half of its value. In usual CDW systems, one expects the presence of the optical gap at about twice the value of the D.C. activated energy [128], and we can only remark here that around that value, about 650cm^{-1} a continuum develops in the metallic direction below the MIT, as we can see in see Fig.4.6. From the same figure, a continuum is present around that energy, 700cm^{-1} at all temperatures, in the $\mathbf{E} \perp \mathbf{b}$ spectrum.

Below MIT, the infrared reflectivity spectra show the appearance of a large number of sharp optical absorption lines for both polarizations (see Figs. 4.4, 4.6 and 4.8). For $\mathbf{E} \parallel \mathbf{b}$ we counted more than 60 additional peaks. They develop gradually below $T_{MI} = 136\text{K}$. This is also illustrated by the temperature dependence of the 950cm^{-1} phonon shown in the inset of Fig. 4.7. However, as we can see from the inset Fig.4.4c, traces of some of the additional phonons are still present in the 145 K spectrum. Some of them can be viewed as splitting of the already present phonons (see Fig. 4.8), as for example at 105cm^{-1} 147cm^{-1} 180cm^{-1} 191cm^{-1} for $\mathbf{E} \perp \mathbf{b}$, or 109cm^{-1} for $\mathbf{E} \parallel \mathbf{b}$. The large phonon in the metallic direction at 515cm^{-1} seems to be split already above MIT. Even though

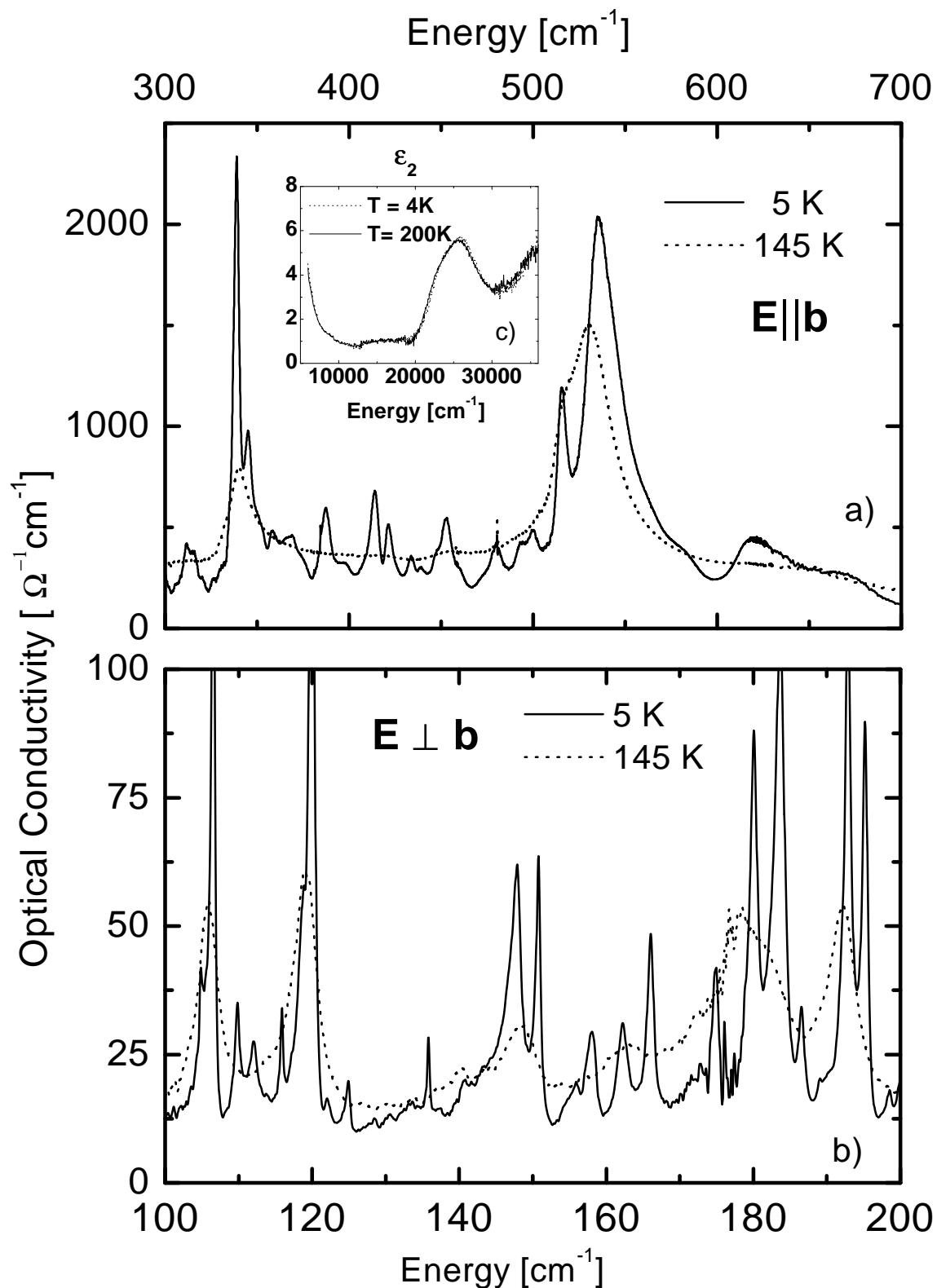


Figure 4.8: Splitting of some optical phonons, which takes place below the MIT temperature $T_{MI}=136\text{K}$. Inset of a): Pseudo-dielectric function ϵ_2 in the high frequency range for $\mathbf{E} \parallel \mathbf{b}$, showing no temperature dependence

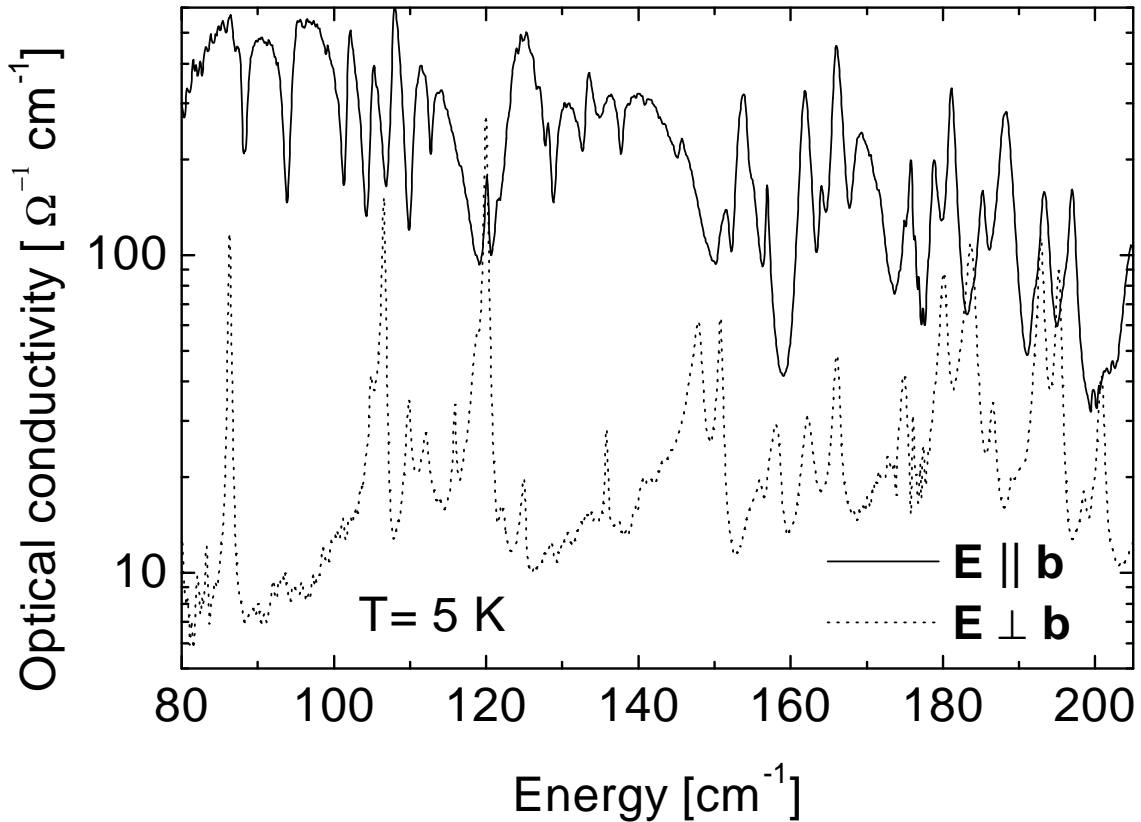


Figure 4.9: A zoom of the optical conductivity of the two directions at 5K.

a change in crystal structure takes place at $T_{MI} = 136K$, which triples the unit cell along b direction[18], we think that the appearance of so many new peaks is a result of strong electron-phonon coupling. In other words, the new phonons are activated below T_{MI} by the structural change, but they become visible because they acquire strength from the coupling with the charge degrees of freedom.

As discussed in the introduction, similar effects were observed in the CDW systems[119, 120] below the Peierls temperature, and polaronic materials [118] below the Verwey transition temperature. Both are in fact charge ordering mechanisms, and in this sense the effect is a signature of this ordering. We want to stress here that $\beta\text{-Na}_{0.33}\text{V}_2\text{O}_5$ is not a usual CDW system, and the mid-infrared feature is not the CDW gap, since it exist at all temperatures. However, this does not exclude the possibility that the MIT is a CDW transition of the quasi-particles which can result from a particular type of physics, Hubbard for example. The reorganization of charge carriers at T_{MI} which are supposed to condense on a single chain chain below T_{MI} [127], suggest however that our system is closer to the polaronic materials presenting the Verwey transition [118], as was also proposed by Mott [22]. With respect to the M.J.Rice mechanism of the phase-phonons [128], we can extract no supplemental information regarding the symmetry of the Raman and far-infrared phonons since their number is huge, and coincidence may easily happen. In Fig. 4.9 we exemplify this by plotting the optical conductivity at 5K in both axes. In optical conductivity it seems that there are phonons which have the same energy in both

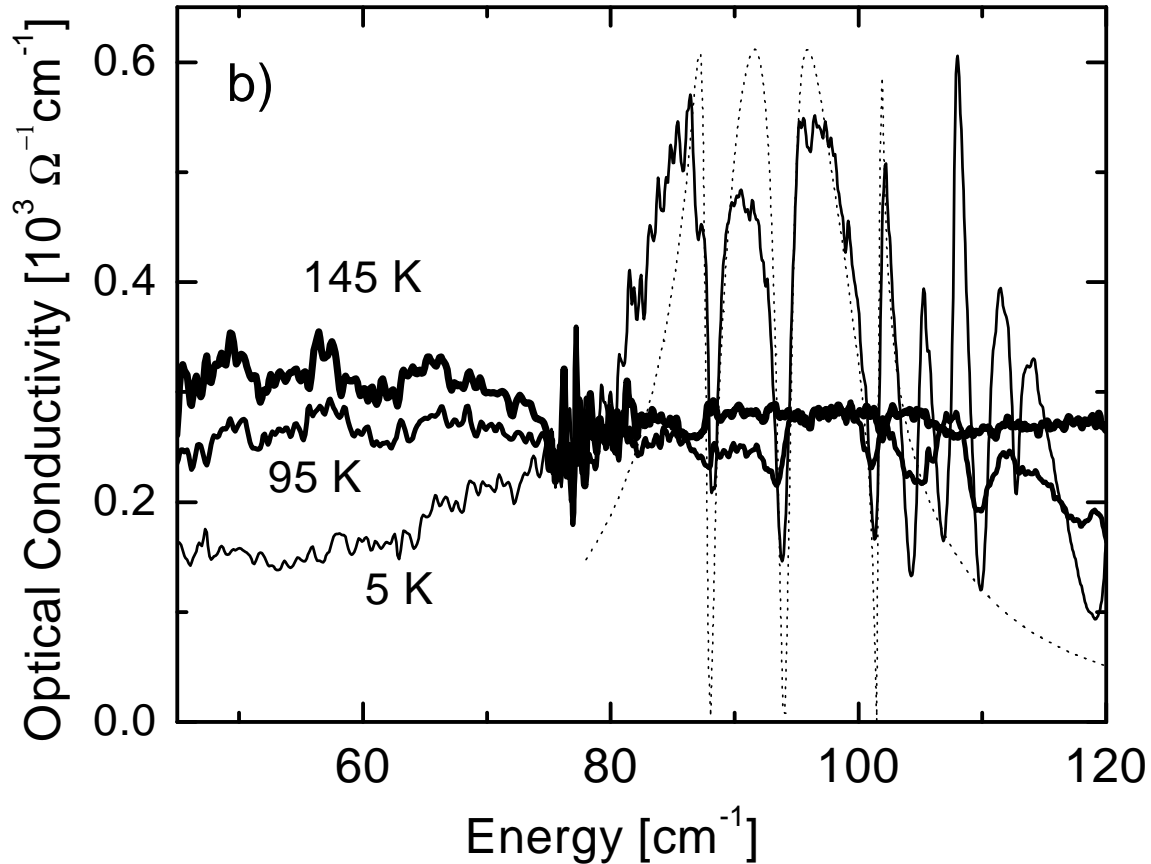


Figure 4.10: Optical conductivity for $\mathbf{E}||\mathbf{b}$ which presents the appearance of a continuum around 100 cm^{-1} . The dotted line is fit performed on the data with the Fano model develop in Ref. [143].

polarizations, as the ones at 105 cm^{-1} and 120 cm^{-1} . If so, they would prove the disappearance of the center of inversion at 5K, but as we said, it may be just coincidence.

At low temperatures, in the metallic direction, spectral weight seems to be transferred from the 50 cm^{-1} region to 100 cm^{-1} , giving rise to a continuum (see Fig. 4.10). The existence of this continuum is made clearer by the presence of the phonon resonances which sit like "dips" on the top of it, confirming a strong electron-phonon coupling. Fig. 4.10 presents fits of the data within a Fano model developed in Ref. [143]. The phonons are assumed to be Lorentzian with no strength in the absence of electron-phonon coupling, and their width is set to zero. They acquire then their strength, width and shape only through a single parameter, which is the coupling strength. As we can see, good fits have been obtained, with the strength of phonons of 2, 2.2, 1.8 cm^{-1} . The origin of the continuum is still unclear, but it must be remarked that some excitations at low energies have been observed in other CDW systems as well. In $\text{K}_{0.3}\text{MoO}_3$ an excitation around 40 cm^{-1} was assigned to a bound collective mode resonance.

4.6 Discussion

An important clue for the interpretation of the optical spectra below 10000 cm^{-1} is provided by the observation that while a gap opens in the optical spectrum and the DC-resistivity below 136 K, the magnetic susceptibility is almost unaffected by the metal-insulator transition (see Fig.4.2). If the gap were of the garden variety like in silicon, the spin-fluctuations would become strongly suppressed below the same temperature where the optical conductivity becomes gapped. However, in $\beta\text{-Na}_{0.33}\text{V}_2\text{O}_5$ there is no formation of a spin-gap when charge transport gets suppressed below $T_{MI}=136\text{ K}$ [17]. This aspect of the data reflects the presence of strong on-site Hubbard-type repulsions between the charge carriers, which in one-dimension causes the electrons to behave like spinless fermions, and it may thus be an experimental candidate for the material which can reproduce the main theoretical expectations of the partly occupied Hubbard chain: spin charge separation, and fractionalization of the charge [144]. This can be due to the polaronic character of the charge carriers and/or a Hubbard model with a large ratio of the on-site Coulomb repulsion U to the band width W . Supporting this, no changes in the optical spectrum of $\beta\text{-Na}_{0.33}\text{V}_2\text{O}_5$ are detected at the magnetic transition temperature $T_{Magn}=22\text{ K}$. The relative independence of the spin and charge channels has been noticed before for the Bechgaard salts [145], the presence of a pseudogap in the optical excitations being opposed to the absence of a gap for spin excitations. A large peak at IR region and, in addition, an in-gap mode was also observed.

Another important clue is provided by considering the optical response of the charge carriers. As discussed above, the integrated spectral weight of the mid-infrared feature for $\mathbf{E} \perp \mathbf{b}$ corresponds to $n^*(10000\text{cm}^{-1}) \simeq 0.10$ electrons per V atom (see inset of Fig. 4.5), which is rather close to the nominal chemical doping of $n = 0.166$ electrons per V atom. The difference between n and n^* can be easily understood from the fact that, in these transition metal oxides, the effective mass of the electrons is about $2m_e$. The high oscillator strength of the mid-infrared peak as given by the value of n^* shows that it arises from the doped charge carriers. In contrast, the spectral weight of the low frequency part up to 1500 cm^{-1} is about 10% of the total mid-infrared feature (see inset of Fig. 4.5). Finally, the relative intensity of the low frequency spectral weight is almost independent of temperature above $T_{MI} \simeq 136\text{ K}$.

From studies of the Hubbard model in one dimension we know that part of the intra-band spectral weight shows up as a band of mid-infrared excitations. However, these studies have also demonstrated that for doping far away from half-filling of the Hubbard band, the intensity of the mid-infrared band is less than 20 % of Drude spectral weight [125, 126]. This rules out an interpretation of the mid-infrared peak in $\beta\text{-Na}_{0.33}\text{V}_2\text{O}_5$ in terms of a pure Hubbard model. At the same time we underscore the crucial role of Hubbard-type correlations for the independence of the spin response from the charge-gap in this material.

The most trivial explanation of the 3000cm^{-1} peak ("MIR peak") would be that it is a direct transition between bands which are formed as a result of the Umklapp-potential of the Na-superlattice below 240 K. However, the potential landscape caused by the Na ions becomes random above 240 K. Although even a random potential would give rise to a mid-infrared peak, the position of the mid-infrared peak would become strongly

temperature-dependent in such a scenario, in contrast to our experimental observations.

The remaining candidate for the mid-infrared band is to assume that the charge carriers are small polarons. Derived basically from the Frank-Condon model, the small polaron peak [117] can be viewed classically as an instantaneous transition from a localized state to a neighboring localized state in a rigid ionic environment. The environment responds to the new electronic configuration by emitting a wave package of multi-phonon oscillations, the envelope of which corresponds to the line shape of a polaron. It acquires not only a peak at several times the frequency of phonons, but also a finite conductivity at low frequencies. Our mid-infrared feature has a finite conductivity at low frequencies. The small polaron optical line shape, being influenced by the movement of ions, depends strongly on temperature [117]. This is indeed what we observe for the mid-infrared feature in its high frequency part (see Fig. 4.6a). The low frequency part is unchanged down to the $T_{\text{MI}} = 136\text{K}$, in contrast to what is expected [117] and measured [130] for the small polarons. This unexpected behavior may have a connection to the disorder potential created by the Na atoms, which could smear out the influence of the temperature at low frequencies. As discussed above, the measured intensity of the 990 cm^{-1} phonon which gradually develops in the insulating direction below T_{Na} being fully developed at T_{MI} (see inset of Fig. 4.7), strongly suggest that the MIT takes place at a temperature where the Na atoms are fully ordered.

The zig-zag ordering of Na ions induces an alternating potential $V_n = (-)^n V_0$ on vanadium sites, which in principle opens a charge gap $2V_0$. This gap must be rather small, as apparently it has little effect on the transport and optical properties of this system below T_{Na} . A strong reduction of the amplitude V_0 could come from a near cancellation of the electric fields from the neighboring rungs of the zig-zag ordered sodium ladder, since this can be viewed as a collection of dipoles aligned alternatively in opposite directions. Importantly, such a cancellation occurs in the ordered state, and in the exact stoichiometry only: for totally random positions of the Na ions, the potential on vanadium sites is also random and its amplitude is about five times larger than the amplitude V_0 in the ordered state. This would explain naturally why the resistivity along the b -direction shows a decrease below the sodium ordering temperature (being almost constant above) [17], and possibly also the insulating behavior of non-stoichiometric samples. A large random potential on the vanadium sites also strongly suppresses the instability towards a periodic state, which is probably why the metal-insulator transition is delayed until Na ions become almost fully ordered. This supports the picture in which the Na zig-zag chain units form below T_{Na} [17], and not above [136].

The small influence of the MIT transition on the magnetic susceptibility suggests thus a polaronic picture and/or a Hubbard model in which electrons propagate along chains with a large ratio of the on-site Coulomb repulsion to the band width. In the latter case, electronic charges and spins are decoupled: the charge excitations in a partially filled chain are spinless fermions, while the spin excitations are spinons [146]. A fermion band is unstable towards a Peierls-like transition into an insulating charge-density-wave (CDW) state. Such a transition could take place at T_{MI} where the tripling of the unit cell in the chain directions was observed. The tripling may be obtained for some particular electron filling of the occupied chains. A strong electron-lattice coupling could also result in a spin-Peierls type of transition, which could open a spin gap [144], but instead, a transition

into a canted antiferromagnetic state was found at $T_{CAF} = 22$ K[19, 20], indicating the importance of interchain spin interactions. The type of polaron, magneto-elastic polaron or spin-polaron may not be determined with certainty from our data. It may well be that both types of renormalization of the bare electrons are involved[147].

4.7 Summary

In summary, optical spectra have been presented for β - $\text{Na}_{0.33}\text{V}_2\text{O}_5$. The spectra show a delayed opening of a charge pseudogap at a MIT temperature $T_{MI} = 136$ K, well below the Na ordering transition at $T_{Na} \approx 240$ K, and support a picture in which the Na atoms order gradually, allowing the formation of the ordered electronic state at T_{MI} . Both the mid-infrared peak at 3000 cm^{-1} and the observation of strong electron-phonon coupling support the picture that the charge carriers in β - $\text{Na}_{0.33}\text{V}_2\text{O}_5$ should be regarded as small polarons. The strong Hubbard-type interactions are responsible for the observed independent behavior of the spin and charge channels at the metal-insulator phase transition.

Below the phase transition the insulating state is a charge ordered phase. Future experiments will have to establish the detailed nature of the charge ordered state. Although in a way a regular array of polarons also represents a CDW, a distinguishing feature in this case, is that in an ordinary CDW the spin- and charge sectors should be gapped simultaneously, which clearly does not happen in β - $\text{Na}_{0.33}\text{V}_2\text{O}_5$ at 136 K, and the spin even orders at a still lower temperature. The nature of the crystallographic phase transition at 136 K (*i.e.* the tripling of the unit cell along the chains) suggests that below 136 K the charges have become ordered with a commensuration of order 3 on the three different types of V-chains and ladders in the unit cell. This would imply that the doped charges are distributed equally over all V-atoms or in a 2/3-1/3 ratio over the V_1 and V_2 atoms, resulting in a high degree of dilution. This is a favorable condition for the formation of small polarons, consistent with the above interpretation of the spectra.

The presence of a strong electron-phonon coupling leads to the appearance of a large number of optical phonons below T_{MI} , in a similar way as the CDW systems[119, 120] below the Peierls temperature, and polaronic materials [118] below the Verwey transition temperature.

Chapter 5

Coulomb energy in $Bi_2Sr_2CaCu_2O_{8+\delta}$

We experimentally try to address the behavior of the correlation energy in the long wavelength limit ($\mathbf{k} = 0$), for underdoped and optimally doped $Bi_2Sr_2CaCu_2O_{8+\delta}$ high temperature superconductors, using an approach which starts from the measured in-plane dielectric function in the interval $50 - 20000\text{cm}^{-1}$. The results show that the Coulomb energy for $\mathbf{k} = 0$ increases in the superconducting state with respect to the extrapolated normal state, with about 0.2meV per Cu atom, a value comparable with the condensation energy. An extrapolation to higher momentum, taking into account the layered geometry of $Bi_2Sr_2CaCu_2O_{8+\delta}$ yields the same result, suggesting that the saving of the energy in the superconducting state is not due to the Coulomb energy, but probably due to kinetic energy, as reported earlier [61].

5.1 Introduction

The high-temperature superconductivity in ceramic compounds containing copper-oxide planes is still an unsolved theoretical problem. This is opposed to the conventional superconductivity, as described by the Bardeen, Cooper and Schrieffer (BCS) [148], whose main predictions are well established in the experimental work. Here, the Fermi-liquid approach, which results in the presence of quasiparticles in the normal state, is still applicable. These quasiparticles would then interact by exchanging phonons, leading to the formation of Cooper pairs, which condense into a coherent macroscopic state at a certain superconducting transition temperature T_c . The pairs have a fully symmetric, or s-wave, internal symmetry, and they lead to an opening of an isotropic gap Δ .

Many of the properties of the high temperature superconductors (HTSC) can be as well described in terms of the usual BCS and Ginzburg-Landau theories. For example, it is believed that the formation of Cooper pairs with zero net momentum is still present, because the usual ac Josephson effect frequency $2eV/h$ is still observed [24], and the observed flux quantum is of the usual size $hc/2e$ [25]. However, HTSC materials differ also in many aspects from the conventional superconductors. In the normal state above T_c no quasiparticles are found, and thus the Fermi-liquid approach is not anymore applicable. The superconducting gap $\Delta(\mathbf{k})$ is highly anisotropic [40] and the formed Cooper pairs have a d -wave symmetry.

To explain these unusual features of the HTSC, different models have been put forward, mostly discussing a "glue" that binds the carriers, different from phonons. One is the presence of a Resonance Valence Bond (RVB) state [52], which is based on a common belief that the Hubbard models, or simplified t - J models, lead to correlation effects which may play the leading role [53]. The SO(5) theories [56] exploit the fact that the HTSC emerge upon doping from their antiferromagnetic compounds, trying to unite the superconducting and antiferromagnetic phases in a larger symmetry group. A model proposed by Hirsch predicts a reduction of kinetic energy when two holes become closer [60]. The forming of the Cooper pairs, which may be regarded as the reason for the presence of the superconducting state, was also proposed to take place because frustrated kinetic energy of single charge carriers may be recovered when pairs are formed [57, 58], or because they may lower the ab -plane zero-point kinetic energy [59]. The presence of the Cooper pairs in the normal state was also proposed [45]. In this case they would Bose-Einstein condense below T_c .

An important issue in the modelling of the HTSC refers to the way the total energy of the system is lowered in the superconducting state. Usually, by choosing a wavefunction formed by Cooper pairs, the expectation value of the Hamiltonian, which is the energy of the system if that wavefunction would be the groundstate, is lowered compared to the case where no Cooper pairs are present. This approach finds a good example in the BCS model of classical superconductors [148]. If we decompose the total energy in the kinetic and Coulomb part, we see that in the conventional BCS case the potential energy in the superconducting state is lowered more than the increase of the kinetic energy, the difference providing the so-called condensation energy which drives the system into the superconducting state. We see that in general, this approach suffers from the poor definition of the "normal state" at $T = 0$.

Nevertheless, important information can be extracted if a different approach is taken. The internal energy of the system, plotted as a function of temperature, may show a kink around the phase transition when entering the superconducting state, as expected for the optimally doped high temperature superconductors. Since the system prefers the superconducting state, the kink should be downward, in the sense that the internal energy is lowered more at the phase transition as a consequence of entering the superconducting state. We think that the same type of plot can be done for the expectation values of the kinetic energy operator of the electrons, or for the electron-electron interaction energy operator. The sign of the kinks in these plots, if present, would give information on the mechanisms leading to the phase transitions. In the conventional BCS case, if measured, the expectation value of the Coulomb energy would show a downward kink in the superconducting state (showing a lowering of the Coulomb energy), and an upward kink for the kinetic energy. This approach does not require a state at $T = 0$ to be called a "normal state", but it gives information about the temperature dependence of different expectation values. Nevertheless, we will refer to an "extrapolated normal state" as a state at $T = 0K$ which has the same expectation values as the normal state ones (above T_c) *extrapolated* to $T = 0K$.

We have shown in a previous paper [61] that, if one relates the transfer of spectral weight of optical conductivity in $Bi_2Sr_2CaCu_2O_{8+\delta}$ to the kinetic energy, the expectation value of the kinetic energy can be extracted. The measurements suggested that the system

lowers its kinetic energy when entering the superconducting state (the kinetic energy shows a downward kink when entering the superconducting state), with a value comparable with the condensation energy. These results have been confirmed by subsequent works [62]. This is opposite to the behavior in the classical superconductors, as discussed previously, and points out to an unconventional pairing mechanism for the HTSC.

As far as the Coulomb correlation energy for the high-temperature superconductors is concerned, Leggett [63] has proposed that this energy would decrease in the superconducting state. This would come from an improved screening due to Cooper pair formation, and it would have thus the same sign as in the classical superconductors. The saving of the Coulomb energy would take place primarily at midinfrared frequencies (0.1-2 eV) and small momentum vectors $q \leq 0.3\text{\AA}^{-1}$. Some attempts have been done to measure these changes using Electron Energy Loss Spectroscopy, but they proved unsuccessful. The optical spectra ($\mathbf{k}=0$) does however shows changes in the midinfrared range when entering the superconducting state, and we can try to relate these changes to the Coulomb energy. We think that, even if optical measurements cannot give a complete (for all \mathbf{k}) answer, it may still give an indication of the behavior of the Coulomb energy.

5.2 BCS superconductors

There is one surprise in the success of the Bardeen-Cooper-Schrieffer (BCS) model of the superconductors [148] which shows, in a way, the general trend of solving problems in solid state physics. Take, for example, the average distance between valence electrons in a metal. This is of the order of few \AA . Calculating the bare Coulomb interaction between two electrons, we get a number of order 5eV. Visualizing now that these electrons would move randomly in the sample, they would create a random potential of the order of a few eV (or tens of thousands K), and consequently no "special effects" would be expected even at room temperature, since they would be smeared out by the random potential. However, as we all know, most of the metals present the transition to the superconducting state at few K, and even much lower in temperature! This shows that the electrons do not behave independently and in a random way, but they rather order in one-electron or many-body states. The huge number of electrons makes it impossible to find out in general the exact nature of those states. However, in the case of classical superconductors, Bardeen, Cooper and Schrieffer were able to find a good approximation for the ground state state [148], which enabled them to explain the main physical properties of the classical superconductors. One can see that there is no theorem that such a state may be in general found, since it may be mathematically too complicated to be accessible, but it is one of the things which solid state physicists are trying to identify!

We will start here with a short reminder on the phonon-mediated interaction for metals. As is known from Fermi Liquid theory, below a certain temperature T smaller than the Fermi energy, not all the electrons must be taken into account to describe the transport properties. In fact, the physics is described by those conduction electrons which are in a range $k_B T$ around the Fermi energy, and the rest may be considered "frozen" in the Fermi sea. The expected interaction among them would still be the repulsive Coulomb force:

$$V(\mathbf{q}) = \frac{4\pi e^2}{q^2} \quad (5.1)$$

In a first stage, a renormalization due to the screening of these conduction electrons occurs, leading in the Thomas-Fermi approximation to:

$$V(\mathbf{q}) = \frac{4\pi e^2}{q^2 + k_s^2} \quad (5.2)$$

where $k_s^2 = 6\pi n e^2 / \epsilon_F$ gives a screening length of the order of few \AA . The interaction is smaller, but still repulsive. However, one should take into account the presence of phonons as well. The electron-electron interaction mediated by phonons is attractive if the energy of electrons is within a ω_D range [149], where ω_D is the Debye frequency. As it was shown in a simple jellium model [150], this can also overcome the screened Coulomb repulsion, leading to a total *attractive* interaction.

Since, as mentioned above, the electrons which "count" are those within kT energy range below and above the Fermi energy, for temperatures $kT \ll \omega_D$ the interactions among all these electrons would be finally attractive, creating thus the premise for the Cooper pairs to form. The relation $k_B T \ll \omega_D$ is fulfilled for most metals at a few K , since the Debye frequency is of the order of hundreds of K .

A many-body Hamiltonian for these electrons, containing a kinetic energy and a Coulomb energy part, can be then approximated as [142, 148]:

$$H_{red} = \sum_{k\sigma} (\mu + \xi_k) n_{k\sigma} + \sum_{kl} V_{kl} c_{k\uparrow}^* c_{-k\downarrow}^* c_{-l\downarrow} c_{l\uparrow} = H_{kin} + H_p \quad (5.3)$$

The first part of the Hamiltonian is the kinetic energy part H_{kin} , and the second term is the reduced interaction energy part H_p , μ being the chemical potential. The operator which creates one electron with the momentum k was denoted by $c_{k\sigma}^*$, and the one giving the number of electrons $n_{k\sigma} = c_{k\sigma}^* c_{k\sigma}$. The energy dispersion of the bare fermions is given by ξ_k . The interaction was set to be present only for the electrons having energies within ω_D of the Fermi energy, as discussed above:

$$V_{kl} = \begin{cases} -V & \text{for } |\xi_k| \leq \hbar\omega_D \text{ and } |\xi_l| \leq \hbar\omega_D \\ 0 & \text{for } |\xi_k| > \hbar\omega_D \text{ or } |\xi_l| > \hbar\omega_D \end{cases} \quad (5.4)$$

with V being a positive constant, because the interaction is attractive. Bardeen, Cooper and Schrieffer have been able to find a good approximation of the ground state (given by the Hamiltonian 5.3):

$$|\psi_S\rangle = \prod (u_k + v_k c_{k\uparrow}^* c_{-k\downarrow}^*) |\psi_0\rangle \quad (5.5)$$

where the coefficients are defined as:

$$v_k^2 = \frac{1}{2} \left[1 - \frac{\xi_k}{\sqrt{\Delta^2 + \xi_k^2}} \right] = 1 - u_k^2 \quad (5.6)$$

Here Δ is the gap energy and, at $T = 0K$, it may be expressed in term of the density of states at the Fermi level $N(0)$:

$$\Delta = \frac{\hbar\omega_c}{\sinh[1/N(0)V]} \quad (5.7)$$

The expectation value of the Hamiltonian on the $|\psi_S\rangle$ groundstate will be lower (because of the attractive interaction) than the one calculated on the "extrapolated normal state" $|\psi_N\rangle$ obtained from 5.5 setting $\Delta = 0$. In fact the difference can be calculated exactly, giving

$$\langle E \rangle_s - \langle E \rangle_n = \left[\frac{\Delta^2}{V} - \frac{1}{2}N(0)\Delta^2 \right] - \frac{\Delta^2}{V} = \delta E_{kin} + \delta E_p = -\frac{1}{2}N(0)\Delta^2 < 0 \quad (5.8)$$

The result shows that the system, by forming the state given by 5.5, decreases its potential energy by $|\delta E_p| = \Delta^2/V$. This decrease is larger in absolute value than the increase due to the kinetic energy $\delta E_{kin} = \Delta^2/V - N(0)\Delta^2/2$, the system preferring thus the superconducting state given by 5.5.

The previous line of arguments, showing the behavior of the Coulomb and kinetic energy expectation values, was possible because the model of the classical superconductors is solved, and one is able to write down the correct Hamiltonian and its solution. What about the general case, and in particular, what about the high temperature superconductors? Can one find out the expectation values of the potential energy and kinetic energy on the ground state? Can one determine which part of energy (kinetic, Coulomb or both) is saved when entering the superconducting state?

5.3 The general form of the Coulomb interaction energy

Nozieres and Pines have shown [64] that in general, the expectation value of the Coulomb energy on the groundstate can be traced down to an experimentally measurable quantity, namely the dielectric complex function $\epsilon(\mathbf{k}, \omega)$. We want to follow in this section their approach, bearing in mind that, due to the momentum space limitations inherent to optical spectroscopy, we have to reduce even further their result, to the in-plane optical dielectric constant $\epsilon_{||}(\omega)$ of $Bi_2Sr_2CaCu_2O_{8+\delta}$.

We start from the "original" Hamiltonian describing the interaction among electrons:

$$H = \frac{1}{2m} \sum_j \mathbf{p}_j^2 + \frac{1}{2} \sum_{i,j} \frac{e^2}{|\mathbf{x}_i - \mathbf{x}_j|} + v(\mathbf{x}) \quad (5.9)$$

where \mathbf{x}_i and \mathbf{p}_i are the position and momentum operators of the i electron, $v(\mathbf{x})$ is the background potential in which the electrons move, and e is the bare charge of the electrons. By Fourier transforming the interaction potential, the positive background removes the term in $\mathbf{k} = 0$, and one can express the Hamiltonian in terms of density operators:

$$H = \frac{1}{2m} \sum_j p_j^2 + \sum_{\mathbf{k} \neq 0} \frac{2\pi e^2}{K^2} (\rho_{\mathbf{k}}^* \rho_{\mathbf{k}} - n) \quad (5.10)$$

where n is the average electron concentration and the density operator $\rho_{\mathbf{k}}$ is given by:

$$\rho_{\mathbf{K}} = \sum_j e^{-i\mathbf{K}\cdot\mathbf{x}_j} \quad (5.11)$$

From the Hamiltonian 5.10, one can write down the expectation value of the Coulomb interaction energy in the ground state as:

$$E_{int} = \langle 0 | \sum_{\mathbf{K} \neq 0} \frac{2\pi e^2}{K^2} (\rho_{\mathbf{K}}^* \rho_{\mathbf{K}} - n) | 0 \rangle \quad (5.12)$$

To make the connection between the Coulomb energy and dielectric function $\epsilon(\mathbf{k}, \omega)$, Nozieres and Pines [64] used the definition of the dielectric constant $\epsilon(\mathbf{k}, \omega)$, which is made in analogy to the Fourier transforms of Poisson equations. By introducing into the system a charge distribution of wavevector \mathbf{q} and frequency ω , the following charge density is obtained:

$$er_{\mathbf{q}}[e^{-i(\omega t + \mathbf{q}\mathbf{x})} + c.c.] \quad (5.13)$$

with $r_{\mathbf{q}}$ real. The Poisson equations are:

$$-i\mathbf{q} \cdot \mathbf{D}_{\mathbf{q}} = -i\epsilon(\mathbf{q}, \omega) \mathbf{q} \cdot \mathbf{E}_{\mathbf{q}} = 4\pi er_{\mathbf{q}} e^{-i\omega t} \quad (5.14)$$

$$-i\mathbf{q} \cdot \mathbf{E}_{\mathbf{q}} = 4\pi e(r_{\mathbf{q}} e^{-i\omega t} + \langle \rho_{\mathbf{q}} \rangle) \quad (5.15)$$

where $E_{\mathbf{q}}$ is the longitudinal electric field and $\langle \rho_{\mathbf{q}} \rangle$ is the expectation value of the density fluctuation $\rho_{\mathbf{q}}$ in the presence of the test charge (see formula 5.11). In other words, the dielectric function $\epsilon(\mathbf{k}, \omega)$ measures the response of the system to the presence of the external oscillating charge, and can be obtained by dividing 5.14 and 5.15:

$$\frac{1}{\epsilon(\mathbf{q}, \omega)} = 1 + \frac{\langle \rho_{\mathbf{q}} \rangle}{r_{\mathbf{q}} e^{-i\omega t}} \quad (5.16)$$

The imaginary part of the dielectric function $1/\epsilon(\mathbf{k}, \omega)$ was directly calculated by Nozieres and Pines [64] using the above expression, and expressed as:

$$Im\left[-\frac{1}{\epsilon(\mathbf{q}, \omega)}\right] = -\frac{4\pi^2 e^2}{q^2} \sum_n |\langle n | \rho_{\mathbf{q}} | 0 \rangle|^2 [\delta(\omega + \omega_{n0}) - \delta(\omega - \omega_{n0})] \quad (5.17)$$

where n runs over the $|n\rangle$ excited states whose energies are ω_{n0} , measured from the ground state. On integrating over all positive frequencies ω , the sum over n drops out, and one obtains:

$$\int_0^\infty d\omega Im\left[-\frac{1}{\epsilon(\mathbf{q}, \omega)}\right] = \frac{4\pi^2 e^2}{q^2} \langle 0 | \rho_{\mathbf{q}}^+ \rho_{\mathbf{q}} | 0 \rangle \quad (5.18)$$

Summing the previous relation over \mathbf{q} , and using relation 5.12 for the ground state, one obtains:

$$E_{int} = \sum_{\mathbf{q}} \left[\frac{1}{2\pi} \int_0^\infty d\omega Im\left[-\frac{1}{\epsilon(\omega, \mathbf{q})}\right] - \frac{2\pi n e^2}{q^2} \right] \quad (5.19)$$

In integral form this becomes:

$$E_{int} = \frac{\Omega}{(2\pi)^4} \int d^3\mathbf{k} \left\{ \int_0^\infty d(\hbar\omega) \text{Im} \left[\frac{-1}{\epsilon(\omega, \mathbf{k})} \right] - \frac{2\pi n e^2}{k^2} \right\} \quad (5.20)$$

where n is the average density of the electrons and Ω is the volume of the sample for which the energy is calculated. Thus E_{int} is likewise determined by the measured dielectric constant $\epsilon(\mathbf{k}, \omega)$. This form was used further by Nozieres and Pines to determine the ground state energy of the free electron gas, by use of the Feynman relation

$$E_0(e^2) = E_0(0) + \int_0^{e^2} \frac{dg}{g} E_{int}(g) \quad (5.21)$$

which assumes the energy to be characterized by the variable coupling constant g (in our case, e^2). From the experimental point of view this relation is hardly useful, since one would need measurements of the dielectric function $\epsilon(\mathbf{k}, \omega)$ for different interaction strengths $e!$

5.4 Coulomb interaction energy of the layered gas

We want to express here the Coulomb energy given by the formula 5.20 considering the special layered geometry of $Bi_2Sr_2CaCu_2O_{8+\delta}$. We will add also few considerations on the non-local effects on the optical dielectric function.

Since we concentrate our attention on the charge carriers from the valence band of $Bi_2Sr_2CaCu_2O_{8+\delta}$ we will use the following screened form for the interaction potential appearing in 5.9:

$$V(\mathbf{x}_i - \mathbf{x}_j) = \frac{e^2}{\epsilon_{sc} |\mathbf{x}_i - \mathbf{x}_j|} \quad (5.22)$$

Here ϵ_{sc} describes the screening by the polarizable ions. Generally, ϵ_{sc} is frequency and momentum dependent, but to a good approximation we will consider it constant and equal to the real part of the optical dielectric function at high frequencies (this is about $\epsilon_{sc} = 3.5$ in case of $Bi_2Sr_2CaCu_2O_{8+\delta}$).

The \mathbf{k} -dependent dielectric function $\epsilon(\mathbf{k}, \omega)$ is the ratio between an externally oscillating electric field and the induced field in the solid, as described in the previous section. Since we are interested in the dielectric constant due to the charge carriers in the system, we treat the external field to be screened by the ion cores. This yields an effective dielectric constant $\tilde{\epsilon}(\mathbf{k}, \omega) = \epsilon(\mathbf{k}, \omega)/\epsilon_{sc}$. By putting this into formula 5.20, the following form of the interaction energy is obtained:

$$E_{int} = \frac{\Omega}{(2\pi)^4} \int d^3\mathbf{k} \left\{ \int_0^\infty d(\hbar\omega) \text{Im} \left[\frac{-\epsilon_{sc}}{\epsilon(\omega, \mathbf{k})} \right] - \frac{2\pi n e^2}{k^2} \right\} \quad (5.23)$$

As we can see, the second term in the integral is temperature independent. The temperature dependence in the interaction energy comes only from the first term, through the dielectric function $\epsilon(\mathbf{k}, \omega)$. Since we will monitor carefully the experimental temperature dependence of the dielectric function (to find out the behavior of the Coulomb energy

when entering the superconducting state), we drop the second temperature independent term.

Moreover, we will take into consideration the layered geometry of the high temperature superconductors such as $Bi_2Sr_2CaCu_2O_{8+\delta}$. Neglecting the small in-plane anisotropy, we can make further the approximation in which $\epsilon(\omega, \mathbf{k})$ is not dependent on the in-plane direction:

$$\epsilon(\omega, \mathbf{k}) = \epsilon(\omega, k, q) \quad (5.24)$$

where k represents the magnitude of the projected reciprocal vector \mathbf{k} on the planes of the layers, and q perpendicular on the planes. Using the above approximations the temperature dependence of the Coulomb interaction energy expressed in 5.23 becomes:

$$E_{int}(T) = \frac{\Omega}{(2\pi)^4} \int_0^{k_m} 2\pi k dk \int_{-q_m}^{q_m} dq \int_0^\infty d(\hbar\omega) Im \left[\frac{-\epsilon_{sc}}{\epsilon(\omega, k, q, T)} \right] \quad (5.25)$$

Defining n_l as the number of layers per unit cell, which has dimensions (a, a, c) , we can write the formula for the Coulomb interaction energy stored in the unit cell as:

$$E_{int}(T) = \frac{n_l}{2} \int_0^\infty d(\hbar\omega) C(\omega, T) \quad (5.26)$$

where the function $C(\omega)$, which may be regarded as the frequency increment of the Coulomb interaction energy E_{int} , is given by:

$$C(\omega, T) = \frac{2a^2c/n}{(2\pi)^4} \int_0^{k_m} 2\pi k dk \int_{-q_m}^{q_m} dq Im \left[\frac{-\epsilon_{sc}}{\epsilon(\omega, k, q, T)} \right] \quad (5.27)$$

The above formula still poses the problem of the integration limits. If we may take $q_m = \pi/s$, where s is the distance between two successive layers, k_m is given by the wave vector beyond which the plasmons are unstable towards electron-hole pairs [151]. For a two-dimensional electron system this may be obtained [152] by solving the equation:

$$k_m^2 = 2me^2[\sqrt{k_m^2 + 2k_mk_F} - k_m] \quad (5.28)$$

where k_F is the Fermi momentum and m the mass of the electrons. Replacing in the upper formula the appropriate Fermi wavevector for $Bi_2Sr_2CaCu_2O_{8+\delta}$ we obtained a cut-off wavevector k_m which is very close to the Brillouin zone boundary wavevector $2\pi/a$, where a is the unit cell dimension along the a direction. This value was also given by Leggett in Ref. [63] as defining the possible "scale" of the in-plane behavior. We have thus decided to choose $k_m = 2\pi/a$ as the cut-off wavevector, and to refer to the Coulomb energy stored in the first Brillouin zone.

We see thus that the main ingredients are given in the formulas 5.25 and 5.27 for calculating the temperature dependence of the Coulomb interaction energy per a certain volume, provided that the dielectric function $\epsilon(\mathbf{k}, \omega)$ is measured at large momentum k as well. But this large momentum sector is not accessible to optical spectroscopy, because optical spectroscopy measures the dielectric constant at a very small \mathbf{k} compared with the Brillouin zone boundary. Measurements of the large momentum sector can be done using inelastic scattering of charged particles with large momentum transfer, but this

technique does not have yet the precision to measure changes associated with the onset of superconductivity. We are thus forced to use extrapolations to simulate the behavior at large \mathbf{k} . Before discussing one of these extrapolations, we make few considerations as regards non-local effects on the optical dielectric function.

It is usually assumed that the complex optical dielectric function $\epsilon(\omega)$ is given as the following limit:

$$\epsilon(\omega) = \lim_{\mathbf{k} \rightarrow 0} \epsilon(\mathbf{k}, \omega) \quad (5.29)$$

However, this is not generally true. The dielectric response is a matrix $\epsilon(\mathbf{q} + \mathbf{G}, \mathbf{q} + \mathbf{G}', \omega)$ in the in the Bragg umklapp wave vectors G and G' [153], since an electric field of small wave vector q will induce microscopic fields of different wave vectors $q + G$:

$$V_{tot}(q + G', \omega) = \epsilon^{-1}(q + G', q + G, \omega) * V_{ext}(q + G, \omega) \quad (5.30)$$

The macroscopic dielectric function measured in the experiment must then be calculated first by first inverting the matrix $\epsilon(\mathbf{q} + \mathbf{G}, \mathbf{q} + \mathbf{G}', \omega)$ in the small \mathbf{q} limit:

$$\epsilon(\omega) = \lim_{\mathbf{q} \rightarrow 0} \frac{1}{\epsilon^{-1}(\mathbf{q}, \mathbf{q}, \omega)} \quad (5.31)$$

This is called the local field correction [153]. The idea behind this correction is that when one applies a long wavelength optical electrical field, the response of the system is given not only by the $q \rightarrow 0$ components, but also by the superimposed Bragg reflections. In a simplified tight binding approach it will lead to the Clausius-Mosotti local field factor. In a nearly free electron solid this local field effect is unimportant, and one can use formula 5.29.

We have chosen to use the above formula 5.29 due to complications in taking into account this local field correction, and since anyway we have to use extrapolations to higher momentum \mathbf{k} in order to calculate the interaction energy. We believe, however, that even though the local field corrections may change slightly the absolute values obtained, they will not lead to a picture very different from the one proposed here.

5.5 Coulomb energy in the low momentum sector: the "k = 0" approximation

As mentioned above, we have to use extrapolations to simulate the behavior at large \mathbf{k} , in order to estimate the temperature dependence of the Coulomb interaction energy with the formula 5.25. A slightly different point of view may be however that, by using optical spectroscopy, we measure directly only the Coulomb energy stored in the *center* of the Brillouin zone, according to formula 5.25.

The amount of Coulomb interaction energy stored in the *center* of the Brillouin zone, which could come out from our measurements, is however sensitive to the choosing of the boundary of this "center". One can choose, for example, a value which is ten times smaller than $k_m = 2\pi/a$, the Brillouin zone boundary, but it may lead to very small values of Coulomb interaction energy. A more direct way is to integrate up to k_m in the in-plane direction and up to $2\pi/s$ in the out-of-plane direction, and to assume that the

temperature dependent changes in the integrated loss function at higher momentum are the same as at low momentum, and given by the in-plane dielectric function $\epsilon_{\parallel}(\omega)$:

$$\Delta \int_0^{\infty} Im \left[\frac{-1}{\epsilon(\omega, \mathbf{k})} \right] d\omega \simeq \Delta \int_0^{\infty} Im \left[\frac{-1}{\epsilon_{\parallel}(\omega)} \right] d\omega \quad (5.32)$$

We call this the "k=0" approximation. The principal reason why we have chosen the in-plane loss function $Im[-1/\epsilon_{\parallel}(\omega)]$ and not the out of plane one $Im[-1/\epsilon_{\perp}(\omega)]$, is that the spectral weight in the former loss function is much larger than in the latter, due to the metallic behavior along the planes. Also, the in-plane optical dielectric function given by $\epsilon_{\parallel}(\omega) = \epsilon(\omega, k_{\parallel} = k_{\lambda}, q_{\perp} = 0)$ (here k_{λ} is the wave vector of light) spans a larger space in the Brillouin zone than the out of plane dielectric function $\epsilon_{\perp}(\omega) = \epsilon(\omega, k_{\parallel} = 0, q_{\perp} = k_{\lambda})$. Last, but not at least, the change of the kinetic energy in the out-plane direction at the phase transition in the high temperature superconductor $Tl_2Ba_2CuO_6$ is two orders of magnitude smaller than the condensation energy [51], whereas the in-plane kinetic energy in $Bi_2Sr_2CaCu_2O_{8+\delta}$ was found to be of the order of the condensation energy [61].

The above "k=0" approximation is, of course, very rough, but it gives us a way to measure the changes of the Coulomb energy stored in the low momentum sector. If this extrapolation would yield values bigger than some limiting values, like the condensation energy, then the changes in the low momentum sector are to be important, otherwise the changes in the large momentum sector are expected to be more important. We emphasize here however that the sign obtained at the phase transition is the true sign for the Coulomb interaction energy stored in the *center* of the Brillouin zone.

This assumption results effectively in choosing $\epsilon(\omega, k, q, T) = \epsilon_{\parallel}(\omega, T)$ in the formulas 5.25 and 5.27. When taking the integration limits $k_m = 2\pi/a$ and $q_m = \pi/s$ (where s is the distance between two successive layers of cooper-oxide planes) into account, it yields the following form of the $C(\omega)$ function defined in 5.27:

$$C_{(k=0)}(\omega, T) = Im \left[-\frac{\epsilon_{sc}}{\epsilon_{\parallel}(\omega, T)} \right] \quad (5.33)$$

We see that this function is proportional to the usual loss function $Im[-1/\epsilon_{\parallel}(\omega, T)]$ and it yields a very simple formula for the interaction energy per unit cell, according to the Eq. 5.26:

$$E_{int}(T) = \frac{n}{2} \int_0^{\infty} d(\hbar\omega) Im \left[-\frac{\epsilon_{sc}}{\epsilon_{\parallel}(\omega, T)} \right] \quad (5.34)$$

Here n is the number of layers per unit cell ($n=2$ in case of $Bi_2Sr_2CaCu_2O_{8+\delta}$).

The only thing left is then to carefully measure the temperature dependence of the in-plane loss function $Im[-1/\epsilon_{\parallel}(\omega, T)]$, integrate over the frequency range (which should be as broad as possible) at each temperature, and then calculate the temperature dependence of the Coulomb interaction energy according to the formula 5.34.

In order to achieve this, an Woollam Variable Angle Ellipsometer, as described in the second chapter of this thesis, was used for temperature dependent in-plane measurements in the frequency range $6000 - 20000\text{cm}^{-1}$. To avoid absorption of residual gas molecules, the samples have been placed in an ultra high vacuum cryostat, with a base pressure of

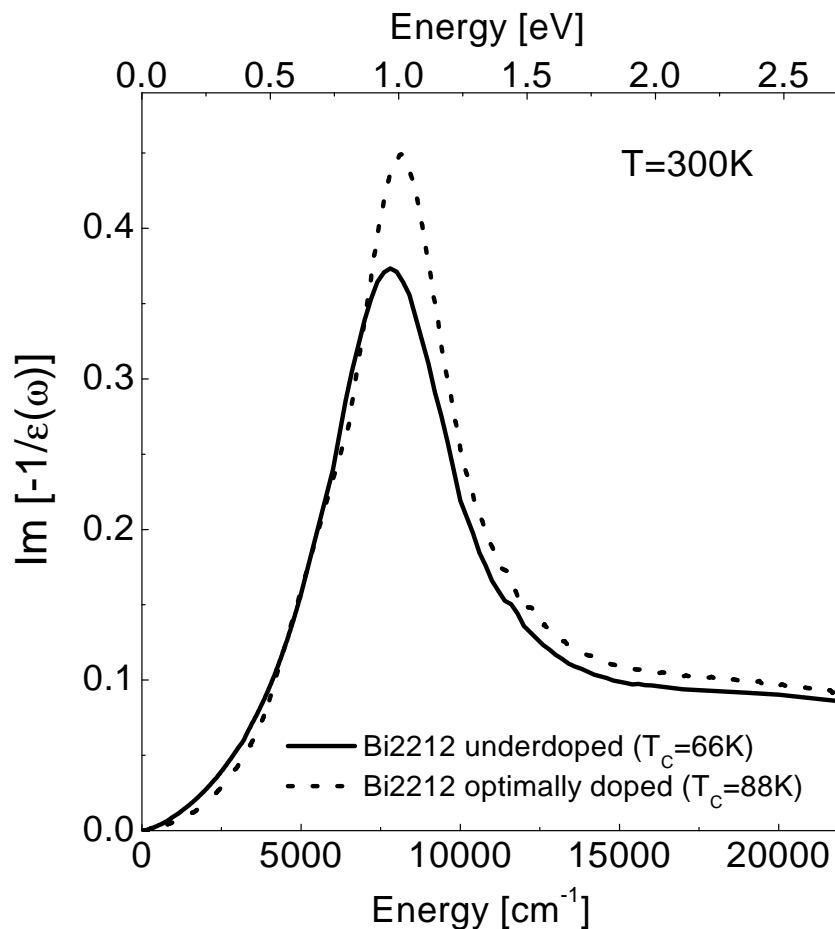


Figure 5.1: The room temperature in-plane loss function $Im[-1/\epsilon_{\parallel}(\omega)]$ of optimally and underdoped $Bi_2Sr_2CaCu_2O_{8+\delta}$

10^{-9} mbar. The *pseudo*-dielectric function of the in-plane (001) face of the samples was then measured. The monochromator of the ellipsometer was kept fixed to one frequency, and the temperature was varied in the cryostat, to acquire as many temperature points as possible. When the whole temperature range 5-300K was measured, the frequency was changed and the procedure restarted. Later, a *c* axis temperature independent correction was applied to the *pseudo*-dielectric function.

For the lower frequency range $50 - 6000\text{cm}^{-1}$ normal incidence reflectivity measurements have been performed. The ellipsometry data were then used as an input for the Kramers-Kronig transformations to obtain accurate information of the dielectric function in the low frequency range. The loss function was then calculated from the dielectric function.

In Fig.5.1 we present the room temperature results for the in-plane loss function $Im[-1/\epsilon_{\parallel}(\omega, T)]$ of the optimally doped ($T_C=88\text{K}$) and underdoped ($T_C=66\text{K}$) samples of $Bi_2Sr_2CaCu_2O_{8+\delta}$. As we can see, the loss function is peaking at the plasma frequency.

Since we are interested in the changes at the phase transition, careful temperature scans have been performed for many frequencies, at an interval of 0.5K . From Fig. 5.2, where we present some particular scans, we see that phase transition changes appear in

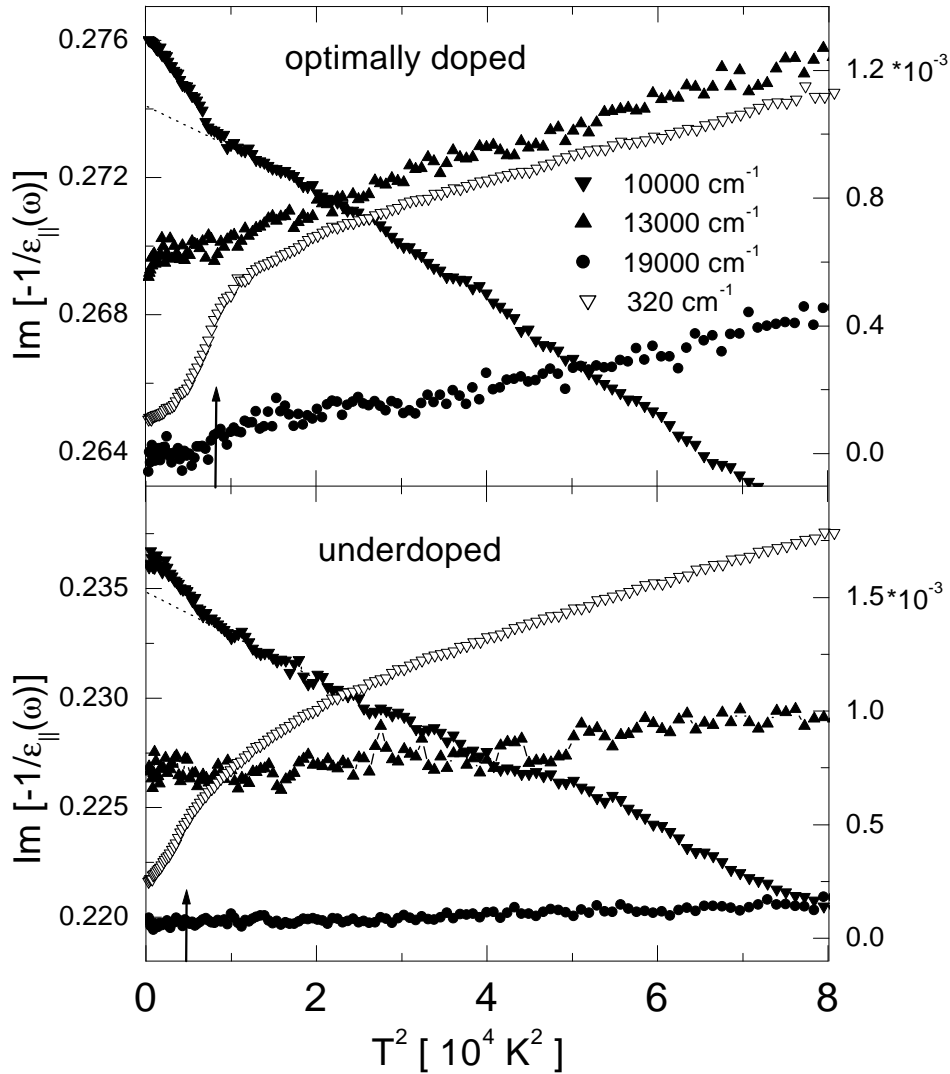


Figure 5.2: Few selected temperature scans of the in-plane loss function $Im[-1/\epsilon_{||}(\omega)]$. The arrows at the bottom of the scale indicate the transition temperature T_c in each of the two cases. The loss functions for 19000cm^{-1} and 13000cm^{-1} have been rescaled with a constant background to fit the window. Full symbols refer to the lefthand scale and open symbols to the righthand scale.

the dielectric function not only in the far infrared range, but also in the visible range. The transition temperatures have been shown in the figure by small arrows. The general characteristic is that the loss function further increases when the system enters the superconducting state in the visible range (see the frequency 10000cm^{-1} in Fig. 5.2) and is further lowered in the FIR range (below 1000cm^{-1}), as expected from the opening of the gap (as exemplified by the 320cm^{-1} frequency in the same plot). At 13000cm^{-1} no clear change is observed in the loss function both in the optimally and underdoped samples. At higher frequencies, a decrease which starts at a temperature higher than T_c may be suggested in the optimally doped samples, as seen from the 19000cm^{-1} plot of Fig. 5.2.

Using formula 5.34, one can now calculate for each temperature the corresponding

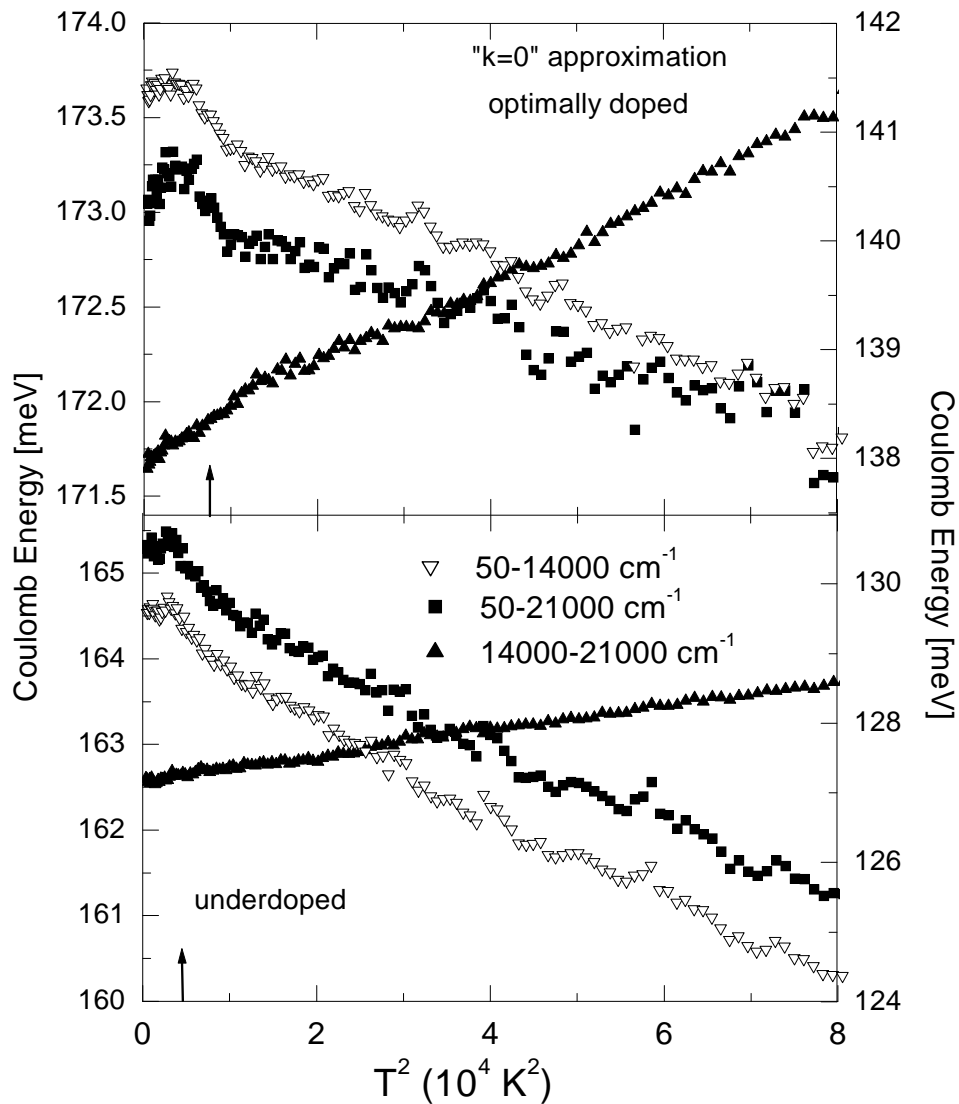


Figure 5.3: Coulomb energy per Cu atoms in the "k = 0" approximation for $Bi_2Sr_2CaCu_2O_{8+\delta}$. The integration over a few frequency ranges according to formula 5.35 is presented. Full symbols refer to the lefthand scale and open symbols to the righthand scale. The data for the frequency range 14000 – 21000 cm^{-1} were rescaled with a constant background to fit the window (140 meV for the optimally doped sample and 128 meV for the underdoped sample). The arrows indicate the phase transition temperatures.

Coulomb energy. An integration up to ∞ is not possible, and we have chosen to integrate over the entire measured range (50 – 21000 cm^{-1}), and also over other small ranges, to quantify which frequency range plays the most important role, using:

$$E_{int}[\omega_1, \omega_2](T) = \frac{n}{2} \int_{\omega_1}^{\omega_2} d(\hbar\omega) Im \left[-\frac{\epsilon_{sc}}{\epsilon_{||}(\omega, T)} \right] \quad (5.35)$$

In Fig. 5.4 and 5.3 we present the results, for different ranges of integration $[\omega_1, \omega_2]$.

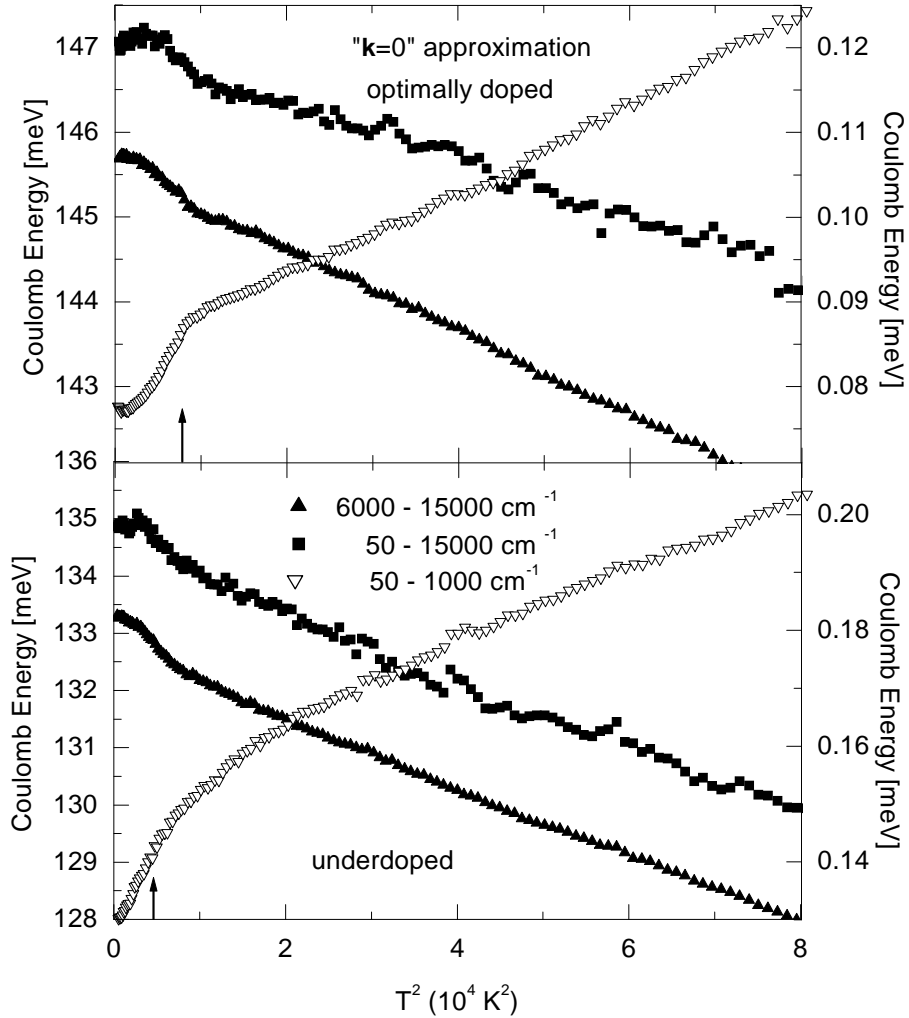


Figure 5.4: Coulomb energy per Cu atoms in the " $\mathbf{k} = 0$ " approximation for $Bi_2Sr_2CaCu_2O_{8+\delta}$. The integration over a few frequency ranges according to formula 5.35 is presented. Full symbols refer to the lefthand scale and open symbols to the righthand scale. The data for the the frequency range $6000-15000\text{cm}^{-1}$ were rescaled with a constant background to fit the window (38 meV for the optimally doped sample and 23 meV for the underdoped sample). The arrows indicate the phase transition temperatures.

First we discuss the optimally doped samples. For the total measured range $50-21000\text{cm}^{-1}$ (see the full squares of the Fig. 5.3) we observe an extra increase of the Coulomb energy when entering the superconducting state (SCS), of about $0.2 - 0.3$ meV per Cu atom. The behavior of the Coulomb energy when calculated on smaller ranges must be put in correlation with the loss function from Fig. 5.2. Thus, for example, in the far infrared range (frequency 320cm^{-1} in Fig. 5.2), the loss function decrease further in the SCS due to the opening of the charge gap. The value of this decrease is however about 10 times smaller than the one for 10000cm^{-1} and it leads to a decrease of the Coulomb energy in

the SC state of only about 0.01 meV, if integrating from $50 - 1000\text{cm}^{-1}$ (see Fig. 5.4).

The main increase in the total measured range $50 - 21000\text{cm}^{-1}$ comes from the range $6000 - 15000\text{cm}^{-1}$ as seen from Fig. 5.4. This is not unexpected, since the loss function shows the plasma peak exactly in this region (see Fig.5.1). At very high energies, in the interval $14000 - 21000\text{cm}^{-1}$ Fig. 5.3 suggests a decrease in the SCS which would start at slightly higher temperatures than T_C . This is due to the previously discussed decrease in the loss function around 19000cm^{-1} . Thus, summarizing, apart from a small extra decrease of the Coulomb energy in the SCS in the lower and possibly very high frequency range, an overall extra increase of the Coulomb interaction energy when entering the SCS of about $0.2 - 0.3$ eV per Cu atom is given by the whole measured range $50 - 21000\text{cm}^{-1}$.

The underdoped $Bi_2Sr_2CaCu_2O_{8+\delta}$ sample seems to present the same behavior as the optimally doped one, with the main difference that the phase transition is not so sharp in our data. The best argument is the shape of the 320cm^{-1} loss function of Fig.5.2. The visible frequency 10000cm^{-1} presented in the same plot indicates however a clear extra increase at the phase transition. Consequently, the range $6000 - 14000\text{cm}^{-1}$ gives a clear extra increase of the Coulomb energy when entering the superconducting state of about 0.3 eV (see Fig. 5.4), which is thus the same value as in the optimally doped samples. This behavior is conserved in the plot of the total measured energy range $50 - 21000\text{cm}^{-1}$.

As a conclusion of this section, it seems that the " $\mathbf{k} = 0$ " approximation indicates an extra increase of the Coulomb energy when entering the superconducting state, for both the optimally doped and underdoped $Bi_2Sr_2CaCu_2O_{8+\delta}$ samples, with a value of about $0.2 - 0.3$ meV per Cu atom. This gives the exact sign of the change of the Coulomb energy stored *only in the center* of the Brillouin Zone, which increases thus in the superconducting state. The absolute value is close to the condensation energy [154], and thus cannot give a conclusive answer as to the question of which part of the Brillouin Zone plays the most important role, but it still suggests that the low momentum one is important.

An open question still remains the unmeasured range, especially at higher frequencies. In the next section we will show, on the basis of a well-known sum-rule, that the changes in the interaction energy given by the frequencies higher the 21000cm^{-1} will not overcome the changes given by the measured range $50 - 21000\text{cm}^{-1}$.

5.6 Transfer of the spectral weight of the loss function

In the previous section we have tried to derive an approximation which connects the in-plane dielectric function $\epsilon_{\parallel}(\omega)$ to the Coulomb energy stored in the small momentum region of the Brillouin Zone. But, in principle, we would still have to integrate in the whole frequency range from 0 up to ∞ , according to formula 5.34. Our measured frequency range $50 - 21000\text{cm}^{-1}$ is finite and we have to check the influence of the remaining ranges. We do this by using the well known sum-rule [155]:

$$\int_0^{\infty} \omega d\omega \text{Im} \left[-\frac{1}{\epsilon(T, \omega)} \right] = \frac{4\pi^2 n e^2}{4m} \quad (5.36)$$

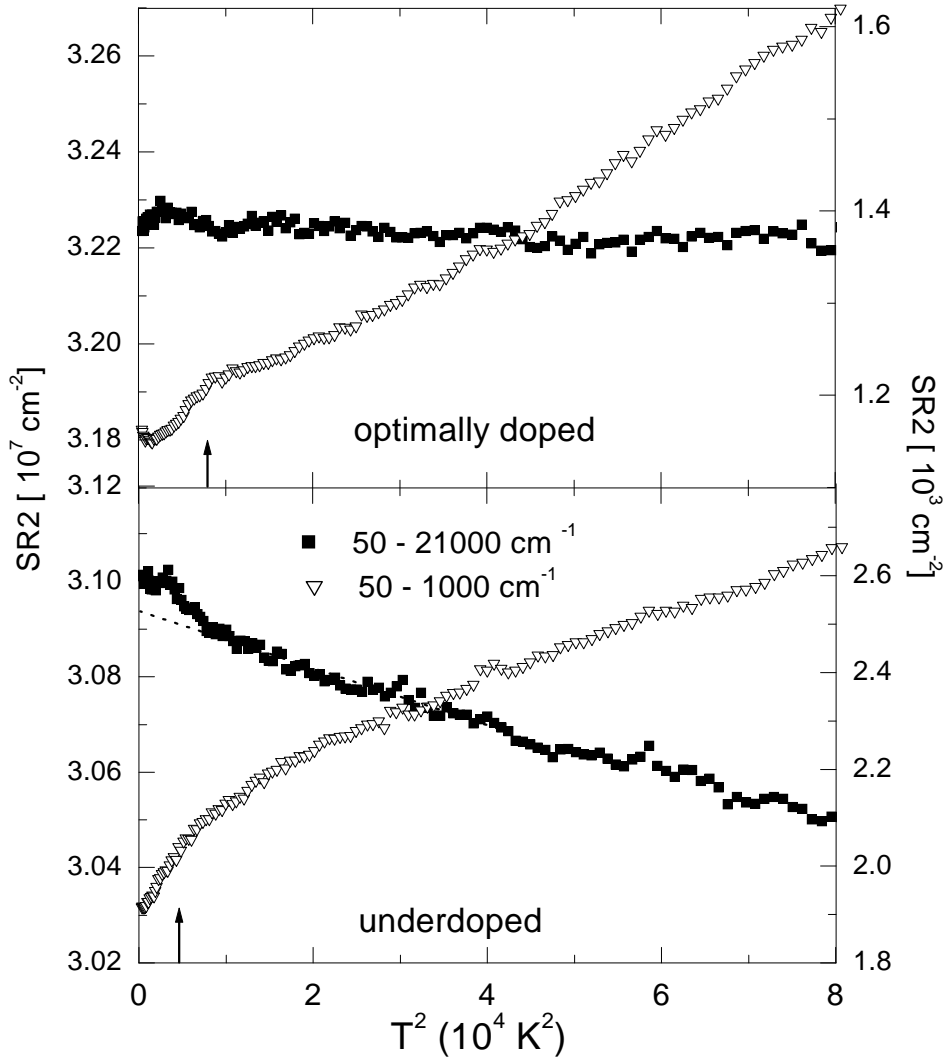


Figure 5.5: Sum rule check on the loss function in the $Bi_2Sr_2CaCu_2O_{8+\delta}$ samples, calculated with the formula 5.37 for different frequency ranges. Full symbols refer to the lefthand scale and open symbols to the righthand scale. The arrows indicate the phase transition temperatures.

The value of the integral in Eq. 5.36 calculated for a finite frequency interval range we designate as $SR2(T)$:

$$SR2[\omega_1, \omega_2](T) = \int_{\omega_1}^{\omega_2} \omega d\omega \text{Im} \left[-\frac{1}{\epsilon(T, \omega)} \right] \quad (5.37)$$

The results for $SR2[\omega_1, \omega_2](T)$ calculated for different frequency intervals are plotted in Fig. 5.5 and Fig. 5.6. As we can see, an overall temperature independent value seems to be obtained for the optimally doped samples for the whole measured range 50 – 21000 cm^{-1} . The sum rule 5.36 seems thus to be satisfied in this case for the 4 – 300K temperature range. However, at a closer look, an upward kink is still present at the phase transition when entering the superconducting state (SCS). This is clearer when integrating only

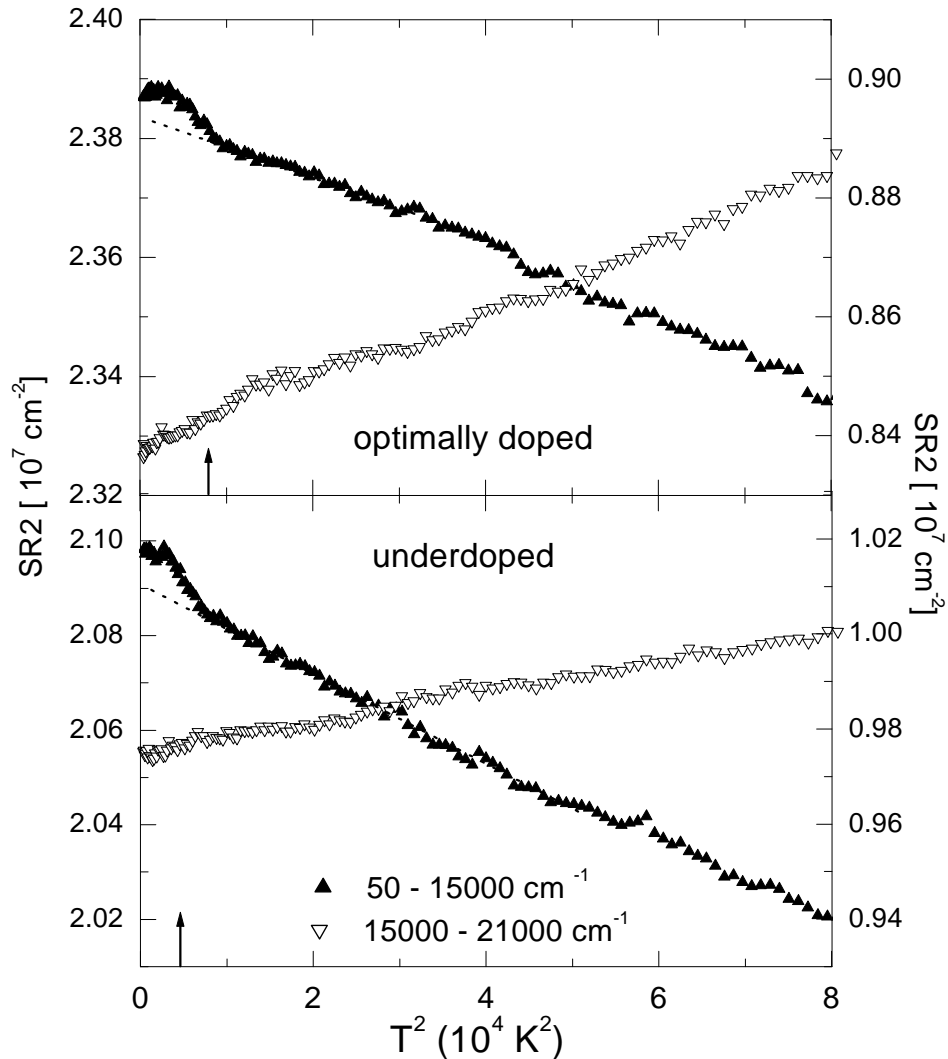


Figure 5.6: Sum rule check on the loss function in the $Bi_2Sr_2CaCu_2O_{8+\delta}$ samples, calculated with the formula 5.37 for different frequency ranges. Full symbols refer to the lefthand scale and open symbols to the righthand scale. The arrows indicate the phase transition temperatures.

up to 15000 cm^{-1} . In the underdoped case, the sumrule 5.36 calculated for the whole measured range $50 - 21000\text{ cm}^{-1}$ (see Fig. 5.5) is not satisfied in the $4 - 300\text{ K}$ range. It also presents an upward kink when entering the SCS.

The qualitative behavior of the sum rule 5.37 is presented in the Fig. 5.7. In the low frequency range (LFR), below ω_{LR} (few thousands cm^{-1}), the loss function of the superconducting state (SCS) at 4 K is lower than the one of the "extrapolated normal state" (ENS), because of the opening of the superconducting gap (as exemplified by the frequency range $50 - 1000$ from Fig. 5.5). By ENS, as discussed in the introduction of this chapter, we understand a virtual state whose properties would equal the normal state properties *extrapolated* to $T = 0\text{ K}$.

In the visible range (VISR), which extend from ω_{LR} (few thousands cm^{-1}) to ω_{HR}

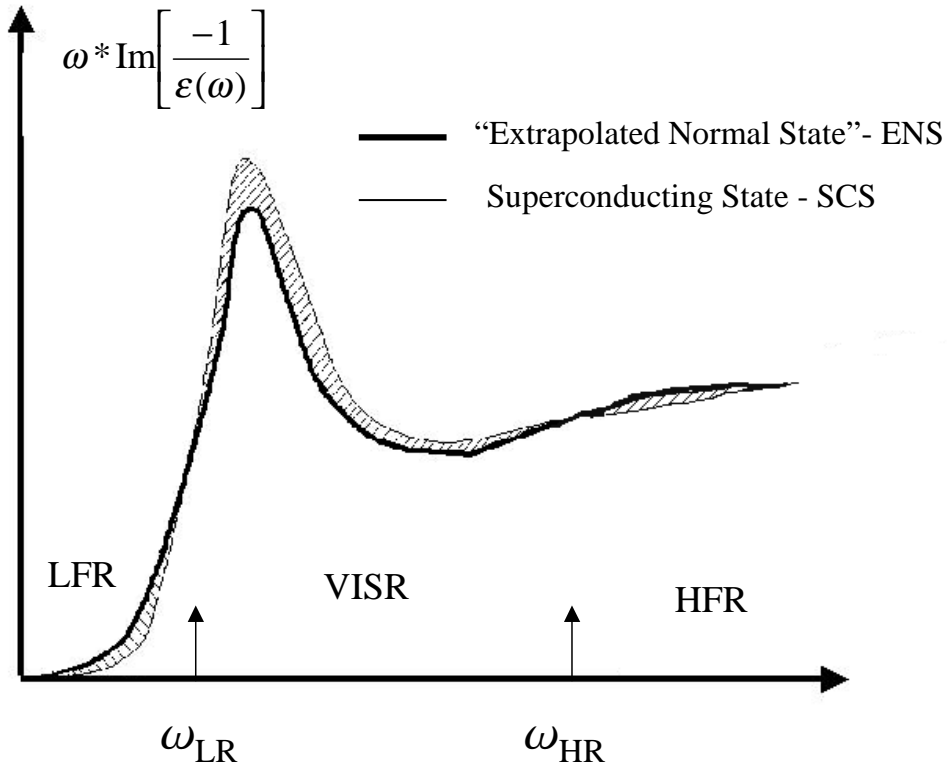


Figure 5.7: Schematic behavior of the "omega times loss" function.

(roughly 14000cm^{-1}), the situation is reversed. Fig.5.5 and Fig.5.6 also show that the phase transition step of the sum rule integral 5.36 in the VISR is few order of magnitude larger than that in the LFR. In other words, the dashed area in the VISR from Fig.5.7 is much larger than the one from the LFR. But according to the sum-rule 5.36, this difference must be compensated at very high frequencies. Since, as seen from Fig. 5.5, the very low frequency does not play an important role, the VISR range stores in the SCS (as compared with the ENS) an *additional* spectral weight coming from the high frequency range (HFR), *i.e.* above ω_{HR} (roughly 14000cm^{-1}). Here, an extra decrease of the loss function in the SC state would be observed. Only a part of this HFR was measured, namely $14000 - 21000\text{cm}^{-1}$. The Fig.5.6 suggests that this may be the case.

This aspect is crucial in determining the sign of the Coulomb energy calculated in the " $\mathbf{k} = 0$ " approximation. The amount of spectral weight transfer in the "omega times loss" function 5.36 must be divided by ω to get the one in the loss function. In other words, an additional transfer from HFR to VISR in the "omega times loss" function 5.36 when entering the superconducting state, as found experimentally (see the frequency range $50 - 21000$ of Fig.5.5), means more gain for the loss function in the VISR than decrease in the HFR.

Consequently, the increase found in the previous section for the Coulomb interaction energy when entering the superconducting state, is partially reduced by the decrease at very high frequencies in the unmeasured range above 21000cm^{-1} but it remains *positive*.

One may wonder about two different discussions of the transfer of the spectral weight. The one just presented involved the omega-loss function. A second one on the optical

conductivity was presented earlier[61]. There it was shown that, when the system enters the superconducting state, additional spectral weight is transferred the optical conductivity from the high frequency part (above 10000 cm^{-1}) to the low frequency part. Does this transfer of spectral weight in the real part of the *optical conductivity* induce the one in the "omega-loss function" 5.37? A rough check was performed by using the approximate formula for the loss function of a Drude peak:

$$\text{Im} \left[-\frac{1}{\epsilon(\omega)} \right] \simeq \frac{\pi\omega_p}{2} \delta(\omega - \omega_p) \quad (5.38)$$

where ω_p is its plasma frequency. More spectral weight in the optical conductivity (quantified by ω_p^2) at low frequency in the SCS than in the ENS means indeed more weight in the loss function around the plasma frequency in the SS state.

From Formula 5.26 and Fig.5.3 we can correct back for the number of layers $n = 2$, dielectric constant $\epsilon_{sc} = 3.5$ and the number of Cu atoms per unit cell $N = 8$ to obtain:

$$\Delta \int_0^\infty \text{Im} \left[\frac{-1}{\epsilon_{\parallel}(\omega)} \right] d\omega \simeq 1.1 \text{ meV} \quad (5.39)$$

According to 5.38 this would lead to an extra increase of the plasma frequency at the phase transition of about $\omega_p \simeq 0.7 \text{ meV}$. The same value is obtained from the transfer of spectral weight in the optical conductivity, as can be seen in Fig 2. of Ref.[61]. Despite the fact that the two spectral weights are related, one should not disregard completely the information preserved in the loss function, since, as argued earlier, it can also give an indication of the changes in the Coulomb interaction energy.

5.7 Coulomb interaction in the layered electron gas: the "DI" - approximation

In this section, a different extrapolation to higher momentum \mathbf{k} , which take into account the layered structure of $\text{Bi}_2\text{Sr}_2\text{CaCu}_2\text{O}_{8+\delta}$ is deduced. The dielectric constant of a layered material can quite generally be written in the form:

$$\tilde{\epsilon}(k, q, \omega) = 1 - V(k, q) [\tilde{k}^2 \Pi'_{\parallel}(k, q, \omega) + \tilde{q}^2 \Pi'_{\perp}(k, q, \omega)] \quad (5.40)$$

where $\tilde{k}^2 s^2 / 2 = \cosh(ks) - 1$ and $\tilde{q}^2 s^2 / 2 = 1 - \cos(qs)$. Here k runs in the in-plane direction, q perpendicular to the layer planes, s is the interlayer distance and Π' is related to the bare polarization bubble. This form is suggested by the random phase approximation method [156].

In the limit $k, q \rightarrow 0$ both Π'_{\parallel} and Π'_{\perp} become finite constants. In the layered material with s being the distance between layers, the interaction potential may be approximated as [157]:

$$V(k, q) = \frac{4\pi e^2}{\Omega} \frac{(s/2k) \sinh(ks)}{\cosh(ks) - \cos(qs)} \quad (5.41)$$

In the small \mathbf{k} limit ($k \rightarrow k_{light}$, $q \rightarrow 0$), from Eq. 5.40 and 5.41, the dielectric function for a layered material can thus be approximated with:

$$\tilde{\epsilon}(k, q, \omega) = 1 + \frac{(ks/2) \sinh(ks)}{\cosh(ks) - \cos(qs)} [\tilde{\epsilon}_{\parallel}(\omega) - 1] \quad (5.42)$$

with $\tilde{\epsilon}_{\parallel}(\omega) = \epsilon_{\parallel}(\omega)/\epsilon_{sc}$. It provides a way of extrapolating the dielectric function at larger momentum \mathbf{k} .

By putting formula 5.42 into formula 5.27, and integrating over q , we obtain the function $C(\omega)$ which leads to the Coulomb interaction energy per unit cell according to 5.26. The integration uses a simple contour integral over the unit circle, since the used limit of the integration is $q_m = \pi/s$, and uses also $k_m = 2\pi/a$ as discussed above, yielding:

$$C_{DI}(\omega) = \frac{1}{\beta^2} \text{Im} \left[\int_0^{\beta} \frac{z^2 f(\omega) dz}{\sqrt{z^2 f(\omega)^2/4 + z * f(\omega)/\tanh(z) + 1}} \right] \quad (5.43)$$

where $\beta = k_m s$ and

$$f(\omega) = \frac{\epsilon_{\parallel}(\omega)}{\epsilon_{sc}} - 1 \quad (5.44)$$

The $C(\omega)$ function calculated in this way for $Bi_2Sr_2CaCu_2O_{8+\delta}$ and designated $C_{DI}(\omega)$, is presented in Fig. 5.8. As we can see, above 12000cm^{-1} its value is about the same as the function $C_{k=0}(\omega)$ of the " $\mathbf{k}=0$ "-approximation defined in 5.33 (which is proportional to the loss function). Below 12000cm^{-1} it is smaller. It is also peaking at higher frequencies.

The temperature dependence for two selected frequencies is presented in Fig. 5.9. The phase transition can be seen in these plots, but the signs of the kinks at the phase transition seem to be opposite to the signs of the normal loss function plotted in Fig. 5.2. Thus, there is an extra decrease this time for 10000cm^{-1} and an extra increase for 17000cm^{-1} when entering the SC state. This behavior is probably related to the to the shift of the plasma peak from a lower value in $C_{k=0}(\omega)$ to a higher value in $C_{DI}(\omega)$ (see Fig. 5.8).

By replacing the function $C_{DI}(\omega)$ into Formula 5.26, we calculated the temperature dependence of the Coulomb interaction energy integrating over different finite frequency ranges:

$$E_{int}[\omega_1, \omega_2](T) = \frac{n}{2} \int_{\omega_1}^{\omega_2} d(\hbar\omega) C_{DI}(\omega, T) \quad (5.45)$$

and plotted it in Fig. 5.10. The behavior is clearer in the optimally doped case. This time the increase in the Coulomb interaction energy takes place in the very high frequency range $13500 - 21000\text{cm}^{-1}$ and it has a value of about $0.3 - 0.4\text{meV}$ pe Cu atom. The frequency range $50 - 13500\text{cm}^{-1}$ gives a smaller decrease of about 0.1meV .

Overall, an increase of $0.2 - 0.3\text{meV}$ for the Coulomb interaction energy E_{int} is obtained when entering the superconducting state, for the total measured range $50 - 21000\text{cm}^{-1}$ (see Fig. 5.10). This value and sign remarkably agrees with the results of the " $\mathbf{k} = 0$ " approximation. The underdoped sample does not show a clear effect for the whole measured range $13500 - 21000\text{cm}^{-1}$ probably due to the smooth behavior at the phase transition.

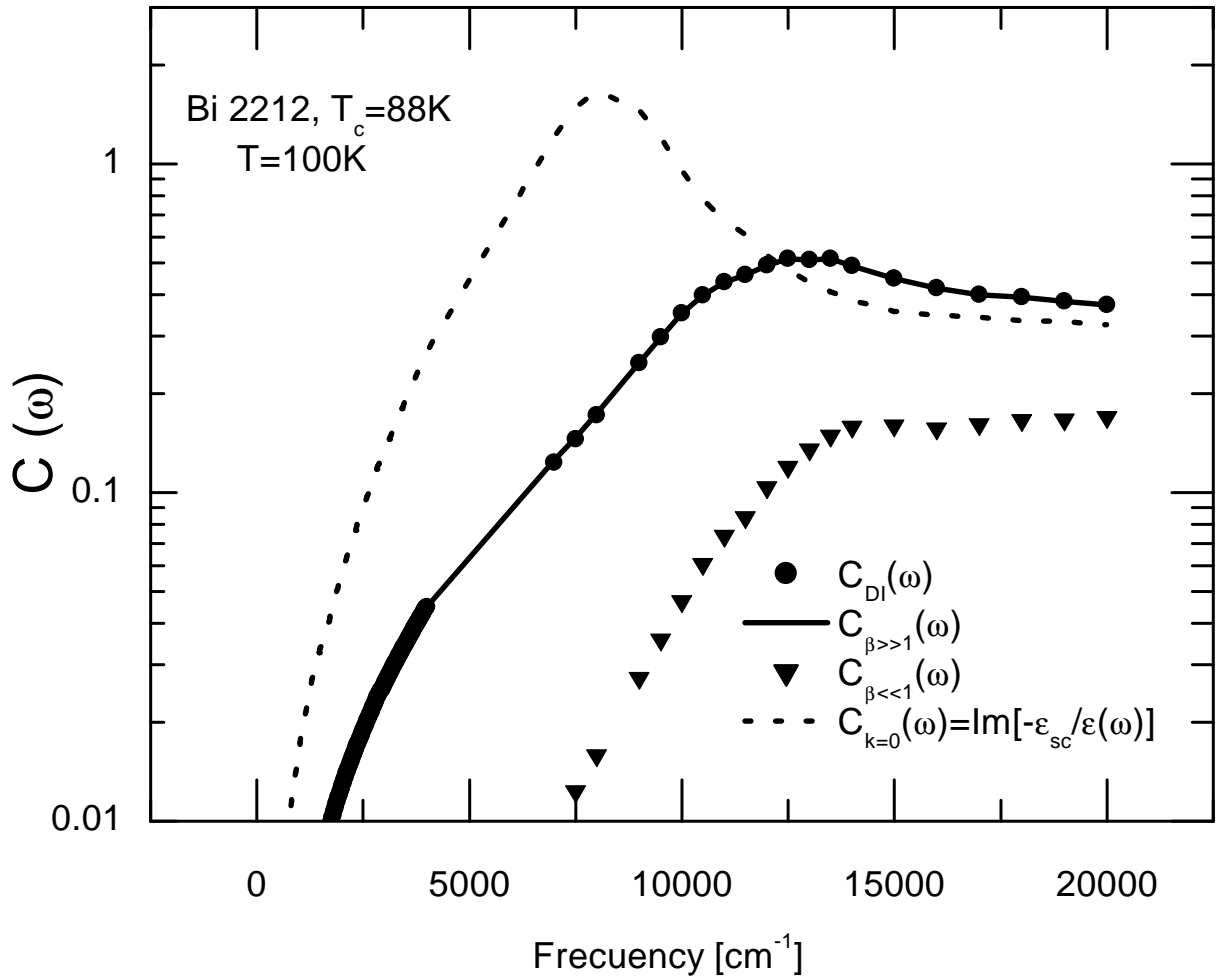


Figure 5.8: Different forms of the $C(\omega)$ function defined in 5.27. The forms are given by the formulas: 5.33 for $C_{k=0}(\omega)$, 5.43 for $C_{DI}(\omega)$, 5.47 for $C_{\beta \gg 1}(\omega)$, and 5.50 for $C_{\beta \ll 1}(\omega)$.

Since the formula 5.43 for the function $C_{DI}(\omega)$ can only be integrated numerically, one may wonder if appropriate approximations may be found. We show here two formulas, for the two cases $\beta \gg 1$ and $\beta \ll 1$. Since, in the case of $Bi_2Sr_2CaCu_2O_{8+\delta}$ $\beta = k_m s \simeq 18$, we start with the first approximation $\beta \gg 1$.

For $\beta \gg 1$, formula 5.43 can be simplified using $\tanh(z) \simeq 1$, considering that $z \gg 1$ on most of the range $[0 : \beta]$:

$$C_{\beta \gg 1}(\omega) = \frac{1}{\beta^2} \text{Im} \left[\int_0^\beta \frac{z^2 f(\omega) dz}{\sqrt{z^2 f(\omega)^2 / 4 + z * f(\omega) + 1}} \right] \quad (5.46)$$

By analytical integration, this yields a $C_{(\beta \gg 1)}(\omega)$ function form suggested previously in Ref.[158]:

$$C_{(\beta \gg 1)}(\omega) = \frac{2}{\beta^2} \text{Im} \left[\frac{4 \text{Ln}[1 + \beta f(\omega)/2]}{f(\omega)^2} - \frac{2\beta}{f(\omega)} \right] \quad (5.47)$$

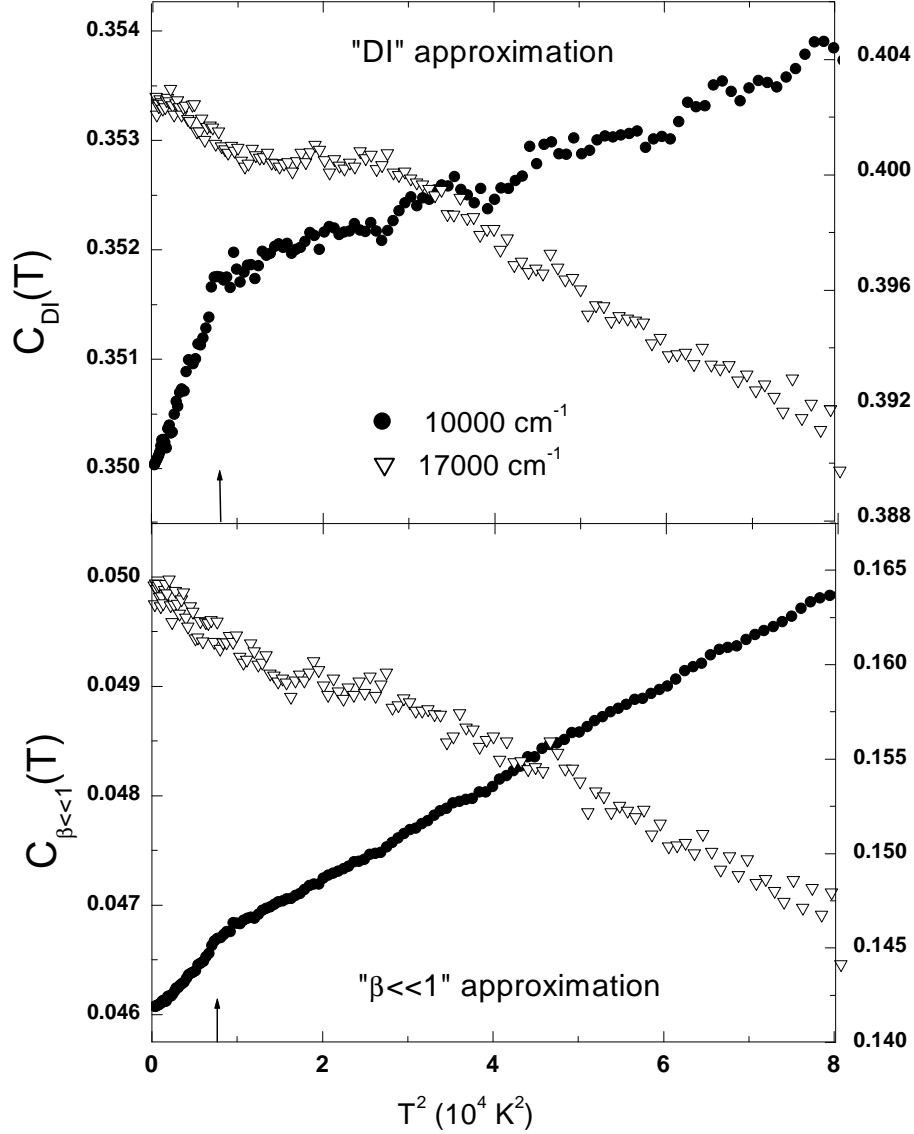


Figure 5.9: The loss function of optimally doped $Bi_2Sr_2CaCu_2O_{8+\delta}$ calculated in the " $\beta \ll 1$ " and "DI" approximations for two selected frequencies. Full symbols refer to the lefthand scale and open symbols to the righthand scale.

with $f(\omega)$ as in 5.44. This function is presented in the Fig. 5.8 as well. Because $k_m s \simeq 18$ in the case of $Bi_2Sr_2CaCu_2O_{8+\delta}$ we can see that it yields almost identical results with the DI approximation formula given in 5.43. Consequently, the Coulomb interaction energy shows the same behavior, as already presented in Fig 5.10.

In the $\beta = k_m s \ll 1$ case, we can write $z < \beta \ll 1$ in 5.43, and $\tanh(z)$ can be then approximated as $\tanh(z) \simeq z$. The formula 5.43 then yields:

$$C_{(\beta \ll 1)}(\omega) = \text{Im} \left[\frac{2h(\omega)}{\beta^3} \int_0^\beta \frac{z^2 dz}{\sqrt{h(\omega)^2 \cdot (z/\beta)^2 + 1}} \right] \quad (5.48)$$

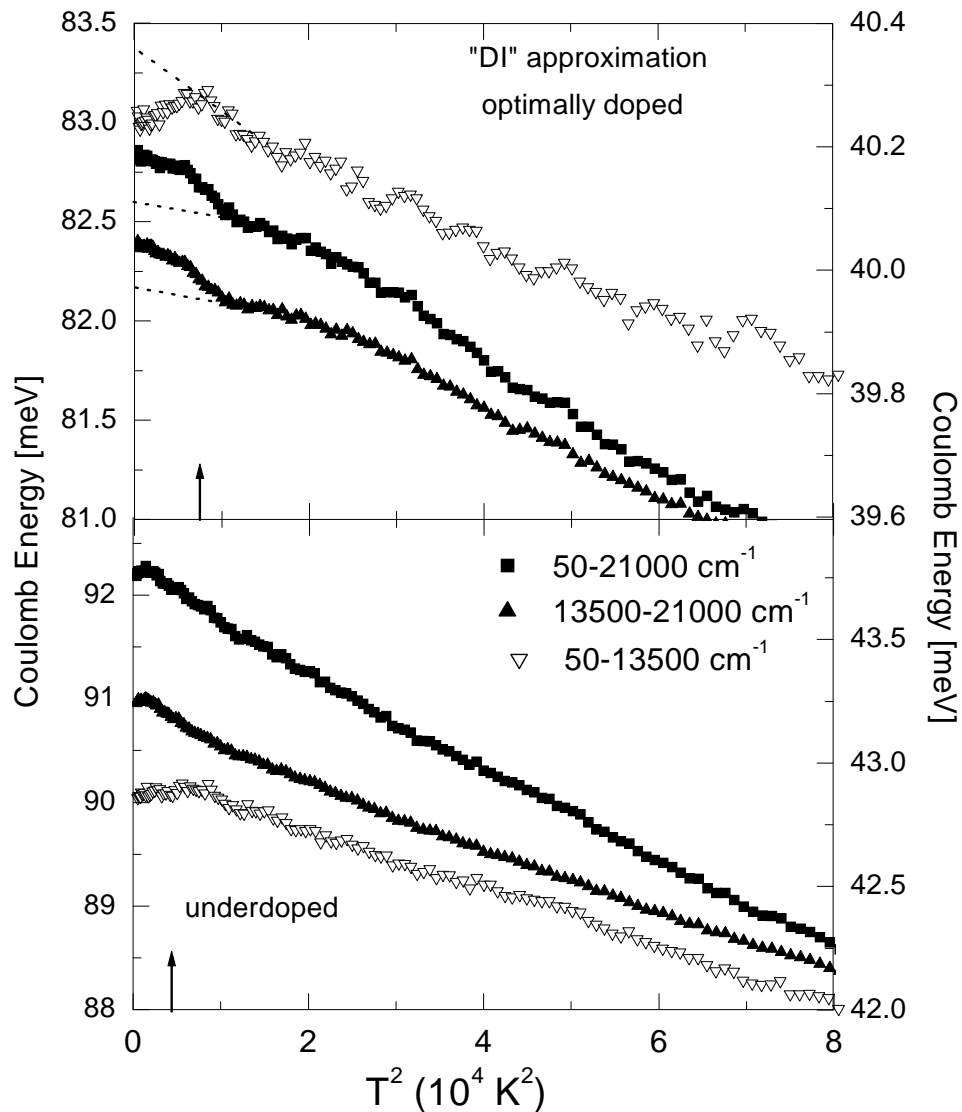


Figure 5.10: Coulomb energy per Cu atoms in the "DI"-direct integration approximation for $Bi_2Sr_2CaCu_2O_{8+\delta}$ calculated for different frequency ranges using formula 5.45. Besides the total measured range, the integration over two other ranges is presented. Full symbols refer to the lefthand scale and open symbols to the righthand scale. The data for the frequency range $13500 - 21000\text{cm}^{-1}$ were rescaled with a constant background to fit the window (39.8 meV for the optimally doped sample and 43.3 meV for the underdoped sample).

where the following definition for $h(\omega)$ was used:

$$h(\omega) = \frac{\beta}{2} \left[\frac{\epsilon_{\parallel}(\omega)}{\epsilon_{sc}} - 1 \right] \sqrt{\frac{\epsilon_{sc}}{\epsilon_{\parallel}(\omega)}} \quad (5.49)$$

Analytically integrating now the equation 5.48, we obtain:

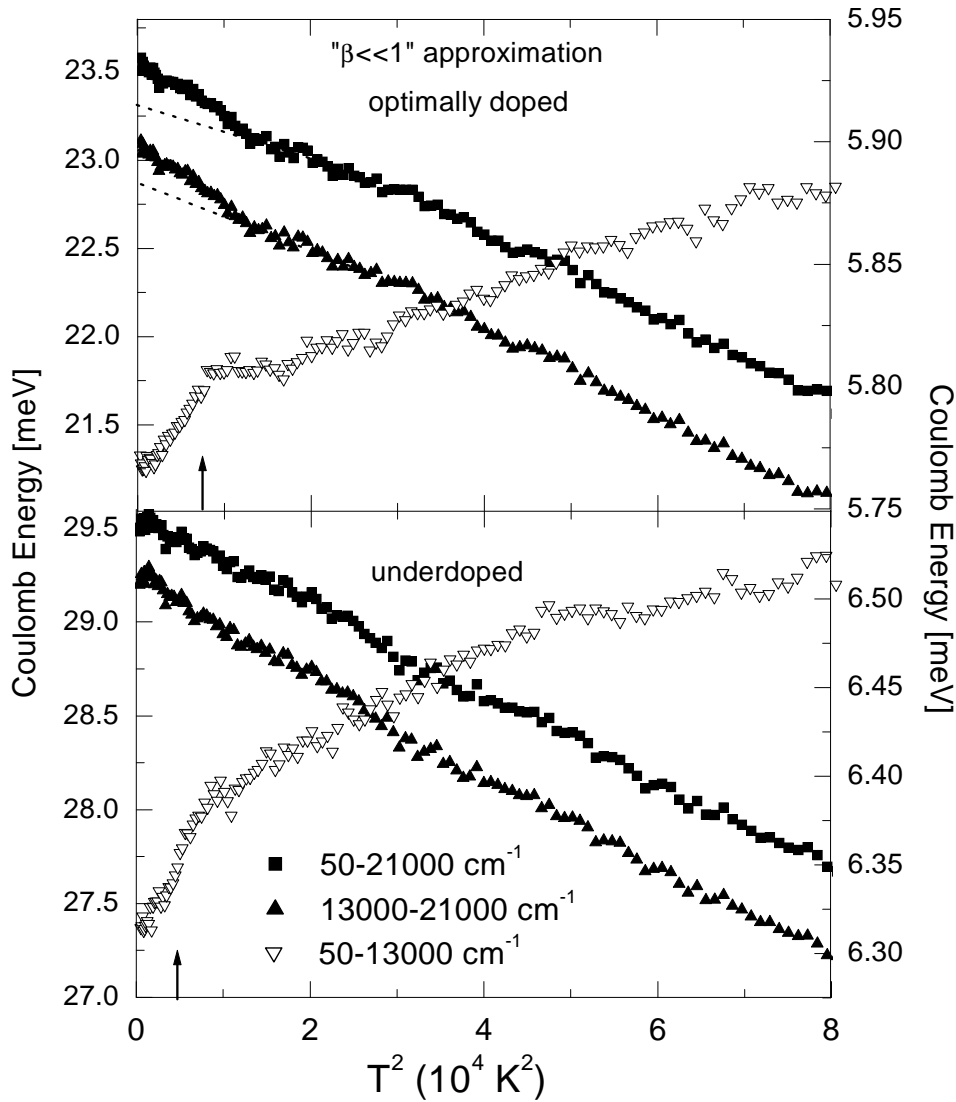


Figure 5.11: Coulomb energy per Cu atoms in the " $\beta \ll 1$ " approximation for $Bi_2Sr_2CaCu_2O_{8+\delta}$. Full symbols refer to the lefthand scale and open symbols to the righthand scale. The data for the frequency range $13000 - 21000 \text{ cm}^{-1}$ were rescaled with a constant background to fit the window (5.3 meV for the optimally doped sample and 6.5 meV for the underdoped sample).

$$C_{(\beta \ll 1)}(\omega) = \text{Im} \left[\frac{\sqrt{1 + h(\omega)^2}}{h(\omega)} - \frac{\text{Ln} [h(\omega) + \sqrt{1 + h(\omega)^2}]}{h(\omega)^2} \right] \quad (5.50)$$

The function $C_{(\beta \ll 1)}(\omega)$ presented in Fig 5.8 gives a smaller value than the one in the "DI"-approximation, with a factor of about 3 in the high frequency range. Its temperature dependence for two selected frequencies 10000 cm^{-1} and 17000 cm^{-1} , plotted in Fig. 5.9, resembles the DI-approximation.

The Coulomb interaction energy in the $\beta \ll 1$ approximation, presented in Fig 5.11,

shows an extra increase in the SC state of about 0.2 meV, when integrating the whole measured range 50 – 21000 for the optimally doped sample. The plot shows also that this increase seems to start at a temperature which is slightly higher than the transition temperature. The underdoped sample does not show obvious changes when entering the SC state. These results must be however treated with caution since, as mentioned above, $\beta = 18$ in case of $Bi_2Sr_2CaCu_2O_{8+\delta}$ and thus the approximation $\beta \ll 1$ may not be appropriate here.

5.8 Pair-correlation functions in the BCS theory

We have seen in the beginning of this chapter (formula 5.12) that, up to a constant factor, the interaction energy can be written as:

$$E_{int} = \sum_k V_k \langle \Psi_0 | \hat{\rho}_k \hat{\rho}_{-k} | \Psi_0 \rangle \quad (5.51)$$

where $\hat{\rho}_k$ is the Fourier transform of the particle density operator, given by the formula 5.11. The interaction potential V_k acts on the valence band electrons, which are considered to be screened by the polarizable ions. Its real space representation is given by the equation Eq. 5.22. The above formula can be rewritten as

$$E_{int} = \sum_k V_k g_k \quad (5.52)$$

if we use the definition of the pair-correlation function:

$$g_k = \langle \Psi_0 | \hat{\rho}_k \hat{\rho}_{-k} | \Psi_0 \rangle \quad (5.53)$$

By using 5.11, one can Fourier transform the above relation and obtain the real space representation of the pair correlation function:

$$g(\mathbf{r}, \mathbf{r}') = \langle \Psi_0 | \hat{n}(\mathbf{r}) \hat{n}(\mathbf{r}') | \Psi_0 \rangle \quad (5.54)$$

The approach above considers the bare electrons of the valence band interacting through the screened potential expressed in Eq. 5.22. The same correlation energy can be however also expressed in terms of the quasiparticles. For example, for a conventional superconductor, one may use the quasi-particles of the normal state Fermi-liquid, which become paired in the superconducting state.

The formula 5.52 then becomes:

$$E_{int} = \sum_k V_k^{qp} g_k^{qp} \quad (5.55)$$

where V_k^{qp} is the interaction between quasi-particles and g_k^{qp} is their pair-correlation function. The above approach may lead to slightly different values of the interaction energies E_{int} , since the quasi-particles do not describe exactly the complete situation, but it would however conserve the main physics involved. The potential V_k^{qp} may change drastically. Even simple RPA-screening replaces the k^{-2} behavior of the bare V_k with a well-behaved function for small k .

The advantage of this approach is that the quasi-particle pair-correlation function may be computed in some cases. For example, the pair-correlation function for the Fermi liquid is [155]:

$$g_k^{ps} = N_e^2 \delta_{k,0} + \sum_p f_p (1 - f_{p+k}) \quad (5.56)$$

In the general BCS approach, one can also compute this pair-correlation function. From the behavior of the observed interaction energy one can then estimate the interaction potential between quasi-particles, knowing the behavior of the pair-correlation function. Consider the difference of the interaction energy in the normal and superconducting state:

$$E_{int}^s - E_{int}^n = \sum_k V_k^{ps} [\langle \Psi_s | \hat{\rho}_k \hat{\rho}_{-k} | \Psi_s \rangle - \langle \Psi_n | \hat{\rho}_k \hat{\rho}_{-k} | \Psi_n \rangle] = \sum_k V_k^{ps} \delta g_k^{ps} \quad (5.57)$$

This equation describes the change in interaction energy when the system prefers the superconducting state $|\Psi_s\rangle$ over the normal one $|\Psi_n\rangle$. The form of the superconducting state $|\Psi_s\rangle$ is known, and it was given in 5.5, namely.

$$|\psi_S\rangle = \prod (u_k + v_k c_{k\uparrow}^* c_{-k\downarrow}^*) |\psi_0\rangle \quad (5.58)$$

In a more general case than the one presented in the introduction, the coefficients are defined as:

$$v_k^2 = \frac{1}{2} \left[1 - \frac{\xi_k}{\sqrt{\Delta_k^2 + \xi_k^2}} \right] = 1 - u_k^2 \quad (5.59)$$

where different forms may be taken for the bandstructure ξ_k and gap Δ_k . The normal state is again defined as the superconducting state with the choice $\Delta = 0$. In Eq. 5.57 we have defined the difference between the pair correlation in the normal and superconducting state, as

$$\delta g_k^{ps} = \langle \Psi_s | \hat{\rho}_k \hat{\rho}_{-k} | \Psi_s \rangle - \langle \Psi_n | \hat{\rho}_k \hat{\rho}_{-k} | \Psi_n \rangle \quad (5.60)$$

This value can now be directly computed, yielding:

$$\delta g_k^{ps} = \sum_p (|u_{p+k}|^2 - \theta_{p+k}) (\theta_p - |u_p|^2) + \sum_p u_{p+k} v_{p+k} u_p^* v_p^* \quad (5.61)$$

where θ_p may be obtained from:

$$\Delta_k = \frac{2\theta_p}{1 - \theta_p^2} \xi_p \quad (5.62)$$

We have chosen to calculate δg_k^{ps} in two cases: a two-dimensional (2D) BCS s-wave superconductor and a 2D BCS d-wave superconductor. The assumed band structure had the same form in both cases:

$$\epsilon_k = \frac{W}{4} [\cos k_x a + \cos k_y a] - \mu \quad (5.63)$$

The order parameter Δ_k has the form

$$\Delta_k = \Delta_0 \Theta(|\epsilon_k - \mu| - \omega_D) \quad (5.64)$$

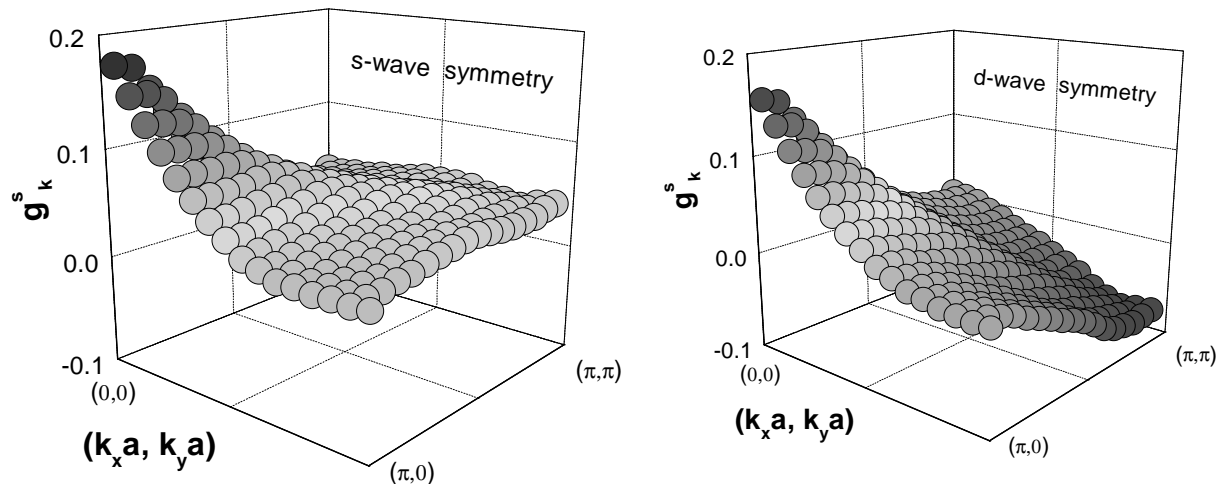


Figure 5.12: The k -space representation of the superconductivity induced change of pair-correlation function δg_k^{ps} for the s-wave (lefthand panel) and d-wave symmetry (righthand panel). Parameters: $\Delta/W = 0.2$, $\omega_D/W = 0.2$. Doping level is $x = 0.25$.

for the 2D s-wave superconductors, and

$$\Delta_k = \Delta_0 [\cos k_x a - \cos k_y a] \Theta(|\epsilon_k - \mu| - \omega_D) \quad (5.65)$$

for the d-wave superconductors.

In Fig.5.12 we present the results. To obtain the plots, we have used $\Delta/W = 0.2$, $\omega_D/W = 0.2$, and $E_F/W = 0.43$. This leads to $x=0.25$ hole doping counted from half filling of the band. To keep this value of the hole doping constant, the chemical potential in the superconducting state was calculated selfconsistently [159–162].

From the lefthand panel of Fig.5.12 we see that the pair correlation function δg_k^{ps} is always positive in the case of s-wave symmetry. Formula 5.55 shows then that the system can lower its interaction energy E_{int} in the superconducting state, if the interaction energy V_k^{ps} is negative (the interaction between the quasi-particles is attractive), at least in some parts of the momentum space \mathbf{k} . This is an expected result for the conventional superconductors having s-wave symmetry.

In Fig. 5.13 we have plotted the spatial representation of the pair-correlation $\delta g_k^{ps}(r-r')$ (see also formula 5.54). From its lefthand panel we see that $\delta g_k^{ps}(r-r')$ reaches its maximum at $r-r'=0$ for s-wave pairing. Thus, in this case, the best interaction which stabilizes the superconducting state by lowering the interaction energy E_{int} , is the on-site attractive potential.

We are however interested more in the case of d-wave superconductors, the case of high temperature superconductors. From the righthand panel of Fig.5.12 we see the pair correlation function δg_k^{ps} is positive near the $(0,0)$ point and negative near the (π,π) point. If the interaction energy would be the one to stabilize the superconducting state, this could take place assuming $V_k > 0$ for k in the (π,π) region, or $V_k < 0$ for k near the origin. The real space representation of $\delta g_k^{ps}(r-r')$, presented in the righthand panel of Fig. 5.13 exhibits a maximum at $(0,1)$ and $(1,0)$. If there would an attractive nearest-neighbor potential V , this would then stabilize the superconducting state through the

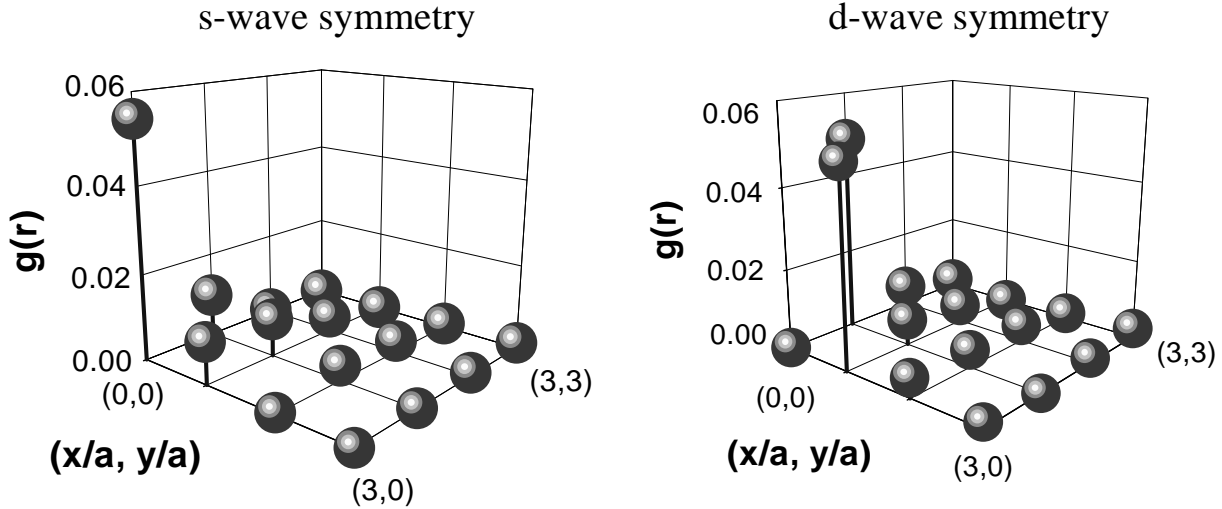


Figure 5.13: The coordinate space representation of the superconductivity induced change of pair-correlation function $\delta g^{ps}(r - r')$ for the s-wave (lefthand panel) and d-wave symmetry (righthand panel). Parameters: $\Delta/W = 0.2$, $\omega_D/W = 0.2$. Doping level: $x = 0.25$

lowering of the interaction energy.

In the previous subsection we have shown that the "k=0" approximation gives the correct behaviour of the Coulomb interaction energy stored in the *center* region of the Brillouin zone. It increases when entering the superconducting state, as shown by the Fig.5.3, and thus the saving of the total energy when entering in the superconducting state cannot come through the $(0,0)$ region of the Brillouin Zone.

From the above calculations, it is still possible that there is a lowering of Coulomb energy given $V_k > 0$ for k in the (π, π) region. The saving of internal energy, when entering the superconducting state, may also come not through a lowering of the Coulomb energy, but of the kinetic energy, as proposed in Ref. [61]. In this case an unconventional pairing mechanism in $Bi_2Sr_2CaCu_2O_{8+\delta}$ is necessary.

5.9 Summary

In this chapter we have experimentally tried to approach the problem of the Coulomb interaction energy of $Bi_2Sr_2CaCu_2O_{8+\delta}$ and its behavior at the superconducting phase transition. Our starting point was formula 5.20, which relates the Coulomb energy to the loss function $Im[-1/\epsilon(\mathbf{k}, \omega)]$. In principle, by measuring its complete momentum dependence, one could directly calculate the Coulomb interaction E_{int} and its temperature dependence.

The formula 5.20 mentioned above is linear in the loss function $Im[-1/\epsilon(\mathbf{k}, \omega)]$, meaning that one has to measure its value in every point of the Brillouin Zone (BZ), and sum up the contributions. Unfortunately, using optical spectroscopy, we have been able to measure carefully the temperature dependence only for the in-plane dielectric function $\epsilon_{\parallel}(\omega) = \epsilon(\omega, k_{\parallel} = k_{\lambda}, q_{\perp} = 0)$, where the momentum k_{\parallel} runs in the in-plane direction, q_{\perp}

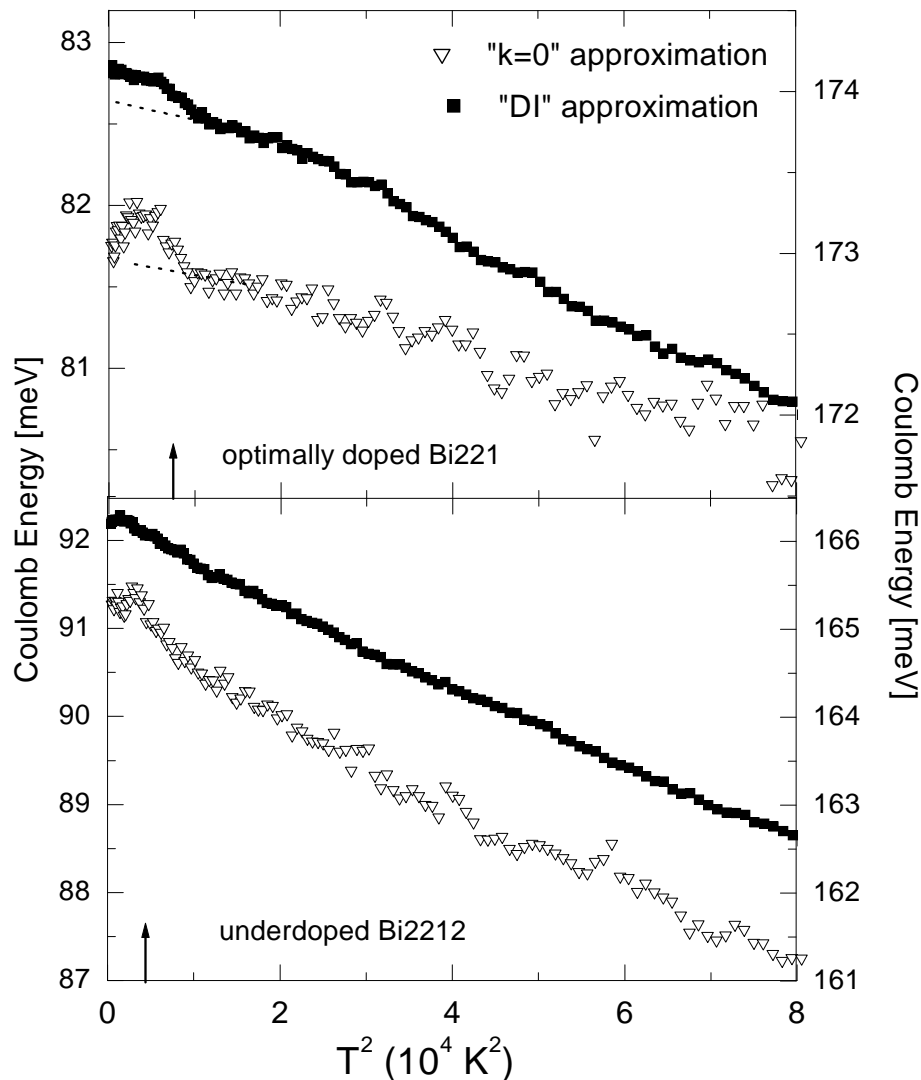


Figure 5.14: Coulomb energy per Cu atoms in the "k = 0" and "DI" approximations for $Bi_2Sr_2CaCu_2O_{8+\delta}$. Full symbols refer to the lefthand scale and open symbols to the righthand scale. The arrows indicate the phase transition temperatures. The integration is done on the whole measured range $50 - 20000\text{cm}^{-1}$.

perpendicular to the planes, and k_λ is the wave vector of light. This leads to a knowledge of the above loss function $Im[-1/\epsilon(\mathbf{k}, \omega)]$ only for a *single* circle of points in the center of the BZ, namely $\mathbf{k} = (k_\parallel = k_\lambda, q_\perp = 0)$.

The behavior of the loss function $Im[-1/\epsilon(\mathbf{k}, \omega)]$ for other points in the center of the BZ, below a certain border of this "center", is expected to be the same as the one given by the measured points $\mathbf{k} = (k_\parallel = k_\lambda, q_\perp = 0)$, because $k_\lambda \simeq 0$. We can thus use the formula 5.20 to sum up all the equal contributions of the loss functions $Im[-1/\epsilon(\mathbf{k}, \omega)] = Im[-1/\epsilon_\parallel(\omega)]$, to get the total Coulomb energy stored in this "center" (basically to multiply with its volume).

The border of the "center" is however difficult to estimate. A value ten times smaller

then the BZ edge would be satisfactory, however it may be underestimated. Due to this problem, we have chosen to sum up the optical loss function $Im[-1/\epsilon(\mathbf{k}, \omega)] = Im[-1/\epsilon_{\parallel}(\omega)]$ in the *whole* BZ, and call this the "k=0" approximation. Thus, the Coulomb energy obtain in this way gives *the same* sign as the one stored in the "center" of the BZ, but the absolute value is only indicative. The advantage of this approach is that, *if* one obtains changes at the superconducting phase transition much larger than the condensation energy, one could conclude safely that the behavior at low momentum is very important, giving thus very probably the correct sign for the total Coulomb energy.

Fig.5.14 summarizes our results for the "k=0" approximation. It shows an extra increase of the Coulomb energy when entering the superconducting state, for both the optimally doped and underdoped $Bi_2Sr_2CaCu_2O_{8+\delta}$ samples, with a value of about 0.2 – 0.3 meV per Cu atom. As mentioned above, this approximation provides the *exact* sign of the change of the Coulomb energy stored *only* in the center of the Brillouin zone, which thus *increases* in the superconducting state. The absolute value is close to the condensation energy of about 0.06-0.25meV per Cu atom [154], being not much larger than that. As discussed above, it cannot give a conclusive answer to which part of the Brillouin zone plays the most important role. It is also not very small, leaving open the possibility that the low momentum part of the BZ plays an important role. We have also shown that the increase of the Coulomb interaction energy in the "k=0" approximation, when entering the superconducting state, is partially reduced by the decrease at very high frequencies in the unmeasured range above 21000cm^{-1} but that it nevertheless it remains an *increase*.

To account better for the layered geometry of $Bi_2Sr_2CaCu_2O_{8+\delta}$ we have used also a different extrapolation for the dielectric function at higher momentum, namely formula 5.42, and denote this approach the "DI" (direct integration) approximation. Its results are also presented in Fig.5.14. Remarkably, in the case of optimally doped samples, it leads to the same sign and value of the Coulomb energy change when entering the superconducting state as the "k=0" approximation. Counted on smaller frequency ranges, the behavior of the two approximations are different, probably due to the shift of the "plasma frequency" of the function $C(\omega)$ (given by Eq. 5.27) from lower values in the "k=0" approximation to higher values in the "DI" approximation (see Fig. 5.8). The behavior in the underdoped samples is not that clear, probably due to changes which starts at higher temperatures than T_c , as suggested also by the plot for the "k=0" approximation.

To conclude, this work shows that the Coulomb interaction energy stored in the *center* of the Brillouin zone, for optimally and underdoped $Bi_2Sr_2CaCu_2O_{8+\delta}$ *increases* when the system enters the superconducting state. It also suggests that this may be the case for the total Coulomb interaction energy, since the absolute values of this increase are comparable with the condensation energy.

Chapter 6

Summary

An optical spectrometer may be unfamiliar to an outsider of the physics community. But in fact, it is a natural evolution of our way of perceiving the environment. Light coming from the sun is scattered by objects. The eye, by receiving this scattered light, gains some information about the objects themselves, such as their color, brightness, and thus shape. In the same way, an optical spectrometer is designed to gain even more information. It has a source to send light on some objects, and a hi-tech detector to measure the reflected light.

After the material is measured, a relation must be established between its optical response and its main physical properties. We consider here the case of solid state materials. These are materials where the atoms are in close proximity to one another, and arranged in repetitive patterns on macroscopic distances, to make the structure as compact as possible (the best know example is NaCl). To establish the above relation, a procedure consisting of two steps is taken. First, for each frequency of the incident light, the optical response of the surface (reflectivity, absorbtion, etc.) is measured. The result is then quantified in the so called dielectric function of the bulk $\epsilon(\omega)$ (*e.g.* some numbers for each frequency). In the second step, this function is further related to the main physical properties of the measured solid state material, through the knowledge of its particular structure, as determined before by a different type of measurement, namely X-ray diffraction. Today, optical spectroscopy became an standard tool of investigating new solid state materials.

The chapters 3 and 4 of this thesis are concentrated on two phases of the same solid state material $\text{Na}_x\text{V}_2\text{O}_5$ (with $x=0..1$). The first phase, namely α' - NaV_2O_5 , presents an interesting transition at the temperature $T_c=35\text{K}$ (which is about -238°C). Part of the electrons responsible for the main physical properties, namely those from the d -shell of vanadium atoms, order in a zig-zag pattern below T_c . The magnitude of this ordering is important in understanding the mechanism behind the ordering process. It can be that those electrons move entirely from the vicinity of one vanadium atom in the vicinity of a different vanadium atom. Or it can be that one electron, being shared equally by two atoms above T_c , will spend, below T_c , more time in proximity of one atom than in the proximity the other, creating thus, on average, a small electron charge distribution.

According to the above scheme, after relating the optical response of α' - NaV_2O_5 to the dielectric function $\epsilon(\omega)$, we have to establish a relation between $\epsilon(\omega)$ and the amount

of electron charge displaced at the phase transition. This relation was deduced from measurements on the related compound α' - $\text{Na}_{1-x}\text{Ca}_x\text{V}_2\text{O}_5$ ($0 \leq x \leq 0.2$). They clearly established that the peak which appears in the optical conductivity spectrum given by $\epsilon(\omega)$ at the energy 0.9 eV (which in frequency is about $2 \cdot 10^{14}$ Hz), is due to a transition between two states of the same electron being shared by only two neighboring vanadium atoms. One state is called bonding energy state and the other anti-bonding state, in analogy with the H_2^+ ionic molecule. We have shown that the energy of this transition, which is thus 0.9 eV, is directly related to the amount of time the electron is shared by one or the other vanadium atom.

By using the above relation, and by measuring the temperature dependence of the energy of the 0.9 eV peak in α' - NaV_2O_5 , we could trace down the amount of charge redistribution at the phase transition. Our measurements showed then that only a small fraction of the electron cloud (namely smaller than 6%) is redistributed at the phase transition.

Our spectroscopic data also provided additional information. For example, a very strong temperature dependence of the intensity of the 0.9 eV peak was observed. After the publication of our results, the effect was explained by theoretical calculations using a so-called t-J-V model, which strongly emphasizes the importance of the interaction between electrons. Also, infrared spectroscopic measurements performed on the α' - $\text{Na}_{1-x}\text{Ca}_x\text{V}_2\text{O}_5$ samples showed their lack of metallicity. This somehow unexpected behavior was related to the sensitivity of one-dimensional systems like α' - NaV_2O_5 to the presence of small additional disorder (introduced by additional atoms like Ca, in α' - $\text{Na}_{1-x}\text{Ca}_x\text{V}_2\text{O}_5$). We think that overall our measurements strongly contributed to a better understanding of the physics involved in the new material α' - NaV_2O_5 , especially to the important problem of the phase transition.

A second phase of the compound $\text{Na}_x\text{V}_2\text{O}_5$ was also investigated, namely β - $\text{Na}_{0.33}\text{V}_2\text{O}_5$. Due to a different sodium concentration, the atoms pack differently in β - $\text{Na}_{0.33}\text{V}_2\text{O}_5$ than in α' - NaV_2O_5 , creating a completely different ordered structure, with different physical properties. Even though the β - $\text{Na}_{0.33}\text{V}_2\text{O}_5$ material has been known for a long time, a crystal with a concentration of sodium atoms close to $x=0.33$ was obtained only very recently. It was shown that it presents interesting physical properties, including a metal to insulator transition at a certain temperature $T_{MI}=136\text{K}$ (which is about -137°C) and superconductivity at even lower temperatures and high pressures.

Our optical spectroscopic study on β - $\text{Na}_{0.33}\text{V}_2\text{O}_5$, described in chapter 4, revealed the main behavior of the electrons when they travel inside the crystal. In this process, they strongly change the positions of the neighboring nuclei, creating a so-called small polaron ("small" because only the nuclei very close to the electron are affected). In addition, a different picture emerged from our optical spectrum (which reveals mainly the charge response of the electrons) than the one in magnetic susceptibility measurements (which gives insight in the behavior of the spins of the electrons). Namely, a gap develops in the optical spectrum below T_{MI} , but not in the magnetic susceptibility. This different behavior of the spin and charge channels at the metal-insulator phase transition, was assigned to a strong interactions between electrons, which does not allow them to be in the proximity of one another.

In addition, our infrared spectroscopic measurements of β - $\text{Na}_{0.33}\text{V}_2\text{O}_5$ revealed the

appearance of a large number of optical phonons below T_{MI} (they can be seen as high frequency vibrations of the nuclei). We think that this is a natural result of the strong coupling between the phonons and electrons. Below the phase transition, the insulating state is a charge ordered phase. Future experiments will have to establish the detailed nature of the charge ordered state.

The last chapter of the thesis presents an optical study of the solid state material $Bi_2Sr_2CaCu_2O_{8+\delta}$. This is called a high temperature superconductor, because below temperatures around $T_c=90K$ ($-183^\circ C$), it conducts electricity without losses. The term "high temperature" denotes a temperature much higher than the one of the previously known superconductors, the so-called classical superconductors, which have transition temperatures of the order of few K. However, this "high temperature" remains well below room temperature $T \simeq 300K$. The hope is that, by understanding the mechanism of superconductivity in $Bi_2Sr_2CaCu_2O_{8+\delta}$, different superconductors may be more efficiently discovered, and finally one may find a material which remains superconducting even at room temperature. However, even though the $Bi_2Sr_2CaCu_2O_{8+\delta}$ superconductors were discovered in the eighties, the understanding of the physical mechanism leading to the superconductivity is lagging behind.

We wanted to attack here a particular physical property of $Bi_2Sr_2CaCu_2O_{8+\delta}$, namely the change in the interaction between electrons at the superconducting phase transition. More precisely, one can quantify this interaction in terms of an *interaction energy*, which in principle is related to the energy necessary to separate all the electrons from one another. A small part of the *interaction energy* changes at the superconducting phase transition, because the electrons reorganize. To measure this change, we started from a general approach previously developed, which relates the *interaction energy* to a general dielectric function, the momentum dependent dielectric function $\epsilon(\mathbf{k}, \omega)$. However, to measure $\epsilon(\mathbf{k}, \omega)$, one has not only to shine light on the surface of the materials, but also to scatter electrons from the crystal at different energies and angles. Today's experimental instruments for measuring $\epsilon(\mathbf{k}, \omega)$ do not provide sufficient resolution for measuring the changes at the phase transition. The optical methods presented here do however have the necessary sensitivity, although they only provide information for a limited range of moments. Thus, they give us only a partial answer.

Our results showed that a part of the *interaction energy* (the one which could be measured with optical spectroscopy, and which is stored in the "optical sector") increases in the superconducting state. Extrapolations have been used to estimate the change, taking into account the particular layered geometry of $Bi_2Sr_2CaCu_2O_{8+\delta}$. They gave a result which is of the order of the condensation energy (if the superconducting state is seen like a golf ball in the hole, the condensation energy is the equivalent of the energy required to pull the ball out of the hole, in other words, the energy required to destroy the superconducting state).

In the classical superconductors, the superconducting state appears because at low temperatures an additional attractive interaction appears between electrons. This is quantified in a lowering of *interaction energy*. Our study for $Bi_2Sr_2CaCu_2O_{8+\delta}$ suggests that this interaction energy *increases* on going into the superconducting state (in other words the electrons repel each other more strongly) and it can thus not provide the mechanism which drives the system superconducting. Even though our study is only indicative with

respect to the *total interaction energy*, it puts some bounds on the further theoretical models, since they would have to be able to explain the increase of the *interaction energy* stored in the "optical sector", as measured by us.

Bibliography

- [1] Y. Ren et. al. *Nature*, 1998:441, 1978.
- [2] G. C. Xiong et al. *Appl. Phys. Lett.*, 66:1427, 1995.
- [3] P.W.Anderson. *The Theory of Superconductivity in the High-Tc Cuprates*. Princeton Univ. Press, 1997.
- [4] J. Galy. *J. Solid State Chem.*, 100:229, 1992.
- [5] J.L.Atwood. *Nature Materials*, 1:91, 2002.
- [6] M. Isobe and Y. Ueda. *J. Phys. Soc. Jpn.*, 65:1178, 1996.
- [7] D.M.Haldane. *Phys. Lett. A*, 93:464, 1983.
- [8] A. Meetsma et. al. *Acta Cryst. C*, 54:1558, 1998.
- [9] H. G. von Schnering et. al. *Z. Kristallogr.*, 213:246, 1998.
- [10] H. Smolinski et. al. *Phys. Rev. Lett.*, 80:5164, 1998.
- [11] M. Mostovoy and D. Khomskii. *Solid State Comm.*, 113:159, 1999.
- [12] L.Hozoi, C.Presura, C. de Graaf, and R.Broer. to be published.
- [13] A. Damascelli et. al. *Phys. Rev. Lett.*, 81:918, 1998.
- [14] S. Golubchik et. al. *J. Phys. Soc. Jpn.*, 66:4042, 1997.
- [15] A.D. Wadsley. *Acta Cryst.*, 8:695, 1955.
- [16] H. Kobayashi. *Bull. Chem. Soc. Japan*, 52:1315, 1979.
- [17] H. Yamada and Y. Ueda. *J. Phys. Soc. Jpn.*, 68:2735, 1999.
- [18] Jun-Ichi Yamaura, M.Isobe, H.Yamada, T.Yamauchi, and Y.Ueda. to appear in *J. Phys. Chem Solids* (2002).
- [19] A. N. Vasil'ev, I. Marchenko, A. I. Smirnov, S. S. Sosin, P. L. Kapitza, H. Yamada, and Y. Ueda. *Phys. Rev. B*, 64:174403, 2001.
- [20] Y.Ueda, H.Yamada, M.Isobe, and T.Yamauchi. *J.Alloys and Compounds*, 317-318:109, 2001.
- [21] T. Yamauchi, Y. Ueda, and N. Môri. unpublished.
- [22] N.F. Mott. *Metal-insulator transitions*. Taylor and Francis, London, 1974.
- [23] B.K. Chakraverty, M.J. Sienko, and J. Bonnerot. *Phys. Rev. B*, 17:3781, 1978.
- [24] D.Esteve et al. *Europhys. Lett.*, 3:1237, 1987.

- [25] C.E.Gough et al. *Nature*, 326:855, 1987.
- [26] Z. Hussain A. Damascelli, Z.-X. Shen. *Reviews of Modern Physics*, in press.
- [27] V.J.Emery and S.A.Kivelson. *Phys. Rev. Lett.*, 74:3253, 1995.
- [28] R.W.Hill, C.Proust, L.Taillefer, P.Fournier, and R.L.Green. *Nature*, 414:711, 2001.
- [29] A.G.Loesser et. al. *Phys. Rev. B*, 56:14185, 1997.
- [30] Philip B. Allen. *Nature*, 412:494, 2001.
- [31] E.W.Carlson, V.J.Emery, S.A.Kivelson, and D.Orgad. cond-mat/0206217.
- [32] A.Lanzara et. al. *Nature*, 412:510, 2001.
- [33] J. Carbotte, E.Schachinger, and D.Basov. *Nature*, 401:354, 1999.
- [34] Joe Orenstein. *Nature*, 401:333, 1999.
- [35] N.K.Sato et. al. *Nature*, 410:340, 2001.
- [36] Piers Coleman. *Nature*, 410:320, 2001.
- [37] S.S. Saxena. *Nature*, 406:587, 2000.
- [38] D. J. Scalapino, J. E. Loh, and J. E. Hirsch. *Phys. Rev. B*, 34:8190, 1986.
- [39] R.Kirtley et. al. *Nature*, 373:225, 1995.
- [40] Z.-X. Shen et al. *Phys. Rev. Lett.*, 70:1553, 1993.
- [41] J.Zaanen and O.Gunnarsson. *Phys. Rev. B*, 40:7391, 1989.
- [42] J.M.Tranquada et. al. *Nature*, 375:561, 1995.
- [43] R.P.Sharma. *Nature*, 404:736, 2000.
- [44] H.A.Mook et. al. *Nature*, 404:729, 2000.
- [45] S.Alexandrov and N.F.Mott. *High Temperature Superconductors and Other Superfluids*. Taylor and Francis, London, 1994.
- [46] D. Basov, H. A. Mook, B. Dabrowski, and T. Timusk. *Phys. Rev. B*, 52:R13141, 1995.
- [47] A. Puchkov, D. N. Basov, and T. Timusk. *J.Phys Cond. Matt.*, 8:10049, 1996.
- [48] T. Timusk and B.Statt. *Reports on Progress in Physics*, 62:61, 1999.
- [49] J.M.Wheatley, T.C.Hsu, and P.W.Anderson. *Phys. Rev. B*, 37:5897, 1988.
- [50] K.A.Moler, J.R.Kirtley, D.G.Hinks, T.W.Li, and M.Xu. *Science*, 279:1193, 1998.

- [51] A.A. Tsvetkov et al. *Nature*, 395:360, 1998.
- [52] P.W. Anderson. *Science*, 235:1196, 1987.
- [53] F.C.Zhang and T.M.Rice. *Phys. Rev. B*, 37:3759, 1988.
- [54] P.W.Anderson. *Science*, 288:480, 2000.
- [55] D.A.Bonn et.al. *Nature*, 414:887, 2001.
- [56] S.C. Zhang. *Science*, 275:1089, 1997.
- [57] P.A.Lee. *Physica C*, 317:194, 1999.
- [58] P.W.Anderson. *Physica C*, 341-348:9, 2000.
- [59] V.J.Emery and S.A.Kivelson. *J. Phys. Chem. Solids*, 61:467, 2000.
- [60] J.E. Hirsch. *Physica C*, 201:347, 1992.
- [61] H.J.A. Molegraaf, C.Presura, D. van der Marel, P.H. Kes, and M.Li. *Science*, 295:2239, 2002.
- [62] A.F.Santander-Syro, R.P.S.M. Lobo, N.Bontemps, H.R.Z.Konstantinovic, and Z.Li. *Phys. Rev. Lett.*, 88:097005, 2002.
- [63] A.J.Leggett. *Proc. Natl. Acad. Sci. USA*, 96:8365, 1999.
- [64] P.Nozieres and D. Pines. *Phys. Rev.*, 113:1254, 1959.
- [65] S. Hecht, S. Schlaer, and M.H. Pirenne. *Journal of the Optical Society of America*, 38:196, 1942.
- [66] D.A. Baylor, T.D. Lamb, and K.W. Yau. *Journal of Physiology*, 288:613, 1979.
- [67] Karl von Frisch. *The Dance Language and Orientation of Bees*. Harvard University Press, 1967.
- [68] T. Ramskou. Solstenen. *Skalk*, 2:16, 1967.
- [69] R.M.A. Azzam and N.M. Bashara. *Ellipsometry and Polarized Light*. North-Holland Publ. Co., Amsterdam, 1997.
- [70] Charles Kittel. *Introduction to solid state physics*. Wiley, New York, 1996.
- [71] D.M.Borsa, S.Grachev, C.Presura, and D.O.Boerma. *Applied Physics Letter*, 80:1823, 2002.
- [72] P. G. Steeneken, L. H. Tjeng, I. Elfimov, G. A. Sawatzky, G. Ghiringhelli, N. B. Brookes, and D.J. Huang. *Phys. Rev. Lett.*, 88:47201, 2002.
- [73] A.B. Kuz'menko, D. van der Marel, P.J.M. van Bentum, E.A.Tishchenko, C.Presura, and A.A.Bush. *Phys. Rev. B*, 63:94303, 2001.

- [74] A.B.Kuz'menko, E.A.Tishchenko, and V.G.Orlov. *J. Phys. Cond. Matter*, 8:6199, 1996.
- [75] WVase32 Experimental Handbook. *Guide to Using WVase32*. J.A. Woolam Co. Inc.
- [76] L.Hozoi, A.H. de Vries, A.B. van Oosten, and R. Broer. *Phys. Rev. Lett.*, 89:076407, 2002.
- [77] A. Carpy and J.Galy. *Acta Crystallogr. Sect. B*, 31:1481, 1975.
- [78] L.N. Bulaevskii, A.I.Buzdin, and D.I. Khomskii. *Solid State Comm.*, 27:5, 1978.
- [79] M.C.Cross. *Phys. Rev. B*, 20:4606, 1979.
- [80] D.C. Johnston, R.K.Kremer, M.Troyer, X.Wang, A.Klumper, S.L.Budko, A.F.Panchula, and P.C.Canfield. *Phys. Rev. B*, 61:9558, 2000.
- [81] J. Ludecke et. al. *Phys. Rev. Lett.*, 82:3633, 1999.
- [82] A.Bernert, T.Chatterji, P.Thalmier, and P.Fulde. *Eur. Phys. Journal B*, 21:535, 2001.
- [83] B. Buechner. private communications.
- [84] T. Ohama et. al. *Phys. Rev. B*, 59:3299, 1999.
- [85] M. Mostovoy, D. Khomskii, and J.Knoester. *Phys. Rev. B*, 65:064412, 2002.
- [86] M. Lohmann, H.A. Krug von Nidda, M.V.Eremin, A.Loidl, G.Obermeier, and S.Horn. *Phys. Rev. Lett.*, 85:1742, 2000.
- [87] M. Poirier, P.Fertey, J.Jegoudez, and A.Revcolevschi. *Phys. Rev. B*, 60:7341, 1999.
- [88] T. Ohama, A.Goto, T.Shimizu, E.Ninomiya, H.Sawa, M.Isobe, and Y.Ueda. *J. Phys. Soc. Jpn.*, 69:2751, 2000.
- [89] C. Presura, D. van der Marel, M. Dischner, C. Geibel, and R.K. Kremer. *Phys. Rev. B*, 62:16522, 2000.
- [90] C.Presura, D. van der Marel, A.Damascelli, and R.K.Kremer. *Phys. Rev. B*, 61:15762, 2000.
- [91] M. J. Konstantinović, Z.V.Popović, V.V. Moshchalkov, C.Presura, R.Gajic, M.Isobe, and Y.Ueda. *Phys. Rev. B*, 65:245103, 2002.
- [92] D.E. Aspnes. *J. Opt. Soc. Am.*, 70:1275, 1980.
- [93] M. Konstantinović et. al. *Phys. Stat. Sol.(b)*, 211:R3, 1999.
- [94] D. Smirnov et. al. *Physica B*, 259:992, 1999.

- [95] K. Kobayashi et. al. *Phys. Rev. Lett.*, 80:3121, 1998.
- [96] P. Horsch and F. Mack. *Eur. Phys. J. B*, 5:367, 1998.
- [97] M. Cuoco, P. Horsch, and F. Mack. *Phys. Rev. B*, 60:R8438, 1999.
- [98] V.C. Long et. al. *Phys. Rev. B*, 60:15721, 1999.
- [99] N. Kenny et. al. *J. Phys. Chem. Solids*, 27:1237, 1966.
- [100] S.Atzkern, M.Knupfer, M.S.Golden, J.Fink, A.N.Yaresko, V.N.Antonov, A.Hubsch, C.Waidacher, K.W.Becker, W. von der Linden, G.Obermeier, and S.Horn. *Phys. Rev. B*, 63:165113, 2001.
- [101] A.Hubsch, C.Waidacher, K.W.Becker, and W. von der Linden. *Phys. Rev. B*, 64:075107, 2002.
- [102] N. Suaud and M.B. Lepetit. *Phys. Rev. Lett.*, 88:056405, 2002.
- [103] M. Aichhorn, P.Horsch, W.von der Linden, and Mario Cuoco. *Phys. Rev. B*, 65:201101, 2002.
- [104] J. Hemberger et. al. *Europhys. Lett.*, 42:661, 1998.
- [105] M. Lohmann et. al. *Solid State Comm.*, 104:649, 1997.
- [106] T. Yosihama et al. *J. Phys. Soc. Jpn.*, 67:744, 1998.
- [107] M.Weiden et al. *Z. Phys. B: Condens. Matter*, 103:1, 1997.
- [108] J. Riera and D. Poilblanc. *Phys. Rev. B*, 59:2667, 1999.
- [109] J.L. de Boer, A. Meetsma, J. Baas, and T.T.M. Palstra. *Phys. Rev. Lett.*, 84:3962, 2000.
- [110] B.Grenier, O.Cepas, L.P.Regnault, J.E.Lorenzo, T.Ziman, J.P. Boucher, A.Hiess, T.Chatterji, and J.Jegoudez. *Phys. Rev. Lett.*, 86:5966, 2001.
- [111] P.W. Anderson. *Phys. Rev.*, 109:1492, 1958.
- [112] Z.V.Popovic, M.J.Konstantinovic, R.Gajic, V.N. Popov, M.Isobe, Y.Ueda, and V.V.Moshchalkov. *Phys. Rev. B*, 65:184303, 2002.
- [113] M. Isobe and Y. Ueda. *Journal of Magnetism and Magnetic Materials*, 177:671, 1998.
- [114] J.C. Parker, D.J.Lam, Y.-N.Xu, and W.Y.Ching. *Phys. Rev. B*, 42:5289, 1990.
- [115] V.G. Mokerov, V.L. Makarov, V.B. Tulvinskii, and A.R. Begishev. *Opt.Spectrosc.*, 40:58, 1976.

- [116] N.I. Lakuzova, V.A. Gubanov, and V.G. Mokerov. *International Journal of Quantum Chemistry*, XII:912, 1977.
- [117] D. Emin. *Phys. Rev. B*, 48:13691, 1993.
- [118] L. Degiorgi, P. Wachter, and C.Schlenker. *Physica B*, 164:305, 1990.
- [119] W.A.Challenor and P.L.Richards. *Solid State Comm.*, 52:117, 1984.
- [120] G.Travaglini and P.Wachter. *Phys. Rev. B*, 30:1971, 1984.
- [121] L.Degiorgi and G.Gruner. *Phys. Rev. B*, 44:7820, 1991.
- [122] T.Yamamoto, H.Tajima, J.I. Yamaura, S.Aonuma, and R.Kato. *J. Phys. Soc. Jpn.*, 68:1384, 1999.
- [123] H. Tajima. *Solid State Comm.*, 113:279, 2000.
- [124] L.Degiorgi, P.Wachter, and D.Ihle. *Phys. Rev. B*, 35:9259, 1987.
- [125] R.M.Fye, M.J.Martins, and D.J.Scalapino. *Phys. Rev. B*, 45:7311, 1991.
- [126] H.J.Schultz. *Phys. Rev. Lett.*, 64:2831, 1990.
- [127] M.Itoh, N.Akimito, H.Yamada, M.Isobe, and Y.Ueda. *J. Phys. Soc. Jpn.*, Suppl.B 69:155, 2000.
- [128] M.J.Rice, L.Pietronero, and P.Bruesch. *Solid State Comm.*, 21:757, 1977.
- [129] B.K. Chakraverty. *Phil. Mag.*, B 42:473, 1980.
- [130] S.K.Park, T.Ishikawa, and Y.Tokura. *Phys. Rev. B*, 58:3717, 1998.
- [131] K.Maruyama and H.Nagasawa. *J. Phys. Soc. Jpn.*, 48:2159, 1980.
- [132] J.B. Goodenough. *J. Sol. St. Chem*, 1:349, 1970.
- [133] M.Onoda, T.Takahashi, and H.Nagasawa. *J. Phys. Soc. Jpn.*, 51:3868, 1982.
- [134] M.Onoda, T.Takahashi, and H.Nagasawa. *Phys. Stat.Sol. (b)*, 109:793, 1982.
- [135] T. Erata, T.Takahashi, and H.Nagasawa. *Solid State Comm.*, 39:321, 1981.
- [136] G. Obermeier, D. Ciesla, S. Klimm, and S. Horn. cond-mat/0203234.
- [137] Y. Kanai, S. Kagoshima, and H. Nagasawa. *J. Phys. Soc. Jpn.*, 51:697, 1987.
- [138] D. Kaplan and A. Zylbersztein. *J. de Physique*, 37:L-123, 1976.
- [139] T.Giamarchi. *Physica B*, 230-232:975, 1997.
- [140] H. Pen. *Ph.D. Thesis*. Rijksuniversiteit Groningen, Groningen, 1997.

- [141] R.M.Fye, M.J.Martins, D.J.Scalapino, J.Wagner, and W.Hanke. *Phys. Rev. B*, 44:6909, 1991.
- [142] M. Tinkham. *Introduction to superconductivity*. McGraw-Hill Inc., 1996.
- [143] Ph. Durand, I. Páidarova, and F.X. Gadea. *Journal of Physics B*, 34:1953, 2001.
- [144] S.C. Zhang, S. Kivelson, and A.S. Goldhaber. *Phys. Rev. Lett.*, 58:2134, 1987.
- [145] V.Vescoli, L.Degiori, W.Henderson, G.Gruner, K.P.Starkey, and L.K.Montgomery. *Science*, 281:1181, 1998.
- [146] M. Ogata and H. Shiba. *Phys. Rev. B*, 41:2326, 1990.
- [147] M. Gruninger, D. van der Marel, A. Damascelli, A. Zibold, H. P. Geserich, A. Erb, M. Klawns, Th. Wolf, T. Nunner, and T.Kopp. *Physica C*, 317-318:286, 1999.
- [148] J.Bardeen, L.N.Cooper, and J.R.Schrieffer. *Phys. Rev.*, 108:1175, 1957.
- [149] C.Kittel. *Quantum Theory of Solids*. John Wiley Sons, London, 1963.
- [150] P.G. de Gennes. *Superconductivity in Metals and Alloys*. Addison-Wesley, New York, 1966.
- [151] M.Apostol. *Z.Physik*, 22:13, 1975.
- [152] A.K.Rajagopal and J.C. Kimball. *Phys. Rev. B*, 15:2819, 1977.
- [153] W.Hanke and L.J. Sham. *Phys. Rev. B*, 12:4501, 1975.
- [154] J.W. Loram, J.Luo, J.R.Cooper, W.Y.Liang, and J.L Tallon. *J. Phys. Chem. Solids*, 62:59, 2001.
- [155] G.D. Mahan. *Many-Particle Physics*. Plenum Press, New York, 1990.
- [156] D. van der Marel. lecture notes,
<http://vsf1.phys.rug.nl/~wwwopt/Publications/trieste2000.pdf>.
- [157] A.L.Fetter. *Annals of Physics*, 88:1, 1974.
- [158] A.J.Leggett. *J. Phys. Chem. Solids*, 59:1729, 1998.
- [159] D. van der Marel. *Physica C*, 165:34, 1990.
- [160] D. van der Marel and G. Rietveld. *Phys. Rev. Lett.*, 69:2575, 1992.
- [161] D. van der Marel G. Rietveld, N. Y. Chen. *Phys. Rev. Lett.*, 69:2578, 1992.
- [162] D. I. Khomskii D. van der Marel and G.M. Eliashberg. *Phys. Rev. B*, 50:16594, 1994.

Samenvatting

Een optische spectrometer is wellicht onbekend voor een buitenstaander van de fysische gemeenschap. Maar in feite is het een natuurlijk gevolg van de manier waarop we naar onze omgeving kijken. Licht dat van de zon komt wordt weerkaatst door objecten. Het oog verkrijgt, door dit weerkaatste licht op te vangen, informatie over het object zelf, zoals de kleur, helderheid en derhalve vorm. Een optische spectrometer is op dezelfde manier ontwikkeld om zelfs nog meer informatie te verkrijgen. Het heeft een lichtbron om licht op objecten te laten schijnen en een hi-tech detector om het gereflecteerde licht te meten.

Nadat een materiaal is gemeten moet een relatie gelegd worden tussen de optische respons en de belangrijkste fysische eigenschappen. We behandelen hier de vaste stoffen, waarin de atomen dicht bij elkaar zitten en georganiseerd zijn in herhaalde patronen op microscopische schaal, om de structuur zo compact mogelijk te maken (het best bekende voorbeeld is keukenzout, NaCl). Om de bovengenoemde relatie vast te kunnen leggen wordt een tweestaps procedure gevolgd. Als eerste wordt voor iedere frequentie van het invallende licht de optische respons (reflectiviteit, absorptie, etc.) van het oppervlak gemeten. Het resultaat wordt dan gekwantificeerd in de zogenaamde dielectrische functie van het systeem $\epsilon(\omega)$ (wat getallen voor iedere frequentie). In de tweede stap wordt deze functie verder gerelateerd aan de belangrijkste fysische eigenschappen van het gemeten materiaal, gebruik makend van de kennis van de specifieke structuur, zoals gemeten door middel van een ander type metingen, namelijk X-ray diffractie. Hedentendage is optische spectroscopie geworden tot een standaard methode om nieuwe vaste stoffen te onderzoeken.

Hoofdstukken 3 en 4 van dit proefschrift zijn geconcentreerd rond twee fasen van hetzelfde materiaal $\text{Na}_x\text{V}_2\text{O}_5$ (met $x=0..1$). De eerste fase, namelijk α' - NaV_2O_5 , heeft een interessante overgang bij een temperatuur van $T_c=35\text{K}$ (rond -238°C). Een deel van de elektronen die verantwoordelijk zijn voor de belangrijkste fysische eigenschappen, namelijk die van de d -schil van de vanadium atomen, rangschikken zich in een zig-zag patroon beneden T_c . De mate van deze rangschikking is belangrijk voor het verkrijgen van een begrip van het mechanisme van dit rangschikkingsproces. Het kan zijn dat deze elektronen volledig van de nabijheid van het ene vanadium atoom naar de nabijheid van een ander vanadium atoom bewegen. Of het kan zijn dat een elektron boven T_c gelijk gedeeld wordt door twee atomen, terwijl het beneden T_c meer tijd doorbrengt in de nabijheid van het ene atoom dan van het andere, en daarmee dus, gemiddeld, een kleine ladingsdistributie creëert.

Volgens bovenstaand schema, na de optische respons van α' - NaV_2O_5 gerelateerd te hebben aan de dielectrische functie $\epsilon(\omega)$, moeten we een relatie vinden tussen $\epsilon(\omega)$ en de hoeveelheid verplaatste elektron lading tijdens de faseovergang. Deze relatie werd

verkregen uit metingen aan het gerelateerde materiaal α' - $\text{Na}_{1-x}\text{Ca}_x\text{V}_2\text{O}_5$ ($0 \leq x \leq 0.2$). Deze metingen lieten duidelijk zien dat de piek die verschijnt in het optische conductiviteits spectrum, gegeven door $\epsilon(\omega)$ bij een energie van 0.9 eV (wat in frequentie ongeveer $2 \cdot 10^{14}$ Hz is), veroorzaakt wordt door een overgang tussen twee toestanden van hetzelfde elektron dat door slechts twee naast elkaar gelegen vanadium atomen gedeeld wordt. De ene toestand wordt bindings toestand genoemd en de andere anti-bindings toestand, analoog aan het H_2^+ molecuul. We hebben aangetoond dat de energie van deze overgang, die dus 0.9 eV is, direkt gerelateerd is aan de hoeveelheid tijd die het elektron deelt met het ene of het andere vanadium atoom.

Door de bovengenoemde relatie te gebruiken, en door de temperatuursafhankelijkheid van de energie van de 0.9 eV piek in α' - NaV_2O_5 te meten, konden we de mate van herverdeling van de lading bij de faseovergang bepalen. Onze metingen hebben aangetoond dat slechts een klein gedeelte van de elektronwolk (namelijk minder dan 6%) herverdeeld wordt bij de faseovergang.

Onze spectroscopische data heeft nog meer informatie opgeleverd. Er is bijvoorbeeld een hele sterke temperatuursafhankelijkheid van de intensiteit van de 0.9 eV piek gezien. Na de publicatie van onze resultaten werd dit effect verklaard met theoretische berekeningen aan een zogenaamd t-J-V model, wat het belang van de interacties tussen de elektronen sterk benadrukt. Tevens lieten infrarood spectroscopische metingen aan de α' - $\text{Na}_{1-x}\text{Ca}_x\text{V}_2\text{O}_5$ monsters een gemis aan metaalachtigheid zien. Dit wat onverwacht resultaat was verbonden met de gevoeligheid van één-dimensionale systemen zoals α' - NaV_2O_5 voor de aanwezigheid van een lichte mate van wanorde (veroorzaakt door extra atomen als Ca in α' - $\text{Na}_{1-x}\text{Ca}_x\text{V}_2\text{O}_5$). Al met al denken we dat onze metingen in belangrijke mate hebben bijgedragen aan een beter begrip van de fysica die een rol speelt in het nieuwe materiaal α' - NaV_2O_5 , en in het bijzonder aan het belangrijke probleem van de faseovergang.

Een tweede fase van het materiaal $\text{Na}_x\text{V}_2\text{O}_5$ is ook onderzocht, namelijk β - $\text{Na}_{0.33}\text{V}_2\text{O}_5$. Ten gevolge van een andere sodium concentratie stapelen de atomen zich anders in β - $\text{Na}_{0.33}\text{V}_2\text{O}_5$ dan in α' - NaV_2O_5 en creëren daarmee een totaal andere geordende structuur, met andere fysische eigenschappen. Hoewel het β - $\text{Na}_{0.33}\text{V}_2\text{O}_5$ materiaal al lange tijd bekend is, is een kristal met een concentratie van natrium atomen dicht bij $x=0.33$ pas zeer recent beschikbaar gekomen. Aangetoond is dat het interessante fysische eigenschappen heeft, waaronder een metaal-isolator overgang bij een temperatuur $T_{MI}=136\text{K}$ (rond de -137°C) en supergeleiding bij lagere temperaturen en hogere drukken.

Ons optische spectroscopie onderzoek aan β - $\text{Na}_{0.33}\text{V}_2\text{O}_5$, beschreven in hoofdstuk 4, openbaarde het belangrijkste gedrag van de elektronen wanneer ze in het materiaal voortbewegen. In dit proces veranderen ze sterk de positie van de nabijgelegen kernen en creëren daarbij een zogenaamd klein polaron ("klein" omdat alleen de kernen dicht bij het elektron worden beïnvloed). Daarnaast kwam van ons optisch spectrum (wat voornamelijk de ladingsrespons van de elektronen weergeeft) een ander beeld naar voren dan van magnetische susceptibiliteits metingen (die inzicht geven in het gedrag van de spins van de elektronen). Beneden T_{MI} opent zich namelijk een 'gap' in het optisch spectrum, maar niet in de magnetische susceptibiliteit. Dit verschillend gedrag van de spin- en ladingskanalen bij de metaal-isolator faseovergang werd toegeschreven aan sterke wisselwerking tussen de elektronen, waardoor de elektronen niet dicht bij elkaar kunnen zijn.

Daarnaast lieten onze infrarood spectroscopische metingen van $\beta\text{-Na}_{0.33}\text{V}_2\text{O}_5$ een groot aantal optische fononen zien beneden T_{MI} (ze kunnen gezien worden als hoog frequente vibraties van de kernen). We denken dat dit een logisch gevolg is van de sterke koppeling tussen de fononen en de elektronen. Beneden de faseovergang is de isolerende fase een ladings geordende fase. Toekomstige experimenten zullen de gedetailleerde structuur van de ladings geordende toestand moeten blootleggen.

Het laatste hoofdstuk van dit proefschrift presenteert een optische studie van het materiaal $\text{Bi}_2\text{Sr}_2\text{CaCu}_2\text{O}_{8+\delta}$. Dit wordt een hoge temperatuur supergeleider genoemd omdat beneden een temperatuur van rond $T_c=90\text{K}$ (-183°C) het elektriciteit geleid zonder energieverlies. De term “hoge temperatuur” slaat op de kritische temperatuur T_c die veel hoger is dan de voorheen bekende supergeleiders, de zogenaamde klassieke supergeleiders, die een overgangstemperatuur hebben van de grootte van enkele K. Echter, deze “hoge temperatuur” blijft nog steeds ruimschoots onder kamertemperatuur, $T \simeq 300\text{K}$. De hoop is dat, door het mechanisme van supergeleiding te begrijpen in $\text{Bi}_2\text{Sr}_2\text{CaCu}_2\text{O}_{8+\delta}$, andere supergeleiders makkelijker gevonden kunnen worden en wellicht vindt men uiteindelijk een materiaal dat zelfs bij kamertemperatuur supergeleidend blijft. Hoewel de $\text{Bi}_2\text{Sr}_2\text{CaCu}_2\text{O}_{8+\delta}$ supergeleiders in de jaren tachtig ontdekt zijn, ligt het begrip van het fysische mechanisme van supergeleiding hierop achter.

We wilden een speciale fysische eigenschap van $\text{Bi}_2\text{Sr}_2\text{CaCu}_2\text{O}_{8+\delta}$ onder de loep nemen, namelijk de verandering van wisselwerking tussen de elektronen bij de supergeleidende faseovergang. Men kan in deze wisselwerking kwantificeren in termen van een *interactie energie*, die in principe gerelateerd is aan de energie die nodig is om alle elektronen van elkaar te scheiden. Een klein deel van de *interactie energie* verandert bij de supergeleidende faseovergang omdat de elektronen zich herorganiseren. Om deze verandering te meten zijn we begonnen met een eerder ontwikkelde algemene aanpak, die de *interactie energie* relateerd aan een meer algemene dielectrische functie, de impuls afhankelijke dielectrische functie $\epsilon(\mathbf{k}, \omega)$. Echter, om $\epsilon(\mathbf{k}, \omega)$ te kunnen meten moet men op het oppervlak van het materiaal niet alleen licht schijnen, maar ook elektronen van verschillende energieën. De huidige experimentele instrumenten om $\epsilon(\mathbf{k}, \omega)$ te meten hebben niet voldoende resolutie om de veranderingen bij de faseovergang te meten. De optische metingen die hier gepresenteerd worden hebben wel de benodigde gevoeligheid en leveren ons dus een deel van het antwoord.

Onze resultaten toonden aan dat een deel van de *interactie energie* (dat deel dat met optische spectroscopie gemeten kon worden en dat is opgeslagen in de “optische sector”) toeneemt in de supergeleidende toestand. Extrapolaties zijn gebruikt om de verandering af te schatten, waarbij rekening is gehouden met de gelaagde structuur van $\text{Bi}_2\text{Sr}_2\text{CaCu}_2\text{O}_{8+\delta}$. Het resultaat was van de orde van grootte van de condensatie energie (als de supergeleidende fase gezien wordt als een golf bal in de hole, dan is de condensatie energie het equivalent van de energie die nodig is om de bal uit de hole te halen. In andere woorden, het is de energie om de supergeleidende toestand te vernietigen).

In de klassieke supergeleiders verschijnt de supergeleidende fase omdat bij lage temperaturen er een extra aantrekkende wisselwerking tussen de elektronen ontstaat. Dit wordt gekwantificeerd door een verlaging van de *interactie energie*. Onze studie naar $\text{Bi}_2\text{Sr}_2\text{CaCu}_2\text{O}_{8+\delta}$ suggereert dat die energie juist toeneemt in de supergeleidende toestand (in andere woorden, de elektronen stoten elkaar meer af) en het kan dus niet zor-

gen voor een mechanisme dat het systeem in de supergeleidende fase brengt. Hoewel onze studie alleen een indicatie geeft wat betreft de totale *interactie energie*, legt het wel beperkingen op aan theoretische modellen, aangezien die de toename dienen te voorspellen van de *interactie energie*, opgeslagen in de “optische sector”, zoals door ons gemeten.

List of publications

Coulomb energy in $Bi_2Sr_2CaCu_2O_{8+\delta}$,

C.Presura, H.J. Molegraaf, D.Van der Marel, M. Turlakov and A.J. Leggett, in preparation.

Superconductivity by kinetic energy saving?,

D. van der Marel, H. J. A. Molegraaf, C. Presura and I. Santoso, Chapter in "Concepts in electron correlation", Edited by A. Hewson and V. Zlatic, in press, Kluwer (2003); cond-mat/0302169.

Superconductivity induced transfer of in-plane spectral weight in $Bi_2Sr_2CaCu_2O_{8+\delta}$,

H. J. A. Molegraaf, C. Presura, D. van der Marel, P. H. Kes, and M. Li Science 295, 2239-2241 (2002).

Charge ordering in the quarter-filled 1D-metal $\beta-Na_{0.33}V_2O_5$,

C.Presura, M.Popinciuc, P. H. M. van Loosdrecht, D. van der Marel, M. Mostovoy, G. Maris, T. T. M. Palstra, H. Yamada and Y. Ueda, Phys. Rev. Lett. 90, 026402 (2003).

Charge and sodium ordering in $\beta-Na_{0.33}V_2O_5$,

P. H. M. van Loosdrecht, C. Presura, M.Popinciuc, M. Mostovoy, G. Maris, T. T. M. Palstra, P.J.M. van Bentum, H. Yamada, T. Yamauchi and Y. Ueda, Journal of Superconductivity: Incorporating Novel Magnetism 15, 587 (2002).

Optical properties and electronic structure of $\alpha'-Na_{1-x}Ca_xV_2O_5$,

C. Presura, D. van der Marel, M. Dischner, C. Geibel and R.K. Kremer, Phys. Rev. B 62 (Issue 24), 16522 (2000).

Optical properties of $\alpha'-Na_xV_2O_5$,

M.J.Konstantinovic, Z.V.Popovic, V.V.Moshchalkov, C.Presura, R.Gajic, M.Isobe and Y.Ueda, Phys. Rev. B 65, 245103 (2002).

Optical properties, electronic structure and magnetism of $\alpha'-Na_xV_2O_5$,

M.J.Konstantinovic, Z.V.Popovic, C.Presura, R.Gajic, M.Isobe, Y.Ueda and V.V.Moshchalkov, Journal of Superconductivity: Incorporating Novel Magnetism 15, 495 (2002).

Low temperature ellipsometry of $\alpha'-NaV_2O_5$,

C. Presura, D. van der Marel, A. Damascelli and R. K. Kremer, Phys. Rev. B 61 (Issue 23), 15762-15765 (2000).

Optical spectroscopic study of the interplay of spin and charge in $\alpha'-NaV_2O_5$,

A. Damascelli, D. van der Marel, C. Presura, J. Jegoudez, and A. Revcolevschi, Phys. Rev. B 61 (Issue 4), 2535-2552, (2000).

Direct two-magnon optical absorption in α' - NaV_2O_5 : "charged" magnons,

A. Damascelli, D. van der Marel, M. Grninger, C. Presura, T.T.M.Palstra, J. Jegoudez, and A. Revcolevschi,
Phys. Rev. Lett. 81, 918-921 (1998).

Electronic structure of α' - NaV_2O_5 : wave-function-based embedded-cluster calculations,

L. Hozoi, C. Presura, C. de Graaf, and R. Broer,
Phys. Rev. B 67, 035117 (2003).

Infrared spectroscopic study of CuO : signatures of strong spin-phonon interaction and structural distortion,

A.B. Kuzmenko, D. van der Marel, P.J.M. van Bentum, E.A. Tishchenko, C.Presura and A.A. Bush
Phys. Rev. B 63, 94303 (2001).

Phonon anomalies versus magnetic ordering in CuO ,

A.B. Kuzmenko, D. van der Marel, P.J.M. van Bentum, E.A. Tishchenko, C.Presura and A.A. Bush
Physica B, 284-288, 1394 (2000).

Evidence for the opening of a band gap in nearly-stoichiometric VO ,

A.D.Rata, C.Presura, I.El'fimov, L. H. Tjeng and T. Hibma,
in preparation.

Electronic structure of epitaxial grown VO_x thin films,

D.Rata, A. Chezan, C.Presura and T. Hibma,
Surface Science, in press

Growth and properties of Cu_3N films and $\text{Cu}_3\text{N}/\gamma\text{-Fe}_4\text{N}$ bilayers,

D.M. Borsa, S. Grachev, C. Presura and D.O. Boerma,
Applied Physics Letters 80, 1823, (2002),

A practical method to solve an optimization problem with constraints,

C. Presura and I.H. Yetkiner,
working paper, CCSO Online Journal, WP No.7, available at <http://www.eco.rug.nl/ccso/quarterly/>

Electron-phonon coupling effects on Yb^{3+} spectra in several laser crystals,

A. Lupei, V. Lupei, C. Presura, V. Enaki and A. Petraru,
Journal of physics 11 (Issue 18), 3769-3778 (1999).

Resonant electron-phonon coupling of Yb^{3+} in YAG,

A. Lupei, V. Enaki, V. Lupei, C. Presura and A. Petraru,
Spectrochimica Acta 55 (Issue 4), 773-782 (1999).

Electron-phonon coupling for heavy RE^{3+} ions in crystals,

A. Lupei, V. Enaki, V. Lupei, C. Presura and A. Petraru,
Journal of alloys and compounds 275 (Issue 1), 196-199 (1998).

Acknowledgements

I think that if we reflect on who we are, or how we got here, we may discover a debt to others that would span a large space-time continuum. Many people who lived centuries ago succeeded, through their discoveries, to crucially influence our present-day life. Others, which we have met one day, may have stepped into our oblivion next day. I believe it is appropriate to acknowledge all of these unknown persons, and it is also necessary to acknowledge those people which we still remember, those we know that have directly shaped our lives and our work. The studies described in this thesis were performed in the Optical Solid State Physics group, University of Groningen, the Netherlands, and it is thus my pleasure to have this opportunity to express my sincere thanks to those who have contributed to this work in one way or another.

In particular I would like to express my gratitude towards my promotor Dirk van der Marel and my co-promotor Paul van Loosdrecht, for the valuable support, encouragement and guidance they have given me in these four years. With a strong theoretical knowledge, Dirk helped me orient better in the multitude of outputs my experiments generated. In every group meeting he tried to raise the scientific standard of our communications and the one of our understanding as high as possible, stretching our brains to limit sometimes. Putting a lot of passion in what he is doing (this sometimes just floods like rivers to his students), in many cases looking like a pure Jules Verne designed scientist, Dirk is a model for all of us, and all I can wish him for future is an even greater success in Geneva! To Paul I wish to warmly thank for the whole technical and theoretical help I received since he came in our group. Thanks to him I was able to grasp some knowledge on Raman spectroscopy techniques, and to finish the work on $\beta\text{-Na}_{0.33}\text{V}_2\text{O}_5$, despite some difficulties. I wonder how many versions of the paper he corrected. More than ten?

The work on $\alpha'\text{-NaV}_2\text{O}_5$ presented in the third chapter of this thesis is a compilation of results obtained with the support and enthusiasm of a number of individuals. As an experimentalist, I should acknowledge first my sample provider, R. K. Kremer. Not only that he provided me with the samples of $\alpha'\text{-NaV}_2\text{O}_5$, but also with single crystals of $\alpha'\text{-Na}_{1-x}\text{Ca}_x\text{V}_2\text{O}_5$, difficult to obtain at the time. Milan Konstantinovic borrowed me the samples of $\alpha'\text{-Na}_x\text{V}_2\text{O}_5$, where I was able to measure a resonance predicted by him in a previous paper. I am indebted also to H.J. Bron for his assistance with the chemical analysis of the $\alpha'\text{-Na}_{1-x}\text{Ca}_x\text{V}_2\text{O}_5$ crystals, and to Anton Chezan for his RBS checks. In the end, a lot of theoretical input was supplied by two very good theoreticians, Maxim Mostovoy and Liviu Hozoi. I am grateful for the cooperation I had with Maxim not only on $\alpha'\text{-NaV}_2\text{O}_5$, but also on $\beta\text{-Na}_{0.33}\text{V}_2\text{O}_5$. This gave me the also opportunity to admire how he tried to find always the "key" experimental value giving the most important "clue" about the physics involved. With Liviu is probably the other way around, since I have tried to keep him "with the feet on the ground", reminding him how the experimental results put always constraints, but nevertheless I really appreciate his new approach on $\alpha'\text{-NaV}_2\text{O}_5$.

The fourth chapter, namely the work on $\beta\text{-Na}_{0.33}\text{V}_2\text{O}_5$, was made possible by Prof. Dr. Yutaka Ueda, who supplied us with very high quality samples. Besides this, we had a vivid e-mail correspondence with him over the physical properties of $\beta\text{-Na}_{0.33}\text{V}_2\text{O}_5$. I acknowledge here my gratitude to him for the time he devoted to me in this way. We performed more structural studies on these samples in the group of Prof. Dr. Tom Palstra, together with his Ph.D. student Gabi Maris. I would like to thank here Gabi for all the work she put in this project. Tom Palstra deserves double acknowledgments, since I've received from him a lot of feed-back, encouragements and expert advice, not only for the work on $\beta\text{-Na}_{0.33}\text{V}_2\text{O}_5$, but also for the one on $\alpha'\text{-NaV}_2\text{O}_5$. Thank you, Tom! Even though last on this list, my former undergraduate Mihaita Popinciuc deserves congratulations not only for his careful way of building up an experimental set-up, but also for his patience of listening dissertations on history and politics during the long nights of measurements.

The work presented in the last chapter on $\text{Bi}_2\text{Sr}_2\text{CaCu}_2\text{O}_{8+\delta}$ was initiated by Prof. Dr. Tony Leggett, after an idea developed by him in one of his previous works. Later, during our encounters, his suggestions were gladly welcomed, together with the ones of his former student Misha Turlakov. They gave me the chance to put the problem in the right context, and to find the best way of extracting the needed information from the experimental data. The outcome may not have a strong point in the way we wanted, but, nevertheless, it may be useful. I would like to express my profound gratitude to Tony also for the careful reading of the thesis and his critical comments, together with the ones of the other two members of the reading committee, Prof. Dr. Mark Golden and Prof. Dr. Daniel Khomskii. The experimental results were obtained in collaboration with one of my best friends in Groningen, Hajo Molegraaf. We tried carefully to acquire the crucial data, including the one on the mid-infrared ellipsometer, where he performed all the work, and where he is the boss (he created the software to make it run, together with a useful software library used by all of us). Besides this, Hajo had a big influence in my attitude towards life, which I hope it will not go away (the attitude I mean...). He taught me how to be more flexible and accept things which I may not like, and how to be open. With my warm thanks, all I can say is "Good luck Hajo!", your future looks good!

Apart from my main projects, I was also involved in other projects, some of them being partly presented in the second chapter. In this way, I have had many times the wonderful experience to feel that, in some small way, I helped someone. I am grateful for the cooperation which Diana Rata proposed me on VO_x , where we tried to measure and interpret the optical spectra, under the careful supervision of dr. Hao Tjeng and Prof. Dr. T. Hibma. UGe_2 was another example, where I enjoyed collaborating with Diana Dulic, Montu Saxena and Catalin Didraga. Diana taught me how to better polish the samples, and make me wonder what precisely goes in the mind of girls, a general question still unanswered by humanity. I am also indebted to Dana Borsa for the collaboration on Cu_3N , to Alexey Kuz'menko for the one on CuO , and to Peter Steeneken for the magneto-optic measurements on EuO . Alexey, thanks for all the answers you gave me to my technical questions, and Peter, we will probably meet more often at Philips, but still, thanks! At last, but not the least, I would like to thank Hakan Yetkiner, with his exotic work (for me) in economics. It made me more confident that there are other things which I may do in life as well. Good luck in future Hakan!

However many collaborations, my daily life spined around my own group. Besides

the people already mentioned (Alexey and Hajo), I enjoyed a lot discussing with Patricio Mena. Patricio, you know what we wait from you and Anita! My roommate Artem Tsvetkov was a cheerful presence, and a good "answering machine" for short questions. Artem, thanks a lot not only for your warm friendship, but also also for the help you provided hosting me for two weeks! Cor Bos, our technician, gave me apples, screwdrivers, and headaches when he dismounted without notice my carefully aligned systems. However, everything was forgiven and compensated by his beautiful design of our new cryostat, and his crucial role in keeping the instruments running. Thanks Cor, and success with your French! I am also indebted to Frans van der Horst for his continuous technical support at the Unix station. And since no work succeeds without a good lunch, I would like to thank Katarzyna Karpinska and Arjen Kamp for the their welcomed presence. During my first years in the group, I've learned a lot from my predecessors Andrea Damascelli and Markus Grüniger, a pair of very good experimentalists. I think that me and Hajo always tried to do at least as good as they did. In those beginning years, also the help of Jeroen van der Eb and Anna-Maria Janner was heartily welcomed. But all our work would not have been efficient without the big help our secretary, Renate Nieborg. Thanks Renate, I really appreciate the kindness with which you tried to solve our complicated "paper works".

Coming from Romania in the Netherlands was for me like walking on a time bridge. However, it came to me as a surprise how many simple things I missed (sun, backyard farm, old friends, you name it...), and how the mother tongue is the easiest way to express your feelings. Fortunately, I had my Romanian friends, from RUG (Alex, Andrei, Catalin, Mihaela, Oana, Marius, Ionut, Bogdan, besides the ones already mentioned) and outside RUG (Ion, Dora, Mark, Simona, Mejdi, Gabi, Rodica, Razvan) to alleviate this homesickness. I would like to thank them all, with special mention to Flori and her husband Toni.

A great help in the beginning of my formation as physicist came from people from the Institute of Atomic Physics, Bucharest. I think that a great teacher was lost when dr. Stoicescu chose to continue in research, but that gave me the opportunity to meet him, and to learn to try to look always beyond the boundaries of what I am doing. Research was however the best choice for Prof. Dr. Voicu Lupei and his wife dr. Aurelia Lupei, who helped me in a crucial moment of my life, and who showed me by personal example the way a scientist should work, for which I would like to warmly thank them as well.

Last, but not the least, I would like to thank my wife Iulia.

Stellingen

1. The main optical absorption peak at 1 eV for $\mathbf{E} \parallel \mathbf{a}$ in α' - NaV_2O_5 is an on-rung bonding-antibonding transition. (Chapter 3)
2. The change in the valence state of individual vanadium atoms at the phase transition in α' - NaV_2O_5 is smaller than $0.06e$. (Chapter 3)
3. The electron doped α' - $\text{Na}_{1-x}\text{Ca}_x\text{V}_2\text{O}_5$ ($0 \leq x \leq 0.2$) does not show metallic behavior. (Chapter 3)
4. A strong electron-phonon coupling exists in β - $\text{Na}_{0.33}\text{V}_2\text{O}_5$, leading to the appearance of a large number of optical phonons below the metal-insulator transition. (Chapter 4)
5. The Coulomb interaction energy stored in the center of the Brillouin zone, for optimally and underdoped $\text{Bi}_2\text{Sr}_2\text{CaCu}_2\text{O}_{8+\delta}$, increases when the system enters the superconducting state. (Chapter 5)
6. At small periodic structures, scatterometry goes specular.
7. The more we have, the less its marginal utility is.
8. The success of the present capitalistic system is a result of giving our internal ego a possibility to satisfy itself.
9. It is less painful to learn from others mistakes, than to learn from our own mistakes.

